Colour Imaging Metrology of Solution-Processed Thin Films

Jack B P Atkinson

Supervised by Prof. Jonathan Howse

A thesis presented for the degree of

Doctor of Philosophy

University of Sheffield

School of Chemical, Materials and Biological Engineering

University of Sheffield

United Kingdom

April 17, 2025

Colour Imaging Metrology of Solution-Processed Thin Films

Abstract

Solution-processed thin polymer films combine favorable optoelectronic properties with low weight, flexibility and environmental friendliness, and are now manufactured at increasing scale. Scalable methods exhibit different drying kinetics, which govern final film thickness and morphology and thus device performance, there is a critical need for in-situ imaging metrology that can track dynamics and directly observe morphology across processes; colour imaging is currently underutilised in these applications.

First, we coupled in-situ broadband RGB reflectance imaging with a centre-point laser reflectance probe during spin coating to establish a calibration-free, colour-to-thickness relationship for dynamic solvent films. By mapping this relationship across a 3 wafer using a bespoke algorithm that resolves cyclical colour changes, we reconstructed transient solvent profiles with 5% accuracy and sufficient spatial resolution to detect common defects.

Next, we upgraded the imaging system with a multi-bandpass dichroic beam splitter and dual image projection to create a six-channel multispectral camera. Narrower detection bands and higher spectral resolution extended the upper thickness limit and enhanced model-based thickness reconstructions. We further demonstrated, for the first time, spectral reconstructions of thin-film interference using six-channel data, accurately recovering both the film's reflectance spectrum and thickness with fewer assumptions than RGB-model methods.

Finally, simultaneous red, green and blue laser illumination is used to produce trichromatic reflectance images, exhibiting strong interference fringes on much thicker films. The much lower linewidth makes these interference colours distinct from previous methods. A newly developed fringe-sequencing interpretation unambiguously retrieves dynamic film thickness, capabilities unattainable with single-wavelength probes. Demonstrated on blade-coated polymer films, this approach promises broad application in real-time metrology of dynamic thin films and interferometric measurements.

This work overcomes the traditional limitations of RGB imaging for thin-film metrology, enabling the widespread use of low-cost, high-resolution, spatially resolved and high-frame-rate RGB cameras across scalable coating processes.

Declaration

I, the author, confirm that the Thesis is my own work. I am aware of the University's Guidance on the Use of Unfair Means [1]. This work has not been previously been presented for an award at this, or any other, university.

[1] www.sheffield.ac.uk/ssid/unfair-means

Acknowledgements

Thank you to everyone who has made my work possible in a professional sense, specifically Professor Jonathan Howse for his supervision, and also to Dr. Andy Campbell, Dr. Hussam Muhamedsalih, Dr. Alan Dunbar, Dr. Alysin Nedoma, Dr. Steve Ebbens, and Chris Passmore who have been engaged in the work and provided great insight through their conversation. Thanks to everyone from the University of Cambridge, the University of Huddersfield and the industrial partners of the Responsive Manufacturing of High Value Thin to Thick Films grant. Thanks to Professor Joan Cordiner for making the department a fantastic place to study.

Special thanks to my parents for instilling in me my work ethic; and to my brother, who is still the hardest working person I know. Thanks to all of my friends, in Sheffield and back home, especially Mahdi, who has kept me company at my desk for the past few years. Of course, a special thanks to Holly, who has supported me endlessly while I do this work. I think it is about time I finished - so I can be the one with a *proper* job.

Contents

List of Figures

List of Tables

Abbreviations

AFM atomic force microscopy

BHJ bulk heterojunction

CCD charge coupled device

CMOS complementary metal-oxide semiconductor

CNN convolutional neural network

CoD coefficent of determination

F8BT poly(9,9-dioctylfluorene-alt-benzothiadiazole)

FFT fast Fourier transform

FWHM full width half maximum

HSI hyperspectral imaging

HSLI hyperspectral luminescence imaging

MBP multi-bandpass

MSE mean square error

NIR near infrared

OFET organic field effect transistor

OLED organic light emitting diode

OPD optical path difference

OPV organic photovoltaic

OSC organic solar cell

P3HT poly(3-hexylthiophene)

PCBM phenyl-C61-butyricb acid methyl ester

PCE power conversion efficiency

PEDOT poly(3,4-ethylenedioxythiophene)

PEG polyethylene glycol

PFB poly(9,9-dioctylfluorene-co-bis-N,N'-(4-butylphenyl)-bis-N,N'-phenyl-1,4-phenylene-diamene)

PffBT4T-2OD poly[(5,6-difluoro-2,1,3-benzothiadiazol-4,7-diyl)-alt-(3,3"'-di(2-octyldodecyl)-2,2';5',2";5",2"'-quaterthiophen-5,5-diyl)]

PFO polydioctylfluorene

PI polyisoprene

PMMA polymethyl metacrylate

PSS polystyrene sulfonate

PVD physical vapour deposition

R2R reel-to-reel

rpm revolutions per minute

SOG spun-on glass

TIPS tri-isopropylsilyly-ethynyl

TMM transfer matrix method

UV ultraviolet

VIS visible (light)

Chapter 1

Introduction

Thin films are an essential class of materials that have revolutionised numerous scientific and technological fields due to their unique properties and versatility. Defined by their extremely small thickness, often ranging from a few nanometres to several micrometres, thin films exhibit distinct physical and chemical behaviours compared to their bulk counterparts. Their reduced thicknesses enable precise control over optical, electrical, and mechanical properties, making them important in applications such as electronics, optics, coatings, and energy harvesting. Thin films are widely used in the development of semiconductors, photovoltaic cells, protective coatings, and flexible electronics, where their ability to enhance performance while minimising material usage, due to high interface area to volume ratio, is particularly advantageous. The fabrication of thin films involves a variety of techniques, broadly classified into physical and chemical deposition methods, including vacuum-based processes such as sputtering and evaporation, and solution-based approaches.

Solution processing has been widely adopted and offers several advantages, including scalability, reduced energy consumption, and improved environmental sustainability. This group of processing methods are particularly suited to certain classes and materials of thin films, enabling the production of high-quality films through techniques such as spin-coating, slot-die coating, blade coating, gravure coating, inkjet printing, and dip coating. To fully harness the potential of solution-processed thin films, *in situ* characterisation techniques are widely used. By providing real-time insights into the dynamic processes occurring during fabrication, *in situ* methods facilitate a deeper understanding of film formation mechanisms, ultimately aiding in the optimisation of material properties and scale-up strategies.

Imaging metrology, which enables the quantification of film characteristics through direct imaging across two-dimensional areas, has emerged as one of the most powerful of these techniques. Colour imaging, despite its inherently low spectral resolution, is an attractive option because of its affordability and ease of implementation with the widespread adoption of Bayer-filtered colour cameras. However, its potential for insight remains largely underused in traditional thin film metrology, where complexity and ambiguity often arise, meaning that high-resolution spectroscopic single-point or monochromatic 2D techniques are typically favoured for straightforward interpretation.

1.1 Research question and aims

This thesis answers the following question:

> Can Bayer filters in standard colour cameras be leveraged to develop new techniques, or improve existing ones, suitable for the *in situ* imaging metrology of solution-processed thin films?

This narrows the aims of the research in three ways. Firstly, the techniques must be direct-imaging to provide spatially resolved film information. Secondly, to be suitable for *in situ* metrology, the frame rate and exposure times of the camera must be high enough to provide interpretable data that have not been distorted by the film movement (the quantitative requirements of this differ between film fabrication techniques). This is the main challenge that prevents commercially available systems, often based on some form of z-scanning interferometry, from companies such as Bruker and Polytec, being employed. Lastly, because of the optical nature of the techniques, they must be able to recover film thickness or film refractive index, or, ideally, both.

In order to answer the research question effectively, this thesis aims to:

1. Lay out a clear picture of the underlying physical principles, developments, trends and current state of techniques that meet the requirements for *in situ* thin film analysis

2. Develop a full and quantifiable understanding of the fundamental limits of broadband colour imaging for film characterisation

3. Overcome the many-to-one colour-to-thickness mappings experienced by broadband colour imaging of films

4. Explore the effectiveness of spectral reconstruction techniques to enhance the power of colour imaging for film metrology

5. Demonstrate the effectiveness of the Bayer filter as a tool in imaging metrology when paired with multiple wavelength monochromatic illumination

1.2 Thesis structure

The remainder of Chapter 1 will outline the structure of the thesis and give details on the publications that have been, are in the process of being, or plan to be submitted as a result of the work. The individual contributions of the author to each publication will be listed below. As a result of the thesis chapters being published in separate papers, the nomenclature in each chapter is defined as it is first used in that chapter. Complete continuity between the papers was not possible; however, it has mostly been preserved.

Chapter 2 is a literature review that introduces polymer thin films, their importance, and their applications. After this, spin coating, blade coating and slot die coating are discussed as solution-based processing methods. The interference phenomena of thin films is then presented in order to give a background in the optical physics that underpins the reflection-based techniques. Other techniques based on different phenomena, such as ellipsometry, are considered out of scope and not deeply discussed. Subsequently, applications of *in situ* reflectance measurements over a range of fabrication methods are then discussed using prominent or groundbreaking examples from the literature to give a full and current view of metrology. This starts at more mature point probe techniques including laser reflection and scattering and white light reflectometry, and moves on to monochromatic imaging, and then finally colour and spectral imaging.

The next three chapters (3 - 5) are the main results chapters of the thesis and are formatted individually as papers with individual abstract, introduction, theory, materials and methods, results and discussion sections. Each chapter has a cover page, that introduces the work in the broader context of the thesis, and an individual reference section where the references used in that chapter can be found. The numbering of references is maintained throughout, and a complete bibliography containing all references is included at the end

of the document.

The sixth chapter of the thesis will be a conclusion in which the results and impact of the work are brought together as a whole. The research question is reflected upon, and the major contributions of the thesis to the field are highlighted. The thesis ends then by recommending the direction of possible future work.

1.3 Included publications

1.3.1 Chapter 3

The entire content of Chapter 3 was published in *Optics and Lasers in Engineering* **184** (2025) with myself (Jack B.P. Atkinson) and first author and my supervisor (Jonathan R. Howse) as corresponding author [1].

In this paper my personal contribution was to writing the original draft, visualisations, software, methodology, investigation, formal analysis, and data curation. Howse's contributions were reviewing and editing the manuscript, validation, supervision, resources, project administration, methodology, funding acquisition, and conceptualisation.

1.3.2 Chapter 4

All of content of Chapter 4 is submitted to *Optics Express* with myself (Jack B.P. Atkinson) and first author, and my supervisor (Jonathan R. Howse) as corresponding author. In addition, Stephen Ebbens from the University of Sheffield is a named author.

In this paper my personal contribution was to writing the original draft, visualisations, software, methodology, investigation, formal analysis, data curation and conceptualisation. Howse's contributions were reviewing and editing the manuscript, supervision, resources, project administration, funding acquisition, and conceptualisation. Ebben's contributions were reviewing and editing the manuscript and equipment (loan of the Optosplit module).

1.3.3 Chapter 5

A future submission of the work in Chapter 5 is planned, with myself (Jack B.P. Atkinson) and first author, and my supervisor (Jonathan R. Howse) as corresponding author. In addition, Hussam Muhamedsalih from the Centre for Precision Technologies at the University of Huddersfield is also a named author.

Prior to journal publication, this work was also presented at the Materials Research Society (MRS) Fall Meeting in Boston on 3 December 2024 in the Optical and Electrical Studies I (CH01.06.03) symposium.

In this paper my personal contribution was to writing the original draft, visualisations, software, methodology, investigation, formal analysis, data curation, and conceptualisation. Howse's contributions were reviewing and editing the manuscript, supervision, resources, project administration, funding acquisition, and conceptualisation. Muhamedsalih's contributions were reviewing and editing the manuscript, resources, equipment (white light source and AOTF), and validation.

References

[1] Jack B.P. Atkinson and Jonathan R. Howse. “In-situ full-wafer metrology via coupled white light and monochromatic stroboscopic illumination”. In: *Optics and Lasers in Engineering* 184.P2 (2025), p. 108692. DOI: 10.1016/j.optlaseng.2024.108692.

Chapter 2

Literature review

2.1 Polymer Thin Films

Polymer thin films have emerged as a versatile and extensively studied class of materials owing to their unique and often tunable properties [2], which offer a wide range of applications. These films exhibit remarkable optical, electrical, and mechanical behaviours that often differ from those of their bulk counterparts, particularly at the nanoscale [3]. Their study has yielded significant insights into polymer physics, establishing them as excellent model systems for investigating both fundamental and applied aspects of materials science.

In the field of electronics, polymer films are employed as dielectric layers in capacitors, gate insulators in transistors [4], and components to enhance lithium-ion battery performance [5]. They also serve as active layers in organic light emitting diodes (OLEDs) and organic photovoltaics (OPVs) [6][7]. The inherent flexibility, lightweight nature, and cost-effectiveness, partly attributable to solution processing, render them ideal for flexible and wearable electronics. Furthermore, polymers can be functionalised with specific chemical groups to broaden their applications, including environmental sensors [8], biosensors, drug delivery systems, and the optimisation of light harvesting and emission [9].

Polymer thin films are also widely utilised as model systems in experimental and theoretical studies of polymer dynamics and phase behaviour [10] [11]. Their optical transparency enables the application of nondestructive optical characterisation techniques such as specular laser reflectance, off-specular laser scattering, spectral reflectance, and ellipsometry [12]. These attributes make polymer thin films particularly suited for studying fundamental processes, including thin film wetting and dewetting, *in situ* film formation,

and instability mechanisms under various environmental conditions.

2.1.1 Spin-coating

Spin coating refers to the process in which a solution is deposited on a disk that is then spun at speeds of a few thousand revolutions per minute (rpm). This results in thinning due to combined hydrodynamic and evaporative effects and is often reported in the literature as a series of four distinct stages [13] [14], as shown in Figure 2.1.

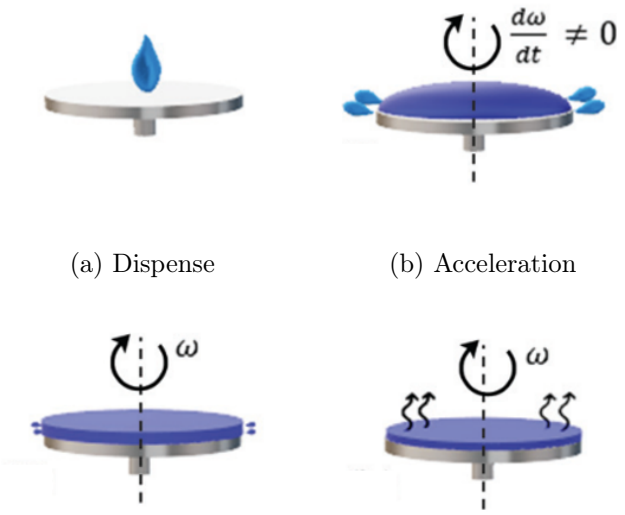

(a) Dispense

(b) Acceleration

(c) Hydrodynamic thinning

(d) Solvent evaporation

Figure 2.1: Schematic outline of the four spin coating stages, reproduced from [14].

1. **Dispense stage -** when the solution is deposited onto the centre of the stationary substrate. This stage may also happen while the substrate is already spinning at a low, constant angular velocity when working with systems where the substrate and solution are reactive or if the solvent is extremely volatile.

2. **Acceleration stage -** when the angular velocity of the substrate increases to the spin speed, $\frac{\partial \omega}{\partial t} \neq 0$. More complex spin profiles have been reported; commonly, initial acceleration to a relatively low speed for a few seconds to spread the solution across the substrate surface and then a second acceleration to the nominal spin speed.

3. **Hydrodynamic thinning stage -** at this stage, fluid viscous forces dominate thinning behaviour and stable fluid outflow can be observed. Edge effects can cause a

slightly thicker rim [15] and fluid is ejected from this in droplets (spin-off).

4. **Solvent evaporation stage -** the fluid thickness has decreased to a point where there is only a very small fluid flow and the evaporation of the solvent is now the main contributor to thinning. As the solvent evaporates, the concentration of the solution reaches a point where the increased viscosity vitrifies the film in place.

Angular velocity, ω, is therefore a highly important process variable. The final thickness of the spun coat film, for Newtonian simple solutions, can be experimentally shown to be proportional to the inverse of the square root of angular velocity, as in Equation 2.1. After these four steps, annealing, heat treatments, and drying methods may be utilised in order to enhance film properties by changing morphology and completely removing excess solvent.

$$h_f \propto \frac{1}{\sqrt{\omega}} \tag{2.1}$$

The first model of the spin coating process, developed by Emsile, Bonner and Peck (EBP) in 1958 [16], was theoretical, one-dimensional, for strictly Newtonian fluids and ignored the effects of evaporation. By equating the viscous and centrifugal forces as in Equation 2.2, the radial velocity of the liquid, v, can be found at any point in a polar coordinate system[1] (r, θ, z).

$$-\eta \frac{\partial^2 v}{\partial t^2} = \rho \omega^2 r \tag{2.2}$$

With integrating employing appropriate boundary conditions, the resulting expression for v can be substituted into Equation 2.3 for q, the radial flow per unit length of circumference

$$q = \int_0^h v \, dz \; = \frac{\rho \omega^2 r h^3}{3\eta} \tag{2.3}$$

The result is a differential in terms of the rate of fluid thinning, $\frac{\partial h}{\partial t}$, and the rate of radial outflow, $\frac{\partial h}{\partial r}$, shown in Equation 2.4, Where $K = \frac{\rho \omega^2}{3\eta}$, ρ is density and η is viscosity.

$$\frac{\partial h}{\partial t} = -K \frac{1}{r} \frac{\partial}{\partial r}(r^2 h^3) \tag{2.4}$$

This equation has a special solution that depends only on t, shown in Equation 2.5, that describes the rate of fluid height as a function of time, and is a key result of the EBP

[1] Note that Equation 2.2 is not a function of θ and is therefore axisymmetric.

model.

$$\frac{dh}{dt} = -2Kh^3 \tag{2.5}$$

The model is limited in ability to calculate final film thickness accurately due to the omission of evaporative effects and struggles in scenarios where Newtonian behaviour is not applicable.

In 1978 Meyerhofer included evaporative effects [13] as a direct extension of the EBP model simply by adding an additional evaporation term, e as seen in Equation 2.6.

$$\frac{dh}{dt} = -2Kh^3 - e \tag{2.6}$$

Meyerhofer established that there was a transition between the hydrodynamic thinning that controls the fluid profile at the beginning of the process and evaporative thinning that dominates in the latter stages. The point of transition between the two thinning stages, assuming that it is abrupt, is found by Equation 2.7, where the thinning by evaporation is equal to the thinning by fluid flow. Here C is the normalised solution concentration of $[0, 1]$ and h_0 is the initial film thickness.

$$e = \frac{(1 - C)2\omega^2\rho h_0^3}{3\eta} \tag{2.7}$$

Spin coating has proved an inherently difficult process to model qualitatively because a mass balance approach breaks down at the spin-off stage, meaning that the resulting film thickness is not a straightforward calculation. A high dependence on the solution properties is also problematic. Despite this, the Meyerhofer model continues to be a useful tool and many subsequent *in situ* studies have confirmed it's validity in a variety of applications. These are expanded on in further detail in Section 2.3.

Spin coating's primary advantage lies in its ability to rapidly produce uniform and reproducible films. Consequently, it is widely employed in semiconductor manufacturing for photoresist application on substrates, typically 300 mm (12 inch) wafers. Moreover, it is an excellent technique for lab-scale fabrication and the research and development of polymer devices such as OPVs [17][18] and organic field effect transistors (OFETs) [19] [20] [21] [22]. In addition, a variety of material systems, including small molecule semiconductors, colloids, fullerenes, and blends, can be easily accommodated. However,

spin coating is less suited to large-scale production due to its inherent batch nature and the practical limits on substrate size. Furthermore, when large-scale fabrication is required or the solution is particularly expensive, spin coating is often not preferred because it can incur losses of up to 98% of the solution volume as spin-off [23].

2.1.2 Blade coating

Blade coating, also known as doctor blade coating, is a film deposition technique in which a solution is first deposited onto a substrate before a blade is drawn over it at a predetermined gap. The capillary flow of the solution fills the gap and, as the blade moves, forms a uniform wet film (see Figure 2.2). The speed of the blade is a critical factor [24]; at lower blade speeds, the process operates in the evaporation regime, whereas at higher speeds it enters the Landau-Levich regime [25], where viscous forces dominate. This regime is preferred because it improves uniformity and reduces processing time, both of which are essential for scale-up. Other important parameters include the gap setting, the blade geometry, and the volatility of the ink system. In 2022 Song et al. used a physics-informed machine learning algorithm to optimise the conditions for blade coating, highlighting the significant challenges of finding and operating within the coating window [26].

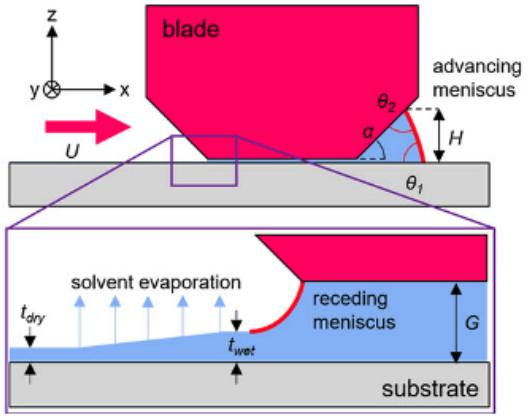

Figure 2.2: Schematic diagram of blade coating , from [24].

Gu et al. [27] note that a major advantage of meniscus-guided deposition techniques, such as blade coating and slot-die coating, is the ability to process semiconducting polymers onto flexible substrates that are lightweight and transparent, in contrast to the rigid, heavy, and opaque nature of silicon-based methods. Furthermore, numerous studies have shown that controlling the morphology of blade-coated films can enhance the performance

of devices, as observed in the fabrication of polymer solar cells [28] and polymer semiconducting transistors [29]. Recently, blade coating has enabled the large-area fabrication of perovskite solar cells up to 15 by 15 cm^2 [30].

Although blade coating is technically compatible with processing reel-to-reel (R2R) as doctor blades on a gravure roll [31], slot-die coating is employed more frequently. Blade coating thus represents a middle ground, offering some of the ease of use and lab-scale advantages of spin coating while enabling high-efficiency coating over much larger areas. Weng et al. highlight that the transition from spin coating to meniscus-guided printing processes in organic solar cell fabrication is challenging due to markedly different drying kinetics [17]. However, once this barrier is overcome, the move to slot-die coating, with more similar geometry and drying kinetics, offers a promising route for further scale-up.

2.1.3 Slot-die coating

The slot die coating process involves a solution being pumped through a precision machined metal slot die head into the gap between the head and the substrate, while relative movement between them leaves behind a wet film of known thickness. It shares many similarities with blade coating in dynamics and can be scaled up perpendicular to coating direction in a similar way, by increasing the aspect ratio of the slot die head. In contrast to blade coating, slot die coating has the advantage of being continuous because indefinite pumping of more solution is possible. Due to this, slot die coating is applied in reel-to-reel (R2R) coating, where film lengths of many hundreds of metres are routinely reached by utilising flexible substrates and series of rollers. Slot die coating can also be achieved at smaller lab scales by finite movement and of the substrate or the head, and repositioning after runs. In all configurations the wet film left on the substrate dries through evaporation, either under ambient conditions or with some additional heating or airflow. Some common slot die coating setups can be seen in Figure 2.3.

When viscous effects are small and operating limits dictated by capillary pressure in the coating bed, capillary models can be used to effectively estimate operating parameters to achieve defect-free films. A diagram of a slot die head under these circumstances is shown in Figure 2.4a. The first quantification of these operating limits was by Ruschak in 1976 [33] and were based on an extension of the Landau-Levich [34] film coating theory; here, the similarities with blade coating are apparent. The model was then further modified by

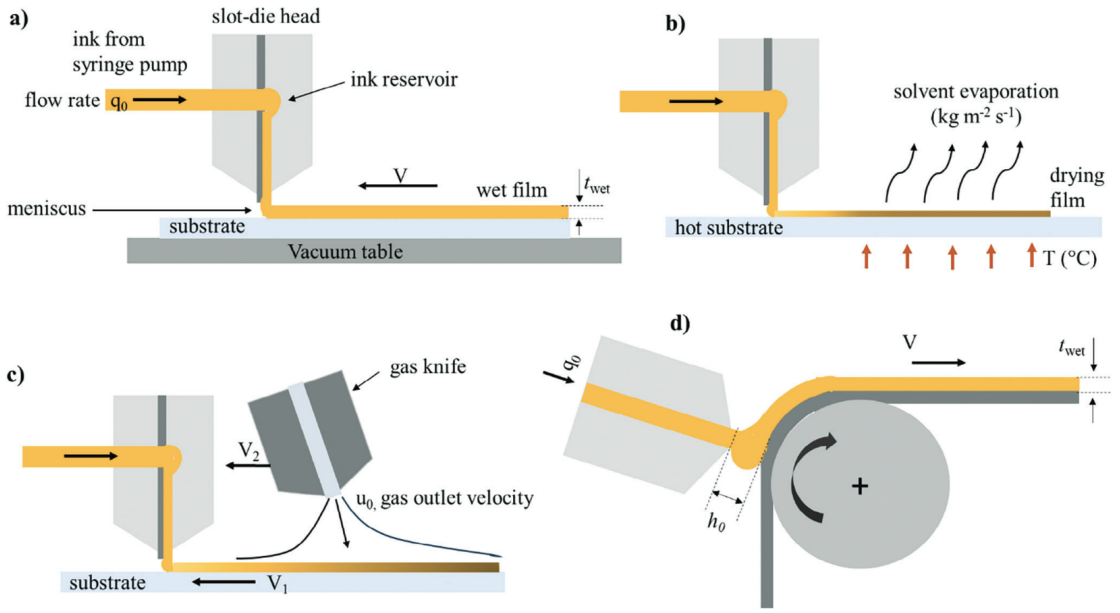

Figure 2.3: Diagrams of the slot die coating process a) as standard b) on a substrate with additional heating to force solvent evaporation c) with the use of a downstream gas knife d) in a slot die over roller configuration often used in R2R processing, from [32].

Higgins and Scriven in 1979 [35], finding that the limits of pressure, Δp, and the thickness of the wet film, t, are set by the capillary number $Ca = \frac{\mu U}{\sigma_d}$ in two simultaneous inequalities, summarised by the operating space in Figure 2.4b. Determining operating parameters such as the web speed, pump rate, gap height, and shim/meniscus guide configuration that keep a specific ink inside this window to prevent defects is one of the main challenges of slot die coating.

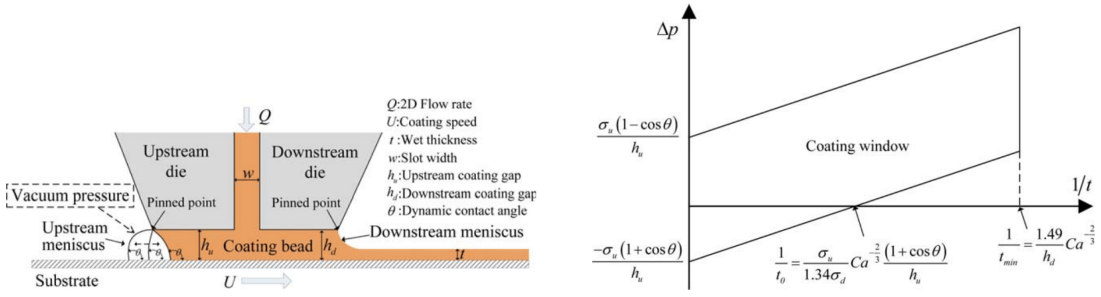

(a) Slot-die head and menisci in capillary flow (b) Capillary model coating window

Figure 2.4: Schematic diagrams of slot-die coating head and window based off capillary models, from [36].

Slot die coating is emerging as the leading technology for producing functional films at scale for use in devices [37]. In the development of printed films, *in situ* metrology techniques that can elucidate the drying kinetics and mechanisms by which the final film's

morphology is formed are valuable for the rational development of inks. In addition, during production, large-area metrology is necessary for quality monitoring and defect detection and characterisation, and closed-loop feedback with such tools as sensors is another focus of the field.

2.2 Film interference effects

This section aims to give a theory of thin film interference and background on the optical effects relevant to the work in this thesis and in the following sections on *in situ* optical metrology of thin films. The fundamental optical phenomenon that occurs is amplitude-splitting interferometry due to optical path differences introduced as the film system splits a beam of incident light. In simple terms, when light that has taken different paths through the film is superimposed, on a screen, at a camera sensor, or in the observers' eye, predictable and characteristic interference fringes are detected.

The Fresnel equations were derived by Augustin-Jean Fresnel in 1827, who was the first to propose that light is a transverse wave, something that earlier principles, both of Fermat[2] in 1662 and Hyugens[3] in 1678, do not capture. They are a result of Maxwell's equations solved at an interface. As a consequence of Fresnel's work, polarisation, the relative orientation of the electric and magnetic fields in light, could be understood quantitatively. The equations link the refractive indices of the two mediums n_{m-1} (incidence) and n_m (refractive) with the angle of incidence θ_{m-1} and refraction θ_m to predict the proportion of reflected, r, or transmitted (refracted), t, amplitude of each polarisation state:

- s-polarised light, or transverse electric (TE), where the electric wave is perpendicular to the plane of incidence

$$r_s = \frac{E_r}{E} = \frac{n_{m-1}\cos(\theta_{m-1}) - n_m\cos(\theta_m)}{n_{m-1}\cos(\theta_{m-1}) + n_m\cos(\theta_m)} \tag{2.8}$$

$$t_s = \frac{E_t}{E} = \frac{2n_{m-1}\cos(\theta_{m-1})}{n_{m-1}\cos(\theta_{m-1}) + n_m\cos(\theta_m)} \tag{2.9}$$

- p-polarised light, or transverse magnetic (TM), where the electric field is parallel to

[2]Fermat's principle states that the path taken by a ray between two given points is the path that can be travelled in the least time

[3]Huygens' principle states that every point on a wavefront is itself the source of spherical wavelets, and the secondary wavelets emanating from different points mutually interfere

the plane of incidence

$$r_p = \frac{E_r}{E} = \frac{n_{m-1}\cos(\theta_m) - n_m\cos(\theta_{m-1})}{n_{m-1}\cos(\theta_m) + n_m\cos(\theta_{m-1})} \tag{2.10}$$

$$t_p = \frac{E_t}{E} = \frac{2n_{m-1}\cos(\theta_{m-1})}{n_{m-1}\cos(\theta_m) + n_m\cos(\theta_{m-1})} \tag{2.11}$$

Figure 2.5 shows these two polarisation states schematically. These four equations simplify significantly at normal incidence $\cos\theta_{m-1} = \cos(\theta_m) = 1$. Here, the dependence on polarisation collapses as shown in Equations 2.12 and 2.13. This is an advantage of optical techniques that utilise normally incident light.

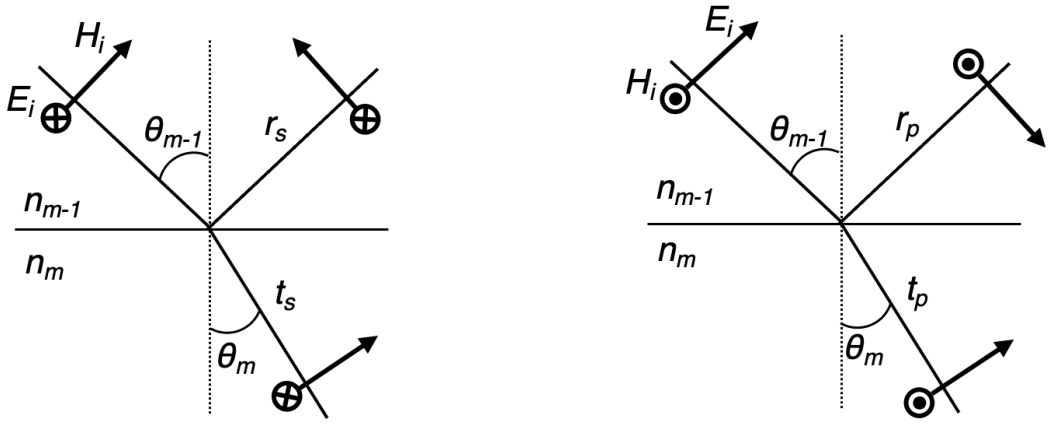

(a) Transverse electric

(b) Transverse magnetic

Figure 2.5: Interaction of polarised light at an interface

$$r = \frac{n_m - n_{m-1}}{n_m + n_{m_1}} \tag{2.12}$$

$$t = \frac{2n_m}{n_m - n_{m-1}} \tag{2.13}$$

Unpolarised light can be considered a rapidly varying random combination of the two polarisation states, and the approximation in Equations 2.14 and 2.15 are often used when unpolarised light is utilised.

$$r = \frac{r_s + r_p}{2} \tag{2.14}$$

$$t = \frac{t_s + t_p}{2} \tag{2.15}$$

These equations can be expressed as only a function of the angle of incidence θ_{m-1}, as this

is usually known or more readily measured, by applying Snells' law.

$$\frac{\sin(\theta_{m-1})}{\sin(\theta_m)} = \frac{n_m}{n_{m-1}} = \frac{v_{m-1}}{v_m} \tag{2.16}$$

There is a π phase shift between the beams that are reflected internally and externally. In other words, when a wave that is in a lower refractive index medium is reflected from a higher refractive index medium, that is $n_{m-1} < n_m$, then the reflected wave has a phase shift π relative to the incident wave. This is an important phenomena to account for in some systems. For example, in the thin film system commonly used to observe Newtons rings, the transmission through glass-air-glass where $n_0 > n_1 < n_2$, the extra phase difference will need to be considered and will effect the interference pattern. However, considering the reflection from a dielectric thin film system, air-film-Si, where $n_0 > n_1 > n_2$ is extremely likely, the reflection does not contain a relative phase shift. A more rigorous treatment of this is discussed in Section 2.2.2.

2.2.1 Two beam approximation

A simple amplitude-splitting interference system can be constructed with a single layer film illuminated by monochromatic light. We first consider only the reflection from the top surface of the film and the bottom surface of the film, as in Figure 2.6. The analysis of this system gives important results for interpreting specular laser reflectance signals. Here, the interference pattern is simply formed by the optical path difference, Δ, introduced between the two beams between points C and D.

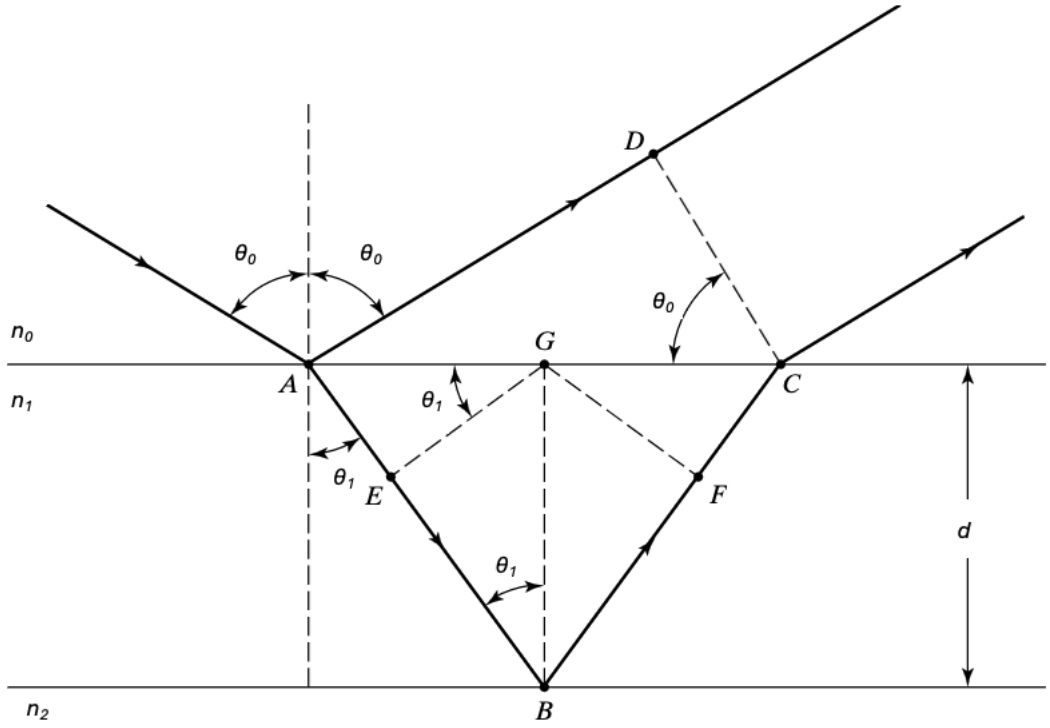

Figure 2.6: Two beam interference in a thin film

$$\Delta = n_1(AB + BC) - n_0(AD) \tag{2.17}$$

Geometrically it can be shown that

$$AB = BC = \frac{d}{\cos(\theta_1)} \tag{2.18}$$

$$AC = 2d\tan(\theta_1) \tag{2.19}$$

$$AD = AC\sin(\theta_0) = 2d\tan(\theta_1)\sin(\theta_0) \tag{2.20}$$

Substituting the relations from 2.18 and 2.20 result in the following expression for the optical path difference

$$\Delta = n_1\left(\frac{2d}{\cos(\theta_1)}\right) - n_0\left(2d\tan(\theta_1)\sin(\theta_0)\right) \tag{2.21}$$

Applying Snell's Law, $n_0 \sin(\theta_0) = n_1 \sin(\theta_1)$ allows for this to be expressed in terms of the angle of refraction in the film, θ_1

$$\Delta = n_1 \left(\frac{2d}{\cos(\theta_1)} \right) - n_0(2d \tan(\theta_1) n_1 \sin(\theta_1)) \tag{2.22}$$

By assuming the surrounding medium is air, $n_0 = 1$, we can simplify and factorise

$$\Delta = 2dn_1 \left(\frac{1}{\cos(\theta_1)} - \tan(\theta_1) \sin(\theta_1) \right) \tag{2.23}$$

Then using the trigonometric identity as in Equation 2.24 to simplify

$$\frac{1}{\cos(\theta)} - \tan(\theta) \sin(\theta) \equiv \cos(\theta) \tag{2.24}$$

results in the following expression

$$\Delta = 2dn_1 \cos(\theta_1) \tag{2.25}$$

So, as expected, the optical path difference depends on the refractive index of the film, it's thickness, and the angle of incidence.

In order for Δ to produce constructive interference from an incident beam of wavelength λ, it must be equal to a integer multiple, m, of that wavelength. This results in beams at points D and C that are completely in phase, because they have been shifted either by 0 (where $d = 0$), or by $m \cdot 2\pi$. Conversely, destructive interference occurs when the phase shift is $m \cdot \pi$ or when Δ is equal to a half integer of the wavelength. These conditions for total constructive and total destructive interference are shown below in equations 2.26 and 2.27 respectively.

$$2dn_1 \cos(\theta_1) = m\lambda \tag{2.26}$$

$$2dn_1 \cos(\theta_1) = \left(m + \frac{1}{2} \right) \lambda \tag{2.27}$$

Thus, information about the refractive index, thickness and incident angle are encoded in the interference pattern. When the refractive index and incident angle are constant, one can deduce the relative thickness of the film by inspecting the fringes that occur at points of equal thickness, sometimes called Fizeau fringes, famous examples including Newton's rings, shown in Figure 2.7.

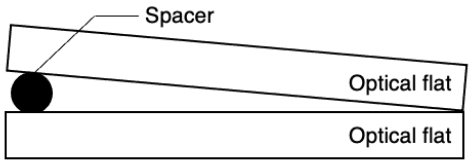

(a) Fitzeau fringe setup of a glass-air-glass wedge shaped film system

(b) The resultant fringes of equal thickness when illuminated with monochromatic light, adapted from [38]

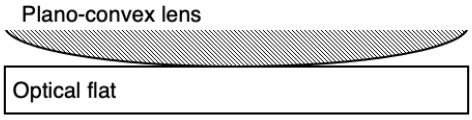

(c) Newtons rings setup of a glass-air-glass film system

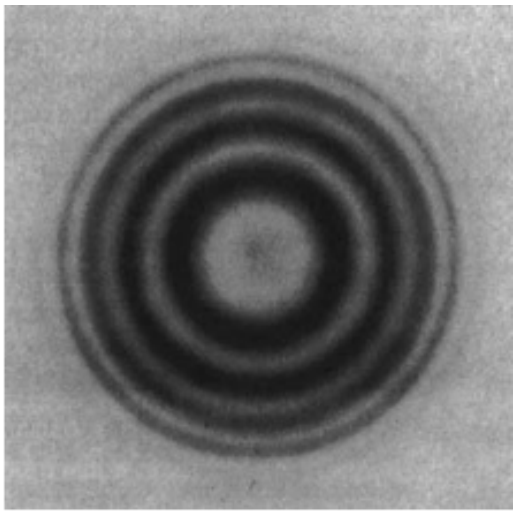

(d) The resultant Newton's rings when illuminated with monochromatic light, taken from [39]

Figure 2.7: Common fringes of equal thickness

In specular reflection studies of a thinning film, the application of the constraint in 2.26, now through time as the film thins instead of spatially, allows a thickness change, Δd to be resolved between the two points in time where sequential peaks (or troughs) m and $m+1$ occur. This is called the Bragg condition for thin film interference, due to the parallels with Bragg's law in the field of x-ray crystallography [40], and is shown in Equation 2.28.

$$\Delta d = \frac{\lambda}{2n_1 \cos(\theta_1)} \tag{2.28}$$

2.2.2 Multiple beam interference using Stokes relations

For the rigorous treatment of thin film interference, we must consider the infinite series of internal reflections that occur. To do this, the Stokes relations, that link Fresnel coefficients, as seen in Equations 2.10 to 2.13 in the previous Section 2.2, for proportions of reflected, r, and transmitted, t, incident lights' electric field, E_i, are used. These relations, given in Equations 2.29 and 2.30, were first formulated by Sir George Stokes in 1852 and are schematically represented in Figure 2.8, showing an interface where $n_1 < n_2$. They arise

from the principal of time reversal, and thus are formulated by assuming that there is no absorbance, something that holds well with polymer films.

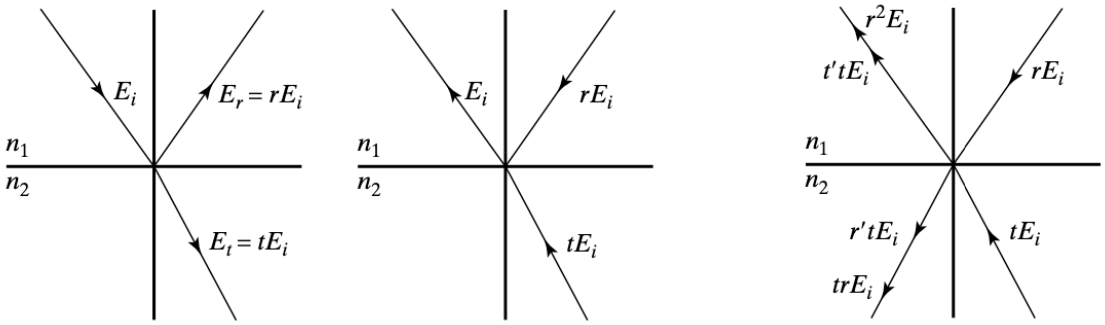

(a) Forwards in time (b) Backwards in time (c) Backwards in time, with all possible rays

Figure 2.8: Schematic representation of the formulation of Stokes relations, taken from [41]

In Figure 2.8a, incident light on a boundary is split between the reflected and refracted part according to the Fresnel coefficients (as in Figure 2.5). Applying the principal of ray reversibility, the scenario depicted in Figure 2.8b is possible, however, the situation where two incident rays only produce one resultant ray is not representative. Figure 2.8c shows the same two incident rays producing the more general two resultant rays, where new quantities r' and t' are the reflection and transmission coefficients for a ray incident from medium 2. In this case, the laws of conservation of energy then result in Stokes relations.

$$tt' = 1 - r^2 \tag{2.29}$$

$$r = -r' \tag{2.30}$$

The phase change discussed qualitatively in Section 2.2 now can clearly be quantitatively understood by inspection of Equation 2.30. This may be more readily interpreted as a π phase change on internal reflection by using Euler's identity to express the equation as $r = r'e^{i\pi}$.

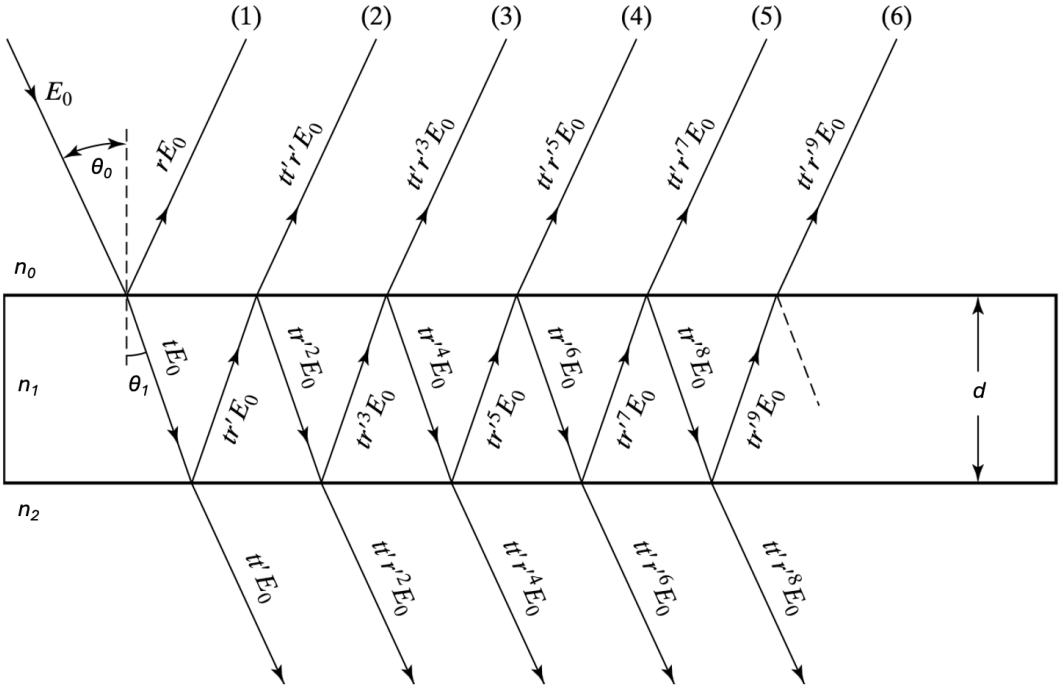

Figure 2.9: Multiple beam interference in a thin film, where n_0 and n_2 are the same surrounding medium

Figure 2.9 shows an extension of Figure 2.6 that now depicts the infinite resulting parallel reflected or transmitted beams due to internal reflection. The phase difference between successive reflected beams (1-6), as before, is given by

$$\delta = k\Delta = \frac{2n_1 d\cos(\theta_1)}{\lambda} \tag{2.31}$$

By expressing the incident ray as $E_0 e^{i\omega t}$ an inspection of the formulae for reflected rays (1-6) shows that the Nth reflected ray (disregarding E_1 which is equal to rE_0, because it never passes through the film) can be expressed as

$$E_N = (tt'r'^{2N-3})e^{i(\omega t-(N-1)\delta)} \tag{2.32}$$

capturing both the modification of amplitude and of phase due to the rays' path.

The resultant reflection, E_R will be the superposition of all these rays, E_N, and the special case ray E_1 such that

$$E_R = \sum_{N=1}^{\infty} E_N = rE_0 e^{i\omega t} + \sum_{N=2}^{\infty} (tt'r'^{2N-3})e^{i(\omega t-(N-1)\delta} \tag{2.33}$$

with some factorisation this can be shown to be a converging geometric series of the from $\sum_{N=2}^{\infty} x^{(N-2)}$ where $x = r'^2 e^{-i\delta}$ and gives

$$E_R = E_0 e^{i\omega t}\left(r + \frac{tt'r'e^{-i\delta}}{1 - r^2 e^{-i\delta}}\right) \tag{2.34}$$

use of the stokes relations to simplify, results in Equation 2.35, and a similar treatment of the transmitted waves results in Equation 2.36.

$$E_R = E_0 e^{i\omega t}\left(\frac{r(1 - e^{-i\delta})}{1 - r^2 e^{-i\delta}}\right) \tag{2.35}$$

$$E_T = E_0 e^{i\omega t}\left(\frac{t^2 e^{-i\delta}}{1 - r^2 e^{-i\delta}}\right) \tag{2.36}$$

For the case where $n_0 \neq n_2$, such as with a thin dielectric film on a substrate, these can be modified accordingly using subscripts 01 and 12 to denote the two different boundaries of the ambient-film and film-substrate respectively

$$E_R = E_0 e^{i\omega t}\left(\frac{r_{01} + r_{12}e^{-i\delta}}{1 + r_{01}r_{12}e^{-i\delta}}\right) \tag{2.37}$$

$$E_T = E_0 e^{i\omega t}\left(\frac{t_{01}t_{12}e^{-i\delta}}{1 + r_{01}r_{12}e^{-i\delta}}\right) \tag{2.38}$$

2.2.3 Reflectance, Transmittance and Absorbance

The fraction of power, P, that is reflected, transmitted, or absorbed by a thin film system is called the reflectance, R, transmittance, T, or absorption, A, respectively. Conservation of energy tells us that these must sum to 1 for any system.

$$R + T + A = 1 \tag{2.39}$$

In this work, absorption of thin film systems is assumed to be negligible unless stated otherwise, that is the extinction coefficient, k, and the absorption coefficient, α, are both zero, simplifying the conservation equation by making $A = 0$ and thus $R + T = 1$. Each coefficient is the ratio of the square of the amplitudes (of the electric field, E) as in Equations 2.40 and 2.41.

$$R = \frac{P_r}{P_i} = \left(\frac{E_R}{E_0}\right)^2 \tag{2.40}$$

$$T = \frac{P_t}{P_i} = \left(\frac{E_R}{E_0}\right)^2 \tag{2.41}$$

The reflectance and transmission are fundamental properties of a system that are readily measured in a laboratory by taking the ratio of light intensities. Following from Equations 2.37 and 2.38 in the previous section and by understanding that $|E_R|^2 = E_R E_R^*$ and $|E_T|^2 = E_T E_T^*$ because E_R and E_T are complex, we can show that in an isotropic non-absorbing thin film system where multiple internal reflection beams are considered, the proportion of light reflected and transmitted is

$$R = \frac{r_{10}^2 + r_{21}^2 + 2r_{10}r_{21}\cos(2\delta)}{1 + r_{10}^2 r_{21}^2 + 2r_{10}r_{21}\cos(2\delta)} \tag{2.42}$$

$$T = \frac{n_2}{n_0}\frac{{t_{01}}^2 t_{12}^2}{1 + r_{10}^2 r_{21}^2 + 2r_{10}r_{21}\cos(2\delta)} \tag{2.43}$$

where

$$\delta = \frac{2n_1 d\cos(\theta_1)}{\lambda} \tag{2.44}$$

These Equations 2.42 and 2.43 are the governing equations for the reflectance and transmittance behaviour of thin films, and show a clear dependence on wavelength, angle of incidence, film thickness and the refractive indices of the three mediums. Due to this, Equation 2.42 can be used to investigate the effects of the film, the refractive index n and the thickness d, on the interference pattern produced by the film as a modification in the reflectance spectrum, $R(\lambda)$. The model uses air as the ambient medium, $n_0 = 1$, and silicon as the substrate, $n_2 = 3.88$, and is at normal incidence.

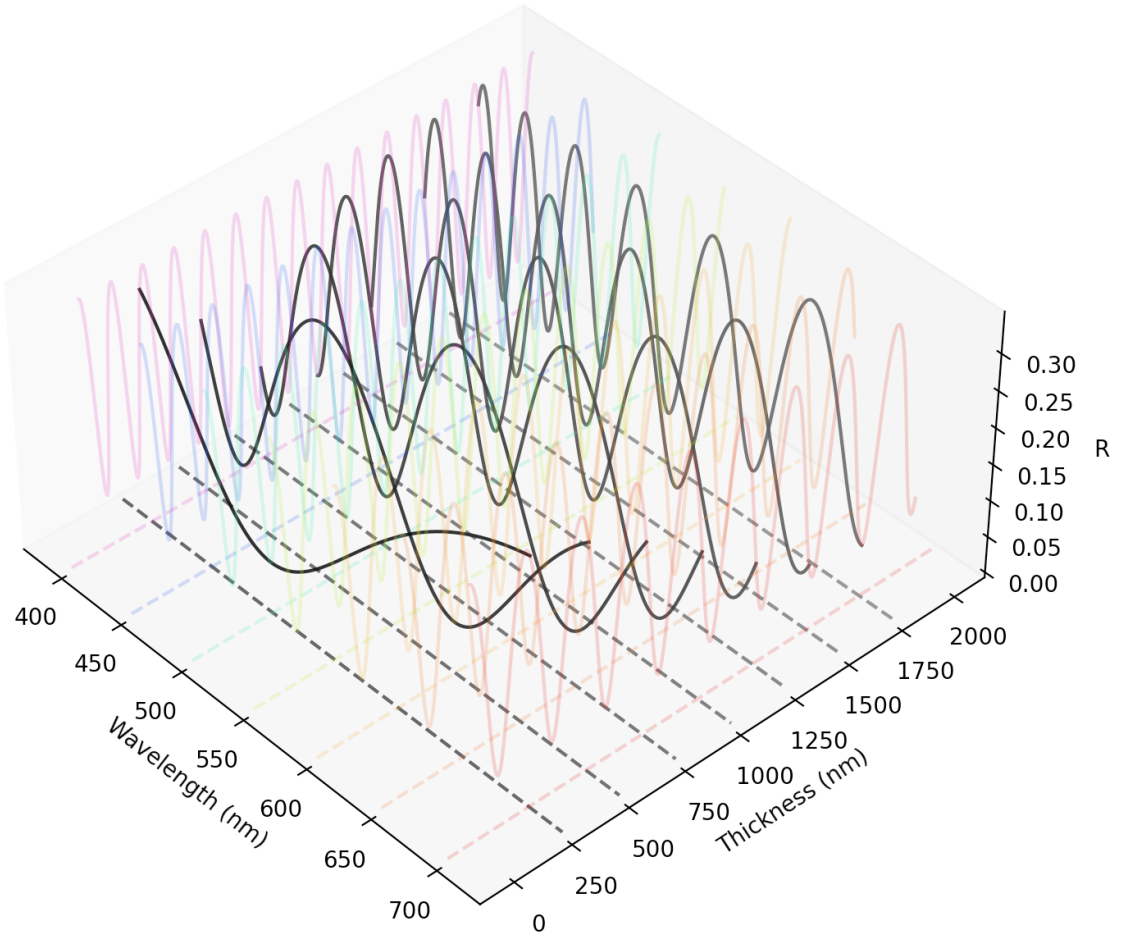

Figure 2.10: Reflectance spectra of a thin film as a function of film thickness

Figure 2.10 shows $R(\lambda)$ as a function of d (at $n_1 = 1.5$). As the thickness of the film increases the number of fringes present increases and the position of the fringe maxima and minima changes, however, the fringe visibility i.e. the difference between a maxima and a minima value in a fringe, stays constant.

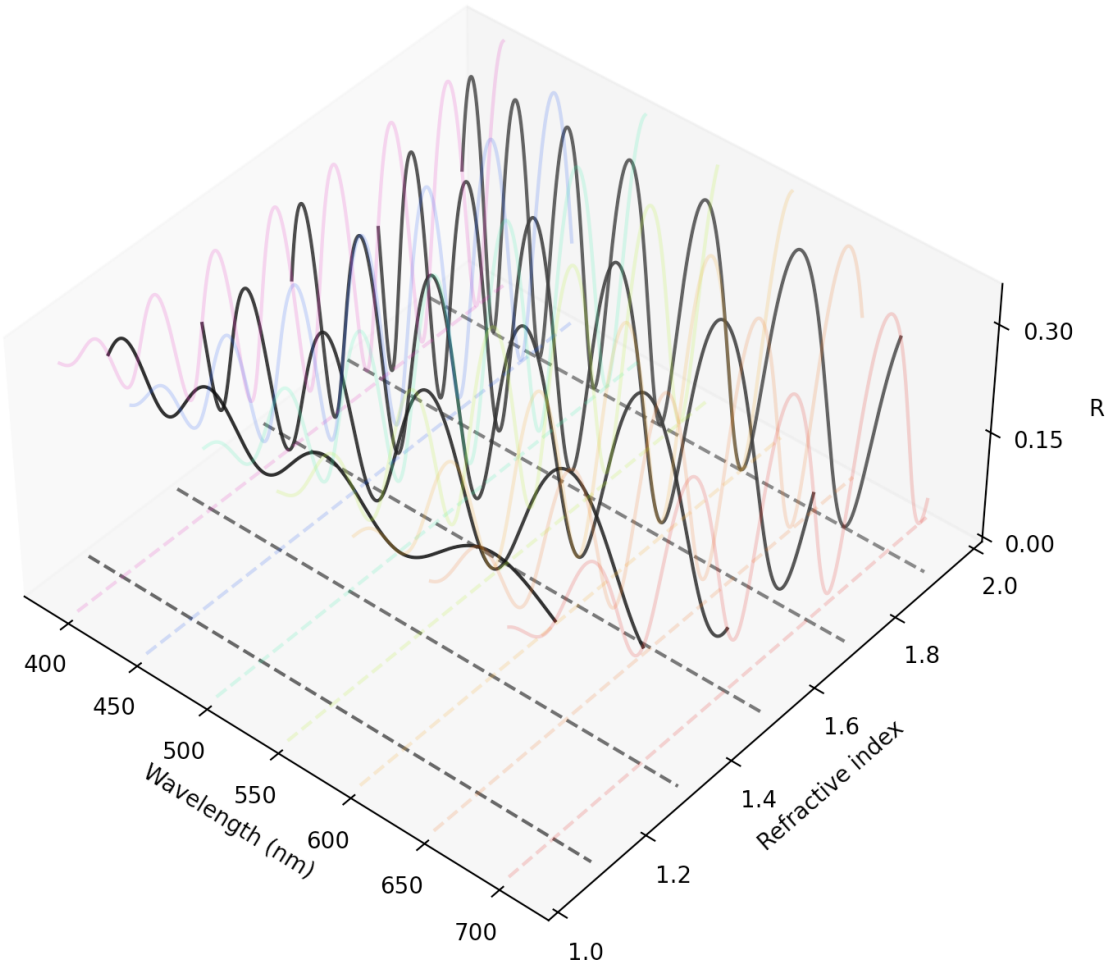

Figure 2.11: Reflectance spectra of a thin film as a function of film refractive index

Figure 2.11 shows $R(\lambda)$ as a function of n_a (at $d = 1500$ nm). Here, increasing the refractive index causes the fringe visibility of $R(\lambda)$ to increase, in addition to moving the position of the fringes. In both Figures 2.10 and 2.11, opaque lines follow R as a function of d and n respectively. The result for monochromatic light discussed in Section 2.2.1 is clear, the fringes are spaced equally in thickness (or refractive index) change.

2.3 Non-imaging studies

2.3.1 Monochromatic reflectance and scattering

The earliest *in situ* studies of films were based on specular reflectance (laser reflectometry, specular reflectometry) methods in which the intensity of a single reflected wavelength is logged. This is easily achieved in dynamic films because of the high data acquisition rates of photodiodes.

In 1993 Horowitz et al. [42] performed a normal incidence a He-Ne laser study as shown in Figure 2.12. Horowitz recorded the reflectance of the laser as a function of time and dubbed this an 'optospinogram' as seen in Figure 2.13a. These fringes of equal thickness are used to track the thinning of the film by resolving the Bragg condition for full constructive interference, as in Equation 2.26, at the time of each peak. The resolution of this condition therefore gives the thinning rate of the film and a thickness profile, shown in Figure 2.13b, is extracted from the optospinogram assuming that the end thickness of the film is zero (the solvent has fully evaporated). Each peak sequentially from right to left indicates a thickness change of $\lambda/2n\cos(\theta_r)$. If the final thickness of the film is non-zero then a thickness profile can also be reconstructed using $d_m = d_{m+1} + d_f$, where d_f is the final thickness, measured ex-situ. In other words, this technique requires a thickness reference point to produce a thickness profile rather than a thinning rate.

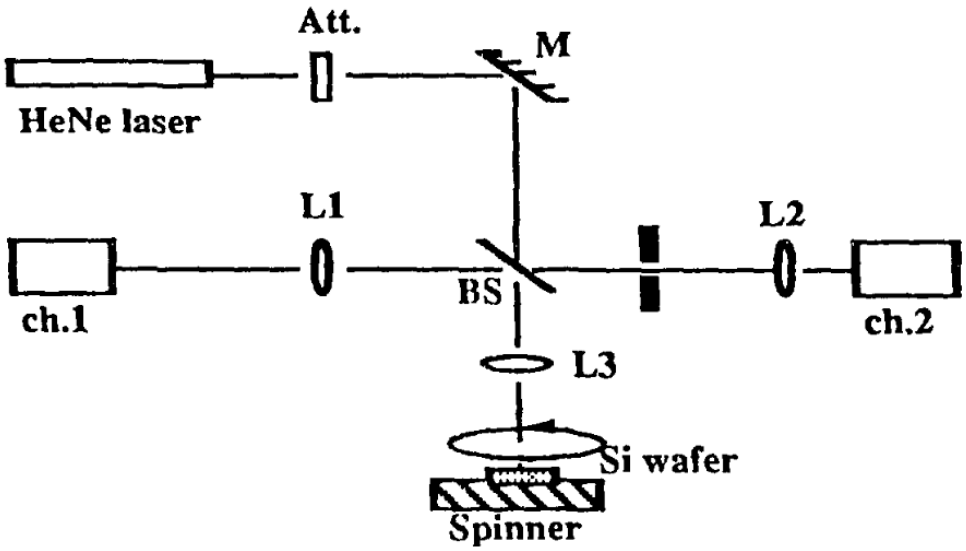

Figure 2.12: A diagram of the first *in situ* normal incidence specular reflectance measurements of spin coating utilising a HeNe laser, mirror (M), beamsplitter (BS), condenser lenses (L1-3) and two channel detection (reference and sample), from [42].

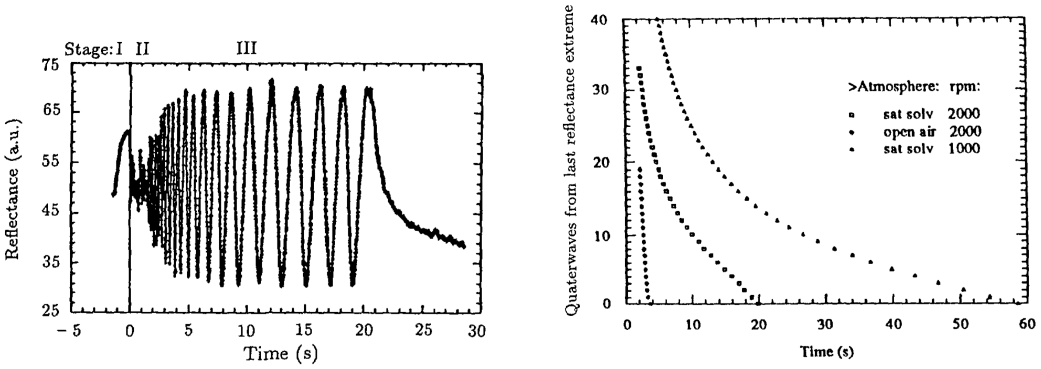

(a) The reflectance against time measurements, dubbed an optospinogram

(b) The thickness profiles of the spun-coat films

Figure 2.13: Figures from Horowitz's [42] first *in situ* laser interferometry study of spun on glass films.

Since 1993, specular reflectometry has been used in a multitude of studies to provide a thickness profile or thinning rate of a film. This includes Horowitz's later 1998 optical viscometry study [43] that showed specular reflection could be used to quantify viscosity during the spin coating process and validated that the spin coating of mineral oil OP20 (Newtonian and non-volatile) showed good agreement with the EBP model. In addition, this technique has notably been used by Birnie et al. [44] [45] and Haas et al. [46] to experimentally determine the drying rate for different pure solvents, complex solvents, and complex solutions, respectively. This drying rate is derived from Meyerhofer's model [13] of the evaporative spin coating process shown earlier in Equation 2.6. Mouhamad et al. also used the information given by specular reflection to compare and fit Meyerhofer, RBD [47] and semiempirical models in environments of differing solvent saturation [48].

In addition, this method is widely used in conjunction with other *in situ* techniques because the laser can be easily reflected off the centre of rotation with minimal invasiveness of other optical setups. For example, it has been used with off-specular scattering to provide thickness profiles [49] [50]. This combination allowed for the interpretation of systematic modulation in peak intensity of the optospinogram as an indication of the separation of the fluid into solute and solvent rich layers with a horizontal interface [51]. It has also been used simultaneously with imaging [52] [15] to provide thickness profiles.

Off-specular scattering is similar to specular reflection in that a laser is reflected off the sample, however, in contrast, the reflection is projected onto a screen, thus capturing both the specular and scattered light. The resulting pattern is captured via a camera, as shown

in Figure 2.14. Simplistically, this allows for the observation of interference patterns from off-specular refection to be captured over a 2D area, giving reciprocal space observation of the film. This can be linked to characteristic length scales within the subject film, allowing for the tracking of the film morphology during the spin-coating process of polymer blends or other compound films.

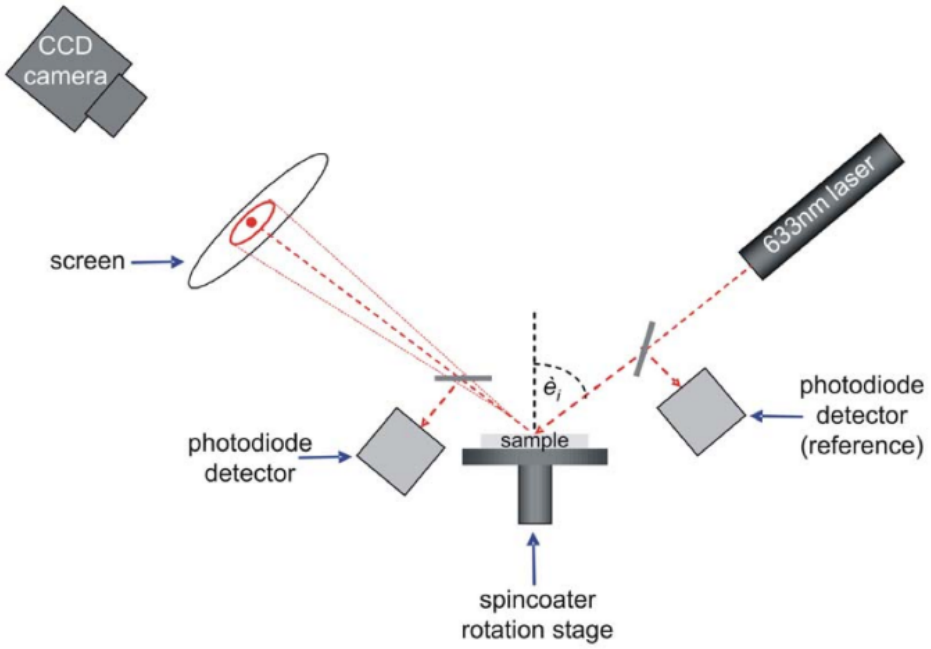

Figure 2.14: A diagram of an *in situ* scattering setup with a 633nm laser, photodiode detectors (for specular reflectometry), a screen, and a CCD camera to capture scattering patterns, from [51].

This off-specular technique was first used by Haas and Birnie in 2001 to characterise defects (striation spacing) in a nondestructive way [53]. From here, it has been a useful tool for investigating the behaviour of ternary polymer solutions, used by Jukes et al. [50] and Heriot and Jones [51] in 2005. Jukes et al. were able to observe the onset of phase separation while monitoring the length-scale evolution in a poly(9,9-dioctylfluorene-alt-benzothiadiazole) (F8BT):poly(9,9-dioctylfluorene-co-bis-N,N'-(4-butylphenyl)-bis-N,N'-phenyl-1,4-phenylene-diamene) (PFB) blend during spin coating. Similarly, but for a polystyrene (PS):polymethyl methacrylate (PMMA) blend, Heriot and Jones produced a mechanism for the lateral stratification observed at some conditions during spinning. The radially averaged light scattering intensity from both of these experiments are shown in Figure 2.15. These experiments indicated, contrary to previous thought [54], that the length scale

shrinks during the spin coating process rather than growing from nucleation.

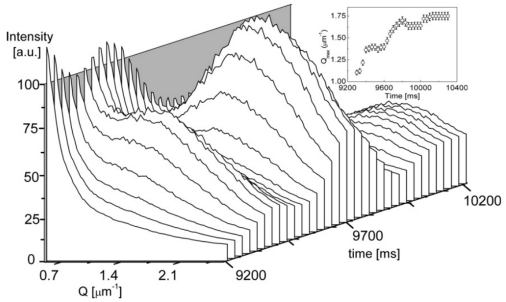

(a) Scattering from a 44:56 F8BT:PFB blend at 2000rpm showing length scale evolution from 5.7 to 3.6μm

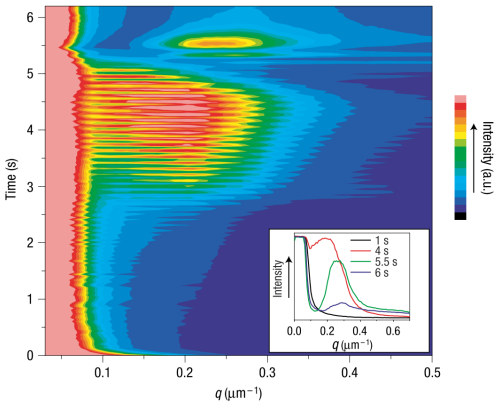

(b) Scattering from a 50:50 PS:PMMA blend showing length scale evolution from 53 to 25μm

Figure 2.15: The radially averaged *in situ* scattering data from [50] and [51] respectively.

Laser scattering was used by Mokarian-Tabari et al. [55] in 2009 while investigating the effect of solvent atmosphere through the use of an environmental cell. Here, the evaporation rate was reduced by an increase in the partial pressure of solvent in the cell. Reduced scattering was observed because of the inability of weaker Marangoni instabilities to break the surface and create cellular patterns. This was confirmed by ex situ optical micrographs of the film surface, showing that the lateral structure in PS:PMMA films can be stabilised or destabilised through evaporation rate. In 2010 Dunbar et al. [49] also used scattering alongside specular reflectivity and ex situ neutron reflectivity in a study that varied the initial concentration of a perovskite solution. This established that lateral phase separation occurs late in the spinning process and that as a result, low-concentration solutions may completely dry before this lateral phase separation can take place. Other studies have also used the techniques to understand the effects of col-solvents in polymer solar cell processing [56].

In blade coating, reflection and scattering techniques have not seen as much widespread use, possibly due to other methods such as reflectance spectroscopy or photoluminescemce [57], which can provide more information and are more easily implemented than in spin coating due to reduced constraints on the speed of data acquisition. Schmit-Hansburg et al. used monochromatic reflection to study the effects of drying gas flow and temperature on poly(3-hexylthiophene) (P3HT):phenyl-C61-butyricb acid methyl ester (PCBM) solutions for bulk heterojunction (BHJ) organic solar cells (OSCs) [58] because the drying kinetics of

the film could be easily extracted. In 2015 Güldal et al. used a multiprobe optical setup, of which scattering was a part, to monitor morphology, also in polymer:fullerene BHJ OSCs [59]. A study by Ternes et al. in 2019 used five laser diodes and photodiode setups along the path of a blade-coated perovskite film to track thickness at different points [60], this setup is shown in Figure 2.16.

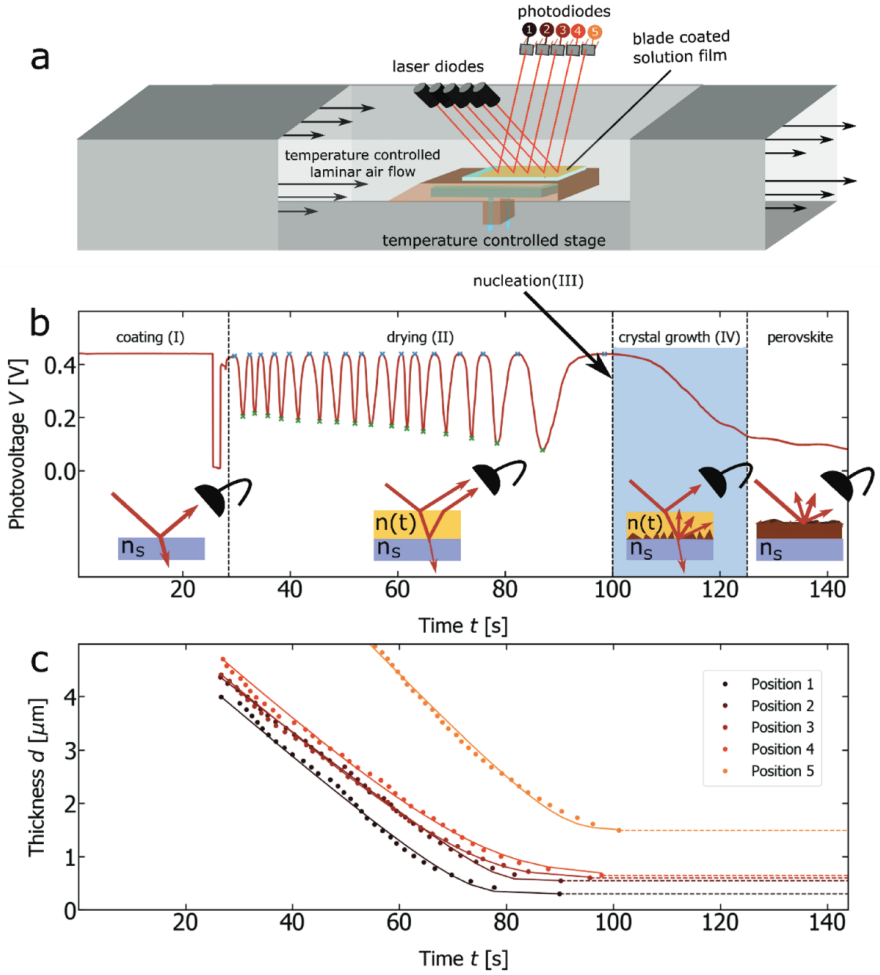

Figure 2.16: a) Schematic depiction of the flow channel setup. Five laser diodes probe the reflectivity of the deposited solution layer as it dries. b) Typical recorded photovoltage signal of the photodiode at position 3 during the drying of a perovskite solution layer. The different steps coating (I), drying (II), nucleation (III) and crystal growth (IV) of the deposition process can be identified from the signal shape. c) Thickness evolution as calculated from the signals of the five photodiodes , from [60].

Point reflectance and scattering have been vital to understanding the thickness profiles and mechanism for lateral separation in various polymer blends, respectively. They continue to be an effective way to track length scales and still hold advantages as *in situ* techniques, especially in configurations that require high data acquisition rates. However, more recently, morphology can be observed directly in real space via imaging.

2.3.2 Spectral reflectance

Obtaining full reflectance (or transmission) spectrum data, $R(\lambda)$, for a thin film system, possible in spectral reflectance (white-light interferometry, white-light spectrometry) measurements using a spectrophotometer, gives additional information when compared to monochromatic measurements. If a sufficiently detailed reflectance spectrum is available for a polymer film, both the refractive index and the thickness can be recovered with remarkable precision, typically much less than 1%. This was first demonstrated (ex situ) by manipulating the expression for transmission of an absorbing ($k \neq 0$) thin film to produce formulae for n_1 and d_1 in closed form by Swanepoel in 1983 for an amorphous silicon film on glass [61]. Before this, iterative procedures were normal [62] [63] [64].

Since then, numerous methods for the characterisation of thin films from spectral data, $R(\lambda)$ or $T(\lambda)$, have been published. These include closed-form solutions similar to Swanepoel's that reduce the MSE to as low as 0.17% for a film of 700 nm [65], simply fitting to simulated spectra, formulation of the problem into an optimisation [66] and peak and valley counting; the method for which is shown in Equation 2.45 where Δm in the number of peaks (interference maxima) between two wavelengths, λ_1 and λ_2. Many spectrometers used for the purpose of film thickness measurements have a large spectral range from UV-VIS-NIR to increase the accuracy of the technique[4].

$$d = \frac{\Delta m}{2\sqrt{n^2 - \sin^2(\theta)}} \cdot \frac{1}{(\frac{1}{\lambda_2} - \frac{1}{\lambda_1})} \tag{2.45}$$

It is clear that with enough spectral data, film characterisation using a reflectance spectrum with a number of techniques is straightforward and can accurately retrieve optical constants [67]. More recent research focusses on speeding up these procedures to realise real-time spectroscopic characterisation of films [68] [69] [70], for more complex systems, or to improve robustness [71]. Spectrometry has also been extensively used for *in situ* monitoring of physical vapour deposition (PVD) processes, due to the ability to give thicknesses of multilayer stacks and alloys [72], especially with the transfer matrix method (TMM) [73].

Morphological and phase changes can also be elucidated *in situ* with spectral reflectometry, as demonstrated by a study of spun-coat polymer:fullrene films by Raab et al. Here, transmission spectra were recorded through the centre of rotation and analysed

[4]KLA Filmetrics F-series of film thickness measurement systems that operate on spectral reflectometry principles typically use wavelengths from 1 nm to 10 µm.

to probe the crystallisation behaviour of the blend [74]. Ro et al. used UV-VIS reflectometry on poly[(5,6-difluoro-2,1,3-benzothiadiazol-4,7-diyl)-alt-(3,3”’-di(2-octyldodecyl)-2,2’;5’,2”;5”,2”’-quaterthiophen-5,5-diyl)] (PffBT4T-2OD) films that were spun-coat, blade coat, and slot-die coat for BHJ OSCs [75]. Spectral reflectometry has indicated where these polymer fullerene solutions aggregate [76], controlling this is related to an increase in power conversion efficiency (PCE) [75].

Rappich et al. give a particularly excellent example of spectral reflectance's informational depth, collecting high temporal and spectral resolution reflection measurements during spin coating of perovskite solutions, shown in Figure 2.17. The transient dynamics of fast changes in the solution height and composition are visible during the first few seconds of spin coating. In addition, thinning could be tracked with the eventual emergence of wider stationary peaks as the final perovskite formed. These data were easily processed using Equation 2.45 to give the thickness profile. However, these data are both radially averaged and surface-averaged as the measurement spot of 3mm diameter moves around 0.63mm relative to surface of the spinning system during each measurement (4000rpm, 3mm radial offset). As with the other techniques discussed in this section, they are therefore unlikely to be able to provide much useful information on defects, nonuniformity and over areas larger than a few millimetres squared. This is a major limiting factor as processing methods scale to meet demand.

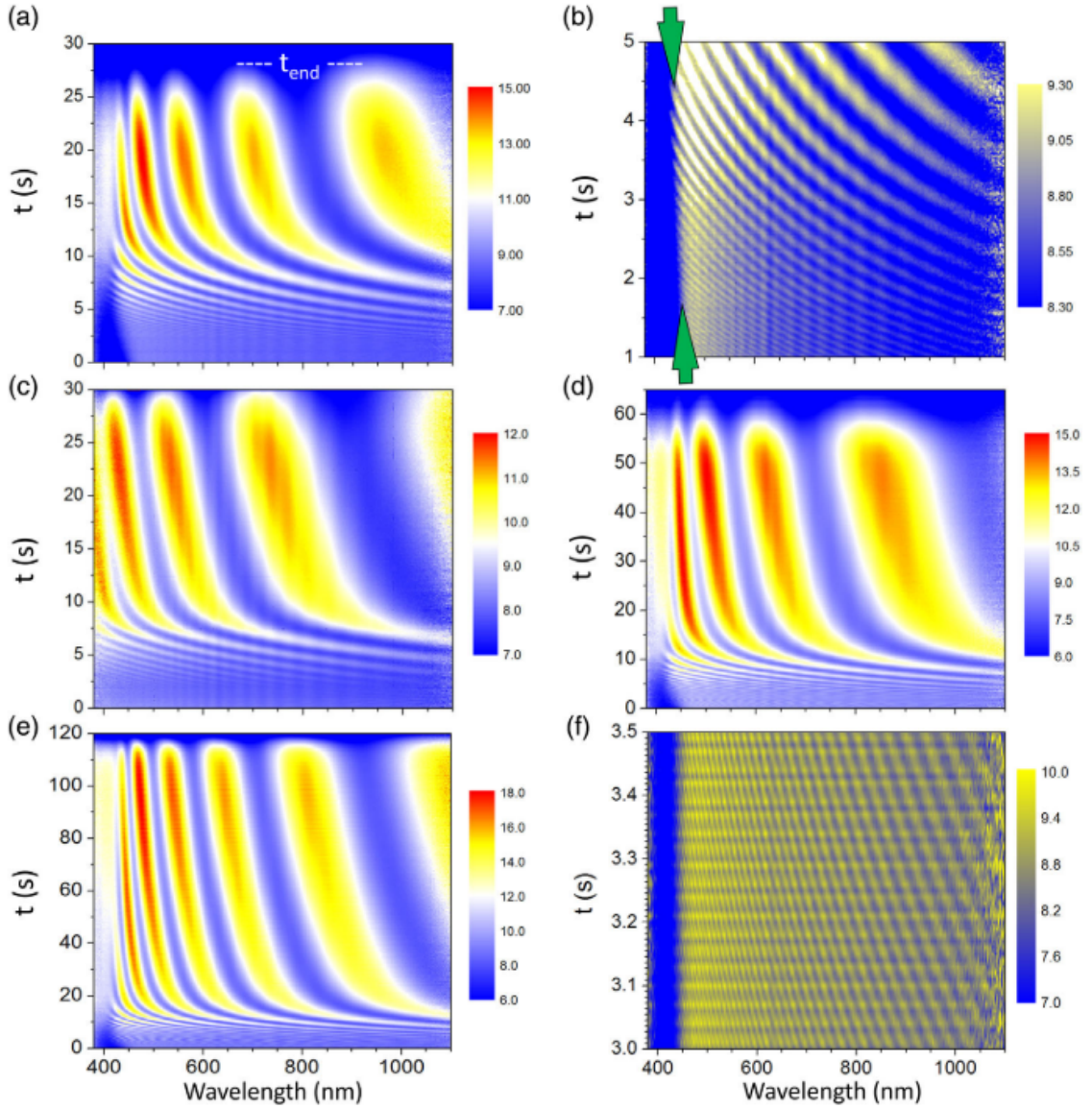

Figure 2.17: *in situ* time resolved spectral reflectance measurements for spun coat perovskite, taken from [77]. a–f) Spectra of the specular reflectance (in %) as a function of wavelength and time recorded during spin coating of(a, b) MAPI. In (c), (d), and (e, f), the spectra for MAPBr, FAPI, and TripleCat precursor solutions are shown, respectively. Note that (b) and (f) are magnifications of the initial 1–5s of (a) and 3–3.5 s of (e). As a solvent, a 4:1 mixture of DMF and DMSO was used. Blue and red denote lowest and highest reflectance, respectively. The green arrows in (b) mark the shift of the absorption in solution within the first seconds of spin coating.

2.4 Imaging studies

Optical techniques are usually extended to imaging to give one of two advantages. Firstly, it can be used for large area inspection of films to gain insight into the drying kinetics of the processing method to facilitate scale up [78], for defect detection/quality control [79] [80]. Secondly, it is used as a tool to directly observe the microscopic morphology of

blended and complex films. This ensured good understanding of fabrication where films have a strong processing-structure-property-performance relationship [81] [82] [83] [84].

2.4.1 Monochromatic

The concept of monochromatic specular reflectance is easily extended to imaging by installing a lens and camera in place of the collection photodiode. Some of the first *in situ* studies of this type were by Purrung and Graves [85] [86], the experimental setup is shown in Figure 2.18a. They used a 20 ns laser pulse coupled to a microscope illuminator installed on a spin coater to capture 35mm film interference micrographs of fluid topologies, in an effort to understand flow over step profiles on a spinning disk. These early film micrographs are shown in Figures 2.18b and 2.18c. These studies were able to reconstruct topologies by using fringes of equal thickness in the interferograms as contour lines.

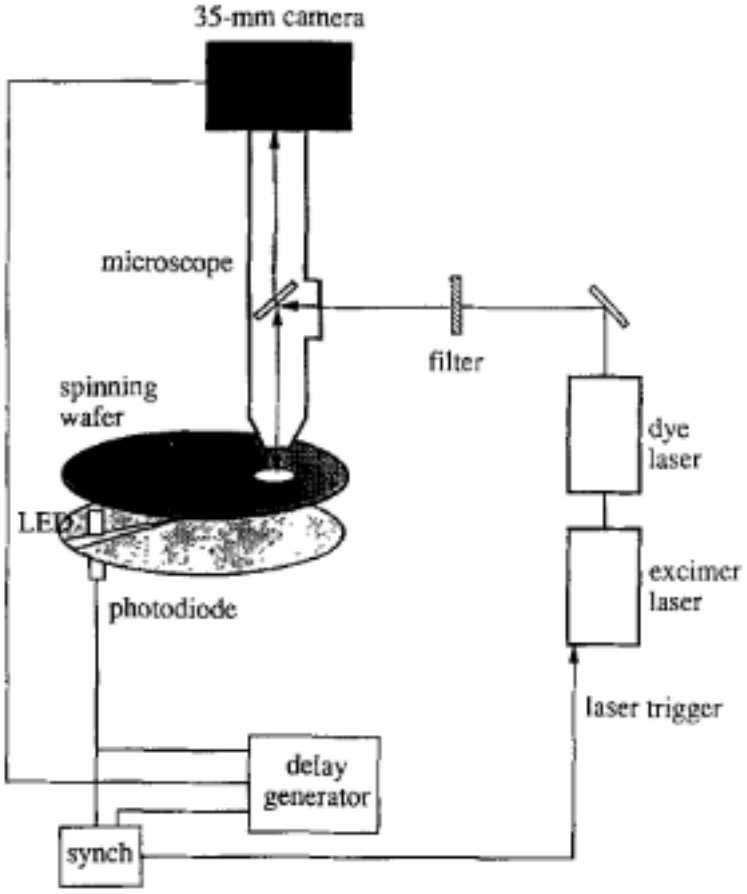

(a) A diagram of the experimental setup used to capture film interferrograms

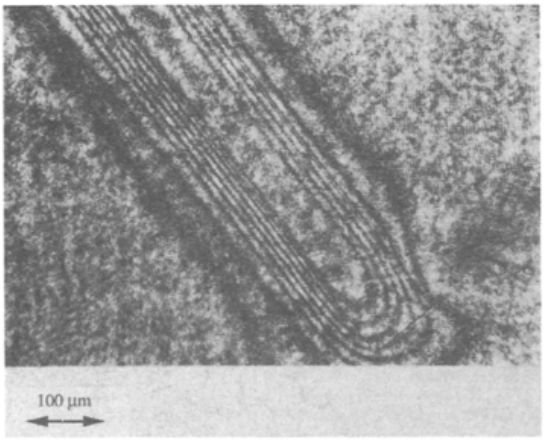

(b) A film interferrogram taken of fluid over a 100um step 2 sec into spin

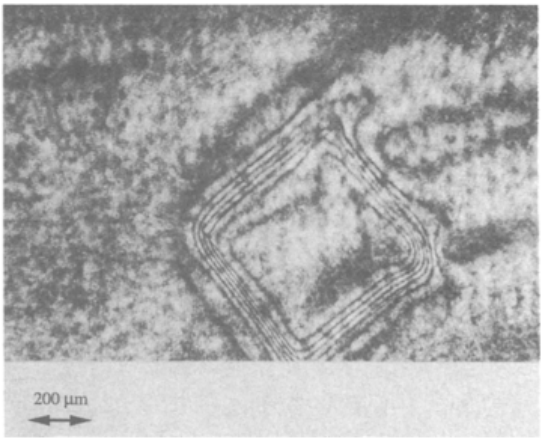

(c) A film interferrogram taken of fluid over a 500um line 1.5 sec into spin

Figure 2.18: Perrung and Graves' experiments on spin coating over topology using monochromatic film interferograms, from [85]

These types of imaging studies have been made much more accessible by recent developments in modern digital cameras, both complimentary metal-oxide semiconductor (CMOS) and charge coupled device (CCD), with high framerates and spatial resolutions.

These are now commonly used in these types of studies, allowing for digital image processing techniques to be applied. In a monochromatic camera, at each (x, y) pixel, the generated pixel activation is given by Equation 2.46.

$$x = \Gamma\left(\xi \int_{\lambda_{min}}^{\lambda_{max}} I(\lambda)R(\lambda)\, d\lambda + \epsilon\right) \tag{2.46}$$

Where x is an integer $[0, 255]$ denoting the value of that pixel in the resulting image, the nonlinear function, Γ, accounts for any gamma correction or sensor nonlinearity, the scalar ξ accounts for geometry and exposure time, $I(\lambda)$ and $R(\lambda)$ account for the illumination spectrum and the illumination spectrum of the imaged objects, respectively, and finally ϵ accounts for random noise of the pixel. The wavelength limits, λ_{min} and λ_{max}, will encompass the visible spectrum, around 400 to 700nm, and may be limited at the lower end by a built-in ultraviolet (UV) filter.

Bergqvist et al. [78] used a high-speed monochromatic camera with relatively low spin speeds to record interferograms of organic thin film formation on a spin coater and blade coater. The 120 µs exposure time was sufficiently fast to allow the 15 mm by 20 mm wafers spinning at 550 rpm to be observed clearly under constant 455 nm laser diode illumination full width half maximum (FWHM) of 20 nm. While information across larger areas could be resolved, this approach would not be suitable at higher angular velocities or to probe smaller length scales. Comparison of interferograms in the two modalities shown in Figures 2.19 and 2.20 reveal differences in the drying kinetics of the spin coating and the blade coating processes, respectively. A very similar setup was used by Chou et al. to follow thickness profiles of spun coat small-molecule semiconductor TIPS-pentacene [87], which has also been directly colour imaged *in situ* by other studies [88].

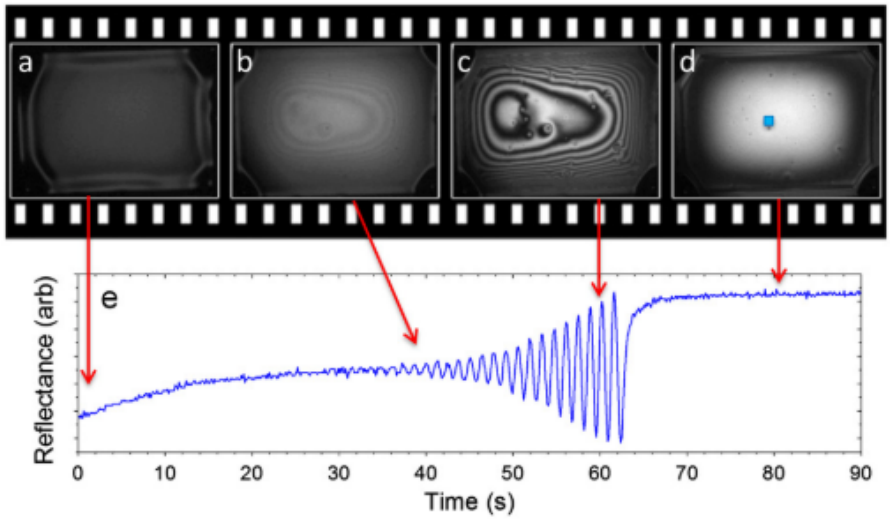

Figure 2.19: (a-d) interferograms of spun coat organic solution and e) the reflectance intensity for a single pixel over time, from [78].

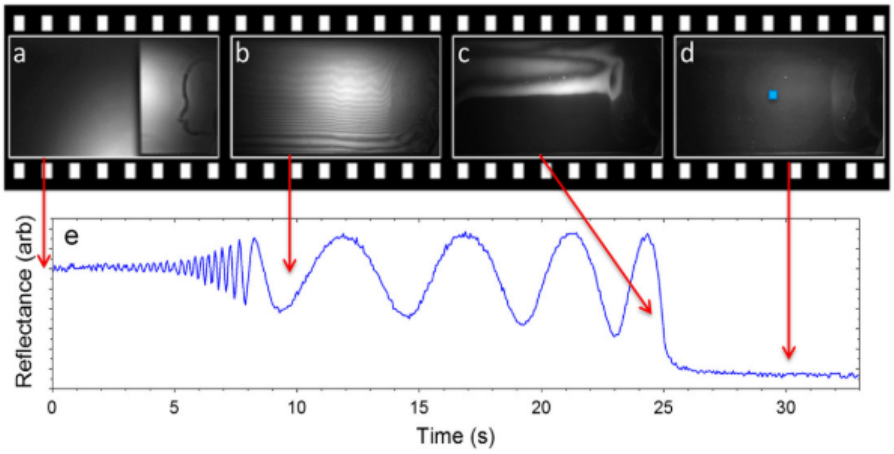

Figure 2.20: (a-d) interferograms of blade coat organic solution and e) the reflectance intensity for a single pixel over time, from [78].

Stroboscopic imaging provides a way to directly observe the spin-coating process at much higher spin speeds and with a higher length-scale resolution. By providing a very short pulse of light during a camera's exposure, films moving at high angular velocity can be imaged as if they are still, even when viewed through a microscope. In 2011, Ebbens et al. [89] used stroboscopic microscopy imaging with laser diode illumination to directly observe the structure development of PS:polyisoprene (PI) films. Optical reflectance images of the film, as well as their Fourier transforms and the radially integrated Fourier transform for the process, are shown in Figure 2.21. From the combination of interference imaging data and ex situ atomic force microscopy (AFM), the topography of the blend could be reconstructed as the blend phase separates into a bicontinuous morphology, shown in Figure 2.22.

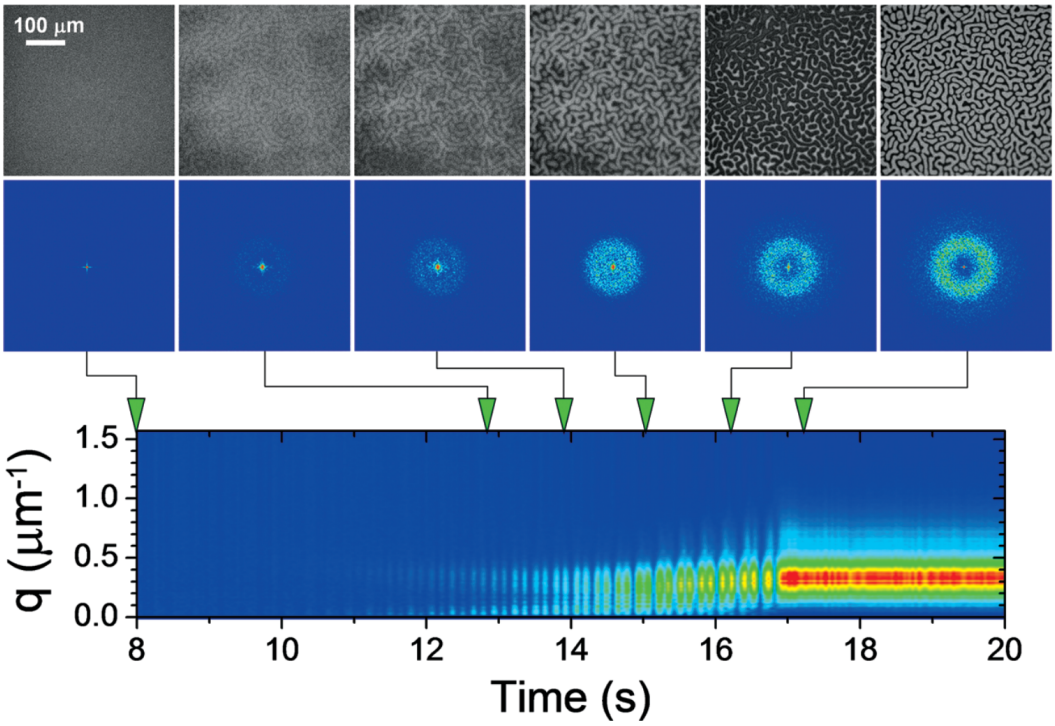

Figure 2.21: Top: optical reflectance images, middle: the top images Fourier transforms, bottom: the radial Fourier transform for the complete spin coating process for a 1:1 PS:PI film, from [89].

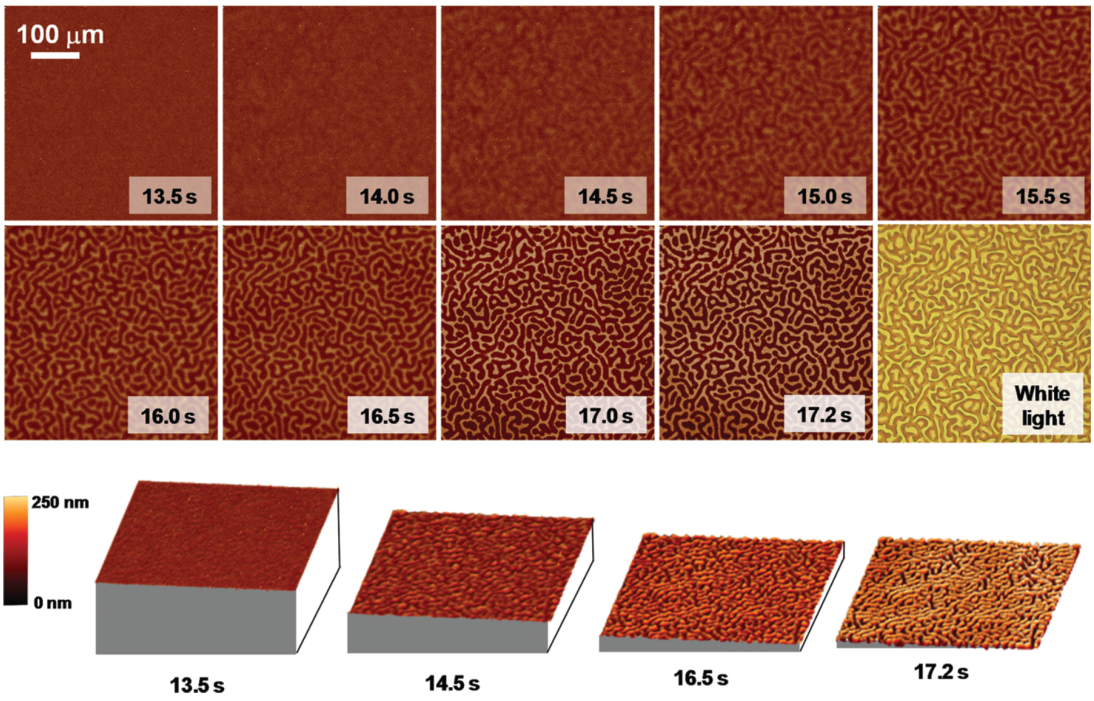

Figure 2.22: Top and middle: the 2D height reconstructions from the reflectance imaging, bottom: the 3D height reconstructions for a 1:1 PS:PI film, from [89].

In 2013 Toolan et al. used stroboscopic imaging in a number of studies. Monochromatic

stroboscopic imaging was used to directly observe PS:PMMA blend's domain coarsening and vitrification into a separated structure, and the effect of spin speed on this [90]. The same technique, with the addition of cross-polarised micrographs to enhance crystal identification, was used to study pure polyethlene glycol (PEG) and PEG:PS mixtures [91]. This allowed, for the first time, *in situ* study of crystallisation and the complex phase separation of PEG:PS during the spin coating process, showing that phase separation and crystallisation occurred separately. This is contrary to the observations for P3HT:PCBM blends using spectral reflection and off-specular scattering [83] and confirmed that control of the spin coating parameters can predictably influence when crystallisation occurs, and therefore the final morphology. This study represented a landmark where *in situ* measurements were collected both in real space and real time. Toolan et al. then used stroboscopic fluorescence microscopy on polydioctylfluorene (PFO):PS blends to provide feedback control on spin speed [92]. Using the fluorescence of PFO and illuminating with spectra overlapping its excitation spectra, compositional and morphological information were captured and, importantly, these effects could be studied separately. Feedback to direct phase separation was determined by the peak of the images' fast Fourier transform (FFT) (q_{max}) and successfully manipulated the spin speed to form a more favourable final morphology, as shown in Figure 2.23. In addition, cognisance of the mechanism by which this final morphology is achieved was also obtained. The observation of a bicontinuous morphology from spinodal decomposition that then grows through Ostwald ripening[5], followed by a break-up, with associated length scale decay, and the formation of distinct islands is different to Heriot and Jones' conclusions that indicated the break-up of transient wetting layers due to interfacial instability [51]. This highlights the importance of *in situ* stroboscopic imaging's real space and real time measurements as a way to explore the spin coating process [93] and the interactions between the multiple mechanisms involved.

[5]Larger polymer-rich domains grow at the expense of smaller ones during film formation, occuring due to differences in chemical potential between domains of varying size, driving the diffusion of polymer chains from smaller, less stable regions into larger, energetically favorable ones

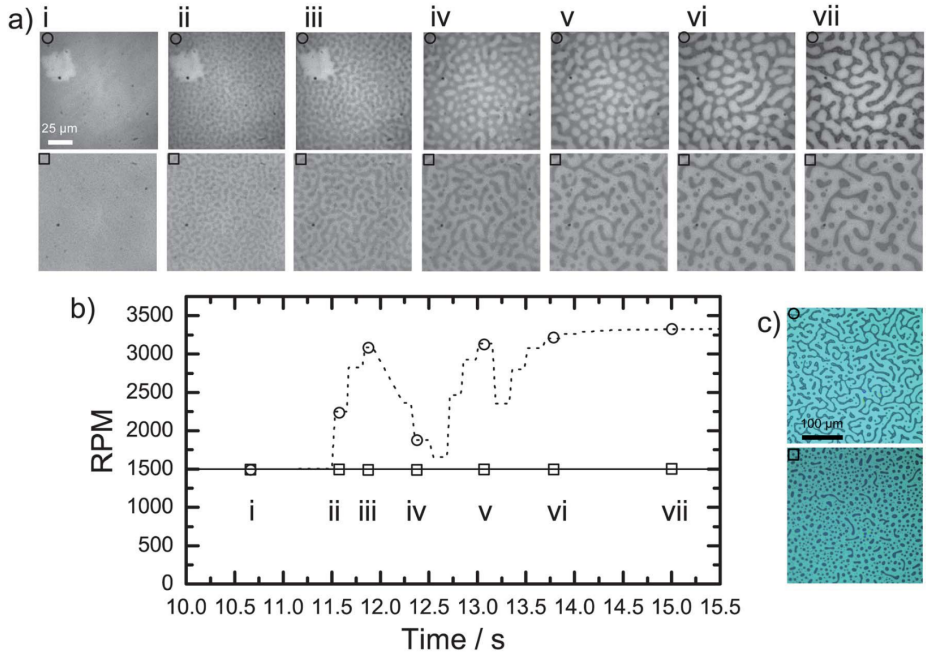

Figure 2.23: (a) Stroboscopic florescence images for non-feedback (circle) and feedback controlled (square) spin coating of 65:35 PFO:PS. (b) The rpm profile of the spin coating and (c) final 20x florescence images, from [91].

A similar study has also been carried out on bar-coated (similar to blade-coated) PS:PMMA blends [94], comparing the differences in drying and final morphology between these and spun-coat counterparts, where it was deduced that bar coating produces more energetically favourable final morphologies due to slower evaporation, as shown by the reflectance images in Figure 2.24a. In the bar-coated experiments, an estimation of solution composition was made from a known wet film thickness and initial solution concentration, and the final thickness was measured by AFM. In this study, a much higher coherence laser diode is used (FWHM 2 nm) and this allows for reconstructions of much thicker films than before, as shown by the reduced signal enveloping in Figure 2.24b. The speckle by increased coherence illumination was mitigated by a rapidly spinning diffuser sheet.

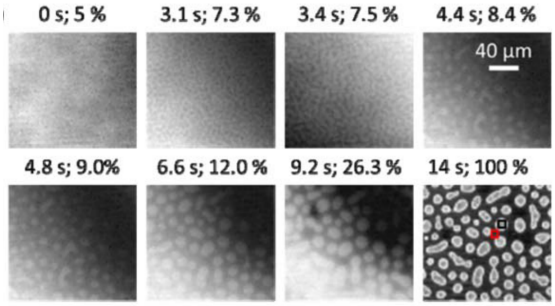

(a) Interferograms

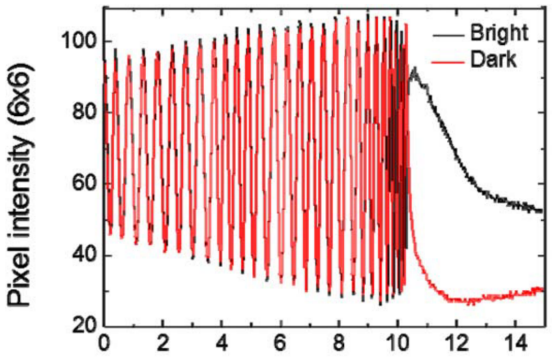

(b) Intensity data for light and dark area of the final interferogram

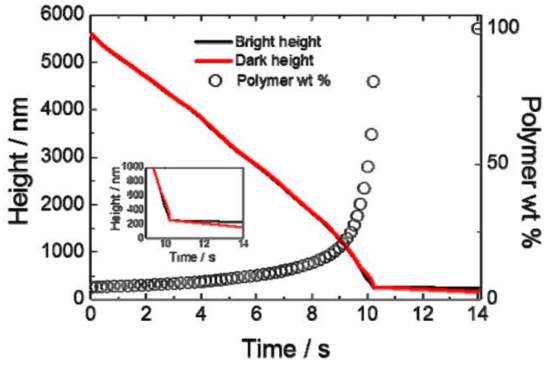

(c) Reconstructed thickness and concentration

Figure 2.24: Haq et al. reflectance imaging study of bar coated polymer blends, taken from [94]

2.4.2 Colour

In order for a camera to 'see' colour, an additional component is necessary that allows the distinction of different levels of different wavelengths of visible light. To do this, a RGB Bayer filter is overwhelmingly the most common way, although there are other techniques such as CYGM filters, vertical colour filters, and prism cameras. A Bayer filter is a mosaic of individual pixel filters that is placed directly in front of the sensor. Figure 2.25 shows the layout of a Bayer filter and an example of filter bands. Green-filtered pixels appear at twice the frequency to give the highest sensitivity in the middle of the colour range, and thus a better reproduction of colour in the resultant image. A result of the mosaicing is that the colour information in the image is incomplete. Interpolation (linear or more complex adaptive algorithms) is used to produce a RGB triplet at each pixel, a process called demosaicing, forming a full-colour image.

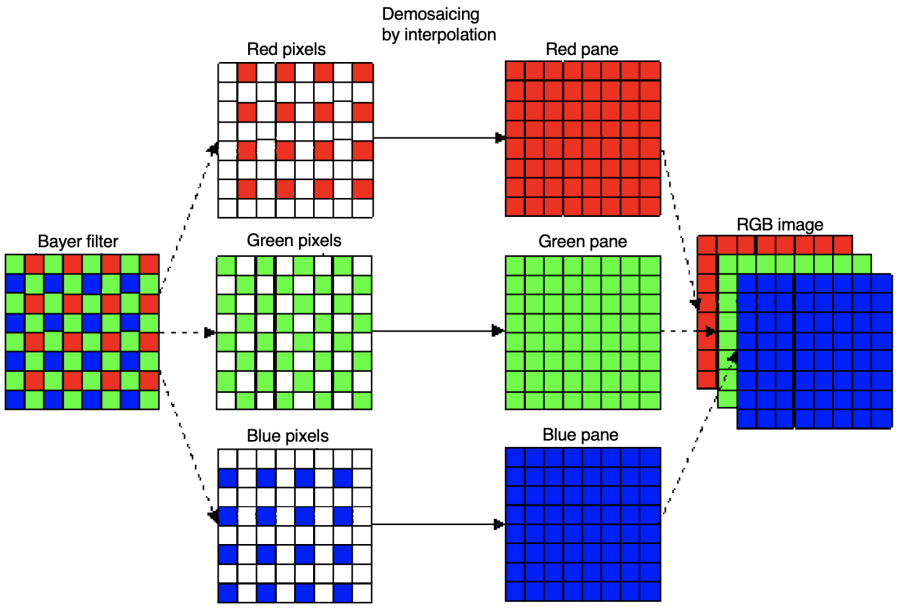

Figure 2.25: A Bayer filter configuration and demosaicing process, adapted from [95]

The spectral response of the camera is simply determined by the bandpass properties of the red, green, and blue components of the Bayer filter. For this reason, different sensors/cameras may have slightly different spectral responses, Figure 2.26 shows the spectral response of the Sony IMX253 sensor. Equation 2.46 presented earlier for monochromatic imaging can now be adapted to a Bayer filtered colour camera by adding these spectral responses denoted by $B(\lambda)_i$, where i is the colour channel. In addition, colour cameras have a colour balance parameter b_i, which can be used to change the relative activation of colour channels. The extended imaging model for a colour camera is shown in Equation 2.47. Now, for $i = 3$ as in a RGB camera, x_i denotes a value in the RGB triplet.

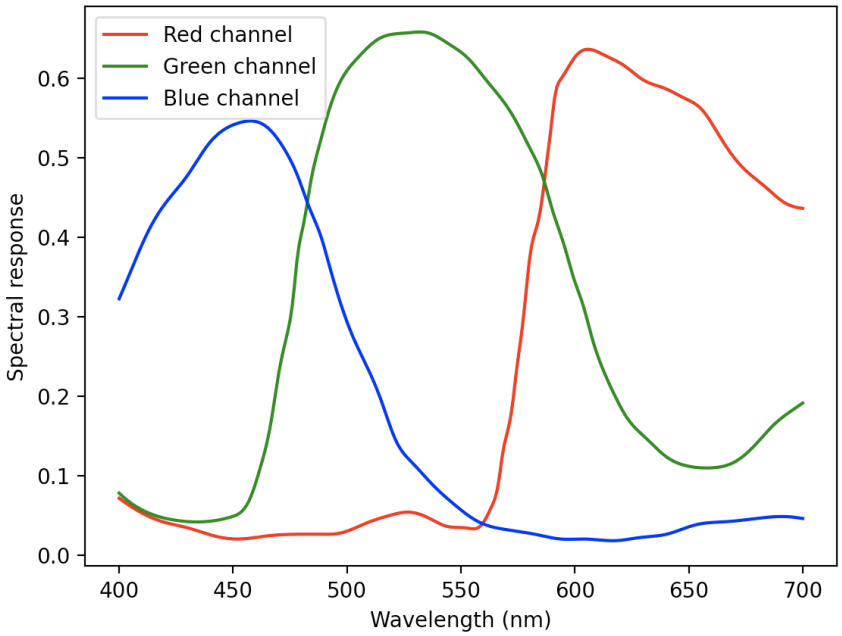

Figure 2.26: The channel sensitivities of the Bayer filter on the Sony IMX253 sensor

$$x_i = \Gamma_i \left(b_i \xi_i \int_{\lambda_{min}}^{\lambda_{max}} I(\lambda) R(\lambda) B_i(\lambda)\, d\lambda + \epsilon_i \right) \tag{2.47}$$

In a 2004 paper, Birnie describes a procedure to match the relative colour difference with a thickness estimation using colour video for spun-on glass (SOG) films [52], however, this was not achieved *in situ*. Reflectance spectra fitting was utilised to determine the thickness of the films and this showed that the 'colour angle' technique developed provided an excellent matching of colour values, thus allowing thickness to be estimated via colour captured by camera. A subsequent study by Birnie et al. in 2010 showed broadband colour interference of thin fluid layers during spin coating [15]. Here, point laser interferometry at the centre of a silicon wafer, spun with pure solvent, provided a thickness calibration that could be mapped radially outwards to the rest of the wafer via colour from the video observations. Frames from the video can be seen in Figure 2.27 that show a) the cyclical nature of colour through thinning and b) the colour moving from the centre outwards indicating that the thinnest part of the fluid is at the wafer's centre. The averaged radial thickness profile due to motion blur, constructed for different times in the video, can be seen in Figure 2.28.

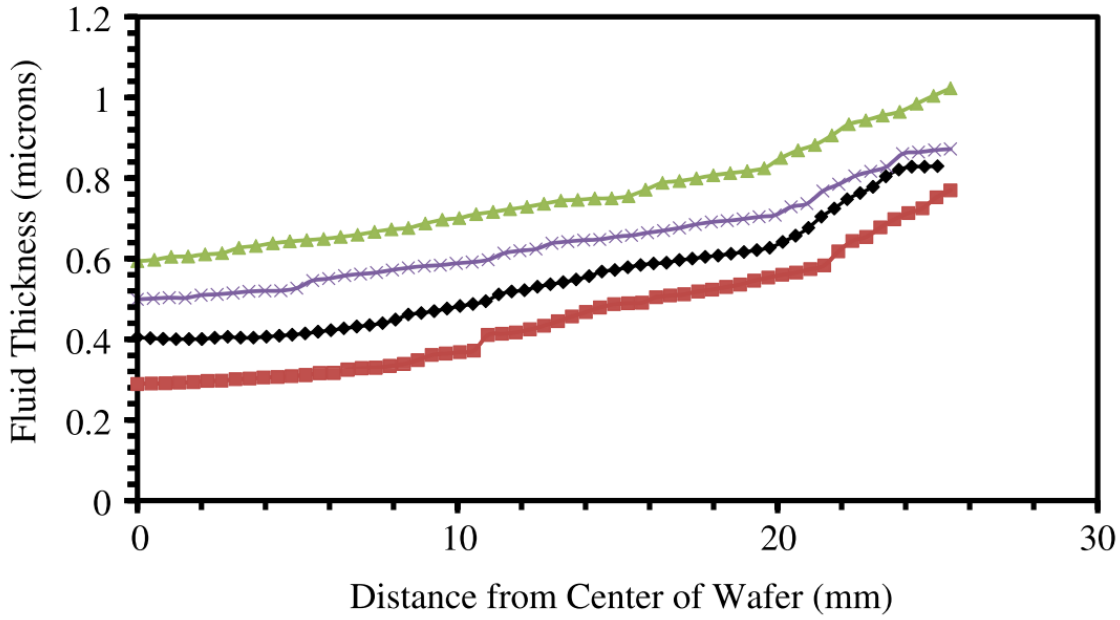

Figure 2.28: The radial thickness profile constructed from 4 different video frames occurring at 3.87, 3.93, 4.00 and 4.07s (top to bottom), taken from [15].

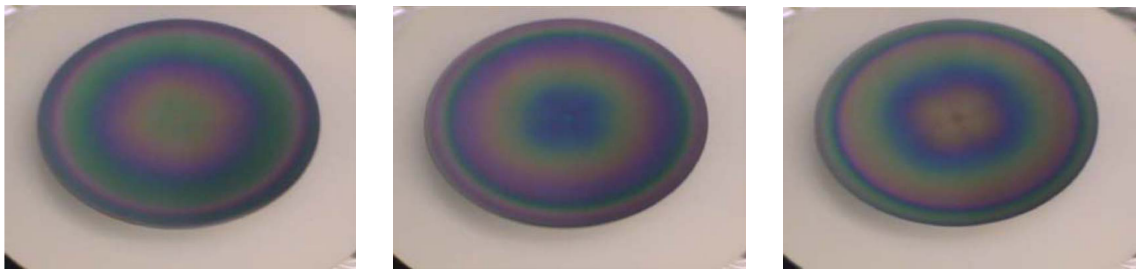

(a) 3.87s (b) 3.93s (c) 4.00s

Figure 2.27: Three sequential images occurring every other frame from the 30fps video of *n*-propanol spinning on a 50mm diameter silicon wafer at 2000rpm, taken from [15].

Broadband RGB film colour has been the subject of other studies (ex situ/static) that aim to reconstruct thicknesses; however, most of these use sequential scanning of some kind such as angle scanning [96], filtered wavelength scanning [97], or chromatic dispersion spatial scanning [98], making them unsuitable for inspection of dynamic scenes. Other methods require part of the image to have a set mechanical/geometrical condition [99] or approach the problem with a 'brute force' fitting method to minimise mean squared error (MSE) to a simulated response. This works well for films less than 1 µm [100] or with satisfactory initial film thickness estimates [101], however, it suffers from the similarity in MSE of correctly and incorrectly fitted solutions at thicknesses higher than this and requires accurate simulation and a priori information.

2.4.3 Hyperspectral

Equation 2.47 can be employed more generally to model cameras with more than three bands. Multisepctral cameras, where $i > 3$, allow a more accurate colour reproduction. Hyperspectral cameras, where $i >>> 3$ can give direct information on the imaged reflectance spectrum, $R(\lambda)$. This higher band imaging can be achieved in many ways, the most simple of which is to just increase the number of different filters in the pre-sensor filter.

Hyperspectral imaging (HSI) combines the informational power of spectroscopy with the advantages of 2D characterisation and is therefore a powerful technique used in a variety of sensing applications [102], recently including dynamic thin film characterisation [103]. For each pixel in a hyperspectral image, the spectral information is recorded at many small wavelength bands, instead of a standard colour cameras' three broad red, green and blue bands. The resultant images are 3D HSI datacubes [104] with x, y and λ dimensions. Push/whisk broom scanners operate by scanning through the x and y range at all λ, band sequential scanners operate by scanning through λ over all x and y, and snapshot HSI captures the entire HSI cube, over all x, y and λ, in one instant. Snapshot HSI is therefore the only mode applicable in the *in situ* monitoring of the spin coating process, however, to date there has not been any direct monitoring of spin coating via snapshot HSI. This is a consequence of the availability of snapshot HSI cameras with sufficient spectral and spatial sensitivity while maintaining a high enough frame rate. Pushbroom (linscan) hyperspectral cameras are extremely well suited to study R2R films because of the inherent movement between the film and the camera, in addition, this type of HSI usually maintains much better spatial and spectral resolutions than snapshot HSI.

Although hyperspectral imaging is an emerging technique, in 2020 Chandran Suja et al. used snapshot HSI to produce automated determination of liquid profiles in dynamic thin liquid films via interferometry [103]. This work demonstrates an accurate topological measurement (within 100nm) as seen in Figure 2.29, with a high signal-to-noise ratio, without the need to consider absolute light intensity. This makes it promising for machine vision in the monitoring of R2R film manufacturing. Near infrared (NIR) HSI has been used in the ex situ 2D topological characterisation of poly(3,4-ethylenedioxythiophene) (PEDOT):polystyrene sulfonate (PSS) spun coat films with a root mean squared error of prediction of 9 nm [105]. This comes as a result of the increased wavelength detection range

of the NIR, resulting in an extremely sensitive dependence on film thicknesses. In addition, the authors showed that this is effective on flexible substrates, indicating a readiness to move to R2R manufacturing.

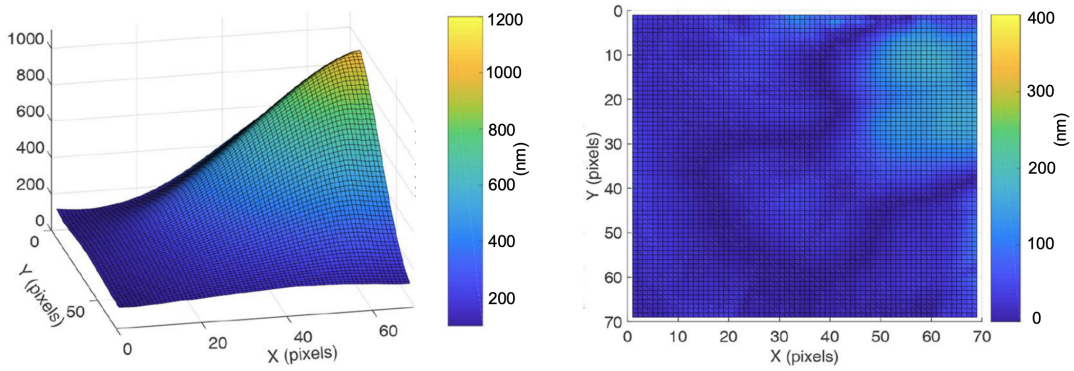

(a) Automatically reconstructed thickness profile after optimisation

(b) Absolute pixel wise height difference between the manual and the optimized thickness profile in (a)

Figure 2.29: The results of Chandran Sudra et al. study using HSI for *in situ* dynamic thin film interferometry, adapted from [103].

Hyperspectral luminescence imaging (HSLI) has been used to determine the characteristics of perovskite solar cells via the construction of absolute maps of the depth-averaged quasi-Fermi level splitting[6] through spectrally and spatially resolved photoluminescence and electroluminescence [106]. Although only demonstrated ex situ, this presents a powerful impact if successfully integrated *in situ* as it could allow the directed manufacture of solar cell characteristics such as open circuit voltage (V_{OC}) at the perovskite fabrication stage via feedback from *in situ* HSLI.

Although not yet applied to the spin-coating process, the power of HSI in thin film characterisation has been successfully demonstrated. As the technology becomes more mature, it will meet the speed demands of *in situ* monitoring and allow for spatially resolved spectral information to be obtained easily, vital for 2D monitoring. This presents distinct advantages for large-area manufacturing, especially in R2R processing. In addition to advancements in technology, deep learning is already being extensively applied to HSI for additional insight, usually for image classification [102] [107] and to improve HSI data [108]. HSI lends itself to these kinds of analyses because of its large data base, however, application in films processing appears limited at this time. These can complement machine learning techniques already existing for spectral data, such as the method developed by

[6]The eV difference between separated electrons and holes

Kim in 2020 that uses a convolutional neural network (CNN) to mitigate the local minima problem present in non-linear fitting of reflectance spectra [71]. More generally, two-dimensional interference patterns are well suited to deep learning approaches for decoding. Many architectures have been successful in improving the pre-processing, analysis, and post-processing stages of optical metrology data [109].

In 2021 Cho et al. from Samsung Electronics Co. Mechatronics R&D Centre published a method that utilised hyperspectral training data and a gaussian process regression (deep learning) model to enhance standard RGB sensing [110]. Using this they were able to obtain fast and precise thickness estimates of wafers from RGB data. This is similar to other methods that use sets of training data to reconstruct spectrums from RGB data [111] [112]. Methods such as these seem like a promising direction to take advantage of hyperspectral data for *in situ* sensing due to speed and resolution limitations currently posed by HSI cameras. Future advancements in HSI technology, such as the use of metamaterials [113], are likely to remove these limitations in future commercially available hyperspectral cameras.

2.5 Summary

Reflectance techniques offer huge advantages when processing polymer films from solution because they are non-contact, non-destructive, and fast. Laser point reflection has been used extensively in solution processing due to ease of implementation and valuable information on drying kinetics [42] [58]. Laser scattering provides indication of morphology changes, albeit in reciprocal space, that are difficult to obtain for dynamic films via other methods [50] [51]. Specular reflectance, with fully resolved spectral reflectance information, is a particularly powerful method because it provides much deeper insight into the film system, including optical constants of multilayer systems [72] and can be used to track phase separations and changes in morphology [74] - even predicting favourable device performances [75] [106]. Nevertheless, these methods are obviously at a disadvantage when scaling processing because they are only effective at a single point, and at this point they are an area-averaged measurement.

The extension of monochromatic reflectance methods to imaging is straightforward and has been used in two major ways. Firstly, over the whole area of the processed film in order

to characterise drying kinetics in different regions, providing a fuller understanding of the film-forming process [78]. This is particularly valuable at larger scales and important when moving between processing methods [78] while maintaining morphologies that are heavily influenced by changing drying kinetics. Secondly, as a technique for directly observing morphology by using the same technique at microscopic scales, i.e. coupled with a microscope (this being a key benefit of optical techniques). These types of studies have been effective in understanding how different polymer blends phase separate [89] [92] [94], and in probing crystallisation kinetics [91], often giving the important link between how the final morphology is formed and rationally producing films with enhanced characteristics for their application.

Issues arise when trying to extend spectral measurements over areas, like what has been so successfully achieved with monochromatic reflectance. To do this requires a hyperspectral imaging; however, snapshot hyperspectral cameras suitable for the task often do not meet the resolution or frame rate requirements for effective *in situ* studies, or are extremely expensive. An area gaining traction is the use of line scan HSI on R2R coaters [114], where more conventional resolutions can be reached due to the inherent movement between the detection and the web. To combat these issues, techniques are being developed that aim to indirectly achieve HSI with less data using deep learning techniques [110].

Currently, there is a gap between easily achieved monochromatic studies that have drawbacks in insight, and comparably very difficult to achieve and expensive hyperspectral imaging studies. Colour imaging seems to be an underutilised resource in film metrology, partly due to the ambiguity that arises in having broadband detection. This issue notwithstanding, the Bayer filter provides cheap access, by virtue of mass production, to facile multi-channel detection over large areas. Exploration of colour imaging, as a trade-off between the spectrally limited by spatially detailed information for monochromatic imaging, and the spectrally detailed but currently impractical use of hyperspectral cameras, is promising.

Table 2.1: Overview of reflectance based techniques used to monitor thin films *in situ*

Technique	**Type**	**Illumination**	**Detection**	**Insight**	**Important references**
Laser reflectance	Point	Monochromatic	Photodiode	Drying rate at a single position	[43]
Laser scattering	Point	Monochromatic	Screen and mono camera	Reciprocal space length scale, averaged at a single position	[51] [50]
Spectral reflectance	Point	Broadband	Spectrometer	Optical constants and (indirectly) morphological/compositional changes	[77]
Mono reflectance imaging	Imaging	Monochromatic (large area)	Digital mono camera	Drying rate at all points, topological contours	[78]
Mono reflectance imaging microscopy	Imaging	Monochromatic	Digital mono camera	Direct imaging of morphology via OPD	[89] [93] [94]
Colour reflectance imaging	Imaging	Broadband	Digital colour camera	Optical constant changes at all points	[15]
Hyperspectral reflectance imaging	Imaging	Broadband	Hyperspectral camera	Optical constants and (possibly) morphological/compositional changes at all points	[103]

References

[2] Aleksei Solomonov et al. “Flexible Soft-Printed Polymer Films with Tunable Plasmonic Properties”. In: *ACS Materials Au* 3.6 (2023), pp. 699–710. DOI: 10.1021/acsmaterialsau.3c00023.

[3] Varun S. Prasath and Kenneth K.S. Lau. “Kinetically Limited Bulk Polymerization of Polymer Thin Films by Initiated Chemical Vapor Deposition”. In: *Macromolecules* 56.24 (2023), pp. 10111–10118. DOI: 10.1021/acs.macromol.3c01868.

[4] Zhengran He, Kyeiwaa Asare, and Yeboah Sheng. “Polystyrene applications in organic electronics”. In: *Discover Electronics* August (2024). DOI: 10.1007/s44291-024-00039-6.

[5] Longjian Xue, Jilin Zhang, and Yanchun Han. “Phase separation induced ordered patterns in thin polymer blend films”. In: *Progress in Polymer Science (Oxford)* 37.4 (2012), pp. 564–594. DOI: 10.1016/j.progpolymsci.2011.09.001.

[6] Hannah J. Eggimann et al. “Efficient energy transfer mitigates parasitic light absorption in molecular charge-extraction layers for perovskite solar cells”. In: *Nature Communications* 11.1 (2020). DOI: 10.1038/s41467-020-19268-w.

[7] Fei Qin et al. “Robust metal ion-chelated polymer interfacial layer for ultraflexible non-fullerene organic solar cells”. In: *Nature Communications* 11.1 (2020), pp. 1–8. DOI: 10.1038/s41467-020-18373-0.

[8] Elena Missale, Marco Frasconi, and Maria F. Pantano. “Ultrathin organic membranes: Can they sustain the quest for mechanically robust device applications?” In: *iScience* 26.2 (2023), p. 105924. DOI: 10.1016/j.isci.2023.105924.

[9] Saif M.H. Qaid et al. “Tuning the optical properties of meh–ppv/pfo hybrid thin films via the incorporation of cspbbr3 quantum dots”. In: *Coatings* 11.2 (2021), pp. 1–15. DOI: 10.3390/coatings11020154.

[10] Sam Coveney. “Fundamentals of Phase Separation in Polymer Blend Thin Films”. In: *Springer Theses* September (2015), p. 179.

[11] Michael P. Howard, Arash Nikoubashman, and Athanassios Z. Panagiotopoulos. “Stratification in Drying Polymer-Polymer and Colloid-Polymer Mixtures”. In: *Langmuir* 33.42 (2017), pp. 11390–11398. DOI: 10.1021/acs.langmuir.7b02074.

[12] Peter Petrik. "Optical thin film metrology for optoelectronics". In: *Journal of Physics: Conference Series* 398.1 (2012). DOI: 10.1088/1742-6596/398/1/012002.

[13] Dietrich Meyerhofer. "Characteristics of resist films produced by spinning". In: *Journal of Applied Physics* 49.7 (1978), pp. 3993–3997. DOI: 10.1063/1.325357.

[14] Joana Moreira, A. Catarina Vale, and Natália M. Alves. "Spin-coated freestanding films for biomedical applications". In: *Journal of Materials Chemistry B* 9.18 (2021), pp. 3778–3799. DOI: 10.1039/d1tb00233c.

[15] Dunbar P. Birnie, Dylan E. Haas, and Carissa M. Hernandez. "Laser interferometric calibration for real-time video color interpretation of thin fluid layers during spin coating". In: *Optics and Lasers in Engineering* 48.5 (2010), pp. 533–537. DOI: 10.1016/j.optlaseng.2009.12.021.

[16] Alfred G. Emslie, Francis T. Bonner, and Leslie G. Peck. "Flow of a viscous liquid on a rotating disk". In: *Journal of Applied Physics* 29.5 (1958), pp. 858–862. DOI: 10.1063/1.1723300.

[17] Kangkang Weng et al. "Optimized active layer morphology toward efficient and polymer batch insensitive organic solar cells". In: *Nature Communications* 11.1 (2020), pp. 1–9. DOI: 10.1038/s41467-020-16621-x.

[18] Bradley P. Kirk et al. "Printing and Coating Techniques for Scalable Organic Photovoltaic Fabrication". In: *Materials* 17.11 (2024). DOI: 10.3390/ma17112511.

[19] Yoshiro Yamashita. "Organic semiconductors for organic field-effect transistors". In: *Science and Technology of Advanced Materials* 10.2 (2009). DOI: 10.1088/1468-6996/10/2/024313.

[20] Yongbo Yuan et al. "Ultra-high mobility transparent organic thin film transistors grown by an off-centre spin-coating method". In: *Nature Communications* 5 (2014), pp. 1–9. DOI: 10.1038/ncomms4005.

[21] Nam Koo Kim et al. "High-Performance Organic Field-Effect Transistors with Directionally Aligned Conjugated Polymer Film Deposited from Pre-Aggregated Solution". In: *Chemistry of Materials* 27.24 (2015), pp. 8345–8353. DOI: 10.1021/acs.chemmater.5b03775.

[22] Liangkun Lu et al. "High-performance flexible organic field effect transistors with print-based nanowires". In: *Microsystems and Nanoengineering* 9.1 (2023). DOI: 10.1038/s41378-023-00551-x.

[23] Niranjan Sahu, B. Parija, and S. Panigrahi. "Fundamental understanding and modeling of spin coating process: A review". In: *Indian Journal of Physics* 83.4 (2009), pp. 493–502. DOI: 10.1007/s12648-009-0009-z.

[24] Severin Siegrist et al. "Understanding Coating Thickness and Uniformity of Blade-Coated SnO2 Electron Transport Layer for Scalable Perovskite Solar Cells". In: *Solar RRL* 7.14 (2023). DOI: 10.1002/solr.202300273.

[25] Maël Le Berre, Yong Chen, and Damien Baigl. "From convective assembly to landau - Levich deposition of multilayered phospholipid films of controlled thickness". In: *Langmuir* 25.5 (2009), pp. 2554–2557. DOI: 10.1021/la803646e.

[26] Ryungeun Song et al. "Physics-informed machine learning for optimizing the coating conditions of blade coating Physics-informed machine learning for optimizing the coating conditions of blade coating". In: *Phys. Fluids* 34 (2022). DOI: 10.1063/5.0098666.

[27] Xiaodan Gu et al. "The meniscus-guided deposition of semiconducting polymers". In: *Nature Communications* 9.1 (2018). DOI: 10.1038/s41467-018-02833-9.

[28] Sebastian A. Schneider et al. "Controlling Polymer Morphology in Blade-Coated All-Polymer Solar Cells". In: *Chemistry of Materials* 33.15 (2021), pp. 5951–5961. DOI: 10.1021/acs.chemmater.1c01050.

[29] Dawei Wu et al. "Blade Coating Aligned, High-Performance, Semiconducting-Polymer Transistors". In: *Chemistry of Materials* 30.6 (2018), pp. 1924–1936. DOI: 10.1021/acs.chemmater.7b04835.

[30] Farshad Jafarzadeh et al. "Stable and sustainable perovskite solar modules by optimizing blade coating nickel oxide deposition over 15 × 15 cm2 area". In: *Communications Materials* 5.1 (2024), pp. 1–9. DOI: 10.1038/s43246-024-00576-3.

[31] Hidenobu Miura and Masato Yamamura. "Direct thickness measurement of doctor-bladed liquid film on gravure roll surface". In: *Journal of Coatings Technology and Research* 12.5 (2015), pp. 827–833. DOI: 10.1007/s11998-015-9714-z.

[32] Jadel Tsiba Matondo et al. “Slot-Die Coating for Scalable Fabrication of Perovskite Solar Cells and Modules”. In: *Advanced Materials Technologies* 9.10 (2024), pp. 1–24. DOI: 10.1002/admt.202302082.

[33] Kenneth J. Ruschak. “Limiting flow in a pre-metered coating device”. In: *Chemical Engineering Science* 31.11 (1976), pp. 1057–1060. DOI: 10.1016/0009-2509(76)87026-1.

[34] B Levich L Landau. “Dragging of a liquid by a moving plate.” In: *Acta Physicochium URSS* 17 (1942), pp. 42–54.

[35] B G Higgins and L E Scriven. “Capillary pressure and viscous pressure drop set bounds on coating bead operability”. In: *Chemical Engineering Science* 35 (1979), pp. 673–782.

[36] Xiaoyu Ding, Jianhua Liu, and A. L. Tequila Harris. “A Review of the Operating Limits in Slot Die Coating Processes”. In: *AIChE Journal* 62.7 (2016), pp. 2508–2524. DOI: 10.1002/aic. arXiv: 0201037v1 [arXiv:physics].

[37] Nam Gyu Park and Kai Zhu. “Scalable fabrication and coating methods for perovskite solar cells and solar modules”. In: *Nature Reviews Materials* 5.5 (2020), pp. 333–350. DOI: 10.1038/s41578-019-0176-2.

[38] J. Kedzierski et al. “Determination of ordinary and extraordinary refractive indices of nematic liquid crystals by using wedge cells”. In: *Opto-Electronics Review* 18.2 (2010), pp. 214–218. DOI: 10.2478/s11772-010-0009-8.

[39] A. H. Jarrett. “Atlas of optical phenomena: M. Cagnet, M. Francon and J.C. Thrierr: Springer-Verlag 1962. 45 pp. 74 DM”. In: *Planetary and Space Science* 11 (1963), p. 584.

[40] W H Bragg and W L Bragg. “The reflection of X-rays by crystals”. In: *Proc. R. Soc. Lond. A.* 88 (1913), pp. 428–438.

[41] Frank L. Pedrotti, Leno M. Pedrotti, and Leno S. Pedrotti. *Introduction to Optics*. Pearson Education, 2008.

[42] F. Horowitz et al. “Real-time optical monitoring of spin coating”. In: *Journal de Physique III* 3.11 (1993), pp. 2059–2063. DOI: 10.1051/jp3:1993253.

[43] F. Horowitz, A. F. Michels, and E. M. Yeatman. "Optical Viscometry of Spinning Sol Coatings". In: *Journal of Sol-Gel Science and Technology* 13.1-3 (1998), pp. 707–712. DOI: 10.1023/a:1008697023104.

[44] Dunbar P. Birnie and Manuel Manley. "Combined flow and evaporation of fluid on a spinning disk". In: *Physics of Fluids* 9.4 (1997), pp. 870–875. DOI: 10.1063/1.869519.

[45] Dunbar P. Birnie and Manuel Manley. "Combined flow and evaporation of fluid on a spinning disk". In: *Physics of Fluids* 9.4 (1997), pp. 870–875. DOI: 10.1063/1.869519.

[46] Dylan E. Haas et al. "Effect of solvent evaporation rate on skin formation during spin coating of complex solutions". In: *Sol-Gel Optics V* 3943.May 2000 (2000), pp. 280–284. DOI: 10.1117/12.384348.

[47] B. Reisfeld, S. G. Bankoff, and S. H. Davis. "The dynamics and stability of thin liquid films during spin coating. I. Films with constant rates of evaporation or absorption". In: *Journal of Applied Physics* 70.10 (1991), pp. 5258–5266. DOI: 10.1063/1.350235.

[48] Y. Mouhamad et al. "Dynamics of polymer film formation during spin coating". In: *Journal of Applied Physics* 116.12 (2014). DOI: 10.1063/1.4896674.

[49] A. D.F. Dunbar et al. "A solution concentration dependent transition from self-stratification to lateral phase separation in spin-cast PS:d-PMMA thin films". In: *European Physical Journal E* 31.4 (2010), pp. 369–375. DOI: 10.1140/epje/i2010-10592-4.

[50] Paul C. Jukes et al. "Time-resolved light scattering studies of phase separation in thin film semiconducting polymer blends during spin-coating". In: *Macromolecules* 38.6 (2005), pp. 2030–2032. DOI: 10.1021/ma0477145.

[51] Sasha Y. Heriot and Richard A.L. Jones. "An interfacial instability in a transient wetting layer leads to lateral phase separation in thin spin-cast polymer-blend films". In: *Nature Materials* 4.10 (2005), pp. 782–786. DOI: 10.1038/nmat1476.

[52] Dunbar P. Birnie. "Optical video interpretation of interference colors from thin transparent films on silicon". In: *Materials Letters* 58.22-23 (2004), pp. 2795–2800. DOI: 10.1016/j.matlet.2004.04.018.

[53] Dylan E. Haas and Dunbar P. Birnie. "Nondestructive measurement of striation defect spacing using laser diffraction". In: *Journal of Materials Research* 16.12 (2001), pp. 3355–3360. DOI: 10.1557/JMR.2001.0463.

[54] Stefan Walheim et al. "Structure formation via polymer demixing in spin-cast films". In: *Macromolecules* 30.17 (1997), pp. 4995–5003. DOI: 10.1021/ma9619288.

[55] Parvaneh Mokarian-Tabari. "Controlling the Morphology of Spin coated Polymer Blend Films". PhD thesis. University of Sheffield, 2009.

[56] Jacobus J. Van Franeker et al. "A real-time study of the benefits of co-solvents in polymer solar cell processing". In: *Nature Communications* 6 (2015), pp. 1–8. DOI: 10.1038/ncomms7229.

[57] Yanfeng Liu et al. "In Situ Optical Studies on Morphology Formation in Organic Photovoltaic Blends". In: *Small Methods* 5.10 (2021). DOI: 10.1002/smtd.202100585.

[58] B. Schmidt-Hansberg et al. "In situ monitoring the drying kinetics of knife coated polymer-fullerene films for organic solar cells". In: *Journal of Applied Physics* 106.12 (2009). DOI: 10.1063/1.3270402.

[59] Nusret S. Güldal et al. "Real-time evaluation of thin film drying kinetics using an advanced, multi-probe optical setup". In: *Journal of Materials Chemistry C* 4.11 (2016), pp. 2178–2186. DOI: 10.1039/c5tc03448e.

[60] Simon Ternes et al. "Drying Dynamics of Solution-Processed Perovskite Thin-Film Photovoltaics: In Situ Characterization, Modeling, and Process Control". In: *Advanced Energy Materials* 9.39 (2019). DOI: 10.1002/aenm.201901581.

[61] R Swanepoel. "Determination of the thickness and optical constants of amorphous silicon". In: *Journal of Physics E: Sci. Instrum.* 16 (1983), p. 1214. DOI: 10.1080/14786430902835644.

[62] Lyashenko S. P. "A simple method for the determination of the thickness and optical constants of semiconducting and dielectric layers". In: *Opt. Spectrosc.* 16 (1964), pp. 80–81.

[63] J Wales, GJ Lovitt, and RA Hill. "Optical properties of germanium films in the 1–5 μ range". In: *Thin Solid Films* 1.2 (1967), pp. 137–150.

[64] J Szczyrbowski and A Czapla. “Optical absorption in DC sputtered InAs films”. In: *Thin Solid Films* 46.2 (1977), pp. 127–137.

[65] Abdelaziz Tchenka, Abdelali Agdad, and Elmaati Ech-Chamikh. “Determination of the thickness and optical properties by reflectance method”. In: *Infrared Physics and Technology* 137.September 2023 (2024). DOI: 10.1016/j.infrared.2024.105117.

[66] I. Chambouleyron et al. “Retrieval of optical constants and thickness of thin films from transmission spectra”. In: *Appl. Opt.* 36.31 (1997), pp. 8238–8247.

[67] Jiři Luňáček, Petr Hlubina, and Milena Luňáčková. “Simple method for determination of the thickness of a nonabsorbing thin film using spectral reflectance measurement”. In: *Applied Optics* 48.5 (2009), pp. 985–989. DOI: 10.1364/AO.48.000985.

[68] Jingtao Dong and Rongsheng Lu. “Characterization of weakly absorbing thin films by multiple linear regression analysis of absolute unwrapped phase in angle-resolved spectral reflectometry”. In: *Opt. Express* 26.9 (2018), pp. 12291–12305. DOI: 10.1364/OE.26.012291.

[69] Kwangrak Kim, Soonyang Kwon, and Heui Jae Pahk. “Fast analysis of film thickness in spectroscopic reflectometry using direct phase extraction”. In: *Current Optics and Photonics* 1.1 (2017), pp. 29–33. DOI: 10.3807/COPP.2017.1.1.029.

[70] M. D. Heinemann et al. “Evolution of opto-electronic properties during film formation of complex semiconductors”. In: *Scientific Reports* 7.April (2017), pp. 1–9. DOI: 10.1038/srep45463.

[71] Min Gab Kim. “Improved Measurement of Thin Film Thickness in Spectroscopic Reflectometer Using Convolutional Neural Networks”. In: *International Journal of Precision Engineering and Manufacturing* 21.2 (2020), pp. 219–225. DOI: 10.1007/s12541-019-00260-4.

[72] Stephan Van Duren et al. “Investigation of reflectometry for in situ process monitoring and characterization of co-evaporated and stacked Cu-Zn-Sn-S based thin films”. In: *Journal of Alloys and Compounds* 779 (Jan. 2019). DOI: 10.1016/j.jallcom.2018.11.337.

[73] Steven J. Byrnes. *Multilayer optical calculations*. 2020. arXiv: 1603.02720 [physics.comp-ph].

[74] Timo Raab et al. “Resolving the Spin Coating Process via in Situ Transmission Measurements”. In: *Journal of Physical Chemistry C* 126.45 (2022), pp. 19542–19548. DOI: 10.1021/acs.jpcc.2c06337.

[75] Hyun Wook Ro et al. “Morphology changes upon scaling a high-efficiency, solution-processed solar cell”. In: *Energy and Environmental Science* 9.9 (2016), pp. 2835–2846. DOI: 10.1039/c6ee01623e.

[76] Maged Abdelsamie et al. “In situ UV-visible absorption during spin-coating of organic semiconductors: A new probe for organic electronics and photovoltaics”. In: *Journal of Materials Chemistry C* 2.17 (2014), pp. 3373–3381. DOI: 10.1039/c3tc32077d.

[77] Jörg Rappich et al. “Fast Optical Reflectance Measurements during Spin Coating and Annealing of Organic–Inorganic Perovskite Precursor Solutions”. In: *Physica Status Solidi (B) Basic Research* 258.5 (2021), pp. 1–8. DOI: 10.1002/pssb.202000479.

[78] Jonas Bergqvist et al. “In situ reflectance imaging of organic thin film formation from solution deposition”. In: *Solar Energy Materials and Solar Cells* 114 (2013), pp. 89–98. DOI: 10.1016/j.solmat.2013.02.030.

[79] Simon Ternes et al. “Correlative In Situ Multichannel Imaging for Large-Area Monitoring of Morphology Formation in Solution-Processed Perovskite Layers”. In: *Solar RRL* 6.3 (2022). DOI: 10.1002/solr.202100353.

[80] Nina Taherimakhsousi et al. “A machine vision tool for facilitating the optimization of large-area perovskite photovoltaics”. In: *npj Computational Materials* 7.1 (2021). DOI: 10.1038/s41524-021-00657-8.

[81] Chuan Liu et al. “Self-assembly of semiconductor/insulator interfaces in one-step spin-coating: A versatile approach for organic field-effect transistors”. In: *Physical Chemistry Chemical Physics* 15.21 (2013), pp. 7917–7933. DOI: 10.1039/c3cp44715d.

[82] Youna Choi, Byoung Hoon Lee, and Heejoo Kim. “Bicontinuous network of electron donor-acceptor composites achieved by additive-free sequential deposition for efficient polymer solar cells”. In: *Current Applied Physics* 20.6 (2020), pp. 760–764. DOI: 10.1016/j.cap.2020.03.011.

[83] Kang Wei Chou et al. “Spin-cast bulk heterojunction solar cells: A dynamical investigation”. In: *Advanced Materials* 25.13 (2013), pp. 1923–1929. DOI: 10.1002/adma.201203440.

[84] Kui Zhao et al. “Vertical Phase Separation in Small Molecule:Polymer Blend Organic Thin Film Transistors Can Be Dynamically Controlled”. In: *Advanced Functional Materials* 26.11 (2016), pp. 1737–1746. DOI: 10.1002/adfm.201503943.

[85] Loni M. Peurrung and David B. Graves. “Spin Coating Over Topography”. In: *IEEE Transactions on Semiconductor Manufacturing* 6.1 (1993), pp. 72–76. DOI: 10.1109/66.210660.

[86] L. M. Peurrung and D. B. Graves. “Film Thickness Profiles over Topography in Spin Coating”. In: *Journal of The Electrochemical Society* 138.7 (1991), pp. 2115–2124. DOI: 10.1149/1.2085935.

[87] Kang Wei Chou et al. “Late stage crystallization and healing during spin-coating enhance carrier transport in small-molecule organic semiconductors”. In: *Journal of Materials Chemistry C* 2.28 (2014), pp. 5681–5689. DOI: 10.1039/c4tc00981a.

[88] Jung Hun Lee et al. “Effect of Crystallization Modes in TIPS-pentacene/Insulating Polymer Blends on the Gas Sensing Properties of Organic Field-Effect Transistors”. In: *Scientific Reports* 9.1 (2019), pp. 1–9. DOI: 10.1038/s41598-018-36652-1.

[89] Stephen Ebbens et al. “In situ imaging and height reconstruction of phase separation processes in polymer blends during spin coating”. In: *ACS Nano* 5.6 (2011), pp. 5124–5131. DOI: 10.1021/nn201210e.

[90] Daniel T.W. Toolan et al. “Direct observation of morphological development during the spin-coating of polystyrene-poly(methyl methacrylate) polymer blends”. In: *Journal of Polymer Science, Part B: Polymer Physics* 51.11 (2013), pp. 875–881. DOI: 10.1002/polb.23288.

[91] Daniel T.W. Toolan et al. “In situ studies of phase separation and crystallization directed by Marangoni instabilities during spin-coating”. In: *Advanced Materials* 25.48 (2013), pp. 7033–7037. DOI: 10.1002/adma.201302657.

[92] Daniel T.W. Toolan et al. “Directed phase separation of PFO:PS blends during spin-coating using feedback controlled in situ stroboscopic fluorescence microscopy”.

In: *Journal of Materials Chemistry A* 1.11 (2013), pp. 3587–3592. DOI: 10.1039/c3ta01530k.

[93] Daniel T.W. Toolan, Richard Hodgkinson, and Jonathan R. Howse. "Stroboscopic microscopy - Direct imaging of structure development and phase separation during spin-coating". In: *Journal of Polymer Science, Part B: Polymer Physics* 52.1 (2014), pp. 17–25. DOI: 10.1002/polb.23410.

[94] Ehtsham Ul Haq et al. "Real time laser interference microscopy for bar-spread polystyrene/ poly(methyl methacrylate) blends". In: *Journal of Polymer Science, Part B: Polymer Physics* 52.15 (2014), pp. 985–992. DOI: 10.1002/polb.23513.

[95] Tsengelidis Savvas. "Algebraic modelling of transformations from Bayer to RGB images". PhD thesis. Technical University of Crete, 2006.

[96] Yoshie Kobayashi et al. "Reconstructing Shapes and Appearances of Thin Film Objects Using RGB Images". In: *Proceedings of the IEEE Computer Society Conference on Computer Vision and Pattern Recognition* 2016-Decem (2016), pp. 3774–3782. DOI: 10.1109/CVPR.2016.410.

[97] Michal Urbánek et al. "Imaging reflectometry in situ". In: *Applied Optics* 46.25 (2007), pp. 6309–6313. DOI: 10.1364/AO.46.006309.

[98] Jiao Bai et al. "A new method to measure spectral reflectance and film thickness using a modified chromatic confocal sensor". In: *Optics and Lasers in Engineering* 154.September 2023 (2022). DOI: 10.1016/j.optlaseng.2022.107019.

[99] L. Gustafsson, E. Hglund, and O. Marklund. "Measuring Lubricant Film Thickness with Image Analysis". In: *Proceedings of the Institution of Mechanical Engineers, Part J: Journal of Engineering Tribology* 208.3 (1994), pp. 199–205. DOI: 10.1243/PIME_PROC_1994_208_371_02.

[100] Garam Choi et al. "Simple method for volumetric thickness measurement using a color camera". In: *Applied Optics* 57.26 (2018), p. 7550. DOI: 10.1364/ao.57.007550.

[101] Nils Bornemann and Edgar Dörsam. "A flatbed scanner for large-area thickness determination of ultra-thin layers in printed electronics". In: *Optics Express* 21.19 (2013), p. 21897. DOI: 10.1364/oe.21.021897.

[102] Garima Jaiswal, Arun Sharma, and Sumit Kumar Yadav. "Critical insights into modern hyperspectral image applications through deep learning". In: *Wiley Interdisciplinary Reviews: Data Mining and Knowledge Discovery* 11.6 (2021), pp. 1–22. DOI: 10.1002/widm.1426.

[103] V. Chandran Suja et al. "Hyperspectral imaging for dynamic thin film interferometry". In: *Scientific Reports* 10.1 (2020), pp. 1–8. DOI: 10.1038/s41598-020-68433-0.

[104] Gary A Shaw and Hsiao-hua K Burke. "Spectral imaging for remote sensing". In: *Lincon laboratory journal* 14.1 (2003), pp. 3–28.

[105] Olesya Daikos et al. "Near-infrared hyperspectral imaging for monitoring the thickness distribution of thin poly(3,4-ethylenedioxythiophene):poly(styrene sulfonate) (PEDOT:PSS) layers". In: *Talanta* 223.1 (2021), p. 121696. DOI: 10.1016/j.talanta.2020.121696.

[106] Gilbert El-Hajje et al. "Quantification of spatial inhomogeneity in perovskite solar cells by hyperspectral luminescence imaging". In: *Energy and Environmental Science* 9.7 (2016), pp. 2286–2294. DOI: 10.1039/c6ee00462h.

[107] Dhritiman Saha and Annamalai Manickavasagan. "Machine learning techniques for analysis of hyperspectral images to determine quality of food products: A review". In: *Current Research in Food Science* 4.December 2020 (2021), pp. 28–44. DOI: 10.1016/j.crfs.2021.01.002.

[108] Rong Wong et al. "HSI-IPNet: Hyperspectral Imagery Inpainting by Deep Learning with Adaptive Spectral Extraction". In: *IEEE Journal of Selected Topics in Applied Earth Observations and Remote Sensing* 13 (2020), pp. 4369–4380. DOI: 10.1109/JSTARS.2020.3012443.

[109] Chao Zuo et al. *Deep learning in optical metrology: a review*. Vol. 11. 1. Springer US, 2022. DOI: 10.1038/s41377-022-00714-x.

[110] Doo-Hyun Cho et al. "High-speed wafer film measurement with heterogeneous optical sensor system". In: *SPIE Vol. 11611 116110H-3*. 2021. DOI: 10.1117/12.2584200.

[111] Ville Heikkinen et al. “Evaluation and unification of some methods for estimating reflectance spectra from RGB images”. In: *Journal of the Optical Society of America A* 25.10 (2008), p. 2444. DOI: 10.1364/josaa.25.002444.

[112] Noriyuki Shimano. “Recovery of spectral reflectances of objects being imaged without prior knowledge”. In: *IEEE Transactions on Image Processing* 15.7 (2006), pp. 1848–1856. DOI: 10.1109/TIP.2006.877069.

[113] Filiz Yesilkoy et al. “Ultrasensitive hyperspectral imaging and biodetection enabled by dielectric metasurfaces”. In: *Nature Photonics* 13.6 (2019), pp. 390–396. DOI: 10.1038/s41566-019-0394-6.

[114] Kerry Maize et al. “Real-Time Metrology for Roll-To-Roll and Advanced Inline Manufacturing: A Review”. In: *Advanced Materials Technologies* 8.2 (2023). DOI: 10.1002/admt.202200173.

Chapter 3

Large-area Broadband RGB Stroboscopic Spin Coating

This chapter was published in full in *Optics and Lasers in Engineering* [1]. Due to being published the nomenclature is defined as it is introduced in the chapter; however, it is mostly consistent with that used in Chapter 2. The chapter retains inline what is included as separate supplementary information documents (non-video) when it was published as the paper, supplementary video urls are included in the final section. Reference numbers will be different from what appears in the published paper to keep references in the thesis unique and consistent.

This chapter explores broadband reflectance imaging using a standard Bayer filter colour camera detection and LED illumination. This is achieved over a large area (3" wafer) in a study on the dynamic fluid profiles of spun coat solvents. The work in the chapter pushes the limits of the LED/Bayer illumination/detection combination for thin film metrology and demonstrates the fundamental restrictions of this illumination and detection combination.

3.1 Abstract

This work presents a novel optical setup to provide scalable *in situ* metrology during spin coating. Stroboscopic white-light imaging provides high-resolution colour videos of the process, at a temporal resolution matching the spin speed, where thin film interference colours are observed. Monochromatic specular reflection intensity data from the centre of rotation provide a thickness profile at this point. By developing a colour-to-thickness relationship *in situ* with the combination of these techniques, and leveraging the large-area data provided by colour imaging, the thickness at any point on the wafer is reconstructed via a mapping procedure with minimal a priori information. Experiments are carried out on full 3" diameter wafers spun with pure xylene or pure butyl acetate, and the thickness profile at all points on the wafer can be determined. Differences in the topology of these solvents whilst drying are linked back to the solvent properties. The colour to thickness mapping procedure is shown to have less than 5% error in determined thickness values between 2 µm and 100 nm. The possible length scale resolved by the imaging is fully discussed as a function of radius, spin speed, strobe pulse duration and hardware used. The studies in this work achieved a minimum lateral resolution of 315 µm when observing a full wafer, which is sufficiently detailed to properly reconstruct thickness variations caused by common spin-coating defects such as comets. The large area and scalable nature of this metrology technique lends itself to applications in semiconductor manufacturing where substrates of 300 mm are standard.

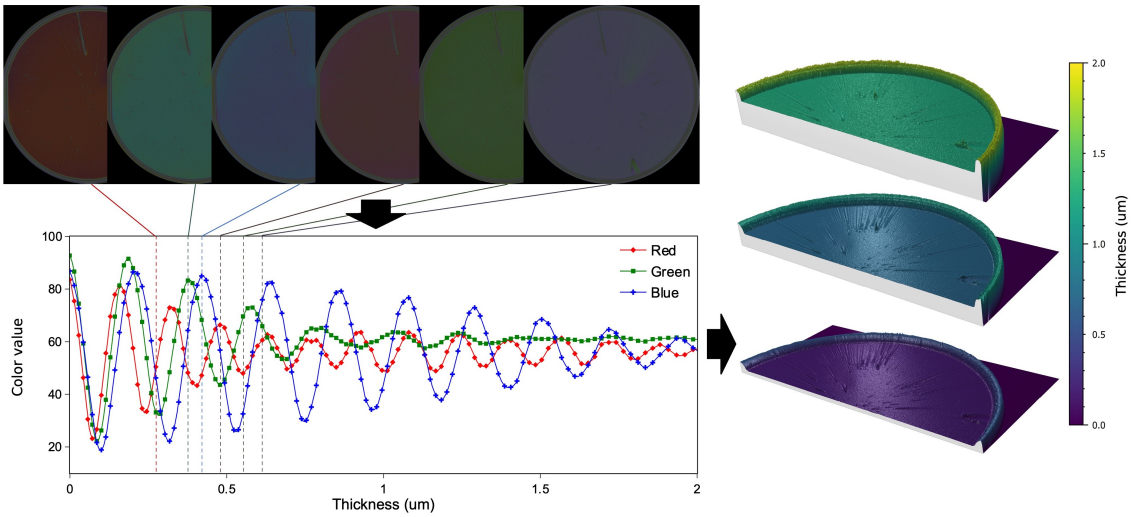

Figure 3.1: Graphical Abstract

3.1.1 Keywords

Spin-coating, metrology, thin film interference, reflectance, full-wafer

3.2 Introduction

Spin coating is an indispensable thin film fabrication technique, offering a simple and reliable approach for depositing thin films with robust control over thickness and morphology. These films find extensive applications across various fields, including photoresists and electronics [115] [116], optoelectronics [117] [118] [119] and energy storage [120], among others. The exceptional versatility of spin coating lies in the techniques ability to accommodate a wide set of materials beyond the standard photoresist, ranging from polymer blends [121] [5] [122] to small molecule crystals [88] and colloids [123] [124] [125] [126], enabling tailored film designs to suit specific application requirements. The effectiveness of each film in its application, regardless of specific morphology, is underpinned by a precise control of the thickness and uniformity.

Spin coating is one of the principal methods for fabricating thin films, especially at the lab scale. This is despite growing interest in larger scale or roll-to-roll (R2R) methods, such as slot-die coating, that are yet to close the gap in controllability and ease of use. Similarly, the dispensed liquid volumes employed in spin-coating, compared to R2R, permits film fabrication with greater efficiencies of materials and costs at lab scale. As a highly non-equilibrium process, on time scales of seconds, it is challenging for researchers to gain insight into the interplaying dynamics occurring during spin coating. Conversely, it is exactly this that places it as such a fast and reproducible method for synthesising these films. *In situ* non-contact reflection and scattering techniques have repeatedly proved a powerful tool over the last three decades, allowing researchers deeper insight into the phenomena at play. This has led to the development of films with more complex and uniform morphology, unlocking optimal structures and affording increased functionality and higher performance.

Techniques such as spectroscopic ellipsometry (SE) [127], specular laser reflection [13] [51], off- specular scattering [50], spectroscopy [128], wide-angle X-ray scattering (WAXS) [129] and grazing incidence x-ray diffraction (GIXRD) [130] have all been utilised *in situ* to monitor spun coat films' thickness and/or morphology. While providing valuable infor-

mation, these techniques are all limited to small areas and consequently only effectively impart information at a single point, usually at the centre of rotation to mitigate the effects of rotation and high angular velocities. This is a major drawback when spun coat films have the potential to vary in both thickness and morphology over the substrate, as evident in non-uniform films. Toolan et al. and Ebbens et al. utilised *in situ* reflectance imaging with stroboscopic illumination to enable direct microscopy of polymer phase separation during spin coating [89] [131] [90], observing how polymers phase separated with a thickness difference. These studies marked an improvement in the active area of the measurement compared to a point, and thus were able to resolve additional morphological information compared to specular reflectance. Bergqvist et al. performed *in situ* reflectance imaging to capture complete thickness information over a 3 cm^2 substrate [78]. Laser or monochromatic LED illumination is used in these imaging studies in combination with digital imaging so that thicknesses can be unambiguously extracted from pixel intensity information via fringe counting. However, in all these studies there is tension between the sampled area size and the lateral (surface metrology) resolution that is probed; the further from the centre of rotation, the increase in radial velocity gives time averaged, and hence surface averaged, data.

Most of these previous studies have employed monochromatic illumination as an aid to straightforward height reconstruction; methods that combine broadband white light and digital imaging encounter additional complexities. The use of white light means that interference fringes denoting a specific change in thickness, such as those visible when single wavelength light is used, do not appear. In contrast, white light produces interference colours that are the sum of different wavelengths at different levels of reflectance, producing a rainbow-like pattern; the same effect causes the multi-colour appearance in bubbles of soap. Birnie et al. used broadband white illumination across a 2" diameter silicon wafer to produce radially averaged thickness profiles by tracking interference colours outwards from a centre point, where the thickness was determined via specular reflection. They directly observed that thickness increased towards the edge of the substrate [15]. These observations challenged existing models that suggested laminar airflow over the wafer and Newtonian liquid flow should result in thinning independent of radius. The data was radially averaged due to image sensor sensitivity and data capture/exposure times generating radially blurred images.

For an isotropic non-absorbing thin film system, the reflectance spectrum is given by Equation 3.1 [132], where r_{10} and r_{21} are the Fresnel coefficients of the film-substrate and the ambient-film interfaces, given by $\frac{n_0-n_1}{n_0+n_1}$, and $\frac{n_1-n_2}{n_1+n_2}$, where n_0, n_1 and n_2 are the substrate, film and ambient refractive indices respectively, and the phase change caused by the optical path difference between subsequently reflected rays $\delta_1 = \frac{2\pi n_1 d\cos(\theta_1)}{\lambda}$.

$$R(\lambda, d) = \frac{r_{10}^2 + r_{21}^2 + 2r_{10}r_{21}\cos(2\delta_1)}{1 + r_{10}^2 r_{21}^2 + 2r_{10}r_{21}\cos(2\delta_1)} \tag{3.1}$$

The reflectance spectrum is therefore dependent on the refractive indices of the system, the angle of refraction in the film (the angle of propagation in the film, found from the angle of incidence from Snell's law), θ_1, the wavelength of light, λ, and the thickness of the film, d. When imaging, this spectrum R is captured by a digital camera sensor in a process modelled by Equation 3.2.

$$x_i = \Gamma_i \left(b_i \xi_i \int_{\lambda_{min}}^{\lambda_{max}} I(\lambda) R(\lambda, d) B_i(\lambda)\, d\lambda + \epsilon_i \right) \tag{3.2}$$

Here, x_i represents the scalar response of each colour channel $i = R, G, B$. $I(\lambda)$ denotes the illumination spectrum, $R(\lambda, d)$ is the reflectance spectrum of the thin film system, $B_i(\lambda)$ is the camera's sensitivity for the i^{th} channel, ϵ_i accounts for the random noise in the i^{th} channel, distributed with a mean of zero. The function Γ_i represents any nonlinearity in the channel, including camera gamma, colour temperature, and non-linear sensor response. The channel's colour balance is denoted as b_i and the scalar ξ_i models the exposure settings, gain and geometry of the setup.

Thickness may no longer be unambiguously defined by the intensities of colour channels alone. This is a well-documented limitation of colour imaging to determine film thicknesses, not just in spin coating but in other areas such as foam [133] [134] and lubricant [99] studies. This issue arises due to the loss of spectral information in digital imaging when a camera converts an incident spectrum to a RGB colour triplet via Bayer filtering and integration by the sensor as shown by Equation 3.2. A representation of this reduction in data is shown in Figure 3.2, that uses Equation 3.1 and 3.2 to simulate a colour camera response to a PMMA film ($n = 1.49, k = 0$) of varying thickness on a silicon substrate ($n = 3.88, k = 0.02$), in air. Past efforts to mitigate the ambiguity have involved manual reference via colourmaps [135], employing existing film profile knowledge [134] [99] [136]

and the use of hyperspectral cameras [103].

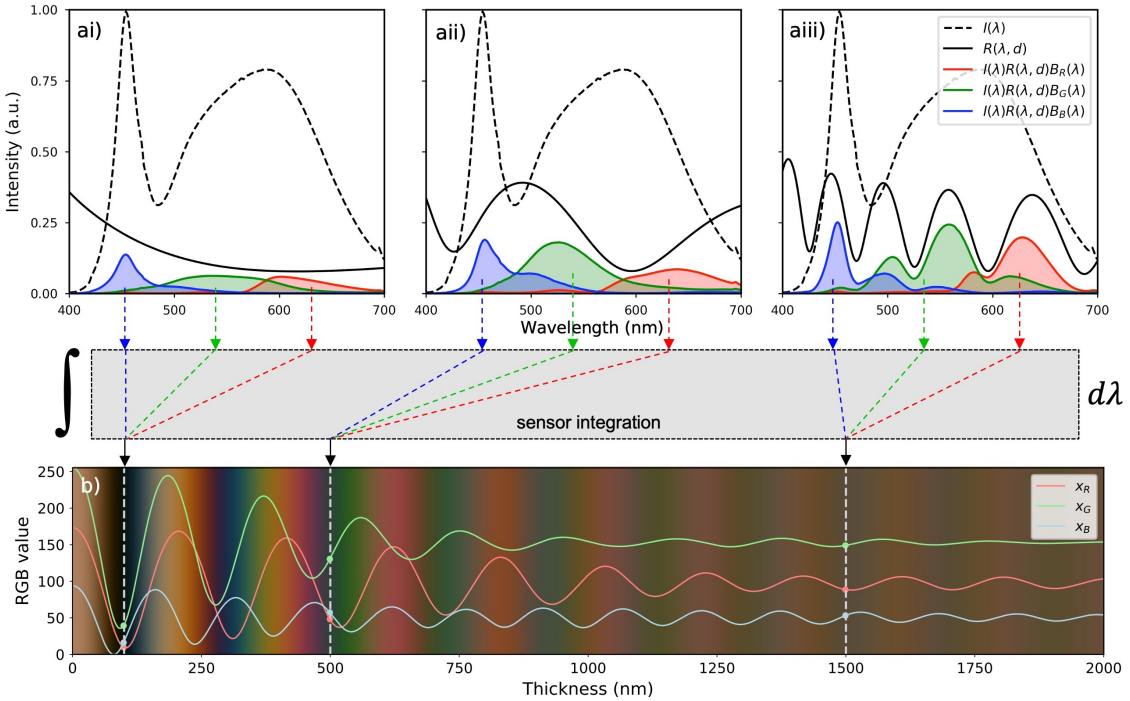

Figure 3.2: Digital imaging of a thin film system; (a) simulated reflectance spectra and channel activation spectra when observing a PMMA film (n=1.49) of 100nm (i) 500nm (ii) and 1500nm (iii) thicknesses with a Sony IMX253 sensor and LED illumination. (b) The normalised RGB triplets for these channel activation's as a function of thickness overlayed on the corresponding simulated colourmap, where the green activation has been reduced by a factor of two to account for relative frequency in the Bayer filter mosaic.

The work presented here seeks to address the small-area limitations of other thickness measurement methods, mitigated by recent high-speed, high sensitivity CMOS sensors, and high- power LED illumination, by presenting a novel technique that leverages digital colour imaging to produce two-dimensional thickness maps of a spun coat solvents over full-wafer areas. These maps can be reconstructed with minimal system knowledge via a colour-to-thickness relationship constructed *in situ*. To achieve this an optical setup has been constructed around a spin coater that simultaneously performs stroboscopic white light imaging and laser spectral reflectance. The ambiguity arising from using broadband white light has been resolved by developing a thickness mapping algorithm that selects the most appropriate solution to the developed colour-to-thickness relationship.

3.3 Materials and Methods

3.3.1 Apparatus

3.3.1.1 Stroboscopic white light imaging

A custom-made spin coater has been installed under an array of 8 x 18 v, 4000 K light emitting diodes (LED) (CXA1510-0000-000F0UG440H, CREE) outputting 6720 lm total, fitted with a 4 mm thick etched glass diffuser. A CMOS camera is mounted at 20°with a full, unobstructed view of the wafer surface and chuck. The diffuser is larger than the wafer and, despite the distance, fills the surface of the imaged wafer. The camera used is a PixeLink PL-X9512 containing a 17.6 mm (diagonal) Sony IMX235 sensor and is fitted with a 50 mm, $\frac{f}{2.2}$ lens. The spin coater is made from a 2.2 twin-shaft MAXON EC-i brushless motor, controlled via Labview. During rotation, a pulse is generated at the same point in every rotation by an optical switch and is used to trigger the start of the camera's exposure which also generates a strobe pulse of 30 µs width for the LED driver circuit, which powers the LED array at 31 v, based upon circuitry reported by Willert et al. The short length of this pulse 'freezes' the wafer for a clear picture, this is discussed further in Section 3.4.3. High-brightness LEDs are well suited to this application due to their rise time in the order of nanoseconds and ability to be run reliably in short pulses well over their rated power [137], ensuring sufficient illumination in the limited time. Data is collected continuously via 10GigE and solid-state M.2 drive, the setup is shown in Figure 3.3.

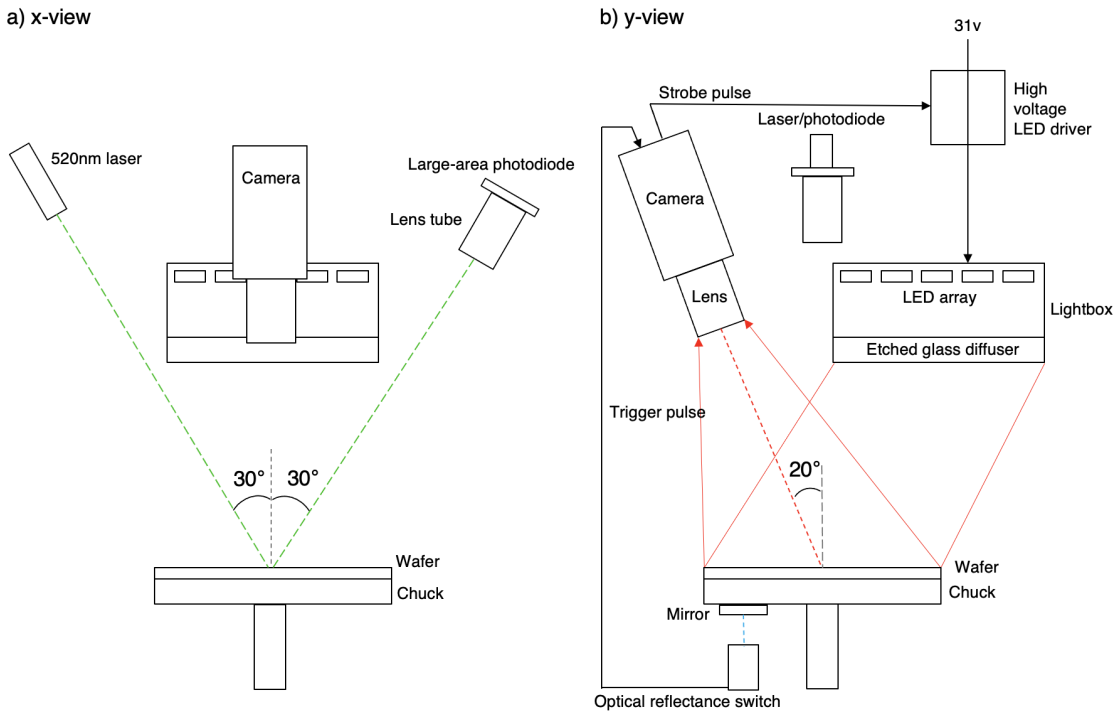

Figure 3.3: A schematic diagram of the stroboscopic imaging and laser reflectance configuration around the spun coat wafer from two perpendicular points of view.

This produces one image per full rotation, resulting in a video where the wafer appears motionless and interference colours can be tracked through time at any point across the surface. Figure 3.3 shows frames of a video captured in this way. Video 2.1-2.3 and 2.4-2.6 show examples of both the raw and processed versions of the videos, for full wafer xylene, full wafer butyl acetate and square wafer xylene respectively, shown at 15 fps for clarity. Example frames of these videos are shown in Figure 3.5 and Figure 3.6 respectivly. Native speed would be 41.7 fps (full wafer) or 33.3 fps (square wafer) equivalent to spin speeds of 2500 rpm and 2000 rpm respectively. Links to and descriptions of all videos can be found in Section 3.6.

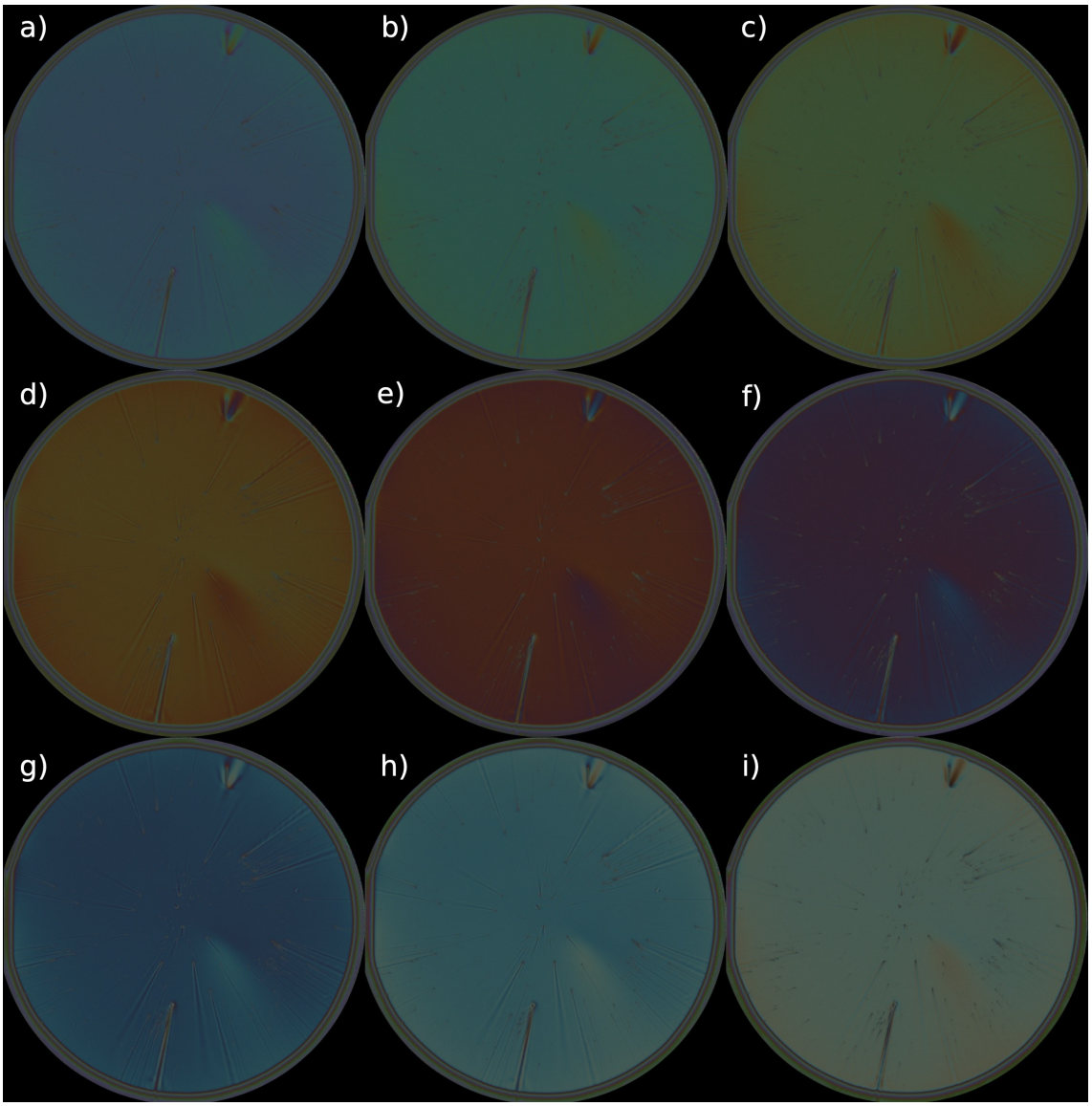

Figure 3.4: A series of 9 stroboscopic images taken from a video of xylene spun on a 3" diameter wafer at 2500 rpm. The images are spaced apart by 48 ms. From (a) to (i) the centre thickness decreases from 0.399 µm to 0.166 µm, with frame (i) being 277 ms before complete drying. Cyclical interference colours can be observed due to the thinning of the film. Edge beads, comet defects, and fluid nonuniformity can be clearly identified qualitatively by colour change within each frame.

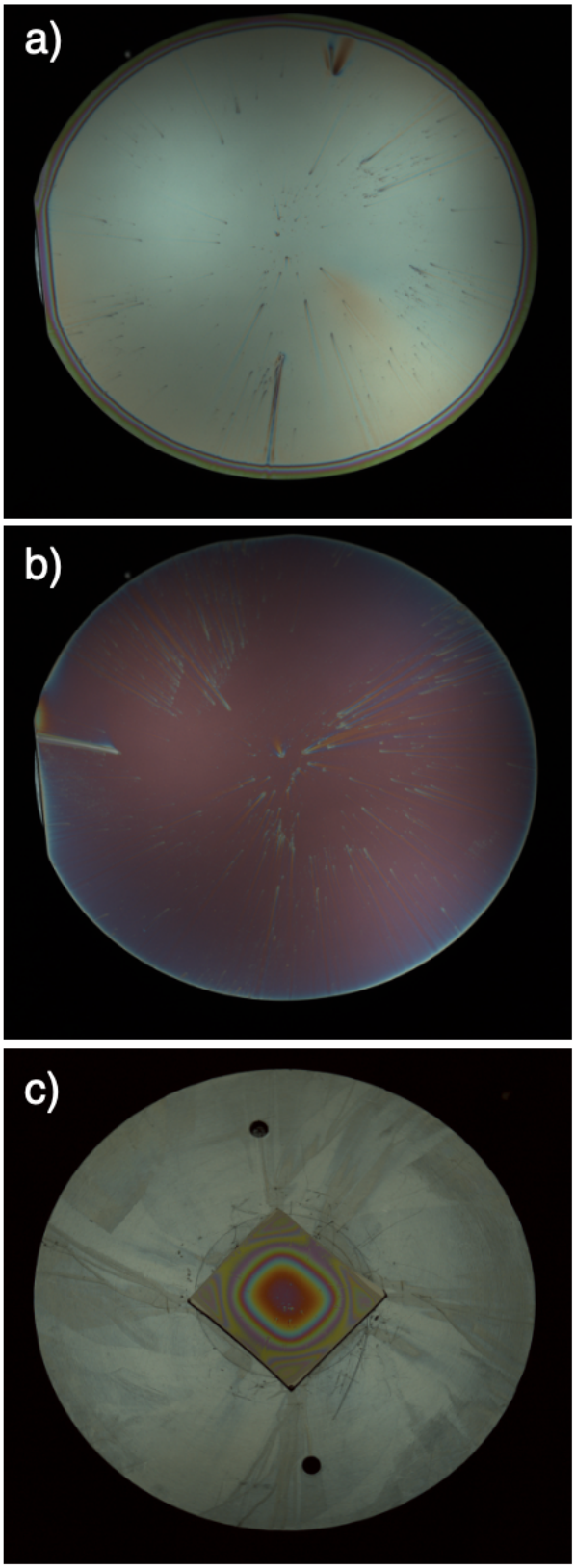

Figure 3.5: Stills of the raw videos from (a) Video 3.1 xylene spun at 2500 rpm on a full 3" wafer (b) Video 3.2 butyl acetate spun at 2500 rpm on a full 3" wafer and (c) Video 3.3 xylene spun at 2000 rpm on a 20 mm × 20 mm cleaved section of wafer, all taken roughly 300 ms before drying occurred.

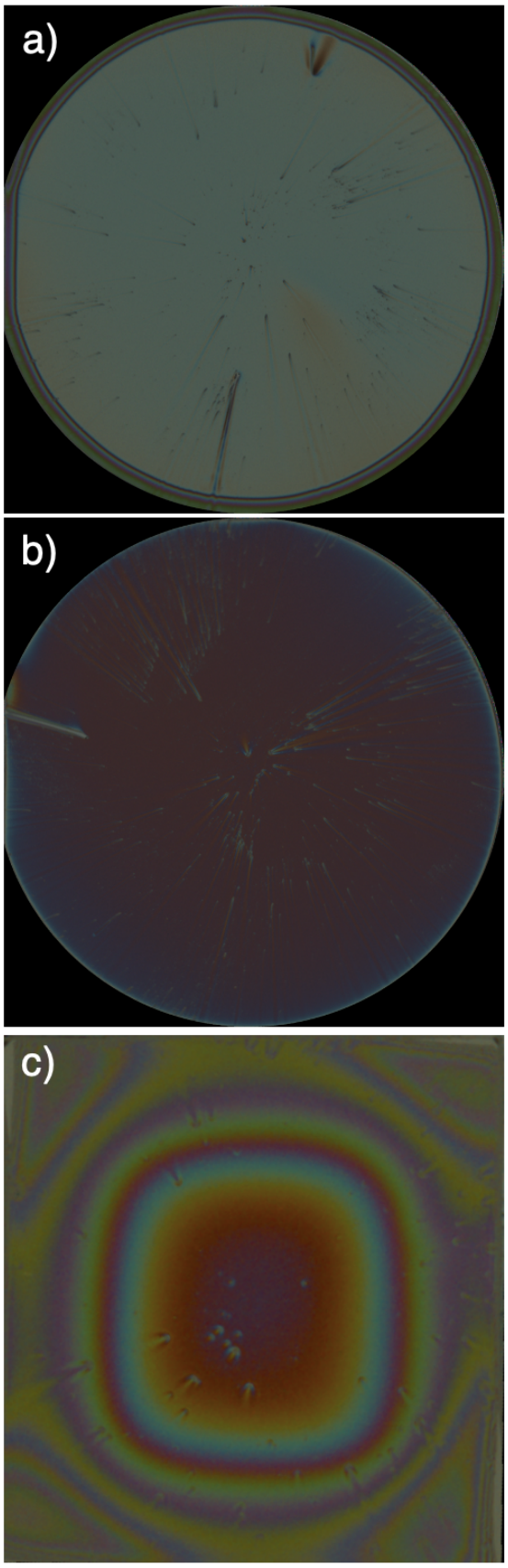

Figure 3.6: Stills from the processed videos (a) Video 3.4 xylene spun at 2500 rpm on a full 3" wafer (b) Video 3.5 butyl acetate spun at 2500 rpm on a full 3" wafer and (c) Video 3.6 xylene spun at 2000 rpm on a 20 mm × 20 mm cleaved section of wafer, all taken roughly 300 ms before drying occurred.

In this study, a camera with a linear sensor response is used and any gamma or colour temperature correction was disabled, removing the nonlinear function, Γ_i, in Equation 3.2. The colour balance values, b_i, used throughout this study are 1.54, 1 and 2.45 for red, green, and blue channels respectively and were set using the camera software and Passport 2 colourChecker (CCPPV2, Calibrite) under the same illumination conditions as the wafers to give an accurate depiction of the interference colours in the produced video. Due to the assurance of linearity by removing Γ_i, these values can be changed after capture as they represent simple scaling factors of the channel response.

3.3.1.2 Specular laser reflection

A 520 nm laser (Thorlabs, PL203) and large area photodiode are also mounted above the spin coater, perpendicular to the LED and camera, so that the laser reflects at 30°off the centre of rotation onto the photodiode. The intensity of the reflected beam shows sequential peaks and can be interpreted as thinning by a length of $\frac{\lambda}{2n\cos(\theta_1)}$, where λ is the laser wavelength, n is the refractive index of the fluid and θ_1 is the angle of light propagation in the fluid (angle of refraction), found by Snell's law. This constraint denotes where the optical path difference (OPD) between the reflection from the top of the film and the substrate is equal to the wavelength of the light to produce points of constructive interference. When only solvent is used, and the final thickness is zero, this relation gives a centre-point thickness profile by counting peaks backwards. This has been a widely used technique employed in many previous studies [17], [18], [26] to impart centre point thickness profiles. Figure 3.7 shows the two simultaneously performed techniques, stroboscopic colour imaging and laser specular reflection, and how they are used to produce an *in situ* colour-to-thickness relationship.

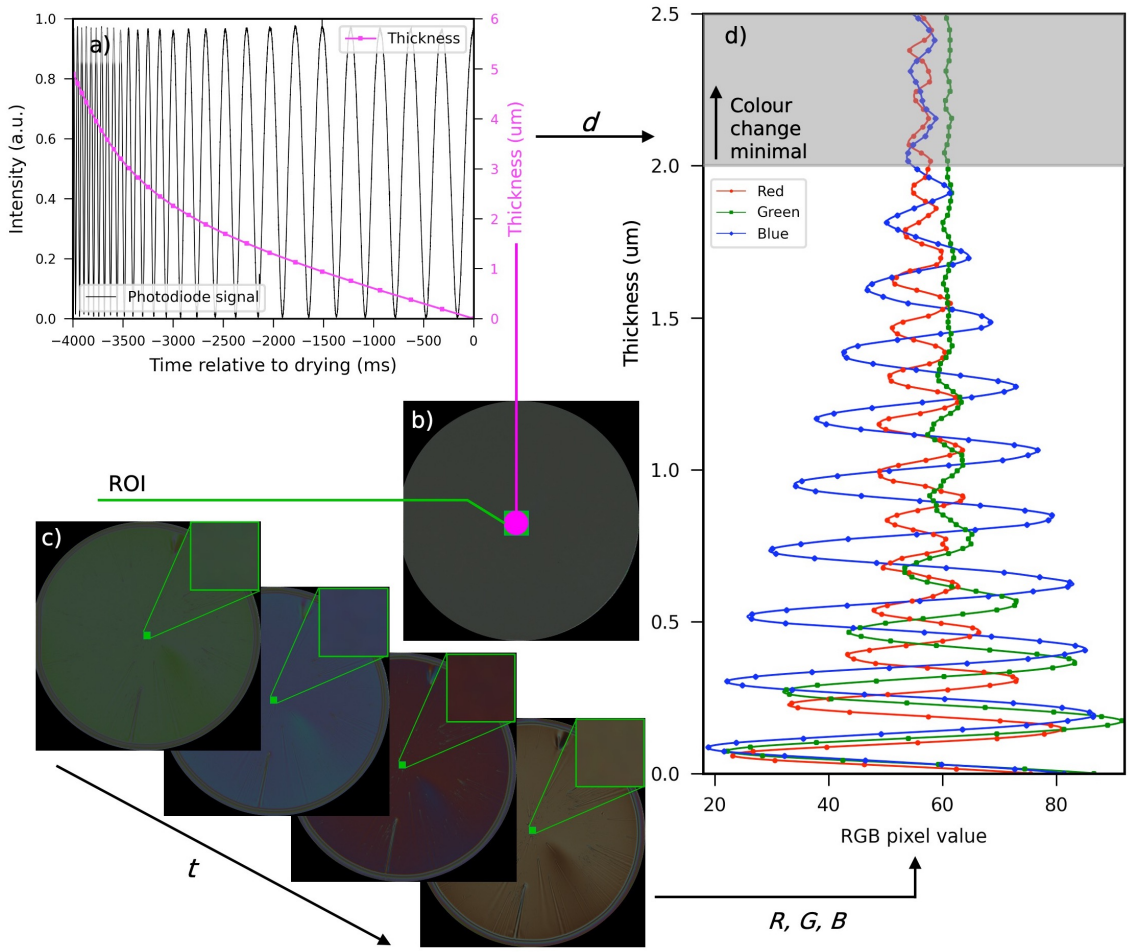

Figure 3.7: (a) The specular reflection intensity (black) and the centre point thickness profile obtained by resolving the Bragg condition (magenta); (b) A schematic of the wafers surface and the 9 pixel x 9 pixel 403 µm x 398 µm laser spot (magenta circle) and overlapping ROI (not to scale) for the RGB colour extraction (green square); (c) The centre RGB values being extracted from each frame; (d) the *in situ* colour-thickness relationship developed from the combination of white light imaging and laser specular reflection data, the grayed out area shows where the colour differences become hard to distinguish.

In an industrial setting the footprint of this metrology setup could be reduced by carrying out the imaging at normal and laser reflectance at near-normal incidence, through a hole in the diffuser screen. This would provide a system that may only need a single mount directly above the wafer, thus making it much more modular. The drawback of this is that the reflection of camera lens, photodiode and laser source is likely to be visible in the center of the wafer and will limit analysis in the area that it occupies. Here, this configuration was not implemented because a larger instrument footprint was acceptable and imaging at 20°resulted in the etched glass diffuser occupying the whole area of the wafer. The postulated normal incidence system would, however, be likely to be marginally more accurate due to the optical path difference of a given thickness change being maximized.

3.3.2 Experiments

The viewpoint of the camera was corrected using NI Vision's grid calibration method to remove the perspective of the non-normal incidence. This uses an image of a 10 mm x 10 mm grid at the camera's viewing angle to fit a polynomial distortion model that then re-interpolates images so that the grid appears regular. This process means that raw images of oval wafers (due to camera angle) can be corrected so that the wafers appear circular. This process also accounts for any distortion due to the lens and sensor misalignment, which here is negligible compared to viewing angle. The process comes with a mean error of 0.04 8mm (approx. 1 pixel), and a standard deviation error of 0.00094 mm (approx. 1/100 pixel) with the edge regions of images having a higher error. The correction procudure also included a flat field step to remove the effects of uneven illumination. The first run with all wafers was completed without the addition of solvent and was used to collect reference flat field images whilst under the same rotation and lighting conditions as subsequent runs.

Substrates were test grade 3" diameter CZ grown <100> Si wafers, or cleaved sub-sections of these wafers, from International Wafer Service. All were rinsed with isopropyl alcohol (IPA) and dried with compressed N_2 or cleaned with CO_2 snow (Sherman, 2007) before mounting. The selected solvent was pipetted onto the wafer until the wafer appeared completely flooded (typically 2 ml). Wafers were spun at 2500 rpm (full wafer) or 2000 rpm (20 mm x 20 mm squares), with an acceleration of 1500 rpm/s, until complete evaporation occurred. Each experimental configuration was replicated 5 times on the same substrate and showed high levels of repeatability. Typically, each sample was complete within 10 s - 15 s.

3.3.3 Colour-to-thickness mapping procedure

The pixels in each frame of the RGB images are software binned to find a mean RGB colour[1] for each bin (2 x 2). A suitable level of binning should reduce the effect of pixel noise, ϵ_i, without excessively reducing the resolution of the produced thickness maps. Processing without binning was found to produce discontinuous surfaces due to pixel noise effects on colour. To determine how the level of binning affected the variance of the RGB colour, a study was conducted on one of the stroboscopic videos, the details are presented in the following Subsection 3.3.3.1. The standard deviation of colour value was shown to

[1]The mean of each colour channel over the bin area

be inversely proportional to the square bin width. This data was then used to inform the amount of tolerance in the colour matching procedure. colour matching of each channel to two standard deviations is used. For 2 x 2 binned videos this means the tolerances are set to 2.58, 1.61 and 2.14 for red, green, and blue channels respectively.

Each bin in the video is then matched to the *in situ* colour-thickness relationship, an example for which is shown for xylene spun at 2500 rpm in Figure 3.7d, to solve for thickness across the whole wafers surface. Due to the one-to-many matching of colour to thickness, each bin may have more than one, or no, possible thicknesses assigned at this stage. All thickness solutions are found for each (x, y) bin over time. The time points that have single solutions are filled in, and a linear regression model is fit to these. This model was constrained to have a negative gradient (thinning through time is assumed). For time points with multiple solutions, the closest point to the model at each time is selected, as long as this point is reasonably close to the model (within 250 nm). This process does not aim to model the thinning, but uses the model as a tool to correctly identify the most likely correct thickness solutions by implementing the assumption of thinning. Thinning behaviour that deviates significantly from the model (i.e. nonlinear) is still conserved because the single closest solution from the pixel colour is ultimately assigned, not the model value. In the results produced in this paper, a linear model was able to accurately resolve the ambiguities because thinning below 2 µm is approximately linear. In addition, multiple solutions are typically spaced far enough apart for resolution in this way due to the nature of the colour signals. Polynomial and logarithmic models were also tested, however a significant improvement was not seen. Using a nonlinear model and constraining the fit parameters to reflect assumptions such as constant thinning may give better performance in solutions with very nonlinear thinning behaviors.

Next, any thicknesses that may have been incorrectly assigned must be identified and removed. This is achieved here by median filter thresholding. Each frame in the video is median filtered with a kernel and compared with the original frame. Values that differ by more than a threshold amount are very different from the surrounding neighbours and are therefore likely to be incorrectly assigned to thicknesses that violate the topology of the fluid; these thicknesses are identified and removed. A kernel size of 15 x 15 bins (1.82 mm^2) and a threshold of 75 nm was chosen. The result of this process is that bins that differ by greater than 75 nm of the median of the surrounding area are identified and removed.

If these parameters are both not tuned properly, there is a risk that small scale features (comets) can be misrepresented in the final thickness map due to the smoothing nature of the processing. The level of smoothing should be reduced so that a comet defect does not change with further reduction of smoothing, in this way the tuning can be automated.

Bins that are not assigned thicknesses are then assigned using a purpose-built iterative linear interpolator in x, y and t dimensions. This method was chosen as the time for computation scales much more slowly than out-of-the-box alternatives that employ more computationally expensive procedures. In addition, the custom-built function could take advantage of multiprocessing to further speed up the process. The error of the interpolation and the time demand for different numbers of points is shown in the following Subsection 3.3.3.2. The computational demand of interpolation is an important consideration in this application when there may be over $1e^8$ bins in each video. Out-of-the-box Python interpolators struggle to deal with matrices of this size within a realistic time frame.

The linear interpolation is expected to give satisfactory results as it maintains realistic topology of the fluid in x, y and t, however, if large areas of unassigned pixels are present, especially if these fall at the edge of the matrix, topological features may be obscured or misrepresented. Care should be taken when using this method to assess small length scale features such as defects, in areas that are sparsely populated with colour-to-thickness solutions, such as the band in Figure 3.8 which occurs at very high fluid gradient. These areas are still small enough (less than 10 pixels, under 0.5 mm) that the assumption of linear fluid profile holds well. In cases such as this, the particular thickness range may not be well described by the colour-to-thickness relationship and therefore thickness solutions cannot be found, this may be because the gradient is so steep that the pixel becomes an average of many colours/thicknesses to produce a colour that is not well described by the developed colour-to-thickness solution.

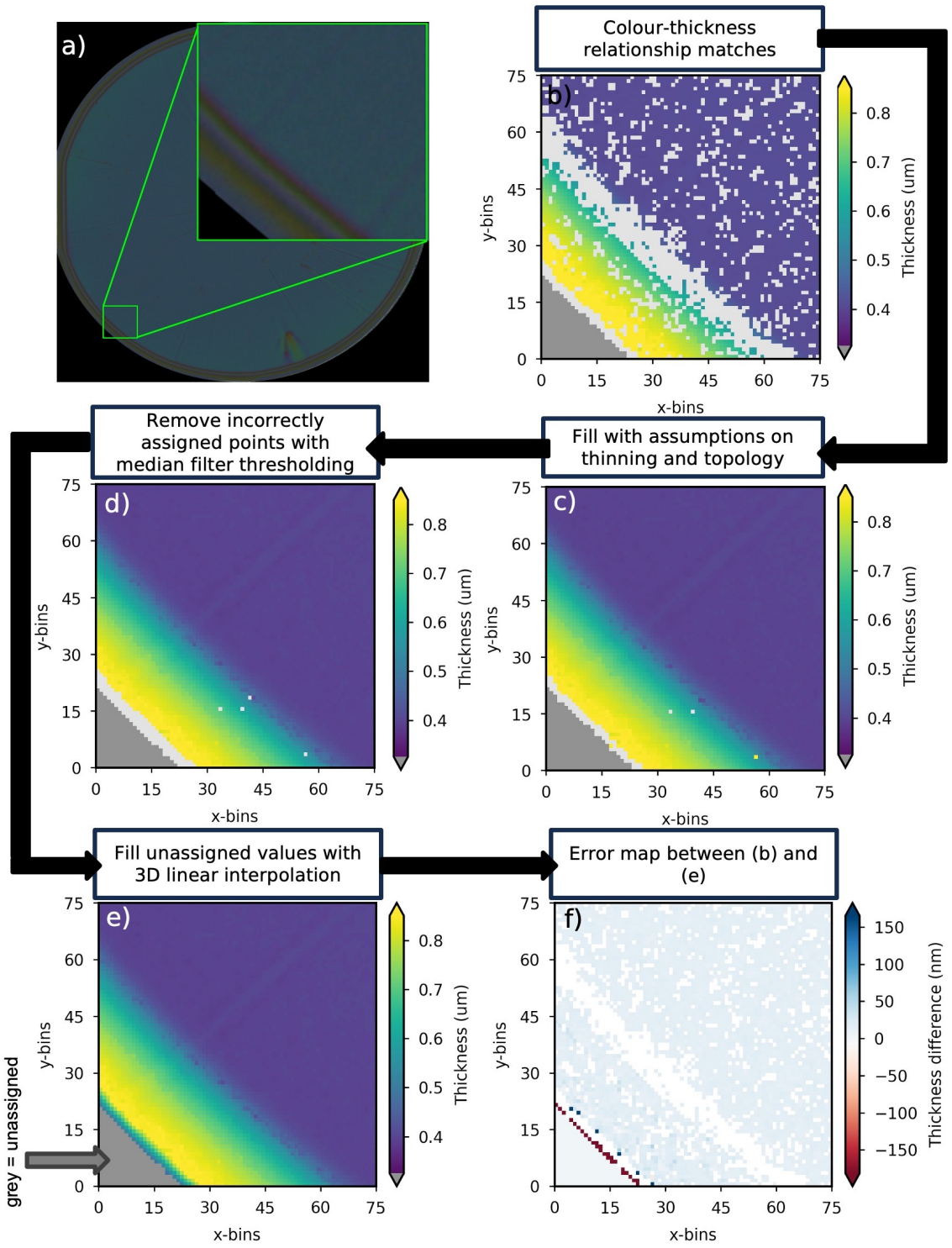

Figure 3.8: A representation of the processing steps taken to produce the final thickness profiles, shown on a 75 x 75 bin subsection of a video frame from the bottom left of the full frame at the wafers edge. (a) the image of the wafer with the ROI annotated (b) the initial colour to thickness matched values (c) filled using assumption of thinning and surrounding pixel values (d) removal of incorrectly assigned points, e.g. bin (56,4) via median filter thresholding (e) 3D interpolation of any further missing points (f) error from (b) minus (e), where both points exist.

This mapping procedure relies on the underlying assumption that the colour changes

observed in the centre of rotation can be applied to all areas on the wafer. The diffuser in place between the LEDs and the spin coater, combined with the flat fielding for the images, ensure that this is satisfied. In addition, there is an assumption inherent in the processing steps that for most points the thickness is correctly identified at the initial stage. This is found to be a reasonable assumption for the systems studied and the matching tolerances used. The number of points that have been assigned or removed at each stage in the processing is summarised in Table 3.1. This shows that the number of pixels changed at each stage in the procedure.

Table 3.1: The percentage of found or removed pixels at each stage of the processing, reported as $\mu \pm \sigma$ for five runs.

Solvent	Substrate	Colour-thickness matches	Filled by assumption	Values removed	Pixels 3D interpolated
Xylene	3" Si wafer	83.02 ± 2.95	15.77 ± 2.82	2.65 ± 0.39	3.86 ± 0.61
Butyl acetate	20x20mm Si section	85.21 ± 1.35	14.00 ± 1.28	2.05 ± 0.73	2.84 ± 0.46
Xylene	3' Si wafer	40.90 ± 5.26	44.21 ± 4.55	12.46 ± 2.52	27.34 ± 3.12

3.3.3.1 Tolerance selection

Three separate 120 pixel x 120 pixel areas of a 100 frame video of interference drying patterns were analysed. The sections were chosen from a video of spun coat xylene and were in areas that are free from defects and uniform in colour. The distribution (violin plots) and linear regression (dotted line) of the standard deviation of each bin within these video sections are shown at different levels of software binning of b x b in Figure 3.9. The analysis confirms that larger binning has a linear influence on standard deviation (or that variance varies linearly with number of pixels in the bin) and the relationships developed have been used to inform the colour matching tolerance. The highest accuracy of the procedure is expected when the tolerance used is equal to the variation present in the colours captured by the cameras.

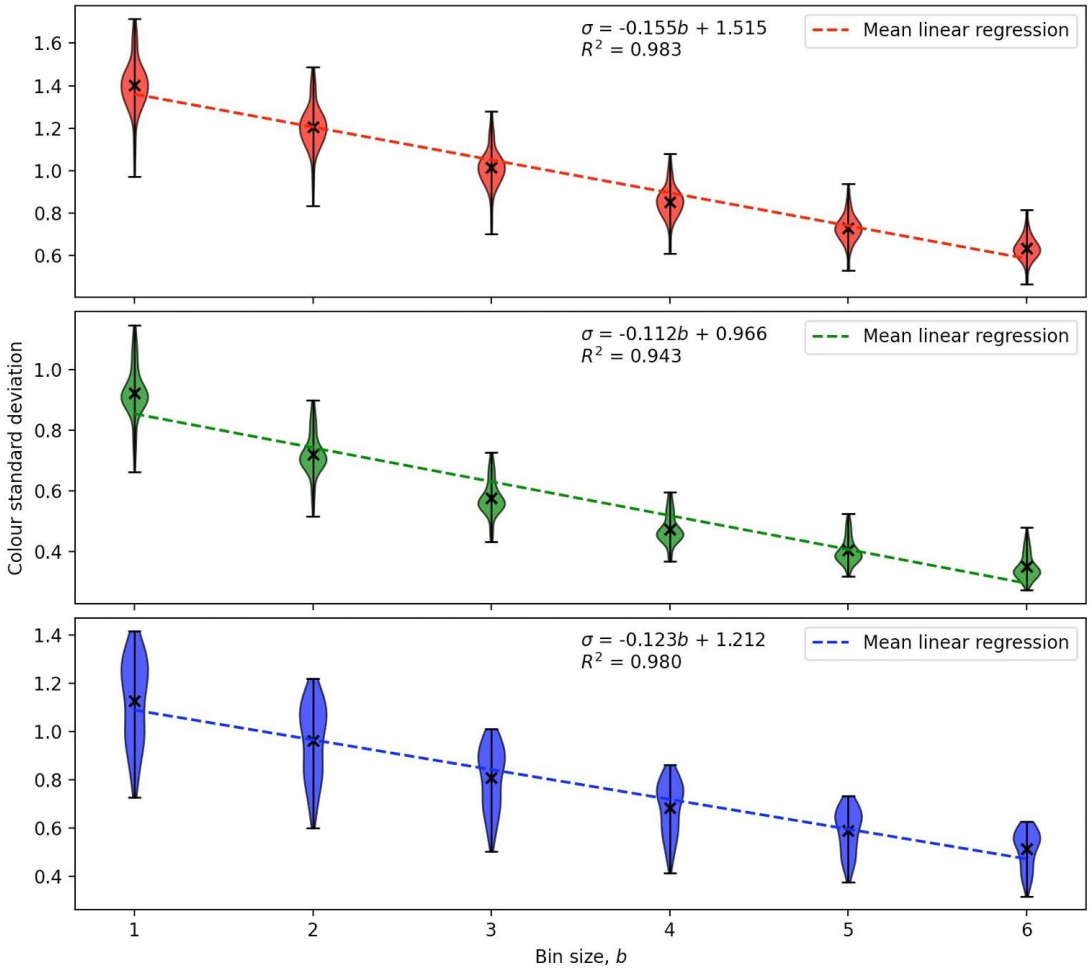

Figure 3.9: Displaying how the level of binning, b, affects the standard deviation of the colour response of three 120 pixel x 120 pixel area sections of uniform thickness. Violin plots show the distribution of the variable vertically via their profile.

3.3.3.2 Custom interpolation for video data

The developed 3D interpolator used to fill missing points is avaliable on GitHub[2] and was benchmarked to ascertain both the feasibility of computational/time demand and the amount of error expected, the results of this are shown in Figure 3.10. A matrix was filled with the function $f(x, y, z) = \sin(0.01x + 0.04y + 0.05z)$ and a random 10% of the data points removed, these were then filled by the interpolator and compared with the original values. Matrices of different sizes were tested to develop a clear picture of how computational demand scaled with size. The tolerance used was $1e^{-30}$ and max iterations were set at $1e^{5}$ but were never reached. A popular linear interpolator Scipy.interpolate.LinearNDInterplator is used for comparison.

[2]https://github.com/jacka-1/fast3Dinterp

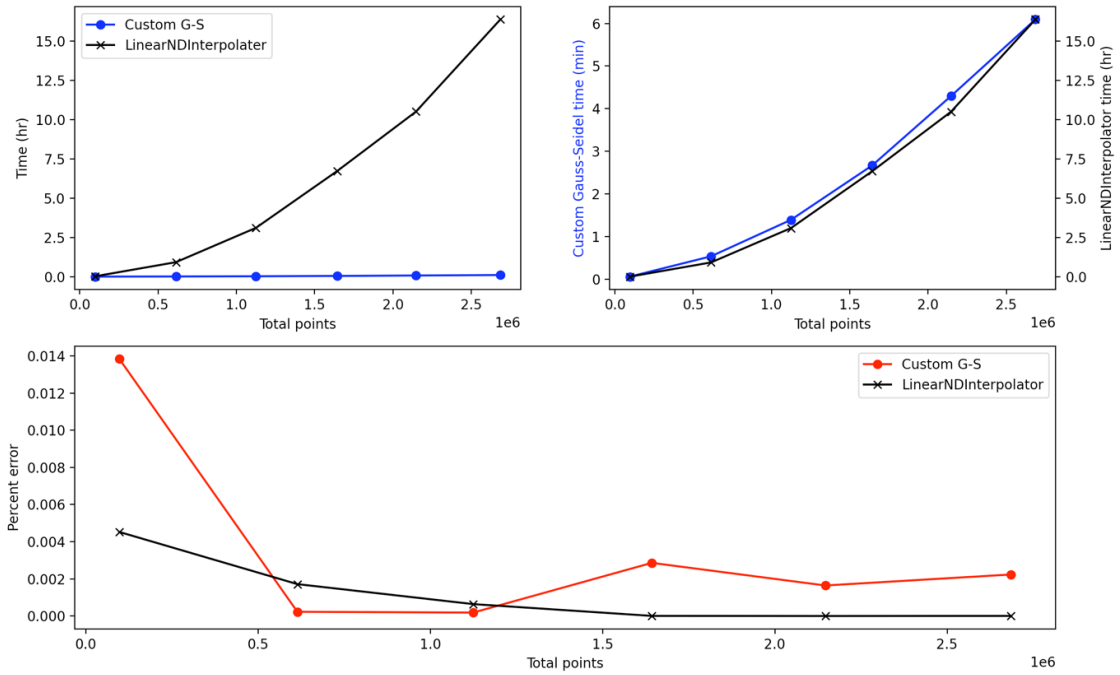

Figure 3.10: A comparison of the time demands and percent error of the custom 3D interpolator used here benchmarked against Scipy.interpolate.LinearNDInterpolator, for 3D matrices of $f(x, y, z) = \sin(0.01x + 0.04y + 0.05z)$ with 10% of the data removed.

Due to the large amount of data to be processed, the computational demand may become a limiting factor of this technique. A 24-bit RGB (RGB24) video of 100 frames and a resolution of 2000 by 2000 pixels represents over 1 GB of data. To process this, careful consideration of the amount of computational power and memory is needed. Because of this, each video was processed on the University of Sheffield Stanage high performance computing (HPC) cluster using 16 Intel Xenon Platinum 8358 cores at 3.4 GHz with a total of 64 GB of memory (4 GiB per core). The full wafer videos take approximately 15 hours to process completely, this reduces for videos with less frames or with a smaller ROI. Although not utilised here, the process is well suited to parallelisation because each pixel stack (through time) can be processed independently, and these processing times are expected to fall dramatically if this is taken advantage of on a GPU.

3.4 Results and discussion

3.4.1 Full wafer

The full wafer thickness reconstructions clearly capture the bulk thinning behaviour of the solvent as evaporation occurs. This can be seen in the 3D renderings in Figure 3.11. The

thicker portion at the edge of each wafer due to the beading effect of the xylene, that was seen in the stroboscopic images in Figure 3.4, is also clearly visible. In addition to this, smaller scale thickness variation effects caused by imperfections or defects can be observed evolving over time with this technique. Their presence is further confirmation of the ability of this set-up to freeze the rotating image, revealing high lateral resolution. Videos 2.7-2.9 contain examples of the resultant animated heatmaps for each run configuration, also played back at 15 fps. These are shown in Figure 3.12 where similarly to before, representative frames at approx. 300 ms before drying have been chosen that correspond with the frames in Figures 3.5 and 3.6.

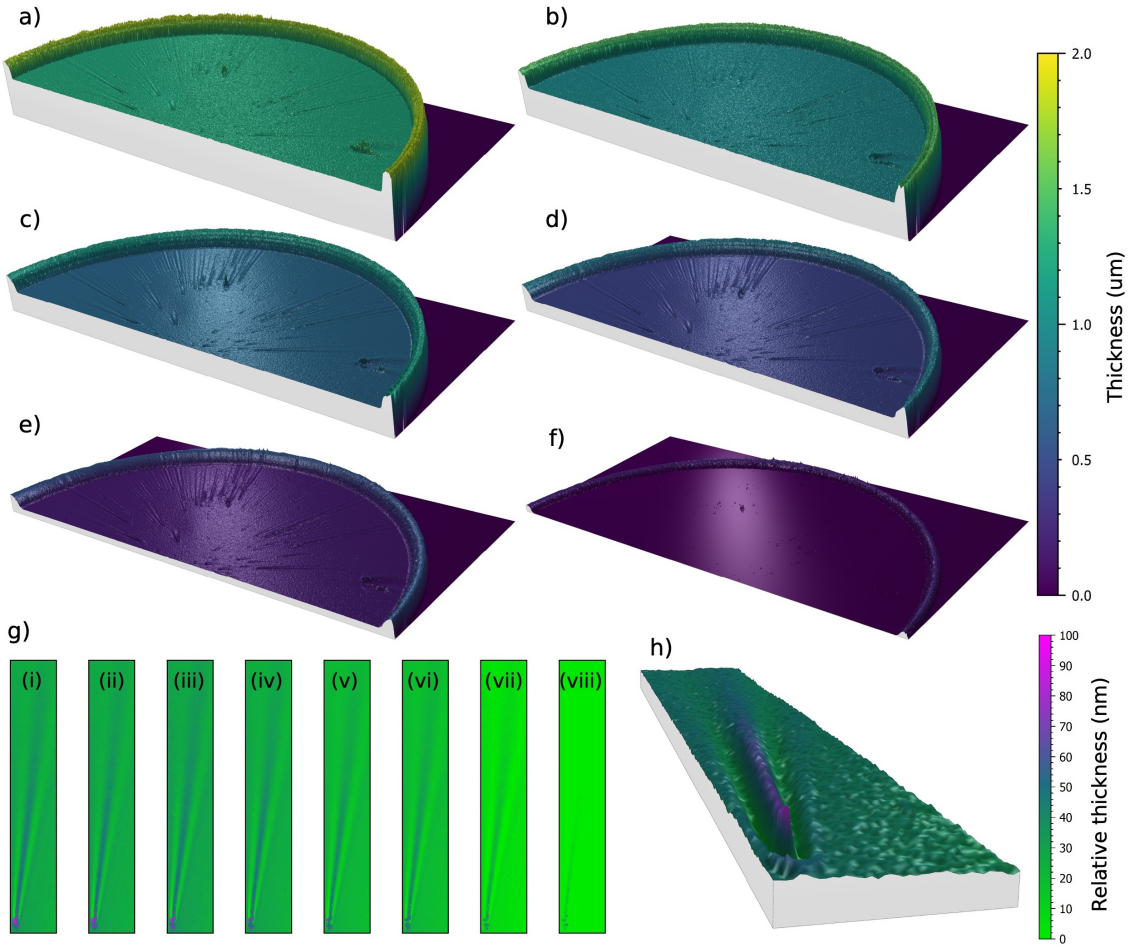

Figure 3.11: Half wafer thickness renders of xylene spun coat at 2500 rpm, taken from times (a) -1951 ms (b) -1541 ms (c) -1132 ms (d) -723 ms (e) -313 ms (f) 96 ms relative to centre point drying; (gi-viii) relative thickness maps of a 30 mm x 3.45 mm section of the wafer containing a comet defect close to drying, at -169, -144, -120, -96, -72, -48, -24 and 0 ms respectively; (h) a relative thickness rendering of the comet defect at -1132 ms.

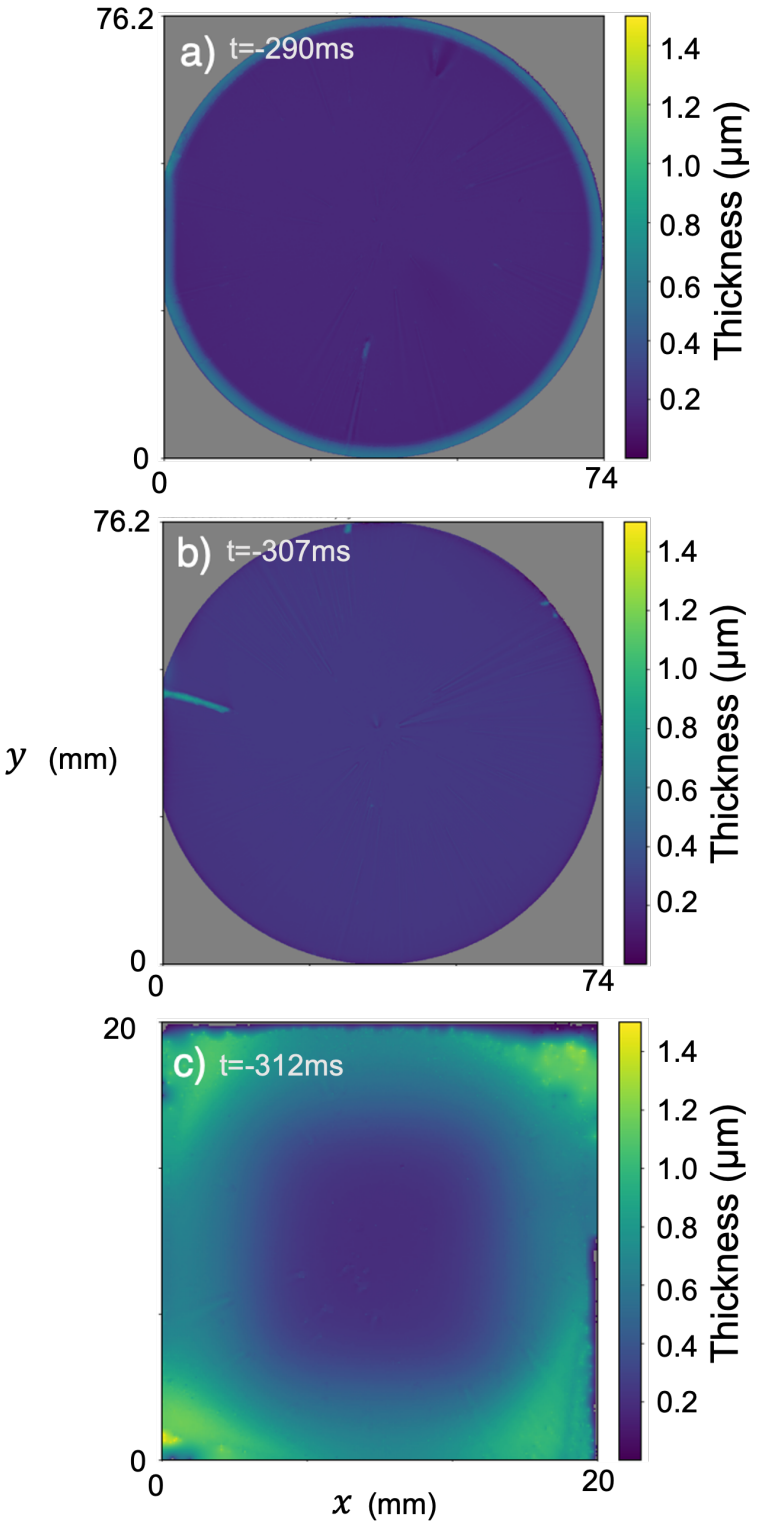

Figure 3.12: Stills from the animated heatmaps (a) Video 3.7 xylene spun at 2500 rpm on a full 3" wafer (b) Video 3.8 butyl acetate spun at 2500 rpm on a full 3" wafer and (c) Video 3.9 xylene spun at 2000 rpm on a 20 mm × 20 mm cleaved section of wafer, all taken roughly 300 ms before drying occurred.

The processed videos and thickness maps reveal that, for spun coat xylene, an edge bead is clearly visible throughout the drying process, however, the bulk of the wafer remains at

a uniform thickness value. In the data from butyl acetate, this beading is not present and the thickness across the wafer is uniform up until the very edge. In both videos, comet defects are present due to foreign objects on the wafer, and these have been preserved well in the mapping to thickness, maintaining a high resolution and clear thickness variations due to disturbance in the fluid flow around them. The examples in Figure 3.11g and 3.11h show that the defect largely maintains a constant relative disturbance up until the drying point. In a cross section perpendicular to the radial flow, the profile of the disturbance caused is a "w" shape and is roughly 100 nm from peak to trough.

Figure 3.13 displays the vertical line profile through the centre point of the wafer at 100 ms intervals relative to the drying time. 5 mm sections from the centre and the edge of the wafer are shown and the rest of the data is omitted for readability. The thickness between frames has been interpolated here to provide profiles at uniformly spaced time points. The spacing of the lines indicate the rate of thinning and this is largely uniform for each point on the wafer, excluding the xylene edge bead. As expected from the relative vapour pressures of the solvents the rate of evaporation of butyl acetate was faster than that of xylene.

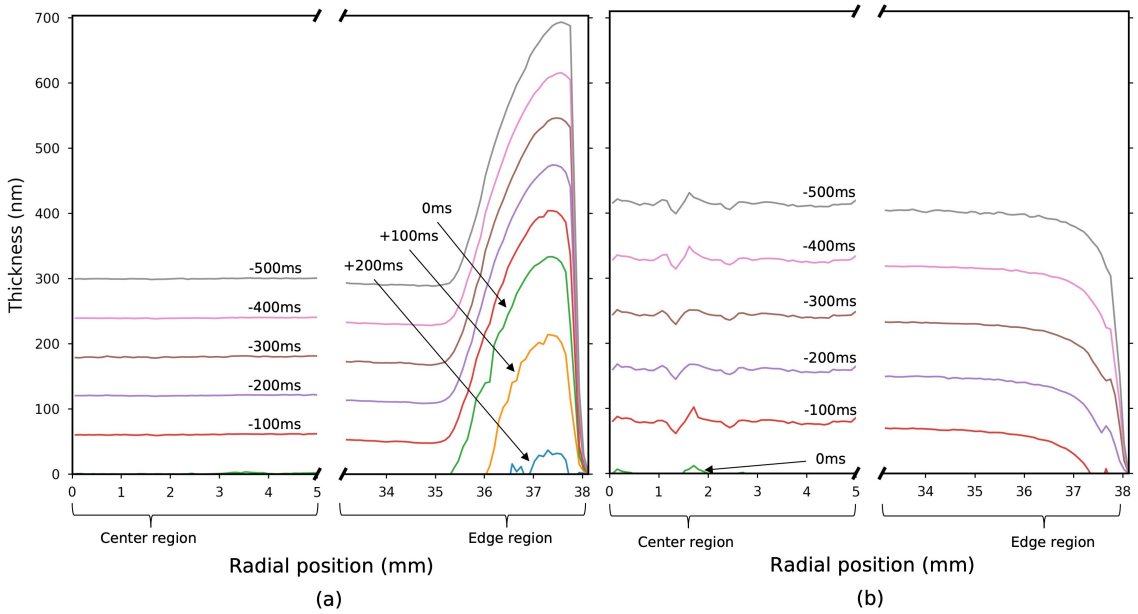

Figure 3.13: The thickness of a radial line profile through the centre point of a wafer at specific times relative to the centre point drying for (a) xylene and (b) butyl acetate spun at 2500 rpm (positive time legends shown in (a), left indicate drying times after the centre of the wave has fully dried).

The difference in evaporation rate of the solvents is further apparent from the frame thickness distributions, shown in Figure 3.14. These show data on the number of pixels at

each thickness value for every frame in the drying video. The "nominal" thickness on the wafer is represented by the diagonal high intensity band, with the gradient of the band representing nominal film drying rate. Variations in thickness from this are seen in the areas of lower and higher frequency around it, coloured as a light blue band.

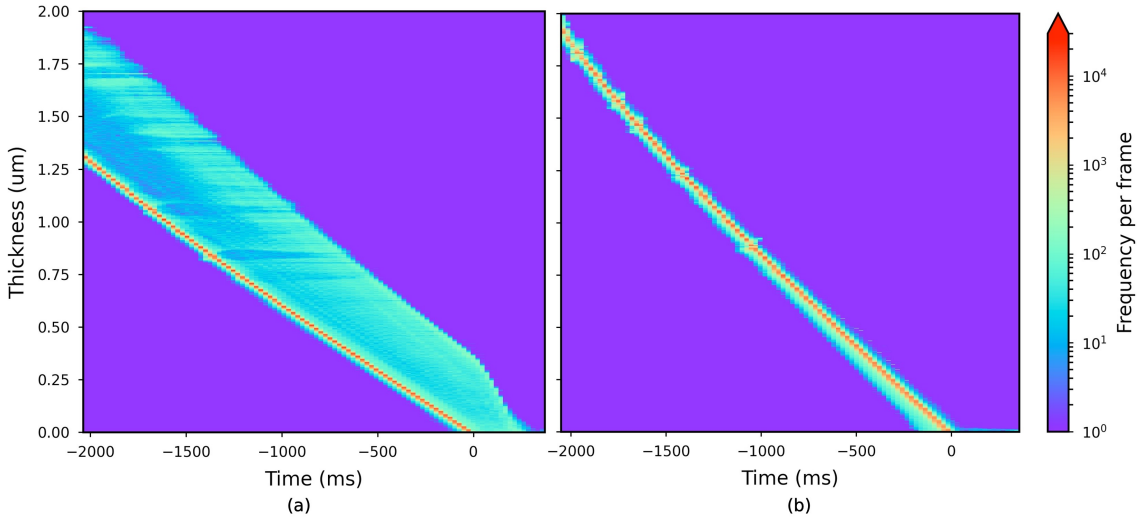

Figure 3.14: Horizontally stacked histograms for each frame quarter (upper left quadrant) where the frequency of each thickness is shown by colour in a log scale, for (a) xylene and (b) butyl acetate spun at 2500 rpm. These histograms are limited to regions below 2 µm where colours can be clearly identified, for both solvents this is around 2 seconds from drying, despite the differences in vapour pressure, due to xylene's edge bead.

The thickness variation above the nominal thickness of xylene persists from -2000 ms to 0 ms (the centre drying point), this is consistent with the observations of a significant edge bead in the images. The maximum height of the edge bead reduces from 0.62 µm above the nominal height of 1.28 µm at -2000 ms to 0.36 µm above the nominal height of 0 µm at the point of drying (0 ms). This shows that the edge bead is thinning faster than the bulk of the wafer but suggests that this is not due to a difference in evaporation rate at different radii, because of the high uniformity at all other points on the wafer. This phenomenon reduces the magnitude of the edge effect closer to the drying point. In contrast, the same data collected for butyl acetate has a much smaller variation in thickness throughout the observed drying, suggesting that here the drying rate is uniform.

It is clear from Figure 3.14a that the edge bead of xylene has already formed over 2 seconds before the drying point, at a nominal fluid thickness of around 1.25 µm, suggesting that the edge bead was present from early in the spinning regime, forming during hydrodynamic thinning. Whilst extrapolation thickness variations to earlier time is limited by

dampened interference colours above 1.5 µm, this edge can be discerned at larger thicknesses qualitatively in the images due to the difference in intensity that it creates. Xylene has a higher surface tension and viscosity when compared to butyl acetate; both solvent properties play a crucial role in the solvent uniformity. The edge bead forms because the xylene can spread less easily over the surface of the wafer due to centrifugal forces and is more likely to form a bead before being ejected from the edge of the wafer due to its high surface tension.

3.4.2 Non-axisymmetric (square) wafer

Spin coating runs were also conducted on cleaved silicon wafer (20 mm x 20 mm), spun at 2000 rpm with xylene. The same type of edge effect that is observed on the full wafer is also observed here, where there is significant beading of the solvent that is visible from 2 µm and is therefore likely first formed in the hydrodynamic thinning regime. In Figure 3.15, additional effects due to the wafer geometry can be seen. The drying of the solvent outside of the non-radially symmetric sections of the wafer are much slower than at the centre.

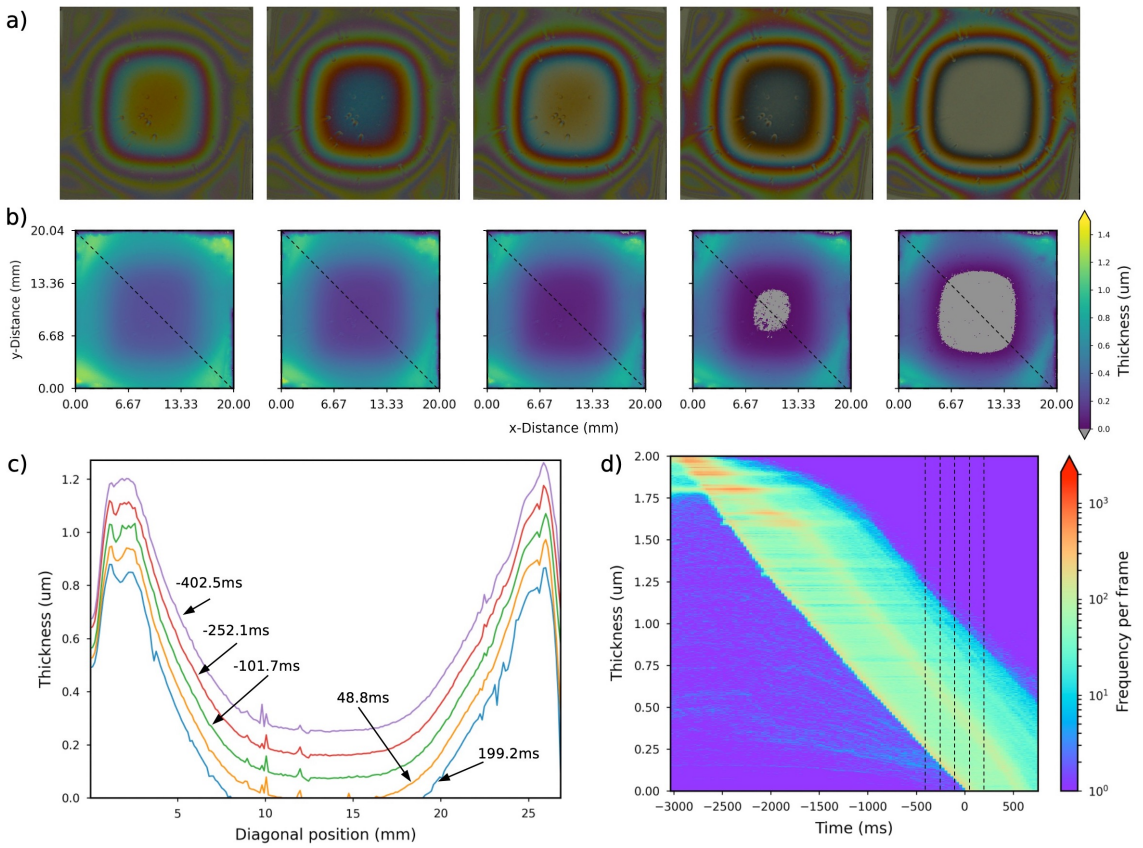

Figure 3.15: (a) frames from the stroboscopic video of xylene spun on a 20 mm x 20 mm wafer at 2000 rpm, (b) the processed thickness heat maps corresponding to the frames in (a), (c) the diagonal line profiles of (b) annotated with the time relative to drying, and (d) the horizontally stacked histograms of the whole drying video, annotated with the timestamps of the frames in (a) and (b).

3.4.3 Length scale discussion

Stroboscopic illumination with LEDs allows for the effective sensor integration time to be controlled well below the minimum shutter times of most cameras. The minimum effective exposure time possible is then only constrained by the rise and fall times of the LEDs, typically in the tens of nanoseconds range [137]. Or, when operating at very small pulse lengths, the intensity of illumination becomes limiting to generate sufficient activation of the sensor with an acceptable signal to noise ratio.

A shorter strobe illumination time results in a smaller length of travel of the moving object, in this case a rotating substrate, during the exposure and a more effective freezing effect. As the radius or the rotational frequency of the substrate increases so does the tangential velocity, requiring shorter and shorter strobe flashes to achieve the same level of detail in the image. The length of the strobe illumination that allows a movement of

distance l by an object rotating at ω rpm with a radius r, is given by Δt in Equation 3.3.

$$\Delta t = \frac{l}{2\pi r(\omega/60)} \tag{3.3}$$

During the digital imaging of a moving subject, a clear image may be formed by accepting movement of no more than the real-world length of 1 pixel. Figure 3.16a shows the maximum strobe pulse times needed to freeze an image in this way. In this scenario, the limit of length scale that can be examined is set by the resolution of the camera rather than the blur created by travel during the strobe pulse. This constraint may be relaxed as the observational length scale needed changes to lengths beyond the resolution of the camera. This may also increase the quality of the photos by ensuring sufficient illumination. Extremely short illumination pulses, even with bright LEDs, run the risk of under illuminating the wafer. This increases the need for large gain, reducing the dynamic range of the resulting images.

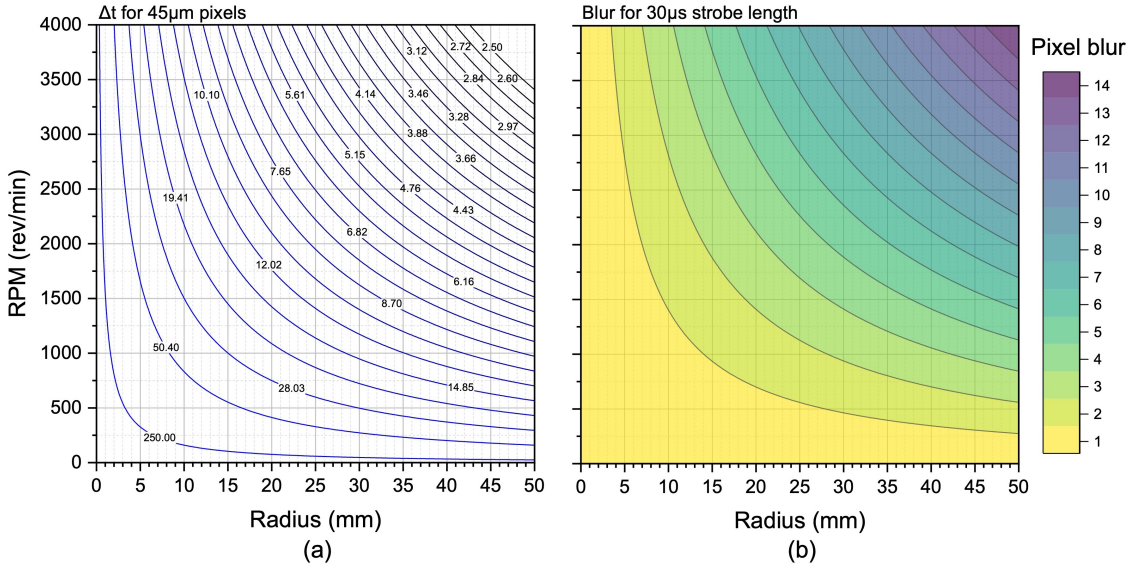

Figure 3.16: (a) Contour plot showing the maximum strobe time in microseconds, from 250 to 2.5 in a reciprocal scale, required to freeze an image to one pixel length and (b) the amount of blur in number of pixels experienced at points for a 30us strobe flash.

In this study, wafers of a maximum radius of 38.1 mm were spun at 2500 rpm. At these conditions the strobe pulse length required is 4.51 μs to achieve the pixel-scale freezing described above at the circumference. The strobe pulse used in this study is 30 μs and is selected to give the most effective trade-off between intensity of illumination and image blur; the strobe length was gradually reduced until no blur was visibly present. A pulse

of 30 µs is 6.65 times longer than the maximum calculated; this is an important ratio and will give the number of pixels travelled across by a point at the edge of the 3" diameter wafer during the strobe, resulting in a theoretical blur length of 299 µm. Any metrology at this radius is constrained to the length of 7 pixels (315um), however, this minimum length scale decreases linearly to just 1 pixel (45 µm) at the centre[3]. Here, this level of blurring in the images is minimal, as to be essentially imperceptible in the raw and processed videos. In the resulting heatmaps, where the pixels have been binned by 2 in each direction, this resolution has been halved. This reduction in resolution can be mitigated by increasing the pixel density of the system by either using a higher resolution camera, modifying the geometry of the setup so that the wafer occupies a larger ROI in the existing camera, or with use of a higher magnification lens (at the expense of FOV).

Since 2001, 300 mm (18") wafers have been used in the semiconductor industry. For spin speeds of 2000 rpm this would require a strobe pulse of 9.52 µs to be imaged at the same level of blur discussed here (or a pulse of 1.43 µs to achieve complete pixel level freezing, with the same camera resolution). This is achievable with modern LEDs as their small size means many high- powered modules can be packed into small arrays to illuminate the surface of the wafer, even in short times.

Another important trade-off considered is the frame rate and resolution of the camera used. Not only does the resolution affect the maximum length scale observable, but in many cameras the ROI size (and therefore the resolution) will affect the maximum achievable framerate. The possible frame rate must be sufficiently high to at least match the number of revolutions per second of the spin coater to achieve a frame every rotation. Above this, it would be possible to run the setup so that an image was achieved every two or three rotations of the substrate, however, especially with quicker drying solvents, this will potentially reduce the number of points in the colour-to-thickness relationship so that it cannot be reliably constructed.

3.4.4 Recovered thickness accuracy discussion

The accuracy of the centre thickness profiles resulting from the laser specular reflection can be checked using a Meyerhofer plot [138] [45]. This used the Meyerhofer model [13] of

[3]Despite these calculations, review of the images at 30 µs strobe length do not show any visible blur at the edges, suggesting that the light pulse is actually shorter than the nominal time, possibly due to the electronic implementation.

a spun coat fluid, presented in Equation 3.4, where $K = \frac{\rho\omega^2}{3\eta}$.

$$\frac{dh}{dt} = -2Kh^3 - e \tag{3.4}$$

By comparing the value of K resulting from literature values of viscosity and density to the value of K calculated from the slope of the linear regression plot of $-\frac{dh}{dt}$ against $2h^3$. The centre point thickness profile's fit to the Meyerhofer model can be evaluated. Here, for each run configuration, the 95% confidence interval of the slope of the plots contained the literature calculated K values. This gives good confidence that the specular laser reflection thickness values at the centre of the wafer are accurate.

The effect of thicker films satisfying constructive/destructive interferences for a broader range of wavelengths gives an upper limit to this approach, as seen in the RGB colour signals in Figure 3.4d. The origin of this dampening of the interference colours is due to the integration on the camera's sensor. As film thickness increases, so does the frequency of the reflectance wave, and the relative activation across the red, green, and blue bands in the Bayer filter becomes more even. Eventually, at high thicknesses, the intensity variation in a single channel becomes much less dependent on thickness, and the colour of the bulk material emerges. This enveloping phenomenon is not present in the laser data because the photodiode is only logging a single wavelength. The impact of this effect is that for films of $n \approx 1.5$ and $k \approx 0$, the maximum thickness that can be resolved by colour analysis is around 2 µm. If the thickness is greater than this, the optical interference is not pronounced enough to interpret as a colour difference in a digital image. It is not possible to reduce this enveloping effect with camera settings and thus this thickness limit is fundamental to the technique.

A significant result of this enveloping phenomena is that the matching procedure, that uses a constant tolerance for each channel, changes accuracy at different thicknesses. In general, it is more accurate at lower thicknesses because the frequency, and therefore gradient, of the colour response is higher which results in a smaller matched thickness range. The tolerances in the matching procedure have been selected to be representative of the variance present in the colour measurements to minimise the error. For example, for the data presented in Figure 3.4, a blue channel value of 60 ± 2.14 will match to 16 thickness values. Thicknesses between 0.028 µm and 0.031 µm at the thinnest solution,

thicknesses between 0.889 µm and 0.895 um at the 8th thinnest solution, and between 1.660 µm and 1.676 um at the 16th thinnest solution. In situations such as this, where a range of values are identified on the 1 nm step interpolation of the colour-to-thickness relationship, the mean of the range is taken as the solution. Matching all three colour channels simultaneously narrows these matched ranges significantly.

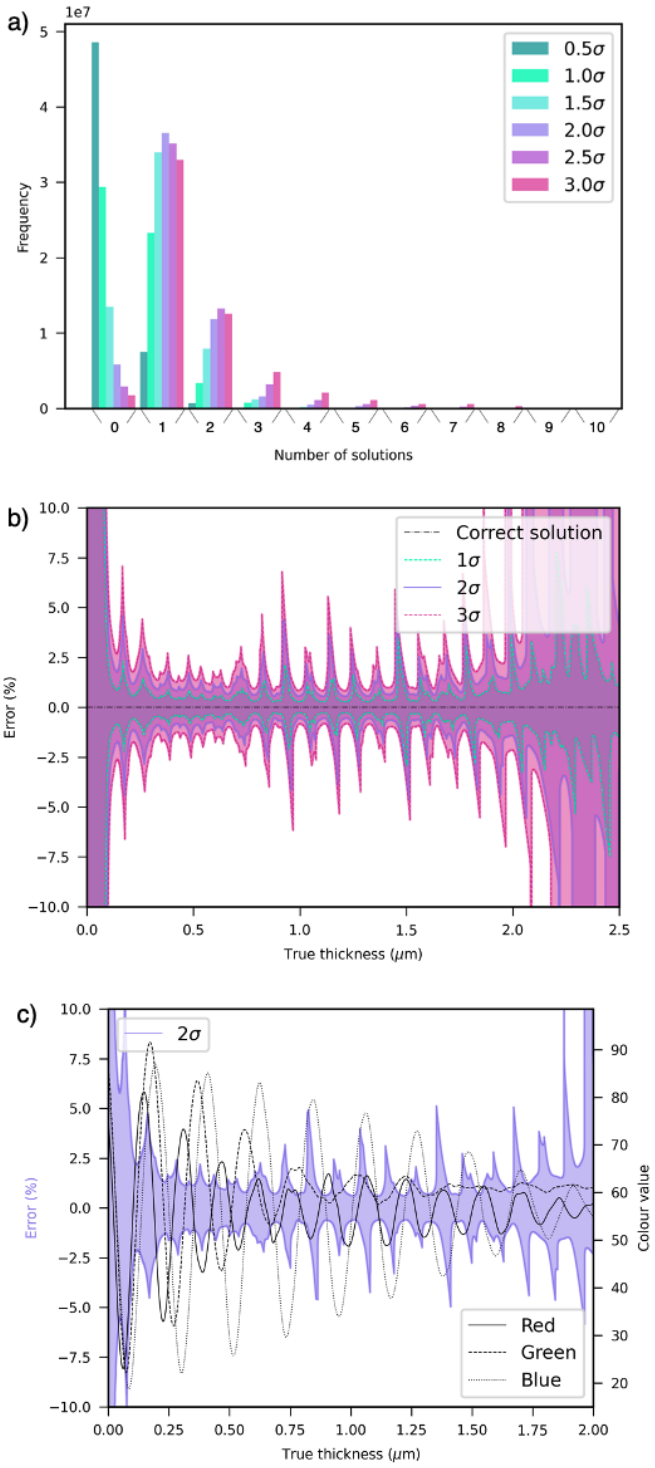

Figure 3.17: (a) The number of solutions identified in the colour-to-thickness relationship when the colour matching tolerance is set to different levels of the camera colour variance (b) the percentage error in thickness that results from matching to different levels of of the camera colour variance, and (c) the error given by the used colour matching tolerance overlayed with the colour-to-thickness relationship.

Figure 3.17a displays the number of solutions found for each pixel for the full wafer video of Xylene spun at 2500 rpm, as the colour matching tolerance is changed between

0.5 and 3 times the identified colour standard deviation. If the colour matching tolerance is too low, thickness solutions fail to be identified and a large number of pixels with no solution are present, however, if the tolerance is too large, the number of pixels with multiple solutions increases, in turn increasing the amount of ambiguities that need to be resolved. Figure 3.17b shows how these different matching tolerances affect the error in the thickness solutions by identifying the range of colour, and therefore thicknesses, within the tolerance at each solution. Setting the matching tolerance too high results in larger potential percentage errors because the matched colour solution can be more different from the pixel colour, and therefore further away from the true thickness. The figure also demonstrates an additional reason why thickness estimation beyond 2μm is not recommended, as the enveloping of the signal drastically increases the potential matched thickness error. Matching to two standard deviations of colour is chosen as it provides a satisfactory trade off in maximizing single solution pixels while keeping these errors low.

Finally, Figure 3.17c displays the percentage error at the matching tolerance used (2 standard deviations of colour) overlaid onto the developed colour-to-thickness relationship. This shows that increases in the error of the matching correlate with the combined steepness of the colour responses, a result of using a constant matching tolerance, because a larger range of colours and therefore thicknesses are matched. Despite this, these errors stay below 5% of the thickness value for almost all the points, apart from extremely low thickness values less than 100 nm.

3.5 Conclusion

In situ stroboscopic white light imaging of a spun coat wafer has been demonstrated over areas of up to 45 cm^2, making this the largest area imaging study of the spin coating process of its kind. The developed metrology technique has been used to produce thickness maps of solvents spun coat on silicon, in addition to full high resolution RGB videos of the process. To successfully achieve this technique, a trade-off between camera resolution, spin speed and strobe pulse length has been found and the interplay of these has been discussed.

Thickness can be resolved at any point on the wafers surface between the development of interference colours at around 2 µm. The resolution and error of these thicknesses is difficult to quantify due to the nature of the reconstruction procedure, however, we find that the

error in the matching procedures thickness values is less than 5%. The use of broadband white LEDs for high illumination intensity has made this technique widely accessible. Moreover, the issue of colour-to- thickness ambiguity, which arises from this approach, has been demonstrated to be resolvable through the application of basic assumptions regarding the film's topology. This technique involves very little *a priori* information, limited to just the refractive index of the solvent at the laser wavelength. The Bayer filter sensitivity and illumination spectrum of the imaging is not required because the colour-to-thickness relationship is constructed *in situ*. This also means that this technique can be applied where fully controlled environments are not available.

In this study we have drawn light on how the physical properties of solvents affect the uniformity over whole-wafer areas. The experiments directly reveal that the evaporation rate of the solvent is uniform over the wafer's surface if the solvent enters the evaporation dominated stages of the process with a uniform profile. However, if an uneven fluid surface is present when entering this stage, then an irregular evaporation rate is observed over the wafer. In this scenario, the evaporation rate of the thicker areas is slightly larger, decreasing the scale of the nonuniformity as the spin-coating progresses. Reasons for entering the evaporation dominated stages with a nonuniform thickness across the wafer may include a high surface tension, high viscosity, or extremely fast evaporation due to a high vapour pressure but is likely to be a complex result of all three of these solvent properties, as well as any effects from non-axisymmetric wafer geometry.

3.5.1 Future work

This work can be extended to directly observe the formation of films with a final thickness that is not zero i.e. spun coat solutions rather than pure solvents. This would require the ex-situ measurement of the film at the centre of rotation with a technique such as SE.

The nature of the thickness selection algorithm means that in future this can be optimised to run in parallel, to take advantage of the proposed technique fully as an *in situ* method.

Due to the recent advances in hyperspectral camera technology, that brings framerates in line with that needed, snapshot hyperspectral cameras could be used to resolve thickness unambiguously, such as in the work by Chandran Suja et al., albeit at an order of magnitude increased cost in terms of $, and an order of magnitude reduction in pixel resolution. To

combat this reduction in resolution, simultaneous hyperspectral and normal digital imaging poses a good solution, that can be used to maintain resolutions currently unavailable in snapshot hyperspectral imaging systems. This would combine both detailed RGB imaging and less well-resolved hyperspectral imaging at each point to maintain high resolutions but enhance colour-to-thickness mapping by reducing the colour ambiguity due to simultaneous matching of more channels.

Methods to estimate spectra from RGB colour triplet have been described in literature [111]. Successful application of these methods would allow the reflectance spectrum to be estimated directly from the imaging data, but doing this accurately is a major challenge. This could then be coupled with existing for thin film reflectometry methods [67] [69] to define a thickness. With proper calibration, this would mitigate the need for the laser specular reflection described here, and the thicknesses of spun coat solvents or solutions could be identified from just the stroboscopic images. Challenges to these approaches include that these methods can require lots of data about the imaging system or require training data consisting of reflectance spectrum and camera response pairs, or both.

3.6 Videos

Despite differing native capture speeds, all videos here are played back at 15fps for clarity.

3.6.1 Raw

These are the non-adjusted images taken by the camera during each spin coating run.

- Video 3.1: The raw stroboscopic video of xylene spun on a full wafer at 2500 rpm `https://drive.google.com/open?id=15HQKCrLV6v5c2H3ebrkW_cVp76JCyKcH&usp=drive_fs`
- Video 3.2: The raw stroboscopic video of butyl acetate spun on a full wafer at 2500 rpm `https://drive.google.com/open?id=15HV6xNsnlEc6VFNFQr2Z1--EvLx9q7mi&usp=drive_fs`
- Video 3.3: The raw stroboscopic video of xylene spun on a 20 mm x 20 mm square wafer at 2000 rpm `https://drive.google.com/open?id=15JVKGlBJ-J94updlz_HrSI2afscz76XR&usp=drive_fs`

3.6.2 Processed

These videos are the perspective corrected and flat field corrected versions of Videos 3.1-3.3.

- Video 3.4: The processed stroboscopic video of xylene spun on a full wafer at 2500 rpm https://drive.google.com/open?id=15HjKdaKPWVKO10nEI71q3NajFth2P5Vo&usp=drive_fs
- Video 3.5: The processed stroboscopic video of butyl acetate spun on a full wafer at 2500 rpm https://drive.google.com/open?id=15JqvDYb2MzgqS9nWrOFsbbI7TRGXRPAF&usp=drive_fs
- Video 3.6: The processed stroboscopic video of xylene spun on a 20 x 20 mm square wafer at 2000 rpm https://drive.google.com/open?id=15LGmCxJqEBEapCuVNdn26Xd6ycma4WeG&usp=drive_fs

3.6.3 Animated heatmap

These videos are animated heatmaps (where the colour corresponds to reconstructed thickness) of Videos 3.4-3.6.

- Video 3.7: Animated reconstructed thickness heatmap of xylene spun on a full wafer at 2500 rpm https://drive.google.com/open?id=15NkN2pJgZzb-wBO7EKXlWUE_1ojer5sY&usp=drive_fs
- Video 3.8: Animated reconstructed thickness heatmap of butyl acetate spun on a full wafer at 2500 rpm https://drive.google.com/open?id=15NOguGyuKKI2tupV3ZDTQ2VJKiPlAOqO&usp=drive_fs
- Video 3.9: Animated reconstructed thickness heatmap of xylene spun on a 20 mm x 20 mm square wafer at 2000 rpm https://drive.google.com/open?id=15MGVkVpXCEkj6-_U-iWNzR3EGmQnQ1c7&usp=drive_fs

References

[1] Jack B.P. Atkinson and Jonathan R. Howse. "In-situ full-wafer metrology via coupled white light and monochromatic stroboscopic illumination". In: *Optics and Lasers in Engineering* 184.P2 (2025), p. 108692. DOI: 10.1016/j.optlaseng.2024.108692.

[5] Longjian Xue, Jilin Zhang, and Yanchun Han. "Phase separation induced ordered patterns in thin polymer blend films". In: *Progress in Polymer Science (Oxford)* 37.4 (2012), pp. 564–594. DOI: 10.1016/j.progpolymsci.2011.09.001.

[13] Dietrich Meyerhofer. "Characteristics of resist films produced by spinning". In: *Journal of Applied Physics* 49.7 (1978), pp. 3993–3997. DOI: 10.1063/1.325357.

[15] Dunbar P. Birnie, Dylan E. Haas, and Carissa M. Hernandez. "Laser interferometric calibration for real-time video color interpretation of thin fluid layers during spin coating". In: *Optics and Lasers in Engineering* 48.5 (2010), pp. 533–537. DOI: 10.1016/j.optlaseng.2009.12.021.

[45] Dunbar P. Birnie and Manuel Manley. "Combined flow and evaporation of fluid on a spinning disk". In: *Physics of Fluids* 9.4 (1997), pp. 870–875. DOI: 10.1063/1.869519.

[50] Paul C. Jukes et al. "Time-resolved light scattering studies of phase separation in thin film semiconducting polymer blends during spin-coating". In: *Macromolecules* 38.6 (2005), pp. 2030–2032. DOI: 10.1021/ma0477145.

[51] Sasha Y. Heriot and Richard A.L. Jones. "An interfacial instability in a transient wetting layer leads to lateral phase separation in thin spin-cast polymer-blend films". In: *Nature Materials* 4.10 (2005), pp. 782–786. DOI: 10.1038/nmat1476.

[67] Jiři Luňáček, Petr Hlubina, and Milena Luňáčková. "Simple method for determination of the thickness of a nonabsorbing thin film using spectral reflectance measurement". In: *Applied Optics* 48.5 (2009), pp. 985–989. DOI: 10.1364/AO.48.000985.

[69] Kwangrak Kim, Soonyang Kwon, and Heui Jae Pahk. "Fast analysis of film thickness in spectroscopic reflectometry using direct phase extraction". In: *Current Optics and Photonics* 1.1 (2017), pp. 29–33. DOI: 10.3807/COPP.2017.1.1.029.

[78] Jonas Bergqvist et al. “In situ reflectance imaging of organic thin film formation from solution deposition”. In: *Solar Energy Materials and Solar Cells* 114 (2013), pp. 89–98. DOI: 10.1016/j.solmat.2013.02.030.

[88] Jung Hun Lee et al. “Effect of Crystallization Modes in TIPS-pentacene/Insulating Polymer Blends on the Gas Sensing Properties of Organic Field-Effect Transistors”. In: *Scientific Reports* 9.1 (2019), pp. 1–9. DOI: 10.1038/s41598-018-36652-1.

[89] Stephen Ebbens et al. “In situ imaging and height reconstruction of phase separation processes in polymer blends during spin coating”. In: *ACS Nano* 5.6 (2011), pp. 5124–5131. DOI: 10.1021/nn201210e.

[90] Daniel T.W. Toolan et al. “Direct observation of morphological development during the spin-coating of polystyrene-poly(methyl methacrylate) polymer blends”. In: *Journal of Polymer Science, Part B: Polymer Physics* 51.11 (2013), pp. 875–881. DOI: 10.1002/polb.23288.

[99] L. Gustafsson, E. Hglund, and O. Marklund. “Measuring Lubricant Film Thickness with Image Analysis”. In: *Proceedings of the Institution of Mechanical Engineers, Part J: Journal of Engineering Tribology* 208.3 (1994), pp. 199–205. DOI: 10.1243/PIME_PROC_1994_208_371_02.

[103] V. Chandran Suja et al. “Hyperspectral imaging for dynamic thin film interferometry”. In: *Scientific Reports* 10.1 (2020), pp. 1–8. DOI: 10.1038/s41598-020-68433-0.

[111] Ville Heikkinen et al. “Evaluation and unification of some methods for estimating reflectance spectra from RGB images”. In: *Journal of the Optical Society of America A* 25.10 (2008), p. 2444. DOI: 10.1364/josaa.25.002444.

[115] Si Joon Kim, Seokhyun Yoon, and Hyun Jae Kim. “Review of solution-processed oxide thin-film transistors”. In: *Journal of Applied Physics* 53 (2014). DOI: 10.7567/JJAP.53.02BA02.

[116] Hiroyuki Matsui, Yasunori Takeda, and Shizuo Tokito. “Flexible and printed organic transistors: From materials to integrated circuits”. In: *Organic Electronics* 75.September (2019), p. 105432. DOI: 10.1016/j.orgel.2019.105432.

[117] Zhicheng Hu, Fei Huang, and Yong Cao. "Layer-by-Layer Assembly of Multilayer Thin Films for Organic Optoelectronic Devices". In: *Small Methods* 1.12 (2017), pp. 1–12. DOI: 10.1002/smtd.201700264.

[118] Chunyang Li et al. "Preparation and optical properties of nanostructure thin films". In: *Applied Nanoscience (Switzerland)* 11.7 (2021), pp. 1967–1976. DOI: 10.1007/s13204-021-01930-4.

[119] Xu Dong Wang et al. "Recent Advances in Halide Perovskite Single-Crystal Thin Films: Fabrication Methods and Optoelectronic Applications". In: *Solar RRL* 3.4 (2019), pp. 1–27. DOI: 10.1002/solr.201800294.

[120] Pan Zhao et al. "Research and Application Progress of Conductive Films in Energy Storage Devices". In: *Advanced Materials Technologies* 2300194 (2023), pp. 1–23. DOI: 10.1002/admt.202300194.

[121] Li Hui Chou et al. "Semiconducting small molecule/polymer blends for organic transistors". In: *Polymer* 191.January (2020), p. 122208. DOI: 10.1016/j.polymer.2020.122208.

[122] K. Dalnoki-Veress et al. "Phase separation morphology of spin-coated polymer blend thin films". In: *Physica A: Statistical Mechanics and its Applications* 239.1-3 (1997), pp. 87–94. DOI: 10.1016/S0378-4371(96)00471-2.

[123] Peng Jiang and Michael J. McFarland. "Large-scale fabrication of wafer-size colloidal crystals, macroporous polymers and nanocomposites by spin-coating". In: *Journal of the American Chemical Society* 126.42 (2004), pp. 13778–13786. DOI: 10.1021/ja0470923.

[124] Moorthi Pichumani et al. "Dynamics, crystallization and structures in colloid spin coating". In: *Soft Matter* 9.12 (2013), pp. 3220–3229. DOI: 10.1039/c3sm27455a.

[125] Daniel T.W. Toolan, Richard Hodgkinson, and Jonathan R. Howse. "Stroboscopic microscopy - Direct imaging of structure development and phase separation during spin-coating". In: *Journal of Polymer Science, Part B: Polymer Physics* 52.1 (2014), pp. 17–25. DOI: 10.1002/polb.23410.

[126] Junhu Zhang et al. "Colloidal self-assembly meets nanofabrication: From two-dimensional colloidal crystals to nanostructure arrays". In: *Advanced Materials* 22.38 (2010), pp. 4249–4269. DOI: 10.1002/adma.201000755.

[127] Tao Wang et al. “The development of nanoscale morphology in polymer:fullerene photovoltaic blends during solvent casting”. In: *Soft Matter* 6.17 (2010), pp. 4128–4134. DOI: 10.1039/c0sm00343c.

[128] Mihirsinh Chauhan et al. “Investigating two-step MAPbI3 thin film formation during spin coating by simultaneous: In situ absorption and photoluminescence spectroscopy”. In: *Journal of Materials Chemistry A* 8.10 (2020), pp. 5086–5094. DOI: 10.1039/c9ta12409h.

[129] Noura Alhazmi et al. “Perovskite Crystallization Dynamics during Spin-Casting: An in Situ Wide-Angle X-ray Scattering Study”. In: *ACS Applied Energy Materials* 3.7 (2020), pp. 6155–6164. DOI: 10.1021/acsaem.9b02470.

[130] Dounya Barrit et al. “Processing of Lead Halide Perovskite Thin Films Studied with In-Situ Real-Time X-ray Scattering”. In: *ACS Applied Materials and Interfaces* 14.23 (2022), pp. 26315–26326. DOI: 10.1021/acsami.2c03153.

[131] Daniel T.W. Toolan et al. “On the mechanisms of colloidal self-assembly during spin-coating”. In: *Soft Matter* 10.44 (2014), pp. 8804–8812. DOI: 10.1039/c4sm01711k.

[132] O S Heavens. “Optical Properties of Thin Films”. In: *Reports on Progress in Physics* 23.1 (1960). DOI: 10.1080/713818200.

[133] John M. Frostad et al. “Dynamic fluid-film interferometry as a predictor of bulk foam properties”. In: *Soft Matter* 12.46 (2016), pp. 9266–9279. DOI: 10.1039/C6SM01361A.

[134] S. Sett, S. Sinha-Ray, and A. L. Yarin. “Gravitational drainage of foam films”. In: *Langmuir* 29.16 (2013), pp. 4934–4947. DOI: 10.1021/la4003127.

[135] Eiki Goto et al. “Computer-Synthesis of an Interference Color Chart of Human Tear Lipid Layer, by a Colorimetric Approach”. In: *Investigative Ophthalmology and Visual Science* 44.11 (2003), pp. 4693–4697. DOI: 10.1167/iovs.03-0260.

[136] Yiran Zhang and Vivek Sharma. “Domain expansion dynamics in stratifying foam films: Experiments”. In: *Soft Matter* 11.22 (2015), pp. 4408–4417. DOI: 10.1039/c5sm00066a.

[137] C. Willert et al. “Pulsed operation of high-power light emitting diodes for imaging flow velocimetry”. In: *Measurement Science and Technology* 21.7 (2010). DOI: 10.1088/0957-0233/21/7/075402.

[138] Dunbar P. Birnie. “Combined flow and evaporation during spin coating of complex solutions”. In: *Journal of Non-Crystalline Solids* 218 (1997), pp. 174–178. DOI: 10.1016/S0022-3093(97)00141-5.

Chapter 4

Multispectral Reflectance Reconstruction and Thickness Recovery

This chapter has been submitted in full to *Optics Express*. Due to being submitted for publication the nomenclature is defined as it is introduced in the chapter. It is mostly consistent with that used in previous chapters with a notable exception that R is now the matrix consisting of training reflectance spectrum vectors $[\mathbf{r_1}, \mathbf{r_2}, ...\mathbf{r_k}]$ and the reflectance spectrum (previously R) has been designated as a calligraphic $\mathcal{R}$. Appendix A corresponds to supplementary material for this chapter. Reference numbers will be different from what appears in the published paper to keep references in the thesis unique and consistent. This chapter does not include a graphical abstract.

The chapter builds on the previous reflectance imaging, altering the RGB detection by incorporating an additional multi-bandpass (MBP) dichroic beam splitter. When used in conjunction with a dual imaging system, this acts as a filter to allow 6 channel, rather than previously demonstrated 3 channel (RGB), imaging. This extends some of the fundamental limitations of standard RGB imaging while ensuring the system can still operate at high resolution and frame rates, suitable for dynamic and *in situ* application.

4.1 Abstract

Multispectral imaging has emerged as a powerful tool for the non-invasive characterisation of thin films because conventional three-channel colour imaging is limited by inherent ambiguities due to short range interference effects. Here we present a cost-effective strategy that transforms a standard colour camera into a six-band multispectral imager through the incorporation of a multi-bandpass dichroic beam splitter. This approach leverages the high spatial resolution and rapid frame rates of commercial consumer cameras while improving on the performance over standard typical of RGB imaging. The additional spectral information available from this setup not only improves the accuracy of colour-based thin film thickness recovery but also extends the measurable thickness range. We demonstrate the technique on a non-uniform polymer film, over a sizeable region with sub-micron precision. We also demonstrate use of spectral reconstruction techniques that can recover the reflectance spectrum for thin films from 6-channel colour, circumventing the need for detailed physical models of illumination and detection by using training data. This open new avenues for *in situ* analysis in scenarios where conventional calibration is impractical. Cost-effective, high-resolution thin film metrology can consequently be achieved using modified imaging hardware combined with spectral processing, impacting the fabrication of devices such as solar cells, transistors sensors and displays.

4.1.1 Keywords

Multispectral imaging, thin film thickness, reflectance imaging, spectral reconstruction, spectroscopy, polymer film

4.2 Introduction

Thin film interference causes visible colour patterns that correlate with film optical thickness, making colour cameras a simple tool for film inspection. Images (macro and microscopic) of films give insights into fabrication processes' drying kinetics [15], can be used for quality control and defect detection [80], or to elucidate mechanisms in morphology development [93]. However, under broadband illumination, a given colour is not uniquely tied to a single thickness, interference colours repeat in cycles as thickness increases [1]. This cyclical reappearance of colours means films of different thickness (separated by roughly

one interference order) can look nearly identical in colour [139]. In practice, using RGB imaging alone yields a narrow unambiguous thickness range of only a few hundred nanometers before this colour ambiguity sets in, or other parameters such as viewing angle are systematically varied [96]. Furthermore, the colour–thickness relationship is sensitive to illumination and material refractive index, requiring careful calibration. While colour imaging is fast, offers high resolution, and is inexpensive, its usefulness in thin film metrology is limited by these factors.

Conversely, recovery of optical constants (refractive index, n, and thickness, d,) from a full thin film reflectance spectrum, $\mathcal{R}(\lambda)$, is well established [61] [65]. This places hyperspectral imaging (HSI) as an obvious choice for spatially resolved thin film studies because the full reflectance spectrum can be recovered at each (x, y) position. In the case where a complete hyperspectral datacube is obtained, the approach of fitting each reflectance spectrum would be robust and facile and could take any of the many approaches available in spectral reflectometry (SR) [140] [67] [69] [68] [141]. Other applications of HSI include 2D material characterisation [142], stress and strain mapping [143], and plasmonic property mapping [144] [145]. These applications highlight the powerful insight and value of spatially resolved spectral information in metrology and characterisation. There are, however, significant challenges in integrating HSI to *in situ* studies.

Hyperspectral cameras fall generally into one of four categories. 1) Spatial scanning or "pushbroom", that completes the datacube by scanning a line (slit) through y at all (x, λ), usually employing prisms or gratings and requiring relative movement between the scene and the camera for a full image. 2) Spatiospectral scanning, like spatial scanning, captures sequential slits' spectra (x, λ) over the camera's sensor area, however, the slit and dispersive element is before the camera, allowing for easier switching to spatial scanning and as a result higher spectral and spatial resolution. 3) Spectral scanning that captures an image at all (x, y), sequentially changing the λ captured, usually by using some form of band-pass filtering that requires moving filter components. 4) Non-scanning or "snapshot" HSI that acquires the full 3 dimensions of the datacube in a single exposure on the 2D sensor, usually achieved by some form of filter mosaic or beam-splitting optics, usually with less channels than their scanning counterparts. Each of these types of acquisition modes use different technologies, but their aim is the same: to acquire an (x, y, λ) datacube.

Dynamic, *in situ* studies typically require information to be collected at fast framerates,

otherwise fast-changing scenes will distort the data. This requirement leaves only snapshot HSI as a candidate. However, snapshot HSI has limitations:

- Snapshot HSI cameras tend to have very low spatial and/or spectral resolutions because the 2D sensor size must be a projection of each datapoint in the 3D datacube.
- The frame rates are limited by large sensor read-off times and low light intensity per pixel.
- These tend to be the most expensive HSI systems as they require the most intricate optical components and largest sensors.

Due to these constraints on resolution, many snapshot cameras reduce the spectral resolution to lower than that of true hyperspectral imaging. These cameras, often referred to as multispectral cameras, are characterized by having more channels than standard colour imaging, but not enough to consider the output completely spectrally resolved. HSI's sampling times for full datacubes generally mean that they are only applied ex-situ, however, it is still a useful tool for thin film metrology. The thickness of PEDOT:PSS, often used as conductive hole transport layer in organic solar cells and other electronics, from 60 nm - 300 nm have been recovered by line scanned datacubes using a chemometric approach with the partial least squares (PLS) algorithm [105]. In addition, large field of view (13 mm $\times$ 0.6 mm) HSI for silicon wafer defect detection has recently been demonstrated by Yoon et al. from Samsung in 2022. This application boasts extremely high 0.25 nm spectral resolution while maintaining 5 µm spatial resolution by using a line scan camera [146]. Finally, multilayer perovskite cells ex-situ luminescence hyperspectral datacubes have been shown by El-Hajje et al. to predict inhomogeneity and estimation of quasi-Fermi level splitting, and therefore device performance [106].

HSI has only recently begun to be applied to limited *in situ* applications in thin film characterisation. The nature of line scan cameras mean that they are readily applied to roll to roll (R2R) processes where relative movement between the scene and the detector is inherent in the process, especially in quality control applications. This opens the possibility for much higher spatial and spectral resolutions by removing the need for 2D imaging data. Snapshot HSI framerates, even at reduced spatial resolutions, have only relatively recently aligned those necessary for real-time or video rate studies. In 2023 Dougan-Surmeier et al. displayed that an in-line real-time HSI imaging system could be successful

in predicting the thickness of a ZTO/Ag/ITO multilayer system [147]. This was achieved with a line scan camera across 220 mm R2R web, and the ground truth was measured with x-ray diffraction (XRD). The author indicates that in addition to thickness, future use could include prediction of other parameters such as crystallinity, phase composition and roughness of thin films, demonstrating the wealth of information provided by film spectra. Line scan HSI has also been used in R2R processes for dimensional characterisation of imprinted nanostructures [148]. Besides R2R applications, HSI has been reported for *in situ* thin film interferometry of single bubble coalescence by Chandaran Suja et al. in 2020 [103]. Shown to retrieve thickness accurately to 100 nm, this study used a 16-band visible snapshot camera from Ximea, capable of up to 170 Hz.

Reducing the spectral resolution requirement to just a few more bands than standard RGB imaging ($4 < n < 8$ bands) results in multispectral imaging. This technique represents a middle ground between RGB and hyperspectral imaging and is often used to record or reproduce colour to a very high tolerance. Multispectral cameras are usually of snapshot type and possess framerates and resolutions that are much more in line with standard consumer cameras, placing them as better candidates for implementation *in situ*.

Multispectral camera output will no longer accurately represent the samples full spectrum. In this case, additional reflectance reconstruction techniques have been leveraged that use training data, comprised of labelled multispectral colours and reflectance spectrum pairs, to attempt to "upsample" a given colour to produce the spectrum [149]. A variety of techniques have been employed in this role and they can be split into two categories, those that require *a priori* information on the illumination spectrum and spectral sensitivity of the channels, and those that do not. Shimano, Terai and Hironaga [150] list the Wiener filter [112] [151], linear model and Shi-Healy methods in the former and the pseudoinverse and Imai-Berns method in the latter. Their study quantifies the reconstruction quality using the mean square error of the reconstructed reflectance of 5, 6 and 7 channel imaging. In addition to these methods, Heikkinen et al. [111] also suggested nonlinear Kernel regression along with the others mentioned. To the authors knowledge, this group of techniques have not been previously used on colours produced by thin film interference to reproduce or characterise a film's reflectance spectrum.

This work presents first a 6-band multispectral imaging ($M = 6$) system using a standard Bayer filtered colour camera and a multi-bandpass dichroic beamsplitter. Four meth-

ods for film thickness reconstruction will subsequently be evaluated. The first method is one that has been demonstrated before and aims to recover thickness by minimizing the mean square error of a modelled and measured colour [100]. In the second method this approach is simply extended to the six-band imaging system to see if performance can be improved. In the third method the reflectance spectrum is recovered using a trained transfer matrix, and the MSE of this spectrum and a modelled reflectance spectrum is then minimized. Finally, thickness recovery is attempted via spectral reconstruction as before, and subsequently peak counting.

4.3 Materials and methods

4.3.1 Imaging

A 6-band imaging system is constructed using a Cairn Optosplit II, shown in Figure 4.1, which is a commercially available dual scene imaging system designed to project the same image onto each half of the sensor by using a dichroic beamsplitter and a series of mirrors and is commonly used for ratio-imaging. In these experiments a multi bandpass dichroic beamsplitter is installed (Delta Optical Film, LF104849) thus achieving imaging of the transmission (nominally 424 nm, 513 nm, 591 nm, 709 nm) and reflection bands (466 nm, 558 nm, 631 nm) on the left and right of the sensor respectively. The setup in six band imaging mode is shown in Figure 4.1, where the Optosplit module has been integrated into a custom normal incidence reflection microscope with a collimated LED illumination source. The lens L_6 is an aberration correction lens provided by Optosplit to attempt to correct the chromatic aberration present (even with the achromatic tube lens L_4) and bring the reflected and transmitted images' focal planes together. Although this improves the aberration, when one image is sharply focused the other is often very slightly out of focus.

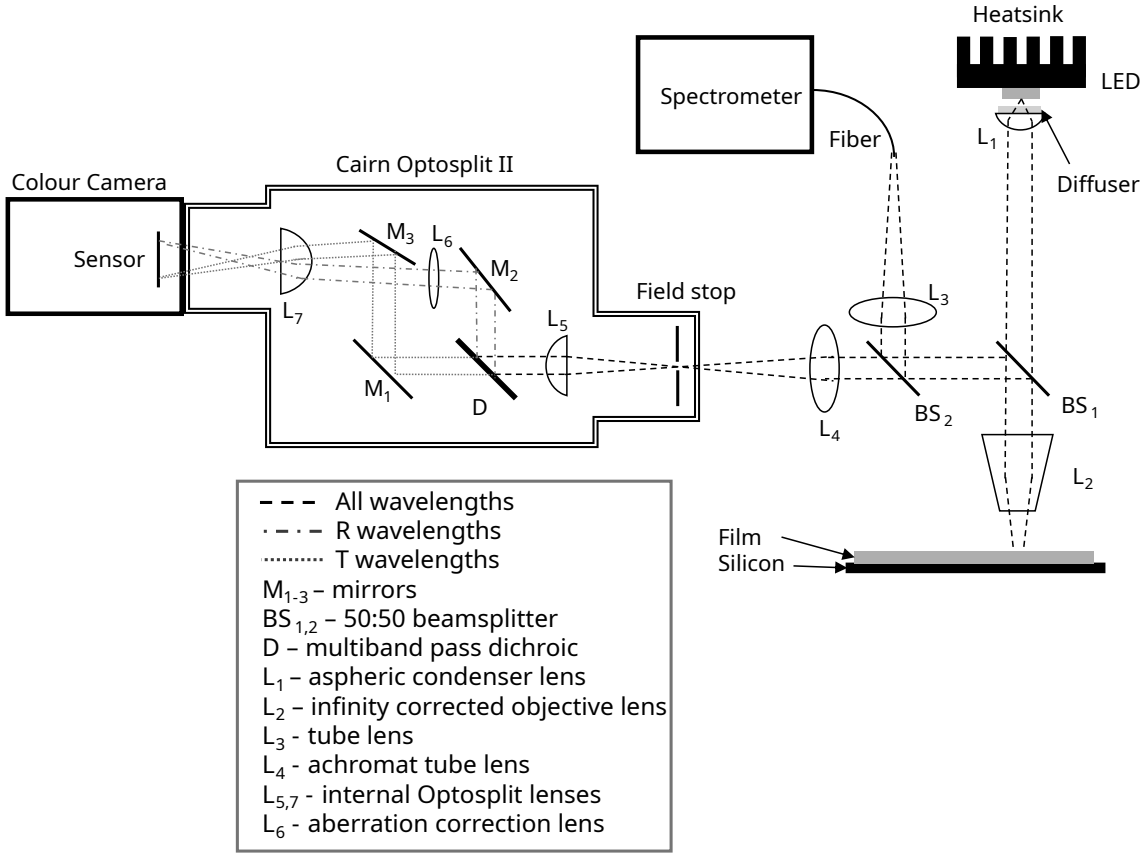

Figure 4.1: Optical setup for simultaneous six band dual imaging and scene spectrum recording

The additional beam splitter (BS_2), lens (L_3) and spectrometer (StellarNet, Black Comet C-100) are only used when taking colour-spectrum pairs of training samples but are retained throughout to maintain the same optical path and attenuation. A 2x/0.10 objective lens (Nikon, MRD0025) was used for all imaging to give a full field of view of 7.90 mm x 5.78 mm (4096 pixels x 3000 pixels). The usable FOV is around half this (3.95 mm x 5.78 mm) when in 6 channel mode when duplicated images are needed on each half of the sensor.

When standard 3 channel (RGB) imaging is needed the Optosplit module is removed and lens L_4 forms a single image directly onto the camera sensor. Figure 4.2 shows the camera Bayer filter, the dichroic transmission, and the product of the Bayer filter and the transmission/reflection of the dichroic that results in 6 channel imaging. All images taken were flat field corrected using bare silicon to correct for the uneven illumination due to the large field of view and the non-perfect collimation of the LED.

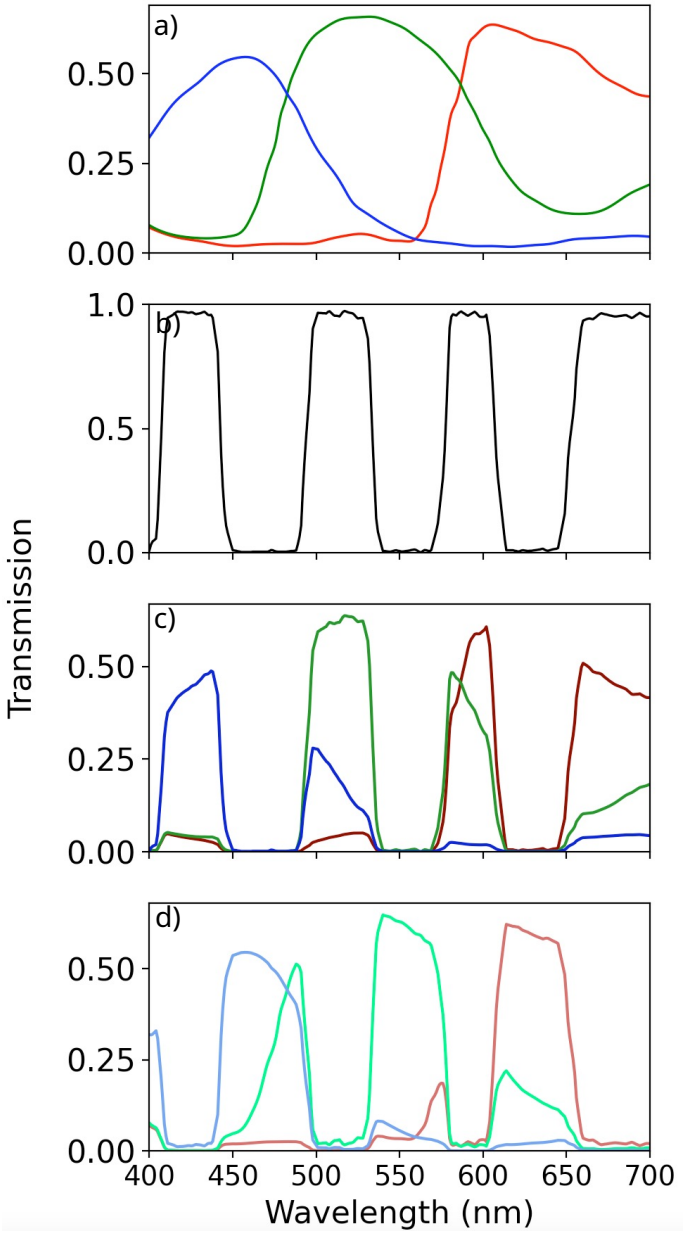

Figure 4.2: a) Bayer filter transmission (RGB) b) MBP dichroic beamsplitter transmission c) transmission imaging spectral characteristics on the left hand side of sensor, RGB(T) d) reflection imaging spectral characteristics in the right hand side of sensor, RGB(R)

4.3.2 Thickness recovery methods

Each of the thickness recovery methods require different levels of *a priori* information as detailed in Table 4.1, but crucially, each can be implemented from outputs of colour cameras and thus are able to be implemented where high frame rates and high spatial resolutions are necessary, such as direct imaging of morphology development in drying films.

Table 4.1: *A priori* information requirements for each thickness recovery method

Method	Calibration or training samples			Model				
	3 channel colour	6 channel colour	Reflectance	$n_{film}, k_{\text{film}}$	n_{sub}, k_{sub}	Bayer filter (T)	Dichroic (T)	$I(\lambda)$
3 channel MSE (1)	X			X	X	X		X
6 channel MSE (2)		X		X	X	X	X	X
Reflectance MSE (3)		X	X	X	X			
Reflectance peak count (4)			X	X				

A complex form isotropic model for normal incidence is chosen for reflectance modelling as in Equation 4.1. Here the Fresnel coefficients of the air/film and film/substrate interfaces are r_{01} and r_{12} respectively i.e. the zero indexed layer is the substrate. These are dependent on the complex refractive indices of the mediums, $n + ik$, as shown in Equation 4.2 and 4.3. The optical path difference (OPD), δ, is shown in Equation 4.4 and is a function of the film thickness, d, the film refractive index, n_1, and the wavelength of light, λ.

$$\mathcal{R}(\lambda, d) = \left| \frac{r_{01} + r_{12} e^{2i\delta}}{1 + r_{01}\, r_{12}\, e^{2i\delta}} \right|^2 \tag{4.1}$$

$$r_{01} = \frac{(n_0 + ik_0) - (n_1 + ik_1)}{(n_0 + ik_0) + (n_1 + ik_1)} \tag{4.2}$$

$$r_{12} = \frac{(n_1 + ik_1) - (n_2 + ik_2)}{(n_1 + ik_1) + (n_2 + ik_2)} \tag{4.3}$$

$$\delta = \frac{2\pi\, d\, (n_1 + ik_1)}{\lambda} \tag{4.4}$$

The angular dependence of the OPD has been omitted because all experiments are at normal incidence. In this work Equations 4.1-4.4 have been used to model a polystyrene film on a semi-infinite silicon substrate in air. This has been done using the transfer matrix method (TMM) using the complex and wavelength dependent refractive indices for silicon [152] and polystyrene [153].

Using the model in Equations 4.1-4.4, the illumination characteristics, and the detection characteristics, the colour response for a given thickness can be calculated. The equations used for this are presented in Section 4.3.2.1 Equation 4.5 for 3 channel colour and Section 4.3.2.2 Equation 4.7 for 6 channel colour. These simulated colours are presented in Figure 4.3. When only the Bayer filter is used, the detection bands are wide, and this causes the colour signal to be significantly dampened beyond 1.5 µm, rendering thickness reconstructions beyond this challenging due to low signal intensity. The cyclical nature of the colour change that occurs every few hundred nanometers are also visible.

In contrast, the introduction of the dichroic beam splitter and collection of both the reflected and transmitted signals has two effects. Firstly, the narrowing of the detected coherence length increases the range of the colour signal oscillations to well beyond 3 µm,

making thickness reconstructions of thicker films feasible, effectively narrowing the broad Bayer filter. Secondly, it is possible to observe that the pattern of lighter and darker fringes between the two sets of colours, regardless of colour, is reversed. This relationship is stronger above film thickness of 2 µm and occurs because the dichroic reflects/transmits opposite signals, evident by the $1 - D(\lambda)$ term in Equation 4.7. In addition, some longer-range order in colour appears to emerge in subsequently light and dark groups of fringes on the order of around 1.5 µm.

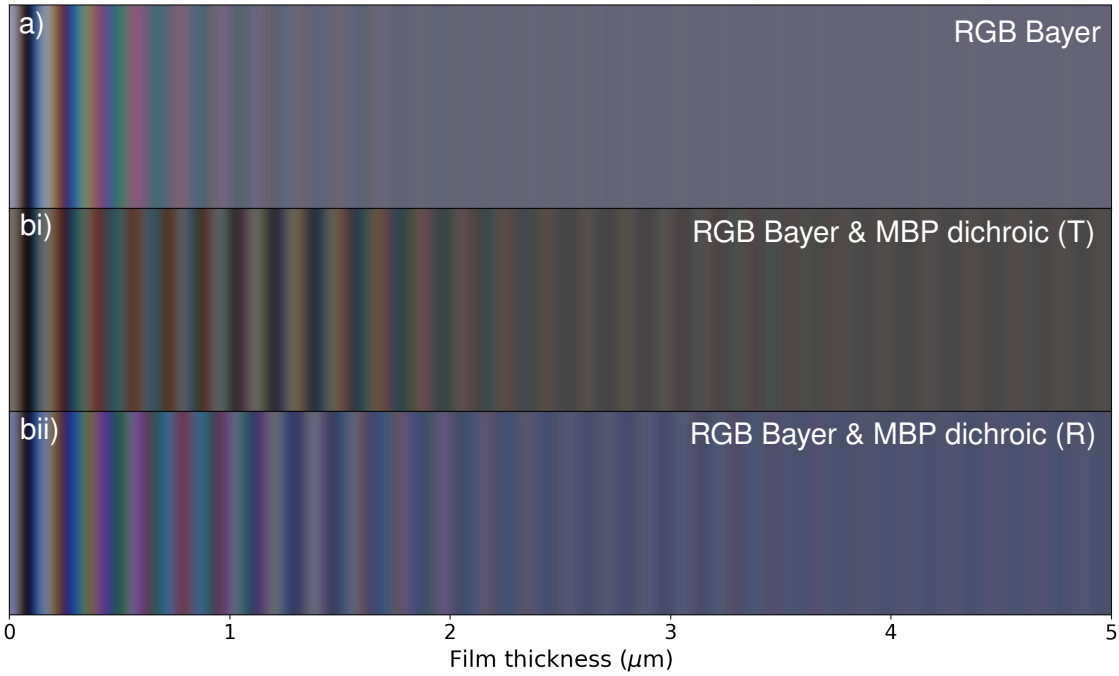

Figure 4.3: Simulated colour captured by a) a standard Bayer filtered colour camera and b) the proposed setup with the MBP dichroic beamsplitter in bi) transmission and bii) reflection for a polystyrene film on silicon, the colour balance and intensity has been adjusted for representative viewing.

4.3.2.1 Minimise RGB MSE (Method 1)

This approach seeks to minimize the mean square error (MSE) between measured 3 channel RGB colour and a modelled 3 channel RGB colour, as demonstrated by Choi et al. 2018 [100]. The minimization of a measured colour against a modelled colour means that the system must be well defined, to model colour-thickness relationship shown in Equation 4.5. This requires the illumination spectrum, $I(\lambda)$ and Bayer filter transmission, $B_i(\lambda)$ where $i = 1, 2, 3$ for red, green and blue channels, respectively. The reflectance spectrum must be modelled across the thickness domain as in Equation 4.1, requiring knowledge of the film and substrate optical constants.

$$\mathbf{p_i}^{\text{model}}(d) = \int_{400}^{700} I(\lambda)\,\mathcal{R}(\lambda, d)\,B_i(\lambda)\,d\lambda, \quad i = 1, 2, 3 \tag{4.5}$$

It will be convenient to express both three channel (RGB) $M = 3$ and six channel $M = 6$ colours as column vectors as follows $\mathbf{p_M} = [p_1, p_2 \ldots p_M]$, with the modelled values denoted by a superscript model. Thus, the selected thickness value is chosen by the minimization of the Euclidean norm (MSE) of the measured and modelled colour vectors as in Equation 4.6.

$$\min_d \left\| \mathbf{p_3} - \mathbf{p_3}^{\text{model}}(d) \right\|_2^2 \tag{4.6}$$

4.3.2.2 Minimise 6-channel colour MSE (Method 2)

Minimize the MSE between 6 channel colours provided by each half of the dichroic filtered sensor and a modelled 6 channel colour. As with method 1, the minimization of a measured colour against a modelled colour means that the system must be well defined with the illumination spectrum, Bayer filter and additionally now, the dichroic transmission $D(\lambda)$. The film and substrate optical constants are necessary as before for the development of the modelled reflectance spectrum.

$$\mathbf{p_i}^{\text{model}}(d) = \begin{cases} \displaystyle\int_{400}^{700} I(\lambda)\,D(\lambda)\,\mathcal{R}(\lambda, d)\,B_i(\lambda)\,d\lambda, & i = 1, 3, 5, \\ \displaystyle\int_{400}^{700} I(\lambda)\big[1 - D(\lambda)\big]\,\mathcal{R}(\lambda, d)\,B_i(\lambda)\,d\lambda, & i = 2, 4, 6. \end{cases} \tag{4.7}$$

This 6 channel imaging and model is then used for thickness recovery in a directly analogous way to the previous 3 channel imaging as in Equation 4.6.

$$\min_d \left\| \mathbf{p_6} - \mathbf{p_6}^{\text{model}}(d) \right\|_2^2 \tag{4.8}$$

4.3.2.3 Minimise reconstructed spectrum MSE (Method 3)

A vector space model of a multi-channel multispectral camera is shown in Equation 4.9, following the notation used by Shimano et al., and is analogous to Equation 4.5. Here, $\mathbf{p}$ is an $M \times 1$ dimensional vector that represents colour output from M channels (as in the previous sections), and $\mathbf{r}$ is a $N \times 1$ dimensional vector that represents the reflectance spectrum of the imaged scene. N is chosen as 30, so that between minimum and maximum

wavelengths of 410 nm and 700 nm respectively, there is a point on the spectrum every 10 nm. S is the $N \times M$ matrix that contains the spectral sensitivities of each channel, and L is the $N \times N$ diagonal illumination spectrum matrix, both at the sample wavelengths.

$$\mathbf{p} = S\,L\,\mathbf{r} \tag{4.9}$$

A reconstruction technique aims to use training data, composed of k correlated measured reflectance, $\mathbf{r}$, and camera channel values, $\mathbf{p}$, where k is the number of training samples, to compute an $N \times N$ transfer matrix, W. The multiplication of this transfer matrix and $\mathbf{p}$, results in a recovered $N \times 1$ dimensional vector of reflectance, $\hat{\mathbf{r}}$ as in Equation 4.10.

$$\mathbf{p}\,W = \hat{\mathbf{r}} \tag{4.10}$$

The pseudoinverse spectral reconstruction technique will be applied here. It is a particularly attractive technique due to the ease of computation and because it does not require any *a priori* information on the imaging or illumination system. The computation of the pseudoinverse transfer matrix W is shown in Equation 4.11, where the superscript + denotes the pseudoinverse of a matrix. R is a matrix composed of k training reflectance vectors $[\mathbf{r_1}, \mathbf{r_2}, \ldots, \mathbf{r_k}]$, and P is a matrix composed of k corresponding 6-band colours $[\mathbf{p_1}, \mathbf{p_2}, \ldots, \mathbf{p_k}]$. This method aims to reconstruct spectral reflectance by computing W such that the Frobenius norm of the test data residuals, $||R - WP||$, is minimized.

$$W = R\,P^{+} \tag{4.11}$$

Once a 6 channel colour has been reconstructed to a spectrum, the MSE is then minimized against the modelled spectrum, as shown in Equation 4.12, to obtain a thickness solution. In this method the minimization between reflectance spectra means that only the film and substrate optical constants need to be defined for development of the modelled reflectance spectrum.

$$\min_{d} \left\| \hat{\mathbf{r}} - \mathcal{R}(d) \right\|_2^2 \tag{4.12}$$

4.3.2.4 Peak counting on reconstructed spectrum (Method 4)

Using an established peak counting method [77] on a reflectance spectrum reconstructed from 6 channel colour, $\hat{\mathbf{r}}$ This method requires the least *a priori* information, with only the film refractive index necessary. However, unlike with the other models, this method does not incorporate the complex refractive index of the mediums and thus assumes a non-absorbing film model. The wavelengths λ_1 and λ_2 are extracted from $\hat{\mathbf{r}}$ as the furthest apart resolved peaks or troughs, and Δm is the order difference between these points. For example, between a peak and a subsequent trough is $\frac{1}{2}$, between two subsequent peaks (or troughs) is 1, and between a peak and the trough after the subsequent peak is $1\frac{1}{2}$, and so on.

$$d = \frac{\Delta m}{2\sqrt{n_1^2 - \sin^2(\theta)}} \cdot \frac{1}{\left(\frac{1}{\lambda_1} - \frac{1}{\lambda_2}\right)} \tag{4.13}$$

4.3.3 Training and calibration

A set of training and calibration films were prepared by spin coating different concentrations of a polystyrene (PS) (350 k) in butyl acetate (BA) solution at a selection of different spin speeds. These displayed flat film thickness colours that were then inspected with the optical setup, at the sample centre, to take corresponding colour and spectrum measurements for both 6 channel (with the MBP dichroic) and 3 channel (without) respectively from a 700 pixel x 700 pixel ROI of approximately 1.35 mm × 1.35 mm. Calculation of the reflectance spectrum used a Si wafer coated in evaporated aluminium (80 nm) as a reference. The sample thicknesses were then measured via ellipsometer with a spot size of approx. 0.3 mm x 1 mm. The complete data for this set of training/calibration samples, including the recovered thicknesses by each method, is available in Appendix A. Figure 4.4a shows the spin coating conditions, thickness and RGB colour (colour balanced post processing using 1.8, 1, 3.5 multipliers for R, G and B respectively to match the colour balance in Figure 4.3) of these samples.

In spin coating, the final thickness is inversely proportional to the square root of angular velocity, and this is clearly displayed in the data. This means that in the thickness range 106 nm – 717 nm covered by the 25 samples, the thicknesses are skewed towards the lower end of the range. A further selection of 7 test samples are spun coat and are not

h

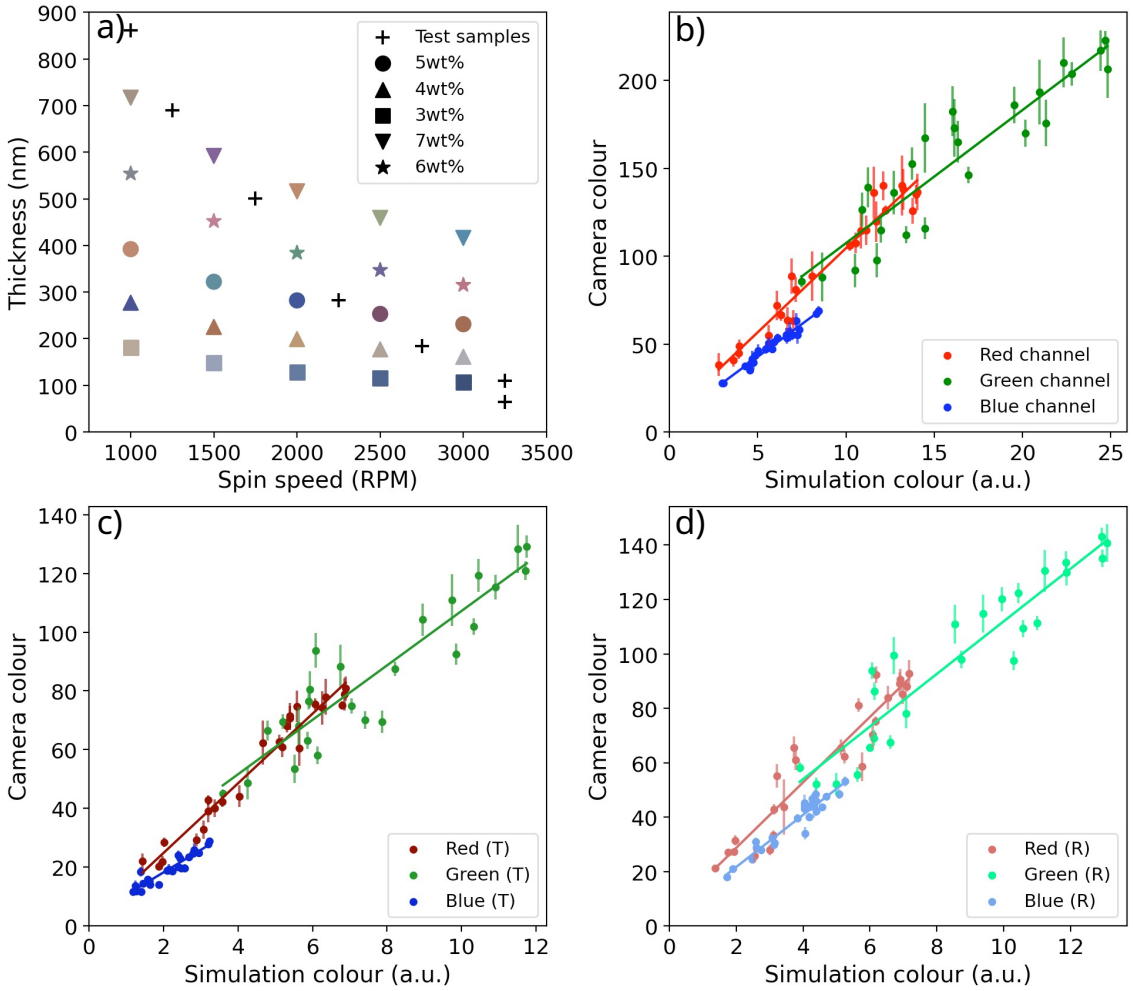

Figure 4.4: a) The spun coat calibration/training samples used as shown by fabrication conditions, measured thickness via ellipsometer and RGB interference colour, test samples used for validation are shown as black plus marks b-d) calibration by linear regression between the simulation colour values (in arbitrary units from simulated scaled [0, 1] curve integrations) and recorded camera values for the spun coat samples for standard RGB, RGB transmission and RGB reflection respectively. Error bars show two times the standard deviation of the colour value over the ROI

used in the calibration or training. The conditions were chosen so that one sample was of greater thickness and one sample was of lower thickness than the range covered by the calibration/training samples. The thickness recovery of these is shown in Section 4.4.1.

Using these samples, the relationship between the simulation colour and the colour captured by the camera could be calibrated. This accounts for camera settings such as the exposure time and gain (0.9), the intensity of the LED and the exposure time. This is achieved with linear regression as shown in Figure 4.4b-c. More advanced non-linear calibration methods may need to be used if the camera does not have a linear optoelectronic conversion function (OECF) or if gamma correction and colour temperature correction are

used. All colour balance values are set to 1 for clarity in interpretation which results in green hued images. However, since the camera conversion is made linear, the colour balance is simply a scalar of the pixel activation and so can be altered post-processing. The linear calibration works effectively to give coefficient of determination (CoD) values in the range of 0.85-0.96. The values used and the validation of the calibration is presented in Appendix A.

4.4 Results and discussion

4.4.1 Uniform test samples

4.4.1.1 Spectrum reconstructions

Before presenting the results of thickness recovery, the effectiveness of the spectral reconstructions from the 6 channel colour data is presented and discussed. Figure 4.5 shows the spectral reconstructions across the 7 spun coat test samples, (+ data series in figure 4.4a) these are separate from those used to train the reconstruction technique, so can give a fair assessment of performance. Overall, the characteristic shape of the reflectance spectrum, linked to the film thickness, is reconstructed with some success. The systematic over prediction of the model compared to the measured spectra can be attributed to the fact that the measured spectra are calculated by using an aluminium mirror as a reference, which has around 90% reflectance, instead of being a perfect mirror. This could be corrected for by either increasing spectrometer gain or illumination intensity by a factor of 1.11 in the reference measurements or multiplying the modelled reflectance values through by that of bare aluminium. Taking this into account, these data also show that the model is accurate at predicting the reflectance of our polystyrene film on silicon system.

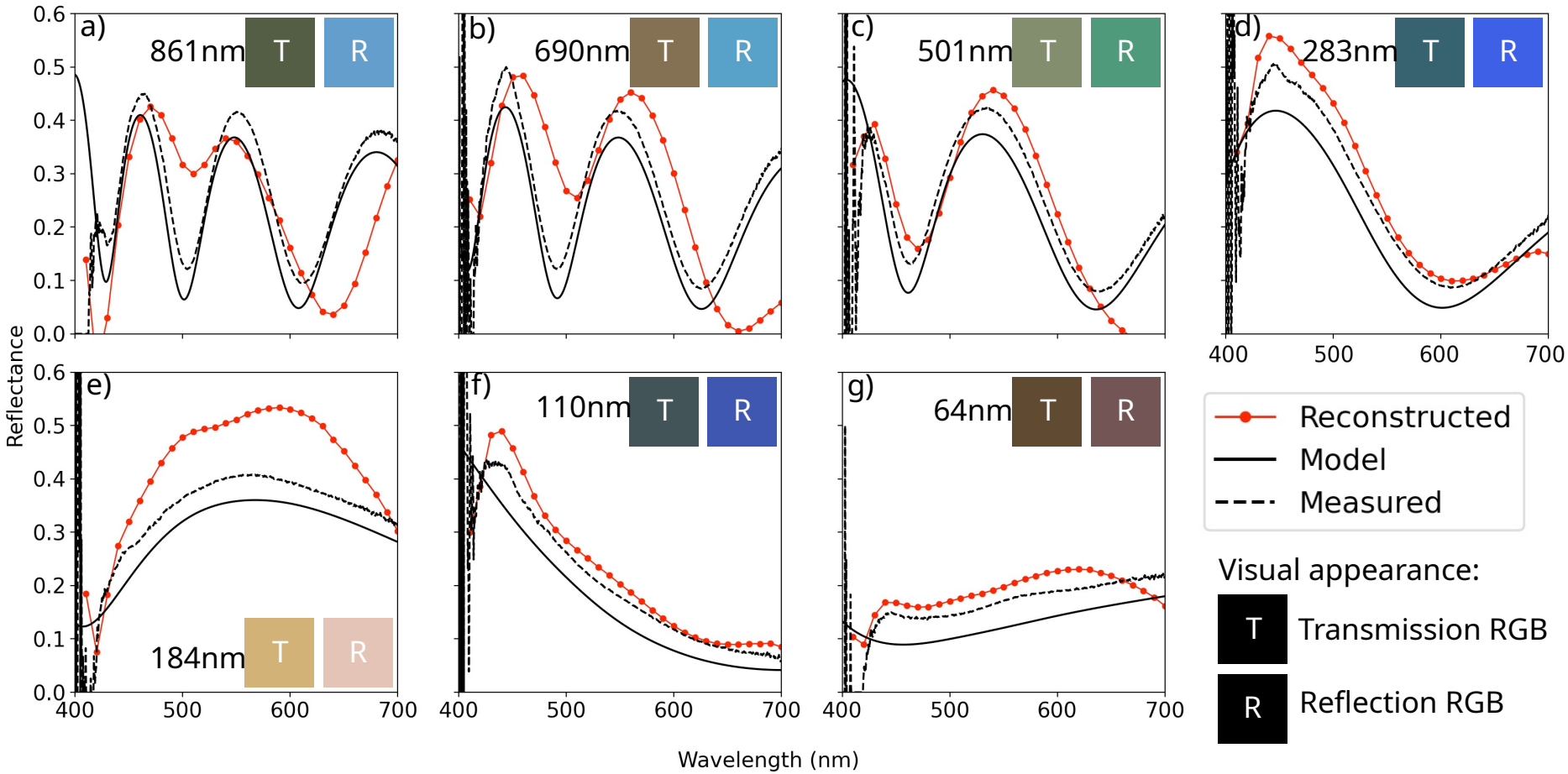

Figure 4.5: a-g) The reconstructed reflectance spectra of the test samples 1-7 respectively, displayed with the reflectance spectra measured by the integrated spectrometer (using aluminium as a reference) and the reflectance spectra predicted by the model. Inset to each sample's graph are the visual appearance in RGB colours in reflection (R) and transmission (T) recorded by the multispectral camera used to reconstruct the spectra, these have been colour balanced in post-processing.

Across these 7 samples there is some variation in the reconstruction performance as shown by Figure 4.6a that displays the error in the reconstruction. Through all thickness samples reconstruction quality is poor at the upper and lower limits of the wavelength range where there is an increased error in the measured spectra because of the overall low illumination intensity here provided by the LED.

The thicker samples also show a higher error, which may be attributed to the fact that the thicknesses of the 25 training samples are skewed low due to the spin coating process. Better reproduction is seen because of a higher density of training samples at lower thicknesses. The thicker samples have more complex spectrums with more features, and this leads generally to a reduction in reproduction quality as an increasing root mean square error (RMSE) as shown by the annotated box plots in Figure 4.6b.

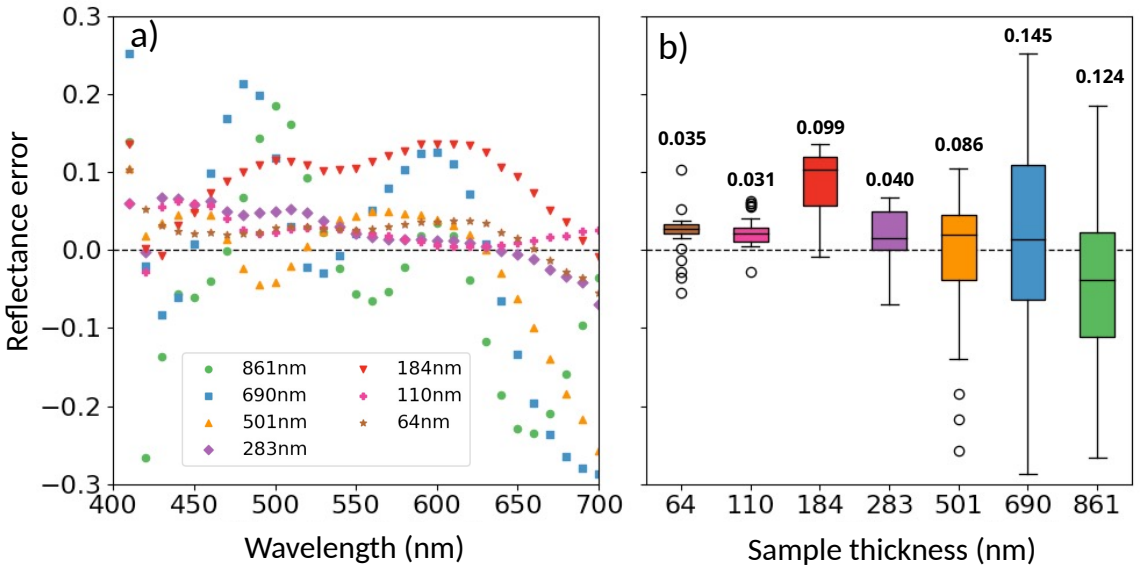

Figure 4.6: a) Scatter plots of the error between the reconstructed and measured spectra as shown in Figure 5 b) Box plots of this error for each of the 7 test samples, annotated above the box with the root mean square error.

The thickest sample at 861 nm was reconstructed with a lower RMSE than the next thickest sample at 690 nm; this is an unexpected result for two reasons. Firstly, this result does not follow the trend set by the other data that suggests more complex and less well trained (i.e. thicker) samples have higher reconstruction RMSE. Secondly, the sample at 861 nm is above the thickness range of the training data (106 nm - 717 nm).

4.4.1.2 Thickness reconstructions

Each thickness recovery method was applied to the colours displayed by the 7 spun coat samples; the results are displayed in Table 4.2 that shows the global minima of MSE minimisation over the domain i.e. the thickness of the smallest MSE value. The thickness is considered accurately recovered if it is in within 5% or 15 nm, whichever is higher, of the thickness measured by ellipsometry. This is an arbitrary choice that can be altered as the requirements of the metrology change, for example, if a known thickness variation results in a critical defect.

Table 4.2: The measured thickness (via ellipsometer) and recovered thicknesses of each spun-coat test sample reported as the global minimum ± the standard error estimated via local curvature using second order finite differences (for methods 1-3 where MSE is minimised)

Test sample	Measured thickness (nm)[1]	Recovered thicknesses (nm)			
		Method 1	Method 2	Method 3	Method 4
1	861	679±15.2	**861±3.6**[2]	316±2.9	390
2	690	313±1.8	**700±4.0**	**715±3.5**	766
3	501	335±1.1	**512±2.4**	**517±2.5**	570
4	283	**286±1.9**	**284±1.0**	**289±2.1**	-[3]
5	184	2±26.7	**178±3.6**	**177±2.9**	-
6	110	277±0.8	**112±0.7**	**124±1.3**	-
7	64	**63±0.3**	**52±0.5**	**52±0.5**	-

Method 1, MSE minimisation of 3 channel colour, satisfactorily recovers two out of the 7 test samples using global MSE minimum, including the thinnest sample, but appears to struggle over 300 nm. On the other hand, Method 2, MSE minimisation of 6 channel colour, recovers all of the test samples, indicating that the increased spectral information is working as intended to overcome the colour-to-thickness ambiguities experienced by Method 1 that utilised just RGB colour.

Method 3, which employs spectral reconstruction on 6 band colour followed by MSE minimisation between reflectance spectrums, rather than colour, is successful at recovering all but sample 1, which was above the range of the spectral reconstructions' training data. Sample 7 was successfully recovered, although this was also below the training data range,

[1] Due to the simplicity of the system (polystyrene on silicon) the ellipsometry fitting procedure has very low uncertainty (much less than 1 nm) and these values are rounded to the nearest whole nanometre, in line with the expected precision of reflectometry-based techniques.

[2] Entries that meet the matching criteria are in bold.

[3] A dash (–) indicates where the recovered spectrum did not have enough extrema to compute Δm.

this can be attributed to a relatively linear colour change in all colour channels for films around 150 nm and below.

Method 4 does not correctly recover the thickness of any of the test films. With test samples 4-7 thickness recovery could not be attempted because the reconstructed spectrum does not have multiple easily identifiable maxima and minima to define Δm, a fundamental limitation of the approach. The accuracy of the thicknesses recovered by this method should be expected to be much lower than the other three due to the assumption of constant refractive index and zero absorption present in Equation 4.13, and the small wavelength difference between λ_1 and λ_2. These data indicate that this approach is not viable with films in the thickness range covered here, but it may be viable at larger thicknesses, however, it still may be ineffective because at these larger thicknesses the RMSE of construction gets worse, as discussed in Section 4.4.1.1.

In the first three methods, the recovered thicknesses in Table 4.2 are the global minima of the MSE. This is not the end of the story; MSE as a function of thickness has many local minima, present due to the cyclical nature of the colour changes. When plotted, such as in Figure 4.7 for test sample 1, it becomes apparent that other secondary and tertiary (and so on) options for recovered thicknesses can be seen, from these sequentially higher and higher MSE minima values.

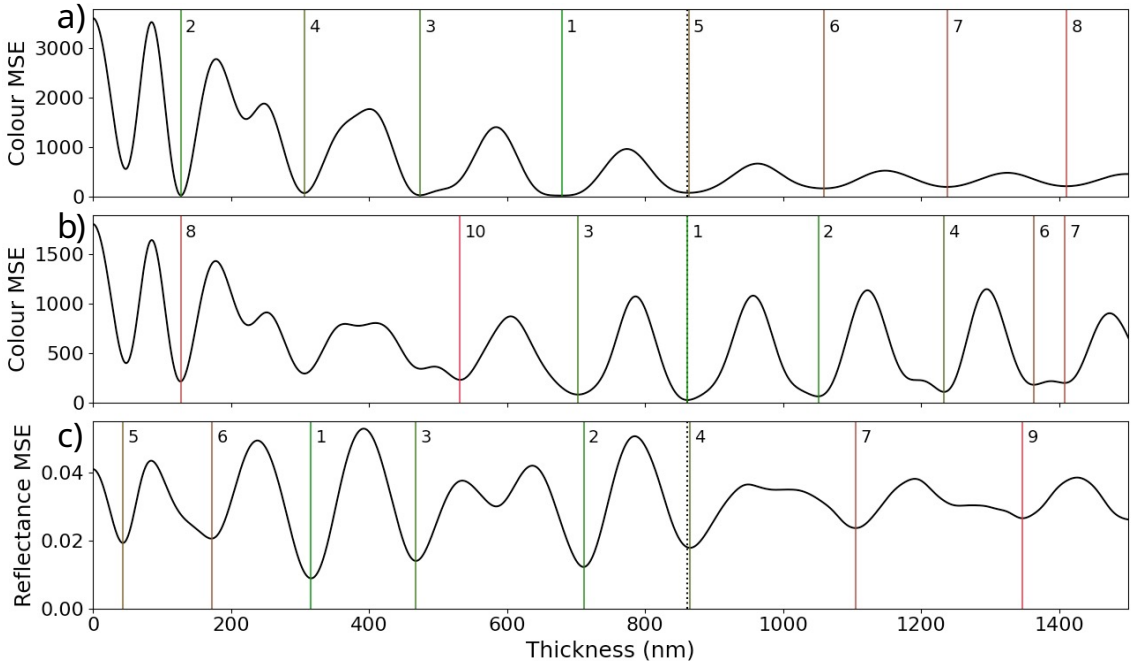

Figure 4.7: The MSE as a function of thickness for sample 1 a) method 1 b) method 2 and c) method 3, where the sample thickness is indicated by a dashed line and sequentially low minima are labelled with vertical lines, starting at 1 with the global minimum.

Once these other minima are considered, method 1 finds a satisfactory solution for all 7 test samples at the fifth minima, and method two at the fourth minima. The results are displayed in the heatmap in Figure 4.8. This consideration of multiple solutions in order to recover the true thickness is a well-known limitation of RGB imaging and arises due to the cyclical nature of colour changes in the thickness domain as demonstrated in Figure 4.3. Processing algorithms that use additional assumptions on physical parameters such as topology [1] have been successfully employed to select true thicknesses from shortlists.

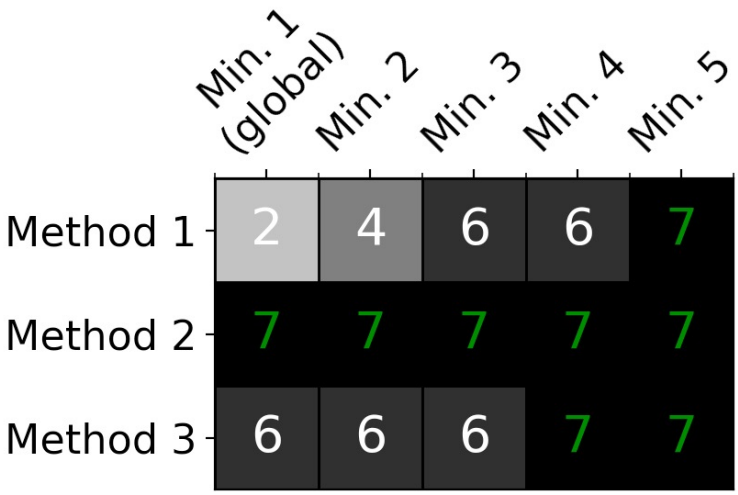

Figure 4.8: A heatmap showing the sequentially ascending minima (from global) needed to recover thickness to a satisfactory degree of accuracy for each method

Methods 1 and 2, where the MSE of a 3 and 6 channel colour respectively is minimised, have also been tested using chromaticity rather than colour values. Performance was worse with fewer thicknesses recovered; however, this approach has the advantage of not needing a calibration step and is likely to build in robustness when uneven illumination across the FOV is present in imaging.

4.4.2 Non-uniform 1D reconstructions

Often a line (1D) or areal (2D) measurement is just composed of many point measurements side-by-side. However, this is often not the most effective technique for recovering 2D film thicknesses, especially when a basic assumption on film topology continuity can be used to reduce effects of the multiple-minimum problem observed in the previous section.

A sample was blade coated on silicon from a 6 wt% solution in a channel between two pieces of tape, approximately 30 µm deep, and left to dry. The resulting film had

an uneven thickness in both x and y directions. A DekTak contact profilometer (Bruker) measurement was taken across the film indicated by the dashed line in Figure 4.9. The profilometer started and ended on the bare silicon left by the removal of the tape to give thickness values of the film between these two points.

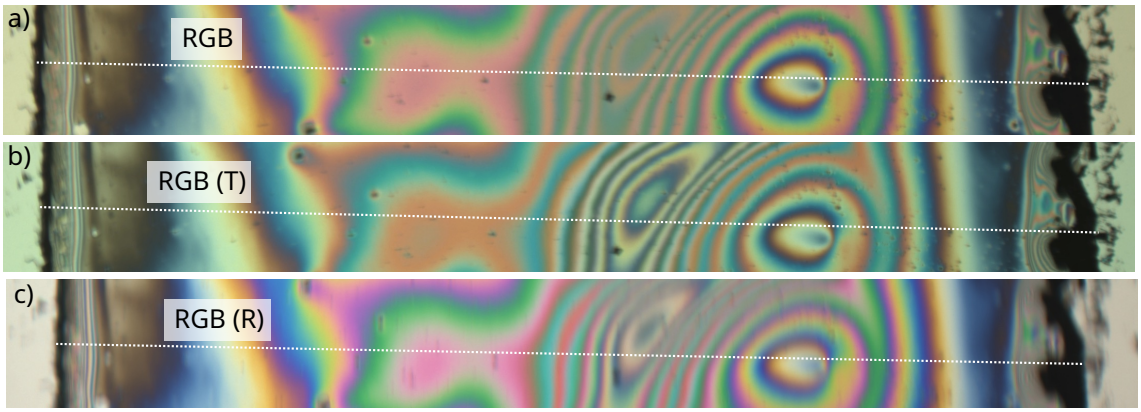

Figure 4.9: a) RGB image b) RGB(T) image c) RGB(R) image of an uneven polystyrene film strip on silicon exhibiting interference colours, with the profilometer path annotated as a white line

Figure 4.10 shows the red, green and blue channels from the standard image and the transmitted and the reflected images (comprising the multispectral image), along the line profiles indicated in Figure 8 using a 3 pixel x 3 pixel (5.8 µm x 5.8 µm) sliding window approach. In thinner areas, strong colour fringes can be seen in all of the colour channels. Where the thickness gradient is shallow the colours modulate slowly, and where the gradient is steeper, the colours modulate more quickly. The reflected and transmitted 6 channel data show continued modulation even above 1.5 micron film thickness, whereas the visibility of the fringes in standard RGB colour becomes very limited, especially in the green channel (because it has the largest width). Across the profile, the thickness maxima and minima are associated with reversals in the colour data. This yields imaginary reflective lines parallel to the colour axis at these points that can be readily distinguished by eye in Figure 4.10.

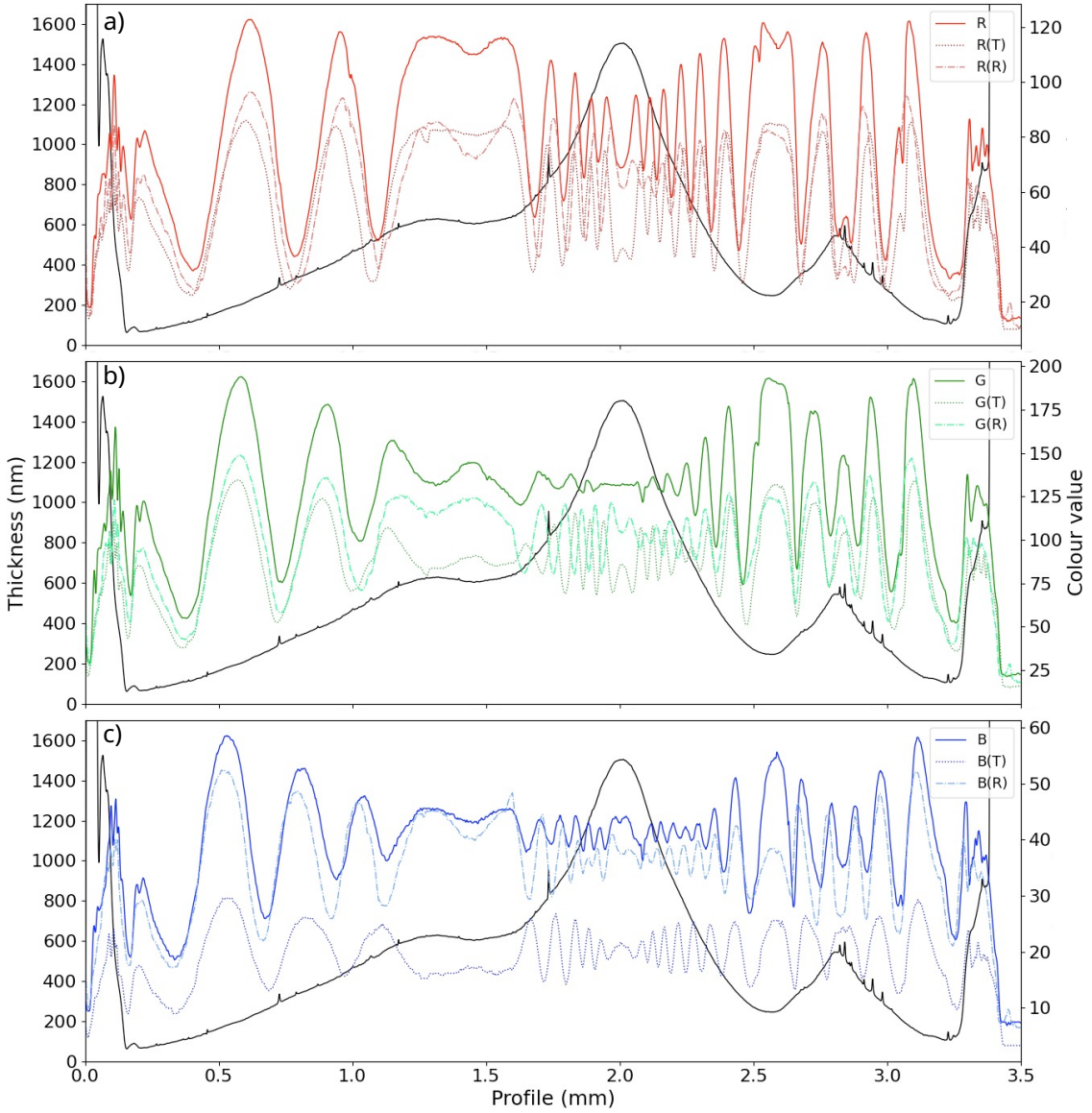

Figure 4.10: a-c) The colour and measured thickness (black line) data for red, green and blue colours respectively of the standard 3 channel imaging, six channel transmission and six channel reflectance imaging from a 3 pixel x 3 pixel mean value sliding window

Thickness reconstruction was subsequently undertaken for the extracted line profiles using Methods 1, 2, and 3; Method 4 was excluded owing to its notably poor performance, especially within the lower thickness ranges observed in this sample. Figure 4.11a presents the MSE heatmaps for each method, these are vertically stacked versions of the MSE functions plotted in Figure 4.7 (which illustrates point, not line, measurements). These are displayed adjacent to the recovered thickness values corresponding to the minimum MSE at each profile location, as shown in Figure 4.11b.

Along the profile, the measured thickness, indicated by the black line, coincides with regions of low MSE on the heatmaps, suggesting that these areas represent the correct

thickness estimates. Nevertheless, these low-MSE regions do not always correspond to the absolute minimum error values, as illustrated in Figure 4.11b.

Method 1 exhibited robust global minima performance at thicknesses below 750 nm, where the modulation of colour is most pronounced. However, at thicknesses above 750 nm, both the cyclical nature of the colour response and the reduction in fringe visibility give rise to a grid-like ambiguity that prohibits accurate reconstruction of the thicker, central portion of the profile.

In contrast, Method 2 produced a low-MSE trace that more closely approximated the measured thickness, as evidenced by the recovered global minima. Fewer local minima were observed, particularly at lower thicknesses, and the method achieved more precise thickness recovery in the thicker regions. The asymmetry in the thickness estimates on either side of the peak suggests that the transmission and reflection images may not have been perfectly aligned or flat-field corrected, thereby resulting in different colour responses at equivalent thicknesses.

Method 3 performed better than Method 1 but did not match the accuracy of Method 2 within the training data range. Notably, its heatmap demonstrated considerably less ambiguity than the other methods, a characteristic that may be advantageous in certain colour-to-thickness applications. However, as expected, Method 3 fails to deliver reliable estimates beyond the limits of the training data, indicated by the extent of the grey background.

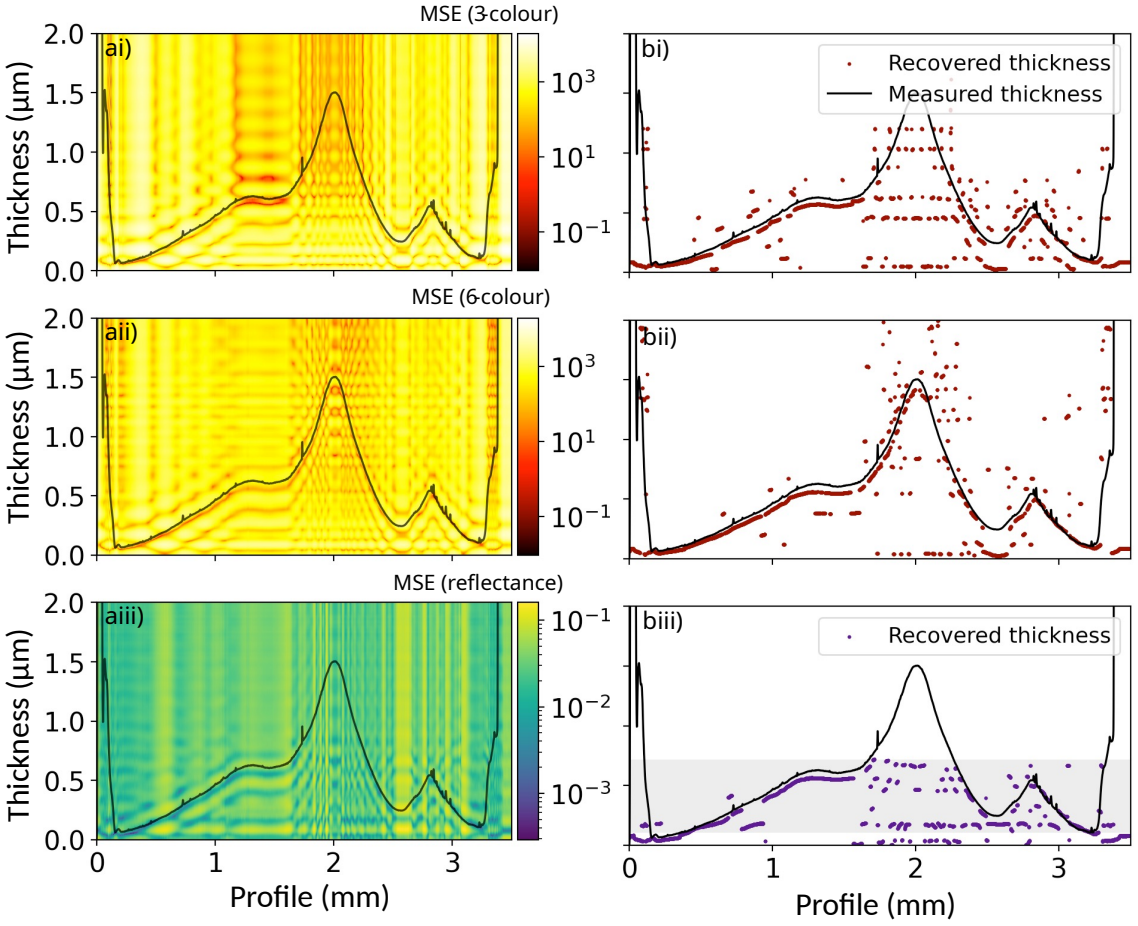

Figure 4.11: a) Heatmaps for the MSE minimization for methods 1-3 (i-iii) respectively and b) scatter plots of the recovered thickness at the global minimum MSE at each position in the profile, in all plots the measured thickness is shown as a black line.

Method 2 shows the best overall performance, but its ability to reconstruct surfaces can be enhanced by adding an additional term to minimisation [154]. This term should penalise the selection of low MSE solutions that are far from the previous solution. This builds in knowledge (and the assumption) that the reconstruction is of a gradually varying surface. The penalty term, Z, simply added to the MSE as in Equation 4.14, which is a modified version of Equation 4.8 and will be referred to as Method 2+. In Equation 4.14, Z is a function of two things, the difference between the thickness domain and previously recovered thickness, $|d - d_{prev}|$ and a scale parameter α that controls/weights how much this thickness difference effects the MSE. Some forms of penalty term are shown in Table 4.3.

$$\min_{d} \left\| \mathbf{p_6} - \mathbf{p_6}^{\text{model}}(d) \right\|_2^2 \; + \; Z \tag{4.14}$$

Each method in Table 4.3 was used to recover the line profile from 6 channel colour

Table 4.3: Different penalty terms with optimal scaling factors when used to recover the line profile

Type	Penalty term (Z)	α	RMSE (nm)
Linear	$\frac{\lvert d - d_{\text{prev}} \rvert}{\alpha}$	1.0	89
Quadratic	$\left(\frac{\lvert d - d_{\text{prev}} \rvert}{\alpha}\right)^2$	99	152
Cubic	$\left(\frac{\lvert d - d_{\text{prev}} \rvert}{\alpha}\right)^3$	162	158
Exponential	$exp\left(\frac{d - d_{\text{prev}}}{\alpha}\right) - 1$	171	161

and this was compared with the measured line profile. Precise control over the parameter alpha is essential for effective implementation of this modification and the optimal values for α reported in Table 4.3 were achieved by iterative reconstruction and selecting one that minimized the error between the measured and recovered thickness. Figure 4.12 shows the differences in line profile reconstructed with different Z terms.

When reconstructing the first thickness, where d_{prev} is undefined, Z is set to zero and Method 2 is used. The choice of this seed position can therefore have major consequences for the resulting surface if reconstruction here is poor, this is examined further in the following Section 4.4.3. If any thickness on the profile is known, for example for a physical reason, this should be used as the see position. Here the profiles were seeded at $x = 0$ with Method 2.

There are some interesting differences in behaviour between the linear penalty term and the quadratic penalty term. The linear penalty term penalises small thickness differences more harshly and as a result leads to very smooth thickness reconstruction with low error below 1.1 µm, however, the peak feature at the highest thicknesses and surface gradient is lost in the reconstruction because the sudden increase in thickness to the next local minima cannot be made. In contrast, the quadratic term sees larger variations around the measured profile because it is not penalised as much for small thickness differences. This results in a profile that has more smaller length scale deviations from the measured thickness, but that can successfully capture all features of the profile.

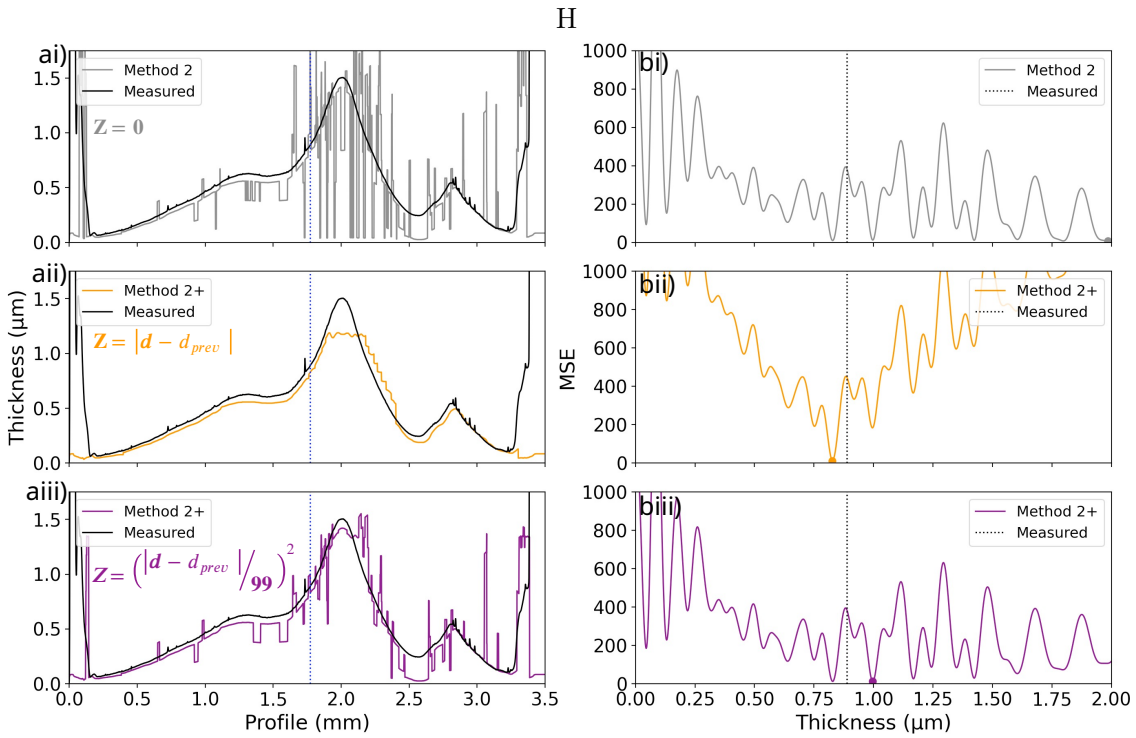

Figure 4.12: a) The reconstructed line profile and the measured line profile using i) Method 2 and optimized Method 2+ with ii) linear and iii) quadratic Z (penalty) terms annotated on the graph b) the MSE from the point annotated with the blue dashed line on a) for each of the Methods, with the measured thickness as the vertical dashed black line

4.4.3 Non-uniform 2D reconstructions

A major advantage of these optical methods is that they can be used to take areal thickness measurements over large areas, or over smaller areas with higher lateral resolution simply by changing the magnification of the objective lens. Here by using low 2x magnification we can get a reflected and transmitted image of 1500 pixels x 1728 pixels each on the camera sensor, at a resolution of around 2 µm per pixel.

Figure 4.13 shows the processing approach of a 2.89 mm x 3.33 mm non-uniform film sample. The pixels are first binned in 3 x 3 to reduce the effects of random noise and lower the processing time. The multispectral image is processed with Method 2+ and a quadratic penalty function using 4 different seed positions annotated as dark grey strips in Figure 4.13c, and the average of two neighbours as the previous thickness value annotated as orange squares in Figure 4.13c. For example, the first processing seeds the top row and left column with Method 2 that does not require a previous thickness value, then, processing proceeds from NE to SW using the average of each new pixel's N and S neighbours as the previous thickness value. This is a strategy implemented to reduce the effect of seed

position and processing direction. Artefacts due to the seed position and the processing direction can be seen as some diagonally shaped (in the processing direction) blocks of equal thickness.

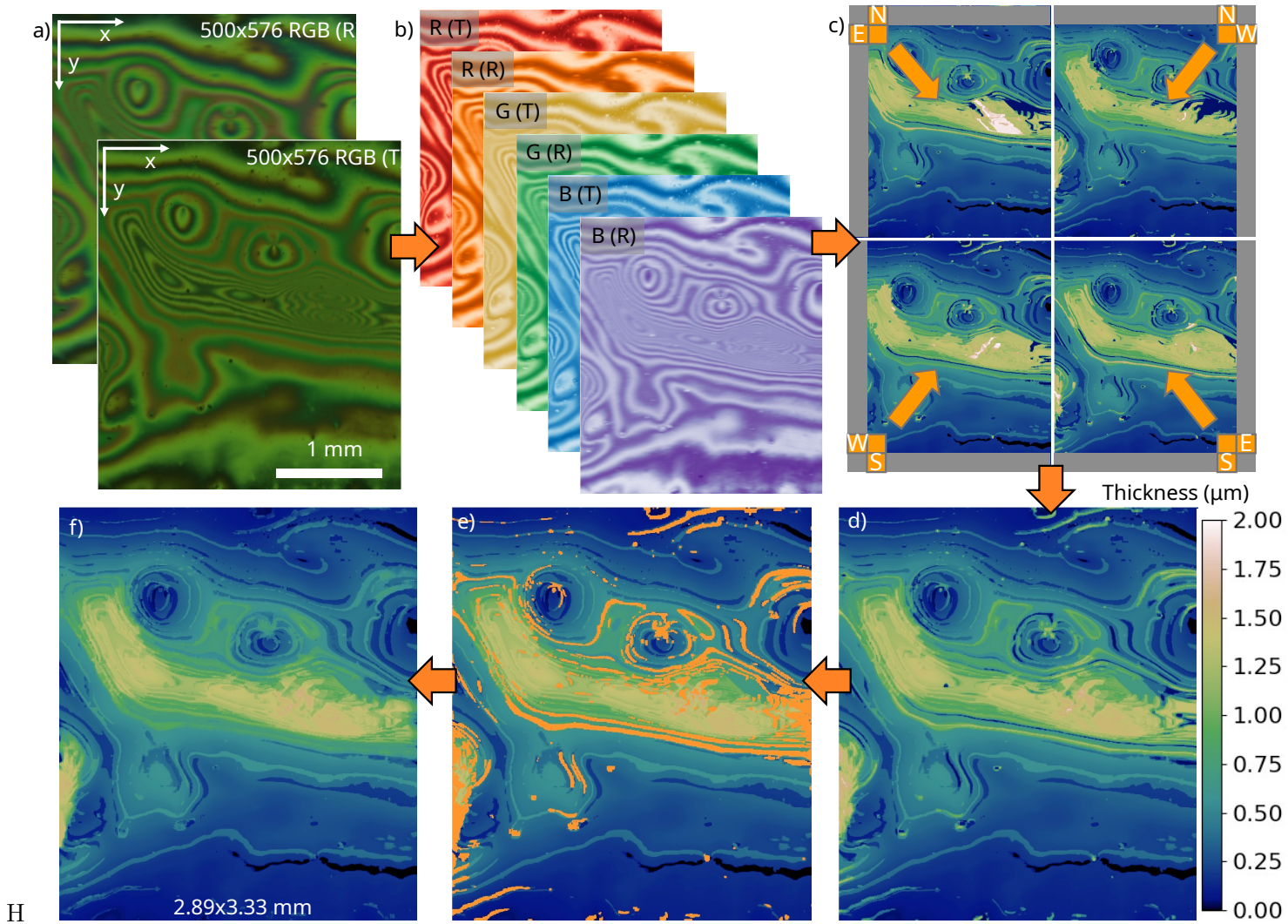

Figure 4.13: a) 3 x 3 binned areas of the transmitted and reflected colours b) the multispectral image extracted from these images c) the reconstructed thicknesses from 4 different seed positions d) the average extracted thickness (colour scale for (d) is consistent throughout the figure) e) thicknesses removed (orange) by median filter thresholding (kernel 35 pixels x 35 pixels, or 40 µm^2, 250 nm threshold) f) the resulting surface filled by interpolation

Post-processing of the scene can further improve the reconstructed thickness, and a previously reported strategy [1] has been used. This median filter thresholding strategy removes any thicknesses that are over 250 nm different from the median of the surrounding 40 μm^2. Control of the threshold value and the kernel size give control over the number of points removed. Finally, interpolation is used to re-fill these points, leaving the final surface.

Figure 4.13 presents the final reconstructed surface for the 2.89 mm x 3.33 mm ROI in three-dimensional surface form. Qualitatively the shape of the surface agrees well to the fringe pattern shown in the images and the line profile measured by profilometer, with a much thicker central ridge. Crater-type features can be seen along the top of the ridge that correspond well to the circular fringe features in the photo, as well as a secondary thicker area in the bottom left of the ROI. Some smaller length-scale artefacts from the reconstruction have remained in the reconstruction shown as ledges where there is a large thickness change. These may be smoothed out in post processing used techniques such as moving averaging or median filtering, at the risk of distorting smaller surface features. Various wavelet analysis filtering approaches used for surface metrology are also applicable here and have the advantage of minimising distortion of features at certain length scales.

4.5 Conclusion

This work demonstrates a cost-effective approach to achieve six-band multispectral imaging by modifying a standard colour camera using LED illumination with an off-the-shelf multi-bandpass dichroic beam splitter. Expanding from traditional three-band (RGB) imaging to six-band imaging has significantly enhanced the effectiveness of colour-based techniques for thin film thickness recovery, while remaining at the high resolutions and frame rates provided by RGB cameras. Our results show that the increased spectral information not only increases reconstruction accuracy when compared to RGB systems, but also extends the thickness range, as evidenced by the reconstruction of a non-uniform polymer film surface over a 2.89 mm $\times$ 3.33 mm region-of-interest (ROI) up to 1.8 µm with a predicted RMSE of less than 152 nm.

The application of spectral reconstruction techniques from 6 channel imaging also showed that thin film reflectance spectra can be recovered with accuracy by using training

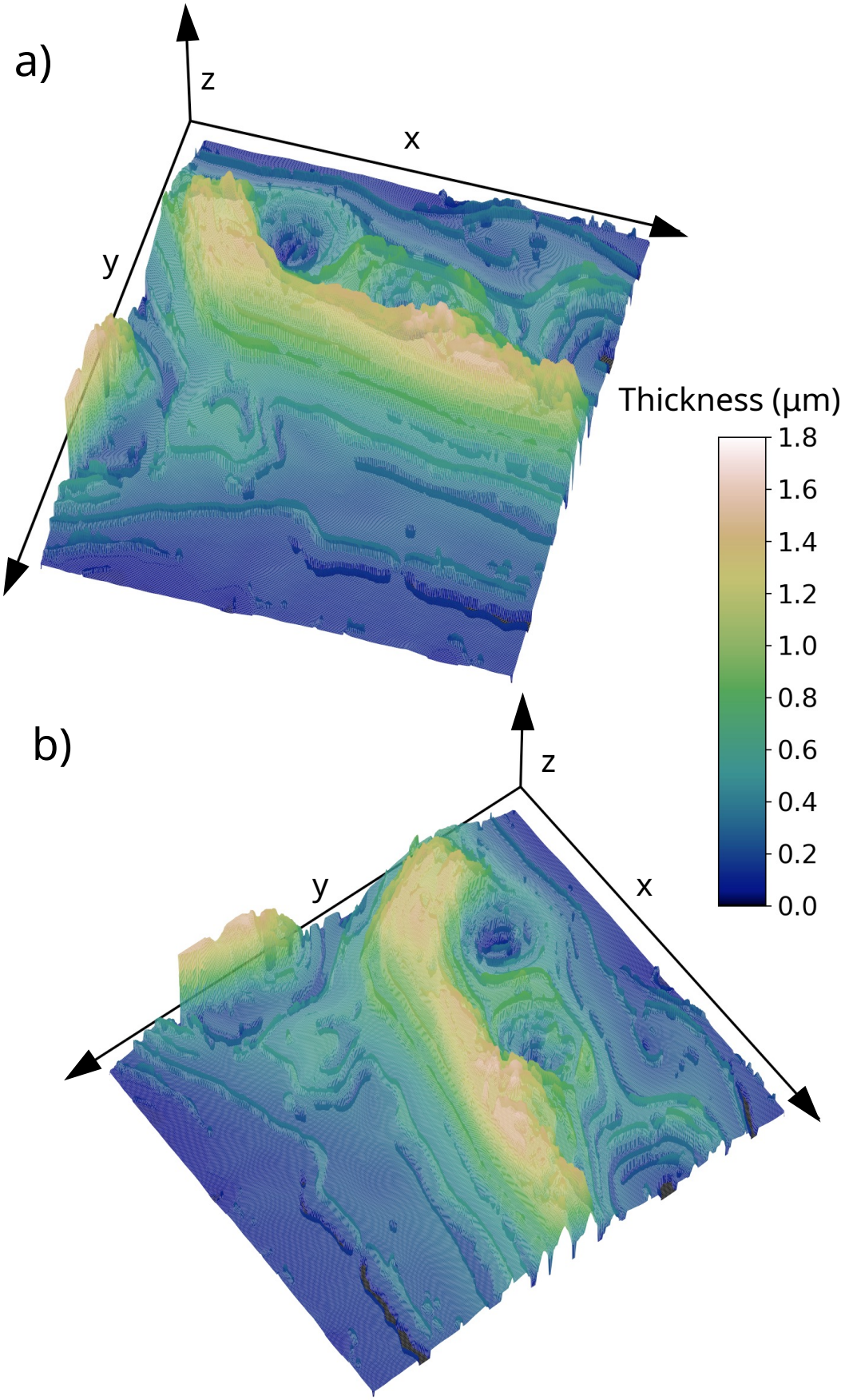

H

Figure 4.14: Recovered area thickness profiles of the 2.89 mm x 3.33 mm ROI at a lateral resolution of 6 µm from two different viewpoints.

data (spectrum-colour pairs). This is the first time that spectral reconstruction techniques have been used in the context of thin film characterisation, and in scenarios where precise knowledge of the illumination and camera characteristics is challenging to obtain, they offer a promising alternative to physically model these conditions.

The methods explored here can be implemented with LED illumination and standard colour camera detection which gives hinge advantages in the possible applications. Due to fast rise times bright LEDs can be easily strobed for freezing fast-moving scenes, and RGB cameras regularly possess frame rates and resolutions orders of magnitude higher than equivalently priced multispectral cameras.

While our study confirms the superiority of six-band over three-band imaging for thickness recovery, it also highlights the need for further research. The system could certainly be improved by use of a fully customized MBP dichroic beam splitter with transmission changes specifically tuned to the Bayer filter to increase signal and reduce crosstalk. Future work should focus on exploring alternative spectral reconstruction methods and transfer matrices to optimize accuracy and extend the technique to a broader range of materials and film conditions. Moreover, as multispectral camera technology and enabling components such as metasurfaces [113] continue to advance, we anticipate that the integration of HSI in demanding *in situ* thin film sensing and characterisation will become increasingly widespread, driving further innovation in both small length scale film morphology design and large-scale production and quality control.

References

[1] Jack B.P. Atkinson and Jonathan R. Howse. "In-situ full-wafer metrology via coupled white light and monochromatic stroboscopic illumination". In: *Optics and Lasers in Engineering* 184.P2 (2025), p. 108692. DOI: 10.1016/j.optlaseng.2024.108692.

[15] Dunbar P. Birnie, Dylan E. Haas, and Carissa M. Hernandez. "Laser interferometric calibration for real-time video color interpretation of thin fluid layers during spin coating". In: *Optics and Lasers in Engineering* 48.5 (2010), pp. 533–537. DOI: 10.1016/j.optlaseng.2009.12.021.

[61] R Swanepoel. "Determination of the thickness and optical constants of amorphous silicon". In: *Journal of Physics E: Sci. Instrum.* 16 (1983), p. 1214. DOI: 10.1080/14786430902835644.

[65] Abdelaziz Tchenka, Abdelali Agdad, and Elmaati Ech-Chamikh. "Determination of the thickness and optical properties by reflectance method". In: *Infrared Physics and Technology* 137.September 2023 (2024). DOI: 10.1016/j.infrared.2024.105117.

[67] Jiři Luňáček, Petr Hlubina, and Milena Luňáčková. "Simple method for determination of the thickness of a nonabsorbing thin film using spectral reflectance measurement". In: *Applied Optics* 48.5 (2009), pp. 985–989. DOI: 10.1364/AO.48.000985.

[68] Jingtao Dong and Rongsheng Lu. "Characterization of weakly absorbing thin films by multiple linear regression analysis of absolute unwrapped phase in angle-resolved spectral reflectometry". In: *Opt. Express* 26.9 (2018), pp. 12291–12305. DOI: 10.1364/OE.26.012291.

[69] Kwangrak Kim, Soonyang Kwon, and Heui Jae Pahk. "Fast analysis of film thickness in spectroscopic reflectometry using direct phase extraction". In: *Current Optics and Photonics* 1.1 (2017), pp. 29–33. DOI: 10.3807/COPP.2017.1.1.029.

[77] Jörg Rappich et al. "Fast Optical Reflectance Measurements during Spin Coating and Annealing of Organic–Inorganic Perovskite Precursor Solutions". In: *Physica Status Solidi (B) Basic Research* 258.5 (2021), pp. 1–8. DOI: 10.1002/pssb.202000479.

[80] Nina Taherimakhsousi et al. “A machine vision tool for facilitating the optimization of large-area perovskite photovoltaics”. In: *npj Computational Materials* 7.1 (2021). DOI: 10.1038/s41524-021-00657-8.

[93] Daniel T.W. Toolan, Richard Hodgkinson, and Jonathan R. Howse. “Stroboscopic microscopy - Direct imaging of structure development and phase separation during spin-coating”. In: *Journal of Polymer Science, Part B: Polymer Physics* 52.1 (2014), pp. 17–25. DOI: 10.1002/polb.23410.

[96] Yoshie Kobayashi et al. “Reconstructing Shapes and Appearances of Thin Film Objects Using RGB Images”. In: *Proceedings of the IEEE Computer Society Conference on Computer Vision and Pattern Recognition* 2016-Decem (2016), pp. 3774–3782. DOI: 10.1109/CVPR.2016.410.

[100] Garam Choi et al. “Simple method for volumetric thickness measurement using a color camera”. In: *Applied Optics* 57.26 (2018), p. 7550. DOI: 10.1364/ao.57.007550.

[103] V. Chandran Suja et al. “Hyperspectral imaging for dynamic thin film interferometry”. In: *Scientific Reports* 10.1 (2020), pp. 1–8. DOI: 10.1038/s41598-020-68433-0.

[105] Olesya Daikos et al. “Near-infrared hyperspectral imaging for monitoring the thickness distribution of thin poly(3,4-ethylenedioxythiophene):poly(styrene sulfonate) (PEDOT:PSS) layers”. In: *Talanta* 223.1 (2021), p. 121696. DOI: 10.1016/j.talanta.2020.121696.

[106] Gilbert El-Hajje et al. “Quantification of spatial inhomogeneity in perovskite solar cells by hyperspectral luminescence imaging”. In: *Energy and Environmental Science* 9.7 (2016), pp. 2286–2294. DOI: 10.1039/c6ee00462h.

[111] Ville Heikkinen et al. “Evaluation and unification of some methods for estimating reflectance spectra from RGB images”. In: *Journal of the Optical Society of America A* 25.10 (2008), p. 2444. DOI: 10.1364/josaa.25.002444.

[112] Noriyuki Shimano. “Recovery of spectral reflectances of objects being imaged without prior knowledge”. In: *IEEE Transactions on Image Processing* 15.7 (2006), pp. 1848–1856. DOI: 10.1109/TIP.2006.877069.

[113] Filiz Yesilkoy et al. "Ultrasensitive hyperspectral imaging and biodetection enabled by dielectric metasurfaces". In: *Nature Photonics* 13.6 (2019), pp. 390–396. DOI: 10.1038/s41566-019-0394-6.

[139] Katsuichi Kitagawa. "Single-shot surface profiling by multiwavelength interferometry without carrier fringe introduction". In: *Journal of Electronic Imaging* 21.2 (2012), p. 021107. DOI: 10.1117/1.jei.21.2.021107.

[140] P. Hlubina et al. "Spectral interferometry and reflectometry used to measure thin films". In: *Applied Physics B: Lasers and Optics* 92.2 (2008), pp. 203–207. DOI: 10.1007/s00340-008-3093-4.

[141] Jungjae Park et al. "A Review of Thickness Measurements of Thick Transparent Layers Using Optical Interferometry". In: *International Journal of Precision Engineering and Manufacturing* 20.3 (2019), pp. 463–477. DOI: 10.1007/s12541-019-00105-0.

[142] Xingchen Dong et al. "Line-Scan Hyperspectral Imaging Microscopy with Linear Unmixing for Automated Two-Dimensional Crystals Identification". In: *ACS Photonics* 7.5 (2020), pp. 1216–1225. DOI: 10.1021/acsphotonics.0c00050.

[143] Prabuddha Mukherjee et al. "Relating Post-yield Mechanical Behavior in Polyethylenes to Spatially Varying Molecular Deformation Using Infrared Spectroscopic Imaging: Homopolymers". In: *Macromolecules* 51.10 (2018), pp. 3836–3844. DOI: 10.1021/acs.macromol.8b00363.

[144] Meguya Ryu et al. "Hyperspectral molecular orientation mapping in metamaterials". In: *Applied Sciences (Switzerland)* 11.4 (2021), pp. 1–13. DOI: 10.3390/app11041544.

[145] Dominic Lepage et al. "Conic hyperspectral dispersion mapping applied to semiconductor plasmonics". In: *Light: Science and Applications* 1.SEPTEMBER (2012), pp. 1–8. DOI: 10.1038/lsa.2012.28.

[146] Changhyeong Yoon et al. "Toward realization of high-throughput hyperspectral imaging technique for semiconductor device metrology". In: *Journal of Micro/Nanopatterning, Materials and Metrology* 21.2 (2022), pp. 1–13. DOI: 10.1117/1.JMM.21.2.021209.

[147] Susanne Dogan-surmeier et al. "Towards in-line real-time characterization of roll-to-roll produced ZTO/Ag/ITO thin films by hyperspectral imaging". In: *J. Phys. D: Appl. Phys* 56 (2023).

[148] Jonas Skovlund Madsen et al. "In-line characterization of nanostructures produced by roll-to-roll nanoimprinting". In: *Optics Express* 29.3 (2021), p. 3882. DOI: 10.1364/oe.411669.

[149] Jingang Zhang et al. "A survey on computational spectral reconstruction methods from RGB to hyperspectral imaging". In: *Scientific Reports* 12.1 (2022), pp. 1–17. DOI: 10.1038/s41598-022-16223-1. arXiv: 2106.15944.

[150] Noriyuki Shimano, Kenichiro Terai, and Mikiya Hironaga. "Recovery of spectral reflectances of objects being imaged by multispectral cameras". In: *Journal of the Optical Society of America A* 24.10 (2007), p. 3211. DOI: 10.1364/josaa.24.003211.

[151] Noriyuki Shimano and Mikiya Hironaga. "Recovery of spectral reflectances of imaged objects by the use of features of spectral reflectances". In: *Journal of the Optical Society of America A* 27.2 (2010), p. 251. DOI: 10.1364/josaa.27.000251.

[152] D. E. Aspnes and A. A. Studna. "Dielectric functions and optical parameters of Si, Ge, GaP, GaAs, GaSb, InP, InAs, and InSb from 1.5 to 6.0 eV". In: *Phys. Rev. B* 27 (2 Jan. 1983), pp. 985–1009. DOI: 10.1103/PhysRevB.27.985.

[153] Xiaoning Zhang et al. "Complex refractive indices measurements of polymers in visible and near-infrared bands". In: *Appl. Opt.* 59.8 (Mar. 2020), pp. 2337–2344. DOI: 10.1364/AO.383831.

[154] Krishnamurthi Ramesh, Vivek Ramakrishnan, and C. Ramya. "New initiatives in single-colour image-based fringe order estimation in digital photoelasticity". In: *Journal of Strain Analysis for Engineering Design* 50.7 (2015), pp. 488–504. DOI: 10.1177/0309324715600044.

Chapter 5

Trichromatic Reflectance Imaging of Blade Coating

This chapter is planned to be submitted for publication after thesis submission, due to this, the nomenclature is defined as it is introduced in the chapter. It is mostly consistent with that used in previous chapters. The only supplementary information in the paper is the videos, whose urls are included at the end of the chapter. Reference numbers will be different from what appears in the published paper to keep references in the thesis unique and consistent.

This chapter builds on the previous chapters' reflectance imaging by altering the illumination source. Instead of LED illumination used in the previous two chapters, a combination of red, green and blue lasers are used. This altogether changes what the reflectance images now represent. They are no longer colours, i.e. summations of many wide (Chapter 3) or medium (Chapter 4) linewidths. The RGB channels now represent single-wavelength snapshots of the scene. This allows for a completely different approach, and culminates in the development of an entirely new metrology technique.

5.1 Abstract

thin films are crucial components of optical and electronic devices due to their unique properties arising from their thickness and morphology. Solution-processed dielectrics offer scalable fabrication but often lack precision in controlling film thickness and final morphology is often formed without elucidating a mechanism, bottlenecking rational development. To address this, *in situ* methods providing spatially resolved film formation insights, via direct imaging, are a focus of the field. Here we present an *in situ* reflectance-based optical metrology technique for monitoring films formed via evaporation. Using monochromatic RGB (trichromatic) illumination and a standard Bayer filter colour camera, the developed colour peak sequencing approach reconstructs film thickness across a wide range. Unlike traditional monochromatic reflectance methods, this technique eliminates the need for costly and time-consuming ex-situ measurements. A model system of blade-coated polystyrene/butyl acetate solution on silicon demonstrates thickness reconstructions from 21 µm wet film to a dry film below 1 µm. This method offers a cost-effective and time-efficient alternative for monitoring thin film formation with broad applicability across various fabrication techniques. By providing time-resolved insights, it facilitates rational thin film development and scale-up.

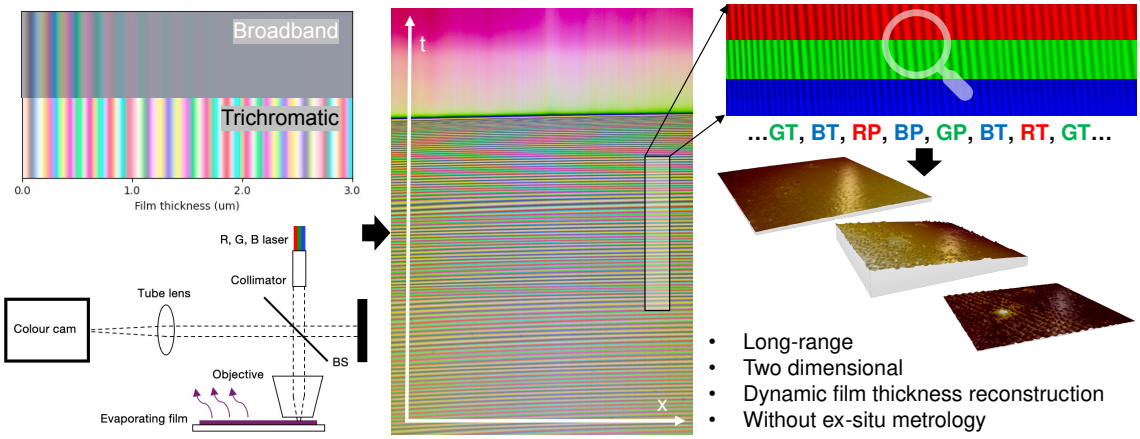

Figure 5.1: Graphical abstract

5.1.1 Keywords

thin film, blade-coating, optical metrology, interferometry, reflectance imaging, DNA sequencing

5.2 Introduction

Solution-processed thin films play a critical role in a wide array of modern devices and applications due to their remarkable optical and electronic properties. These films are fabricated using a variety of techniques, ranging from smaller-scale batch processes, such as dip coating, blade coating, or spin coating, to more scalable industrial methods like gravure printing and slot die coating. The latter methods are compatible with continuous roll-to-roll (R2R) processing, making them suitable for larger-scale production.

The choice of fabrication method and the conditions under which it is applied directly influence the film's thickness and morphology, the structural and surface characteristics at both the micro and nanoscopic level, which in turn determine its final properties and performance. During all the mentioned fabrication processes, a wet film of the solution is deposited, which subsequently thins as the solvent evaporates, leaving behind a solid, dry film. This transformation process is central to understanding and optimizing the film's formation and subsequent properties.

The ability to characterize these films effectively during both the formation and in the final state is significant. Metrology techniques that can provide detailed information over large areas are essential for the development of new inks, optimization of processing conditions, and the successful scaling up of fabrication methods. Moreover, *in situ* metrology that captures real-time data during film formation is invaluable. Such techniques enable a deeper understanding of how processing conditions influence film morphology and properties, thereby facilitating an informed and targeted approach to the improvement of the process conditions and routes.

A plethora of noncontact and non-destructive techniques exist that are suitable to be used *in situ* with solution processed thin films, to provide information at a single point. Optical methods are readily implemented and include spectroscopy [128], ellipsometry [155] [156] specular laser reflection [13] [51] [50] [44] and laser scattering [50] [53] while x-ray techniques such as wide-angle x-ray scattering [129] and grazing incidence x-ray diffraction [157] often require more specialised setups due to the practical barriers imposed by the high intensities required needed for sufficient temporal resolution, typically only available at synchrotron sources. Each of these techniques gives subtly different information about the structure and morphology development, however, many are confined to single spots

and are thus surface and time averaged data from the probe point.

Specular reflectance-based methods offer a promising advantage because they are more readily applied to direct imaging of 2D areas to reveal morphological information. This is simply achieved by replacing the area photodiode with a digital camera sensor. With monochromatic or near monochromatic illumination interference peaks can be resolved for optical path difference (OPD) changes revealing surface topology and morphology [78] [89] [94] [91] [86]. Other studies have shown that Bayer filtered colour cameras can be leveraged with reflected broadband illumination to reconstruct thickness close to the drying point [15] [100] [1]. This type of approach greatly extends the feasible area monitored and greatly reduces the cost associated with large-area laser illumination, however, challenges are encountered due to the cyclical nature of the colour changes.

Reported monochromatic reflectance (and transmission, although this is lesser utilised due to its weak signal) techniques suffer with peak order ambiguity. The rate of OPD change can be deduced between peaks and troughs of constructive and destructive interference, however, an unambiguous optical path cannot be determined without additional information, this is explained in detail in Section 5.3. In practice, this means that for a solution processed film, the final film must still be measured with ex-situ tools such as AFM [89], interferometry or mapping spectroscopy/ellipsometry for complete characterisation. This can often be time consuming due to the scanning of point measurements, or expensive, and often both.

In this paper we present a three wavelength "trichromatic" reflectance microscopy technique that utilises time-variant colour interference patterns. When decomposed, into sequences of red, green and blue peaks and troughs, these patterns allow us to clearly characterise the film thickness over large vertical ranges and with high lateral resolution. This technique demonstrates both final film thickness determination without ex-situ measurement and reconstruction of the wet film surface changes during the process, prior to final film vitrification. An evaporating film from a blade coated polystyrene solution is used as a model system.

The approach requires a monotonic optical path difference to be present to work. This can either be with a thickness decrease across an images FOV, or as demonstrated here, thinning through time for a pixel.

This is a novel approach to utilising three wavelengths for film thickness recovery, that

differs drastically from other proposed three-wavelength methods such as from Kitagawa (2012) [139] that estimates thickness using global fitting and Picart et al. (2015) [158] that uses calibrated intensities. Our proposed method does not need any global fitting, does not assume the target area is homogenous and does not require calibration. This positions it as a flexible and robust way to reconstruct thicknesses, more suitable for use in environments where parameters such as intensity and film refractive index may drift, such as continuous coating lines.

5.3 Theory

A thin film system forms an amplitude splitting interferometer when reflecting incident monochromatic light. The 'reference' beam is the portion of the beam that propagates through the film and reflects from the stationary film-substrate interface, and the 'object' beam is the portion of light that reflects from the top surface of the film at the air-film interface. The exact proportions of these are determined by the Fresnel coefficients, dependent on the refractive indices of the mediums, the angle of incidence and the polarisation state of the light. In the case of a solution processed film, the air-film interface is usually moving towards the substrate as the film thins via evaporation. This causes a modulation in the intensity of the superimposed reflected wavefronts as sequential constructive and destructive interference occurs at an optical path difference of a whole Δ_p and whole plus one-half Δ_t wavelength, respectively. Thus, examination of the intensity of the reflected signal reveals the thinning rate of the film. Equation 5.1 and 5.2 show this condition for peaks (maximum intensity) and troughs (minimum intensity) respectively, where n_1 is the refractive index of the film, d_1 is the thickness of the film, θ_r is the angle of refraction (i.e. the angle of propagation inside the film), λ is the wavelength of light, and m is the order of the fringe[1].

$$\Delta_p = 2n_1 d_1 \cos(\theta_r) = m\lambda \tag{5.1}$$

$$\Delta_t = 2n_1 d_1 \cos(\theta_r) = (m + \frac{1}{2})\lambda \tag{5.2}$$

[1]Equation 1 is sometimes referred to as the Bragg condition for thin film interference due to similarities between this and Bragg's law that describes behaviour of x-rays reflecting from sequential layers of crystal lattices

A thinning of $\Delta_\lambda = \frac{\lambda}{2n_1 \cos(\theta_r)}$ occurs between two sequential peaks or troughs, m and $m+1$, for a single wavelength.

Using the non-absorbing isotropic model of a dielectric thin film at normal incidence, as presented in Equation 5.3, the expected reflected signal intensity of an incident monochromatic laser source can be modelled as a function of thickness. Here, n_0 gives the substrate refractive index and n_2 gives the ambient refractive index ($n_2 = 1$ for air throughout). The optical path difference is given as δ in Equation 5.4 and does not contain the cosine function as normal incidence is modelled[2]. Likewise, the Fresnel coefficients shown by Equations 5.5 and 5.6 are not polarisation state dependent, also due to normal incidence. Reflectance, the ratio of reflected to incident illumination intensity, R, is plotted in Figure 5.2a as a function of film thickness d_1, for wavelengths of 447 nm, 533 nm, and 619 nm for blue, green, and red light, respectively. The shorter wavelengths modulate from peak to peak more quickly producing a higher frequency signal because a smaller change in the optical path difference causes consecutive constructive and destructive interference. The positions where Equation 5.1 is resolved at the signal peaks are indicated by vertical lines.

$$R = \frac{r_{10}^2 + r_{21}^2 + 2r_{10}r_{21}\cos(2\delta)}{1 + r_{10}^2 r_{21}^2 + 2r_{10}r_{21}\cos(2\delta)} \tag{5.3}$$

$$\delta = \frac{2\pi n_1 d_1}{\lambda} \tag{5.4}$$

$$r_{01} = \frac{n_0 - n_1}{n_0 + n_1} \tag{5.5}$$

$$r_{21} = \frac{n_1 - n_2}{n_1 + n_2} \tag{5.6}$$

The peaks and troughs in R, resolved by Equations 1 and 2, also can be identified by differentiating the expression for R in Equation 3 with respect to d_1 and equating it to zero. This results in Equation 7, which has roots for film thickness; $d_1 = \frac{(2\pi n_1 + \pi)\lambda}{2\pi n_1}$.

$$\frac{dR}{dd_1} = -\frac{8\pi n_1 r_{10} r_{21}(r_{10}^2 - 1)(r_{21}^2 - 1)\sin(2\delta)}{\lambda(1 + r_{10}^2 r_{21}^2 + 2r_{10}r_{21}\cos(2\delta))^2} = 0 \tag{5.7}$$

[2]A note on nomenclature; the optical path difference δ has been used where any continuous value can be taken, whereas Δ_p and Δ_t, introduced earlier in Equations 5.1 and 5.2, is specific to resolving a peak or trough respectively

If both n_1 and d_1 are then considered a monotonic function of t (here an arbitrary quadratic and cubic are chosen), as shown in Figure 5.2b, the result is a change in a lateral distortion of data in Figure 5.2a due to the way time and optical thicknesses are mapped. However, and most crucially, the sequential order of the peaks and troughs remains the same and is dependent only on the relative magnitudes of the illumination wavelengths. It follows that the peak and trough sequence, or more specifically a short sequence, of the red, green, and blue wavelength signals, can be used as a 'fingerprint' to unambiguously identify the position of the film in its drying evolution, provided that n_1 and d_1 are both monotonic in t.

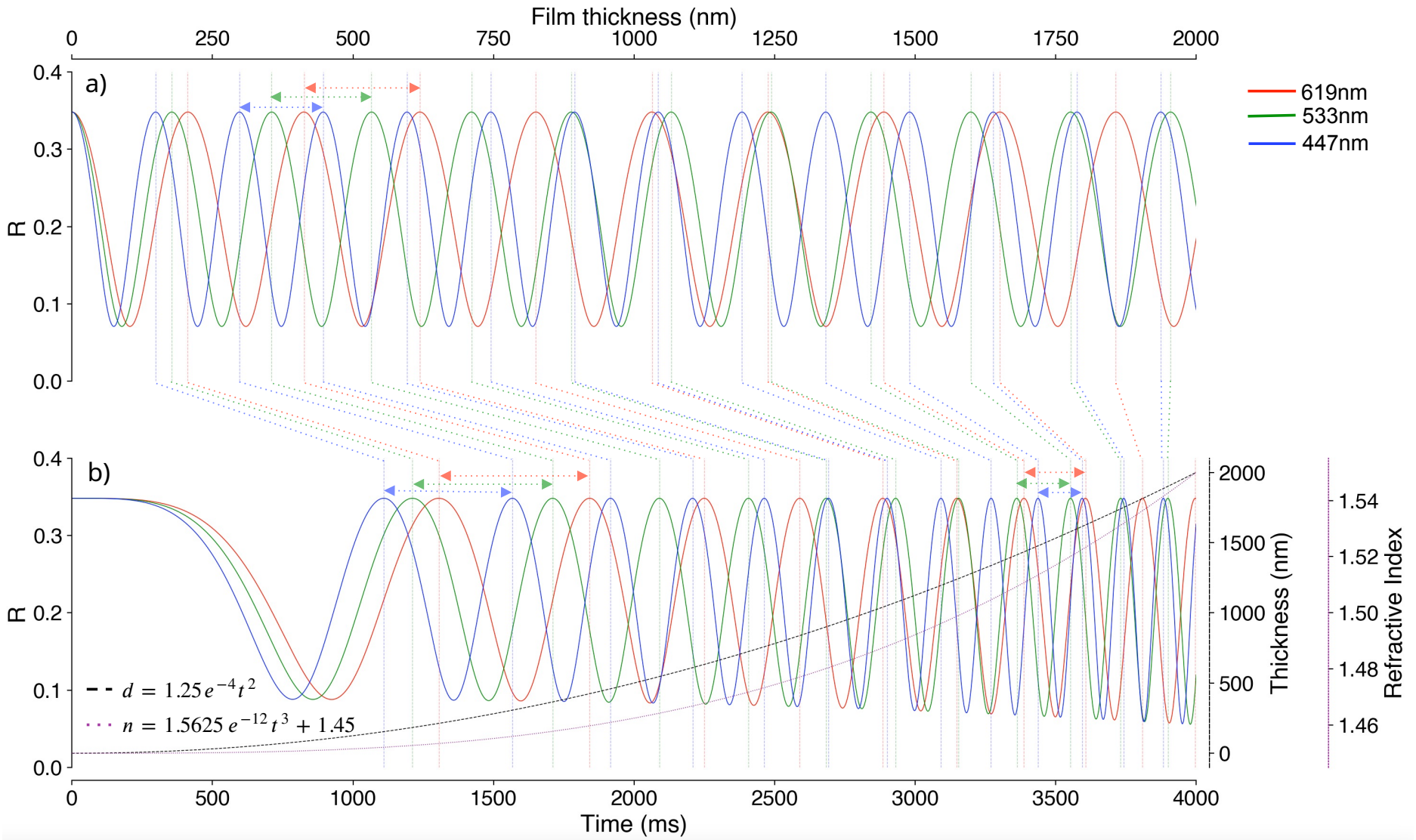

Figure 5.2: a) Simulation R values shown as a function of thickness, for $n_1 = 1.5$ and $n_0 = 3.88$ (silicon) (b) Simulation of R values as a function of time, in a signal where both n_1 and d are arbitrary monotonic functions of t. The peaks have been joined between graphs to demonstrate that the peak (and trough) order is not affected. The arrows between peaks on both graphs show points between which a change in thickness of Δd_λ takes place.

For the wavelengths used here, the peak and trough sequence, illustrated schematically in Figure 5.3, is:

$$\begin{aligned}&\mathrm{RP}_0, \mathrm{GP}_0, \mathrm{BP}_0, \mathrm{BT}_0, \mathrm{GT}_0, \mathrm{RT}_0, \mathrm{BP}_1, \mathrm{GP}_1, \mathrm{BT}_1, \mathrm{RP}_1, \mathrm{GT}_1, \mathrm{BP}_2, \mathrm{RT}_1, \mathrm{BT}_2,\\ &\mathrm{GP}_2, \mathrm{BP}_3, \mathrm{RP}_2, \mathrm{GT}_2, \mathrm{BT}_3, \mathrm{GP}_3, \mathrm{RT}_2, \mathrm{BP}_4, \mathrm{GT}_3, \mathrm{BT}_4, \mathrm{RP}_3, \mathrm{BP}_5, \mathrm{GP}_4, \mathrm{BT}_5,\\ &\mathrm{RT}_3, \mathrm{GT}_4, \mathrm{BP}_6, \mathrm{RP}_4, \mathrm{GP}_5, \mathrm{BT}_6, \mathrm{BP}_7, \mathrm{GT}_5, \mathrm{RT}_4, \mathrm{BT}_7, \mathrm{GP}_6, \mathrm{RP}_5, \mathrm{BP}_8, \mathrm{GT}_6,\\ &\mathrm{BT}_8, \mathrm{RT}_5, \mathrm{GP}_7, \mathrm{BP}_9, \mathrm{RP}_6 \ldots\end{aligned}$$

where R, G, and B indicate 447 nm, 533 nm, 619 nm wavelengths of light, the suffix P or T denotes a peak or a trough, and the subscript shows the fringe order, m. This sequence, subsequently referred to as the reference sequence, is ultimately determined by the relationship of the magnitudes of the wavelengths used.

Figure 5.3: A schematic depiction of the reference sequence formed by the laser wavelengths used in the study

It is important to note that due to the monochromatic nature of the illumination the approach is in theory valid for all film thicknesses up to many millimetres, although focus issues, depths of field of the objectives, and dispersion would hinder this. Ignoring these factors, the peak sequence is non-recurrent until the lowest common multiple of the illumination wavelengths divided by two times the refractive index is met, this is shown in Equation 5.8.

$$d_{max} = \frac{LCM(\lambda_R, \lambda_G, \lambda_B)}{2n_1} \tag{5.8}$$

At an approximation of $n_1 = 1.5$ this gives the maximum theoretical resolvable thickness to be 52.6 mm, upon which thickness is reached the colour sequence begins to repeat in a way that is indistinguishable from 0 nm (ignoring absorption).

In the reference sequences used in this chapter, the wavelength dependence is further modelled for more accurate recovery, especially as dispersion effects become more prominent at higher thicknesses and are likely to change peak orders. The silicon substrate [152]

contributes more to this effect than the polymer solution, which is generally less dispersive, but has still been modelled based on wavelength-dependent literature values of complex refractive indices and volume fractions. Silicon was chosen as a substrate because it is commercially relevant in many coating processes, it has high reflectance, and the high refractive index difference with dielectric films maximises fringe visibility.

This effect of extending the range is displayed in Figure 5.4 that shows the interference colour sequence for increasing film thicknesses, using trichromatic illumination (Figure 5.4a) and comparing it to broadband illumination/detection as typical in colour camera Bayer filters (Figure 5.4b). The non-recurrent nature of these colours in trichromatic illumination is shown in Figure 5.4c. Whilst there appears to be some repeat nature to this sequence, (showing 16 repeats over 20 µm) the detailed peak and trough sequence is unique when examined at detail. Figure 5.4 and Figure 5.5 were produced using the transfer matrix method (TMM) implemented into Python by Byrnes [73] assuming infinitely thick ambient and substrate mediums and accounting for material dispersion.

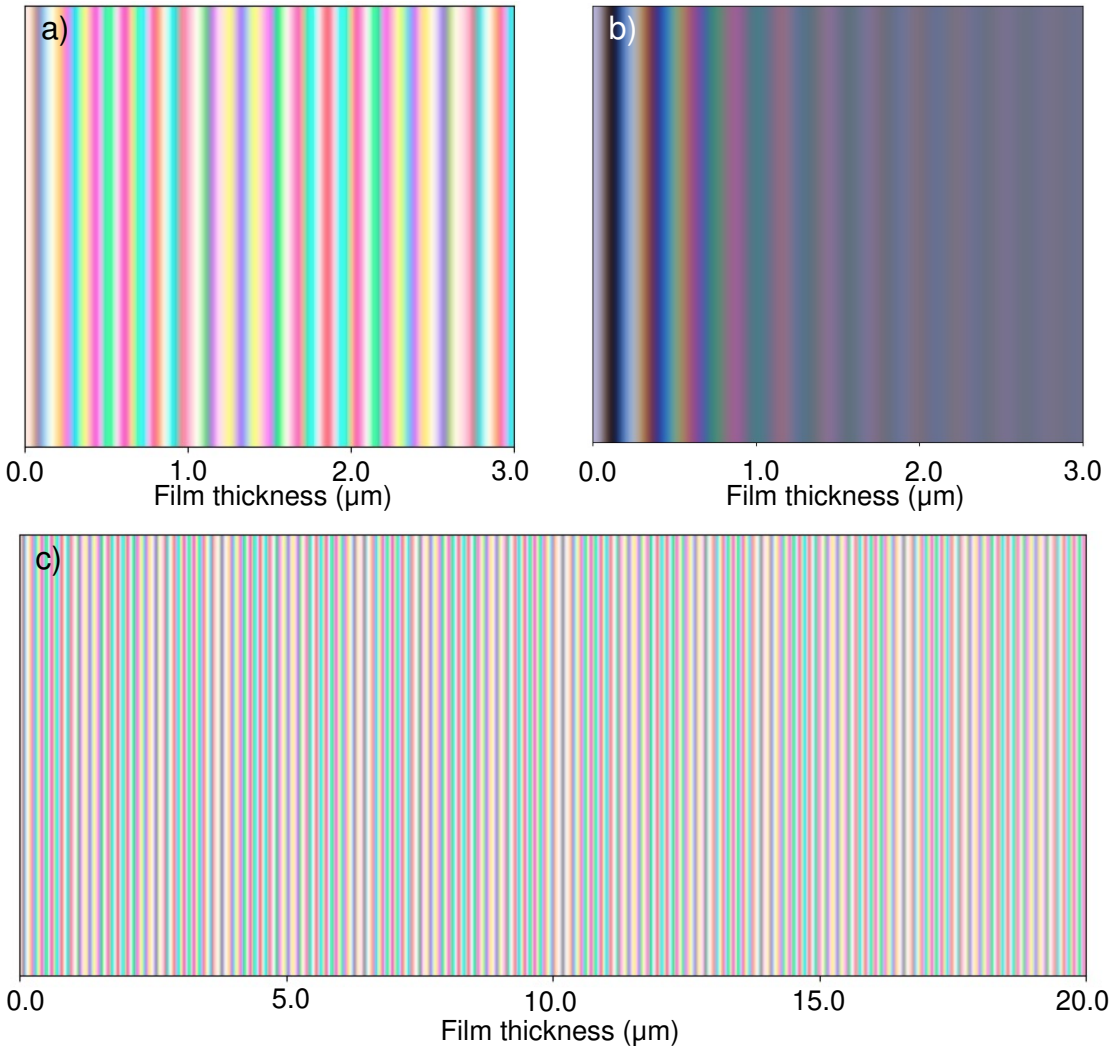

Figure 5.4: a) Apparent interference colour as a function of thickness for n_1=1.5 on Si a) under laser illumination used here and b) LED broadband illumination and Bayer filter combination used in Chapter 3 and 4 c) the same representation as (a) with a larger thickness domain showing minimal weakening of the signal as thickness increases.

The uniqueness of this sequence approach can be seen by considering the peaks and troughs of a thin film displayed in a ternary diagram of RGB chromaticity colour space, denoted R*, G*, B*, as shown in Figure 5.5. The values of R*, G*, B* for a drying film (3 µm to 0 µm) under similar illumination for Figure 5.4b (used in Chapter 3), are shown in Figure 5.5a. As the film dries, the RGB values remain disparate, mapping out a path within a large R*G*B* space. However, for film thicknesses greater than around 2 µm, all thicknesses occupy the central region, preventing an RGB value from being directly mapped to a thickness. Additionally, as the film evolves, the data drying line crosses paths, indicating identical RGB for two different thicknesses, further hindering identification.

In comparison, Figure 5.5b shows the same film thinning using trichromatic illumina-

tion. Notice that the data remains disparate and does not converge on a point, sweeping out a large area of RGB space. Whilst the data still does overlap, the use of a sequence allows for unambiguous determination of the film drying by considering larger sections of the thickness domain and not just point values.

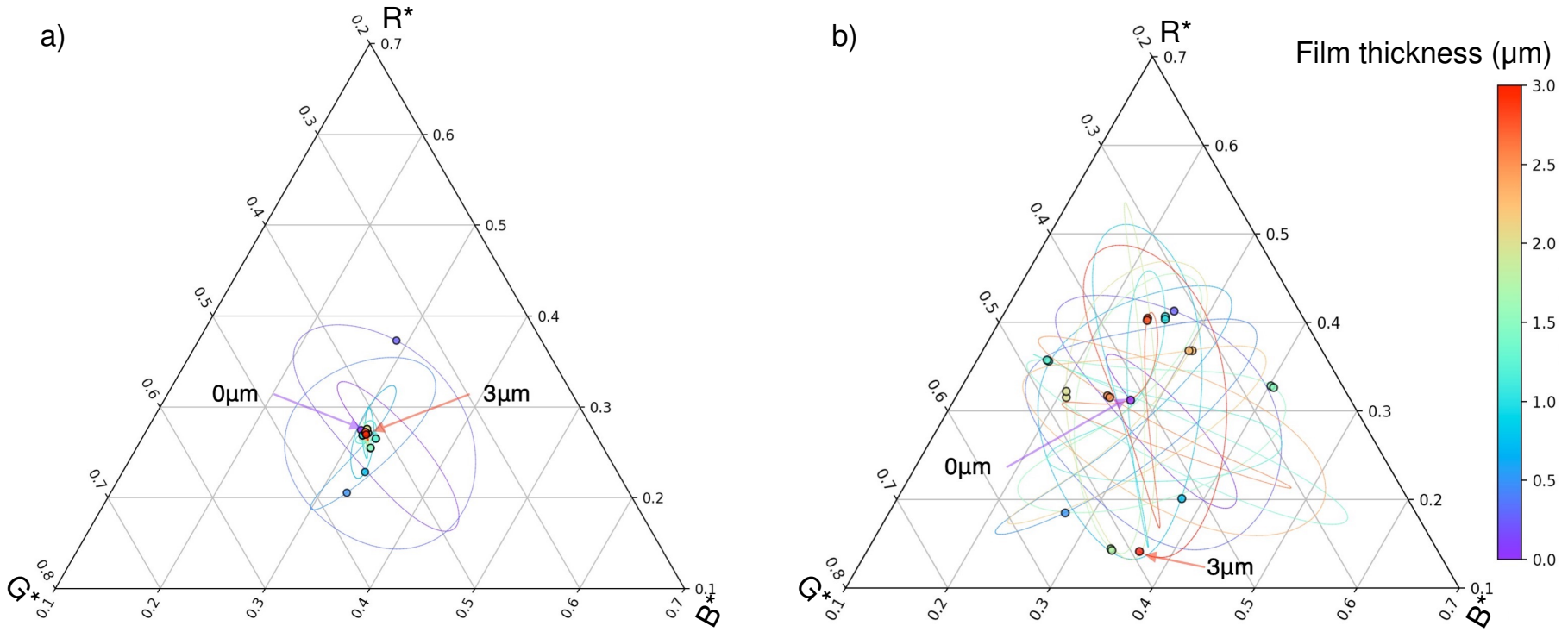

Figure 5.5: Chromaticity of the film interference, as detected by the Sony IMX235 (Bayer filtered) sensor used in this study under (a) D56 broadband illumination and (b) the laser illumination used in this study, plotted on a ternary plot with markers every 250 nm from 0 µm - 3 µm, the zero positions differ slightly due to the variation of signal strengths between the two illuminations.

If the refractive index is known, or can be reasonably estimated, the thickness at any peak or trough is then recoverable. Due to the optical path differences' dependence on both n_1 and d_1, it is not expected that unambiguous recovery of both variables at once is possible. Either n_1 or d_1 may be recovered by assuming an appropriate value of the other at all points in time. This manuscript will aim to recover d_1 by assuming that n_1 varies linearly between the refractive index of the solution n_{sol} and of the solute n_{film} between the maximum and minimum resolved times, t_{dry} and t_0 respectively, as shown in Equation 5.9.

$$n_1(t,\lambda) = \left(\frac{n_{sol}(\lambda) - n_{film}(\lambda)}{t_0(\lambda) - t_{dry}(\lambda)}\right) t + n_{sol}(\lambda) \tag{5.9}$$

5.4 Materials and methods

5.4.1 Imaging setup

A laser-pumped white light source (Laser Components Ltd, LS-WL1) was used to generate three RGB wavelengths filtered by the acousto-optic tuneable filter (AOTF)[3]. The resulting filtered RGB illumination information is given in Table 5.1 and is coupled into a multi-mode fibre connected to a doublet collimator (Thorlabs, F810SMA-635). This focuses the collimated beam through a 50:50 beamsplitter (Thorlabs, CCM1-BS013/M) and into a 5x/0.15 long working distance objective lens (Nikon, MUE12050). Imaging is achieved by reflection from the sample back through the objective and beamsplitter and is focused by an achromatic tube lens (Thorlabs, AC254-200-A-ML) onto a CMOS camera sensor (Pixelink, PLX-9512) capturing at 15 fps with a field of view of 800 pixels x 600 pixels or 550 µm x 412.5 µm. The camera sensor has a linear response, and the gain is switched off (set to 1). A schematic diagram of the experiment is shown in Figure 5. Note, there is a trade-off between requirements for high frame rate, the need for narrow linewidth (nm) illumination, and the weak signal intensity provided through the beamsplitter.

Table 5.1: Characteristics of the illumination used

	Red	Green	Blue
Nominal (nm)	618.8	532.6	447.7
FWHM (nm)	1.4	1.1	0.6

[3]This resulted in non-monochromatic (large linewidth) lasers that are non-ideal for the application. Three single mode lasers are preferable, however, could not be obtained at the time of the experiment

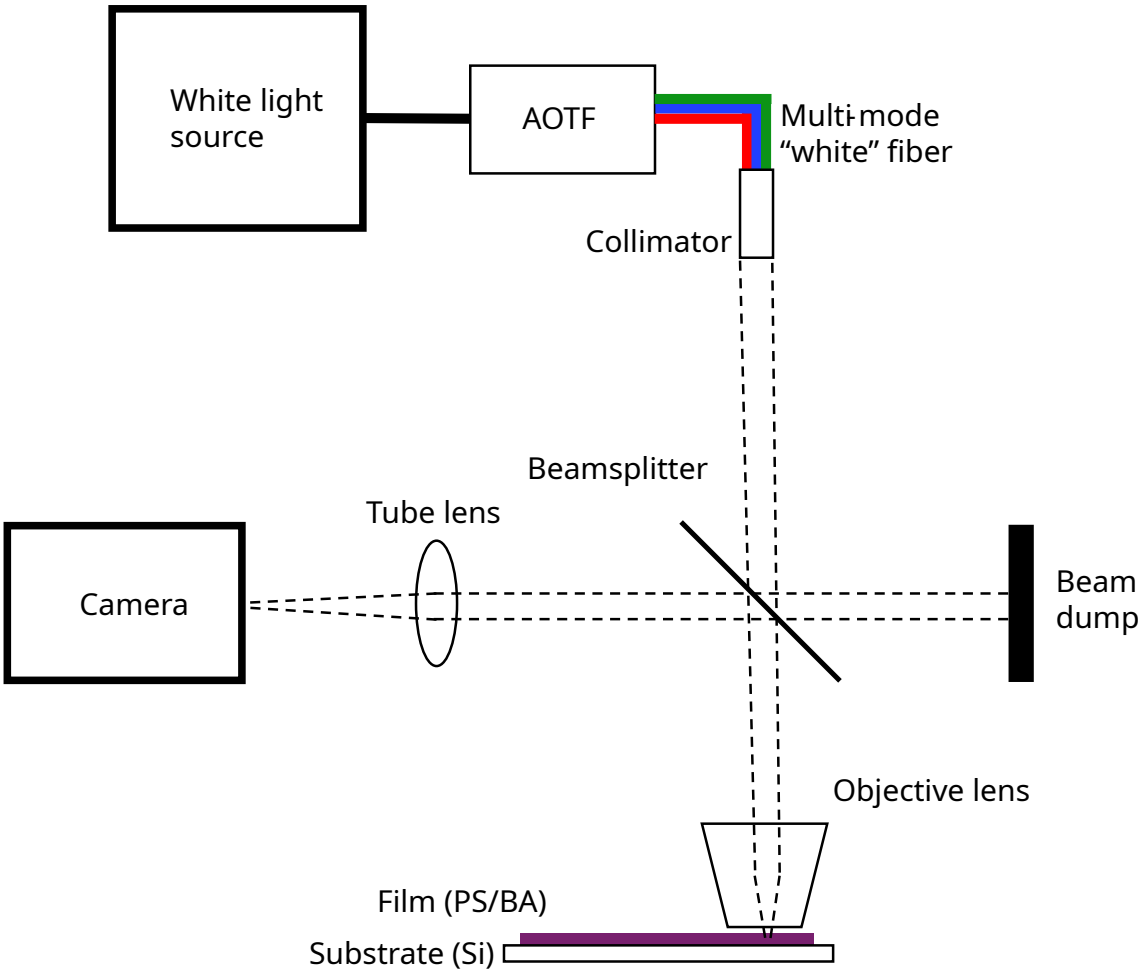

Figure 5.6: A schematic of the optical and electronic setup used to acquire *in situ* trichromatic laser reflectance imaging

5.4.2 Coating method

The solution was prepared by dissolving 2.7 wt% 300 k polystyrene (PS) in butyl acetate (BA) and stirring until complete dissolution of the polystyrene beads was observed. The substrate was a 30 mm x 30 mm piece of silicon, prepared by washing with an isopropyl alcohol-soaked lens tissue. A micropipette was used to deposit 125 µL of solution onto one end of the silicon. Then, a clean microscope slide with 60 µm spacers at each end (tape) was drawn across the droplet with even downwards pressure so that a relatively uniform wet fluid film was formed. The substrate was then quickly positioned underneath the pre-focused optical setup and the video recording was started. The coating direction in the video is from left to right.

5.4.3 Crosstalk correction

The PixeLink PL-X9512 camera used contains a Sony IMX235 sensor with a Bayer filter. The Bayer filter is designed to separate the incident white light into discrete red, green and blue signals. However, there is a degree of overlap between each colour, meaning that, for example, the green channel will also be sensitive to blue light and red light. Each image should therefore be corrected to remove this colour channel crosstalk before further processing to ensure that the red, green and blue camera channels only give representative reflectance intensities for the respective laser wavelengths. Figure 5.7 demonstrates how the Bayer filter in the camera results in crosstalk due to the spectral sensitivity overlap of the colour channels and the illumination wavelengths.

To correct the crosstalk, a correction matrix is generated by assuming that each of the observed intensity R', G' and B' at a pixel, is the sum of the weighted pure channel intensities R, G and B where the weights are cross talk coefficients [159] [160] [161], as in Equation 5.10.

$$\begin{bmatrix} R' \\ G' \\ B' \end{bmatrix} = \begin{bmatrix} 1 & c_{rg} & c_{rb} \\ c_{gr} & 1 & c_{gb} \\ c_{br} & c_{bg} & 1 \end{bmatrix} \begin{bmatrix} R \\ G \\ B \end{bmatrix} \tag{5.10}$$

These coefficients can then be found by illuminating a white target by each wavelength individually and solving. For example, under red laser illumination, $B = G = 0$ and $R' = R$; the coefficients c_{gr} and c_{br}, representing the crosstalk of green in the red channel and blue in the red channel respectively, are recovered by Equation 5.11. Here, the monochromatically illuminated images were taken as the mean of 20 images to reduce the effect of random noise.

$$\begin{bmatrix} \frac{R'}{R} \\ \frac{G'}{R} \\ \frac{B'}{R} \end{bmatrix} = \begin{bmatrix} 1 \\ c_{gr} \\ c_{br} \end{bmatrix} \tag{5.11}$$

After the coefficients populating this matrix are determined, each raw $[R' \ G' \ B']$ pixel value in a colour image can be corrected simply by matrix multiplication of the Moore–Penrose inverse (pseudoinverse) of the coefficient matrix, as shown in Equation

5.12. Examples of images before and after the correction are shown in Figure 5.8 (see Section 5.5.1).

$$\begin{bmatrix} R' \\ G' \\ B' \end{bmatrix} \begin{bmatrix} 1 & c_{rg} & c_{rb} \\ c_{gr} & 1 & c_{gb} \\ c_{br} & c_{bg} & 1 \end{bmatrix}^{+} = \begin{bmatrix} R \\ G \\ B \end{bmatrix} \tag{5.12}$$

This is a facile method to ensure that the red, green, and blue panes of the images taken represent the reflectance levels of only the red, green, and blue lasers respectively. As such, the RGB channels can be considered monochromatic images at 619, 533, and 447 nm. For the specific camera and laser settings used here, the coefficient matrix is shown in Equation 5.13. The images used here were of a bare silicon wafer to account for any dispersion in the silicon reflectance, which is the main source of dispersion in the system. This technique cannot be used to account for the dispersion of the film system itself, which will introduce some error to this crosstalk correction approach.

$$\begin{bmatrix} 1 & c_{rg} & c_{rb} \\ c_{gr} & 1 & c_{gb} \\ c_{br} & c_{bg} & 1 \end{bmatrix} = \begin{bmatrix} 1 & 0.198 & 0.045 \\ 0.290 & 1 & 0.070 \\ 0.129 & 0.479 & 1 \end{bmatrix} \tag{5.13}$$

5.4.4 Sequence matching procedure

To carry out the sequence matching, a modified version of the Waterman-Smith algorithm [162] has been adopted from the field of molecular biology. Originally this was developed to robustly match DNA sequences on a mathematically rigorous basis, even when mismatches and deletions are present. Once the strings are changed from ***A, C, G*** and ***T*** to ***RP, RT, BP, BT, GP*** and ***GT***, it serves to match the sequence extracted from pixel colour values through time to the reference sequence, while retaining robustness to noise that may cause switches or unidentified peaks in the sequence, analogous to mismatches, insertions and deletions present in DNA sequencing. The algorithm seeks a match by maximising the score at each possible position between a reference and query sequence, assigning +2 for an element match, -1 for an element mismatch and -1 for a deletion. The mathematical rigorousness and robustness are especially important at points where these peaks and

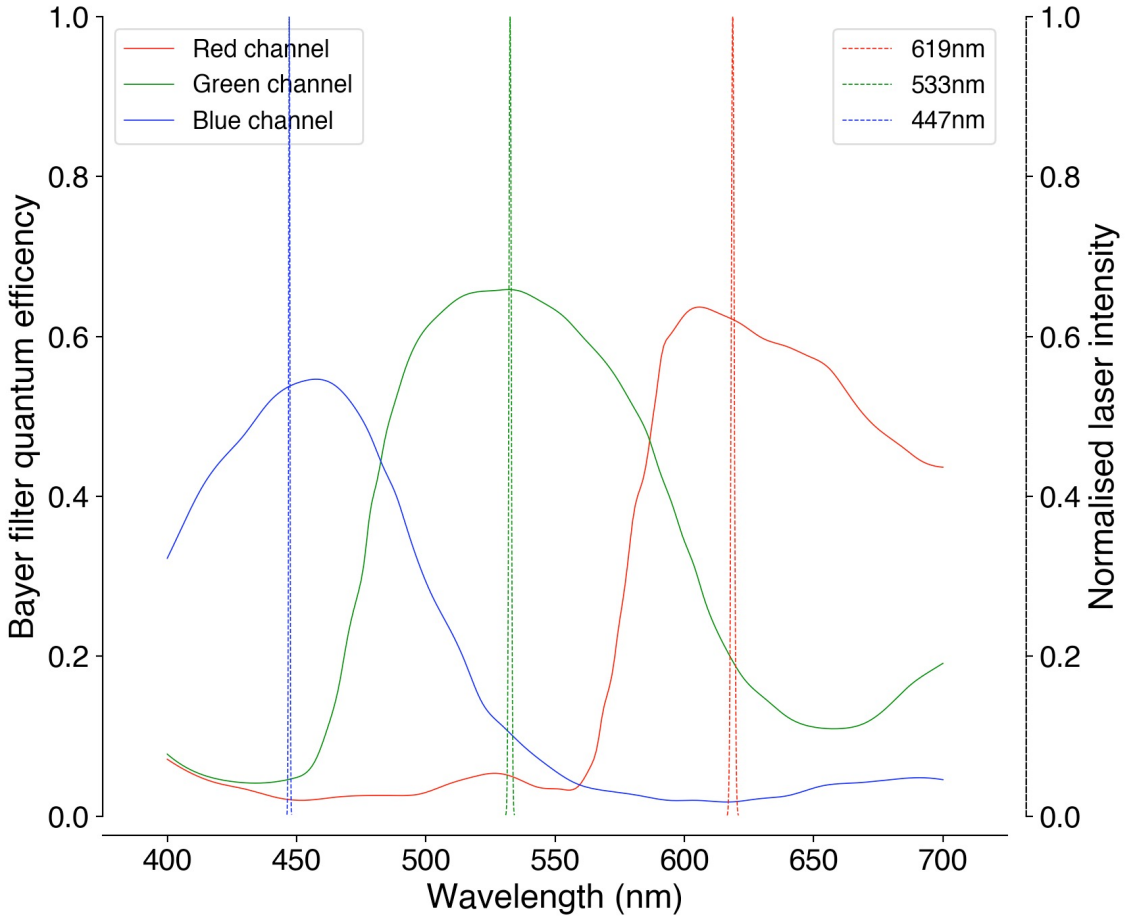

Figure 5.7: The quantum efficiency of each channel in the camera used overlaid with the red, green and blue lasers normalised outputs, the dashed boxes indicate the contributions of channel crosstalk and are annotated with the associated coefficient.

troughs occur very close together and may switch due to the sampling temporal resolution, effectively missing a peak(s).

5.5 Results and discussion

5.5.1 Colour video peak sequencing

The resultant colour video is available as Video 5.1, and is also available from Dryad repository[4]. The video shows strong interference colours from the outset, which slowly change over time as the film dries over the proceeding 74 s. The drying of the film can be split into three distinct qualitative drying regimes. Zone I; the drying rate is mostly uniform as shown by evenly spaced fringes that sweep from the top right to the bottom left of the field of view in the direction of drying. In this regime the film is still very solvent rich and some change in topology due to fluid flow can be observed. After this, (zone II) once enough evaporation has occurred there is a moment before final drying where an edge bead and drying front can be seen. The film's thickness gradient is significantly higher than before as indicated by more closely spaced fringes. From this point the film is mostly dry and the last of the trapped solvent evaporates (zone III). Figure 7 shows a series of timepoints from the video (S1) that demonstrate these different drying regimes clearly.

Figure 5.8 (a_B-e_B) shows that the monochromatic blue frames are less well resolved, potentially due to chromatic aberration of the collimation lens that was designed for 635 nm (red) light. This has reduced the fringe visibility sufficiently so that when the fringes are tightly spaced in zone II they are not as well resolved. For this reason, the peak matching algorithm was performed on a block of peaks and troughs from before this point, in zone I, where the more slowly modulating and therefore better resolved peaks could be utilised. All frames were binned 4 x 4 before processing to reduce the effects of random noise, reducing the lateral resolution from 0.6875 µm per pixel in the original video to 2.75 µm.

[4]https://doi.org/10.5061/dryad.95x69p8wm

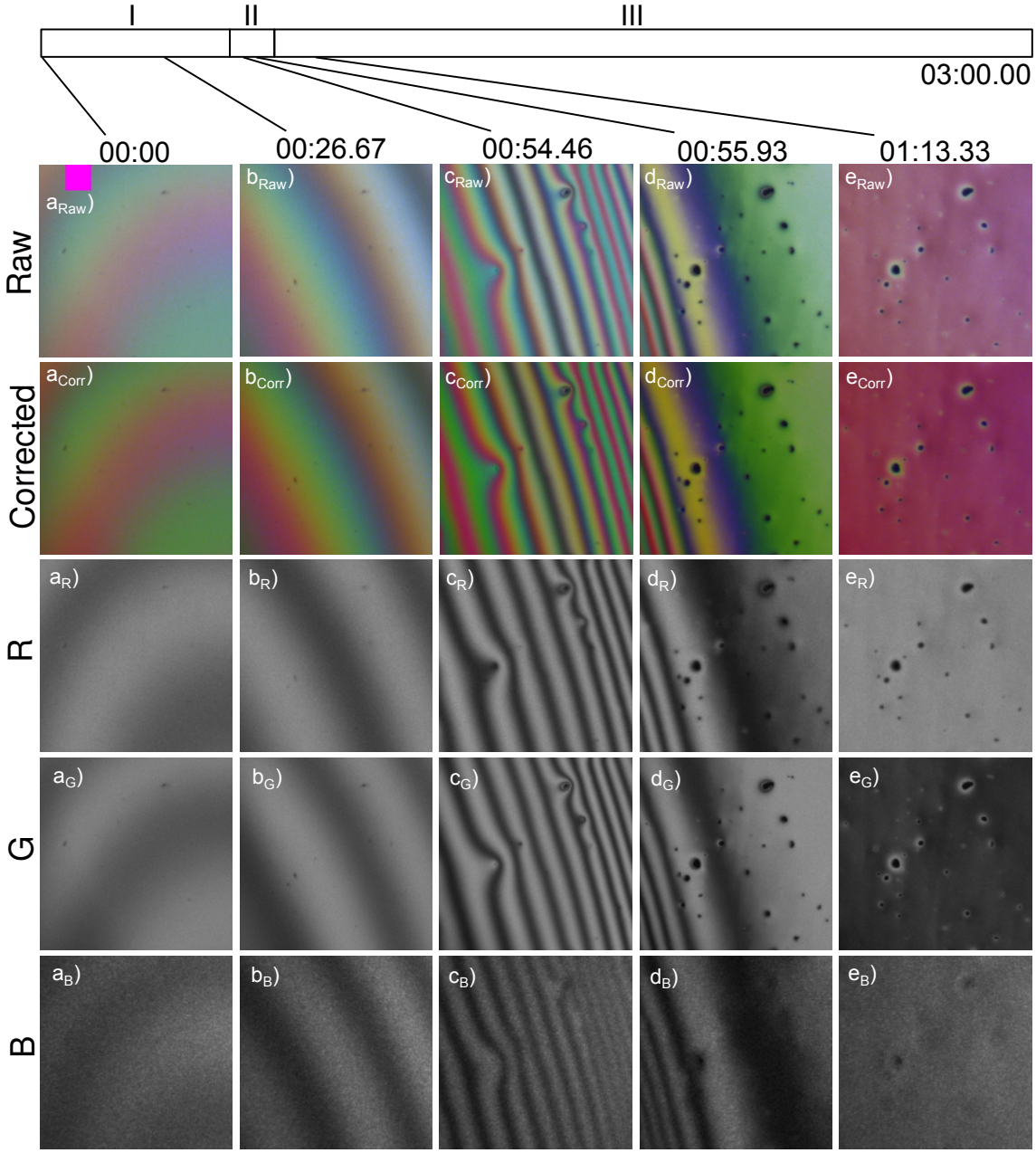

Figure 5.8: A selection of frames a) 1 b) 400 c) 817 d) 839 e) 1100 from a 300 pixel x 300 pixel bottom-left subsection of the colour video where at each chosen time point the raw, crosstalk corrected, red, green and blue frames are shown and indicated by the label subscript. The durations of the three distinct drying regimes are shown in the bar at the top of the figure. The magenta square in a_{Raw}) corresponds to the data shown in Figure 5.10.

A clear picture of the drying through time can be built up by stacking a single column of pixels from each frame horizontally as shown in Figure 5.9. The drying zones are indicated and show how the fringe appearance changes. The duration and location of drying zones are, however, specific to the pixel due to the nonuniform drying.

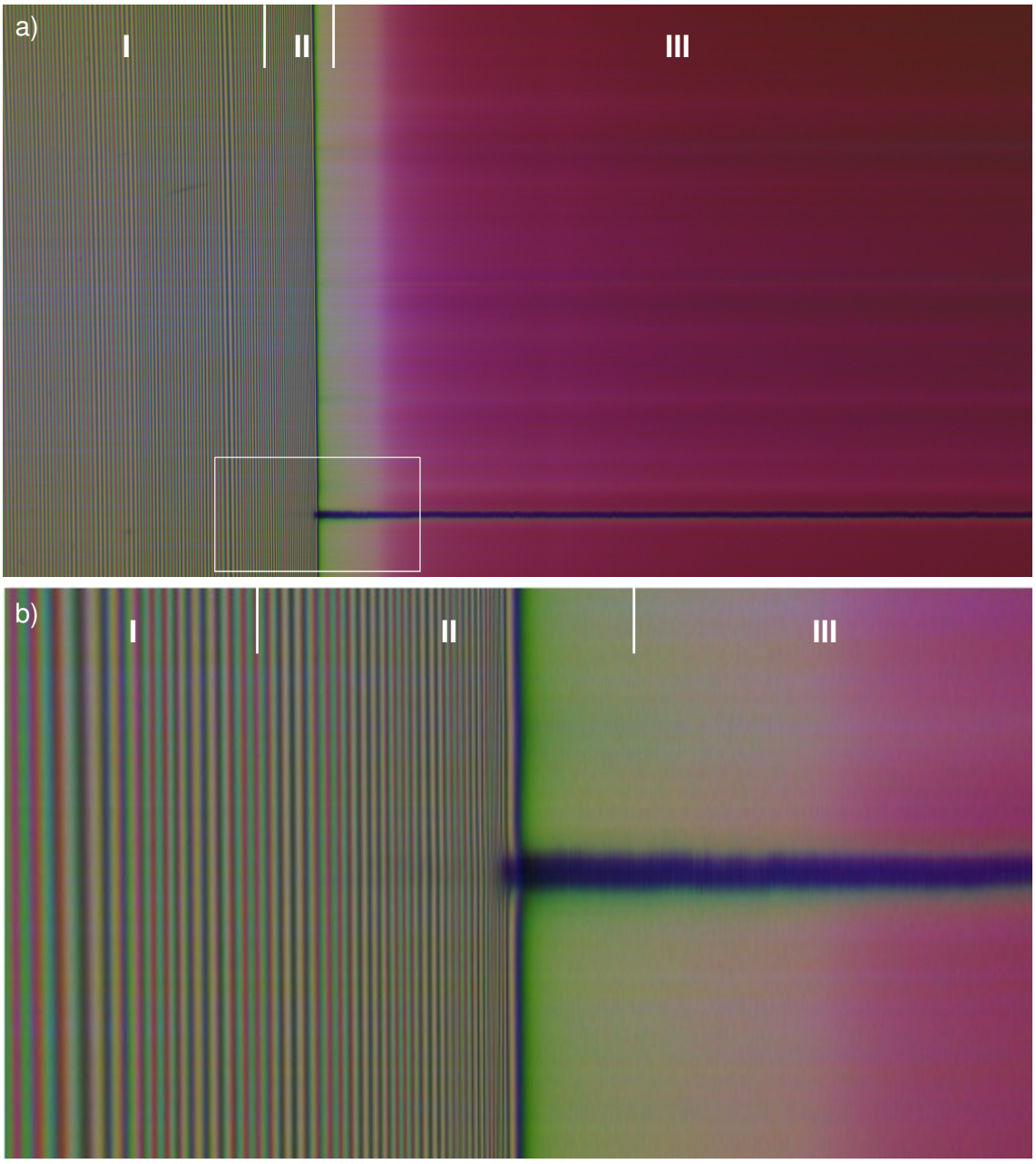

Figure 5.9: Horizontally stacked vertical line profiles taken from the center of (a) the full frames, spanning a time of 180 seconds horizontally and a height of 412.5um vertically, and (b) an enlarged view of the area outlined in (a) showing the high fringe frequency of the edge bead and a piece of debris on the film.

Data for binned areas is interpolated through time by a factor of 1000 using a cubic spline that passes exactly through all points, before peak and trough detection is then used to identify the points resolved by Equations 5.1 and 5.2. Data for the binned area annotated by the magenta square (shown at 10x scale) in Figure 5.8 is shown in Figure 5.10.

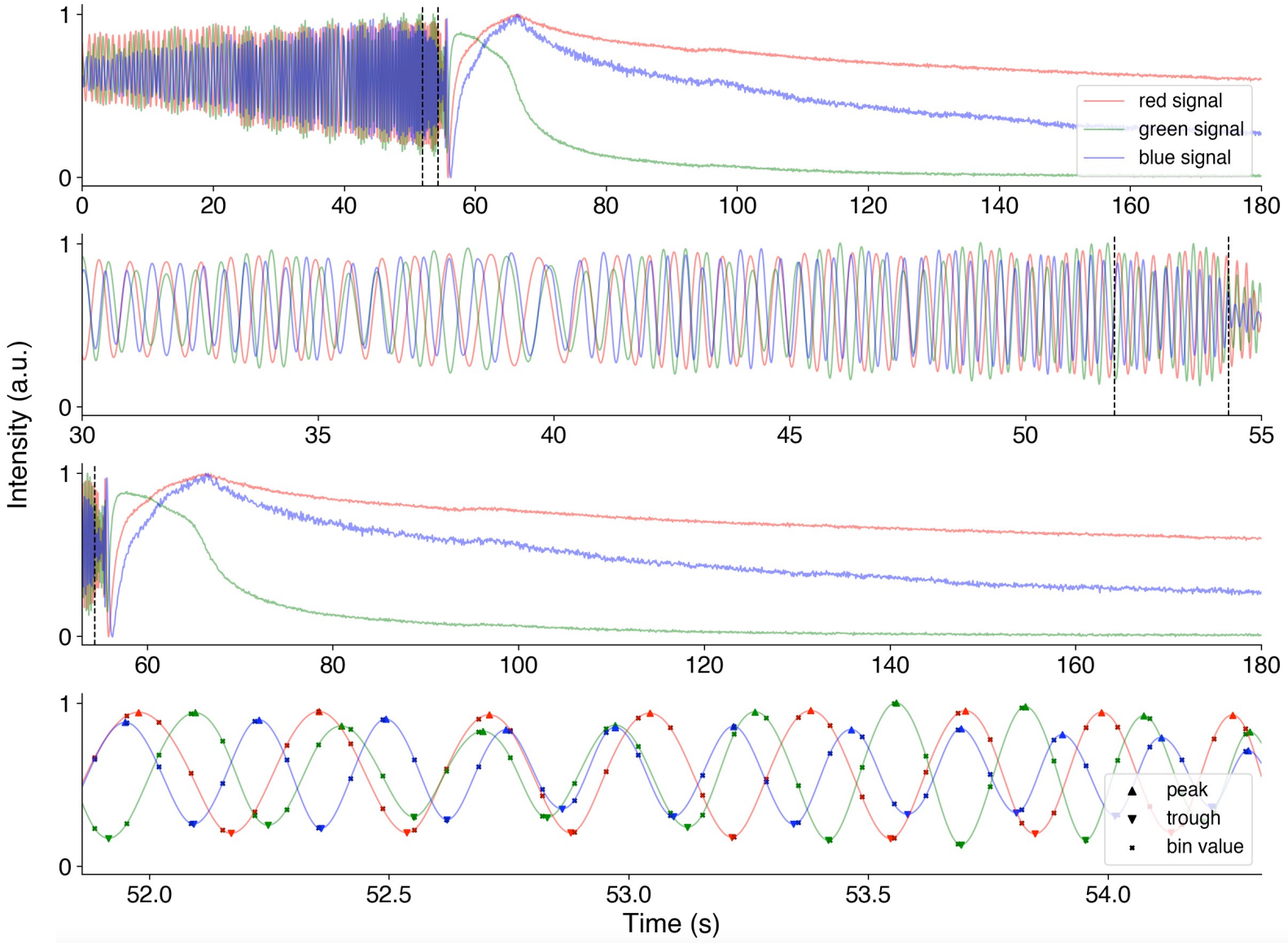

Figure 5.10: Data from the highlighted region in Figure 5.8. a) the data across the entire time domain b) the data from drying zones I and II c) the data from drying zones II and III d) the section of data used for initial sequence matching, additionally showing the original data points and the peaks and troughs that have been detected, this area is highlighted between the dotted vertical lines in (a-c).

Whilst no single peak in isolation can be used to identify a single value of thickness, a short sequence of peaks and troughs, typically 50 identifiers long, can be used to identify a film drying phase and thickness. This in turn allows for individual peaks and troughs to be assigned to unique optical thicknesses, both within the sequence itself and then either side of this sequence in time, developing full knowledge of thickness of the entirety of the drying process.

With the data shown in Figure 5.10d, the signal sequence shown between 51.88 s and 54.30 s, shows strong, clearly identifiable peaks and troughs and is;

> ...RP, GT, BP, RT, GP, BT, BP, RP, GT, BT, GP, RT, BP, GT, RP, BT, GP, BP, RT, GT, BT, RP, BP, GP, RT, BT, GT, BP, RP, GP, BT, GT, RT, BP, GP, BT, RP, GT, BP, RT, BT, GP, RP, BP, GT, BT, RT, GP, BP, RP...

When aligned using the Smith-Waterman algorithm, the reference and signal (query) sequences result in the following order identification:

> ...RP_{14}, GT_{16}, BP_{20}, RT_{14}, GP_{17}, BT_{20}, BP_{21}, -, GT_{17}, RP_{15}, BT_{21}, GP_{18}, RT_{15}, BP_{22}, GT_{18}, RP_{16}, BT_{22}, GP_{19}, BP_{23}, RT_{16}, GT_{19}, BT_{23}, RP_{17}, BP_{24}, GP_{20}, -, BT_{24}, RT_{17}, GT_{20}, BP_{25}, -, GP_{21}, RP_{18}, BT_{25}, GT_{21}, RT_{18}, BP_{26}, GP_{22}, BT_{26}, RP_{19}, -, BP_{27}, GT_{22}, RT_{19}, BT_{27}, GP_{23}, -, BP_{28}, RP_{20}, GT_{23}, BT_{28}, RT_{20}, GP_{24}, BP_{29}...

Where a hyphen shows an insertion or a mismatch. Using the first element RP_{14} that appears at 54.30 seconds, the thickness can be calculated by first calculating the film refractive index (at 619 nm) using Equation 5.9, and then using Equation 5.1 to give a thickness of 2794 nm.

This approach is then applied to all peaks and troughs, for all three colour planes, for all time values for this particular binned pixel, moving both forward and backwards in time, identifying a film optical thickness as a function of time. Other identifiers for reconstruction could be used e.g. the other roots of Equation 5.8 which give the signals inflection points, where $m + \frac{1}{4}$ and $m + \frac{3}{4}$ are resolved, however, this is beyond the scope of the current work. Using more and more identifiable points on the signals obtained eventually leads to an approach that is increasingly like Fourier transform profilometry [163] [164].

5.5.2 Recovered thickness

The thickness profiles for three positions in the field of view (FOV) are represented in Figure 5.11. Good agreement is seen in the recovered thicknesses for each position, starting from 21 µm until a thickness of approximately 2750 nm is reached, which corresponds to the point where the sequence matching was resolved at the end of drying zone I and is shown further in Section 5.5.3. At thicknesses below this there is significant deviation in the panes from one another, as predicted from the raw images, due to the increased fringe frequency and reduced fringe visibility. For this reason, the thicknesses reported in the remainder of the paper at all points are from the red pane. We reason that this gives the most accurate thickness values because the red fringes have the slowest modulation with optical path difference and are therefore the best resolved.

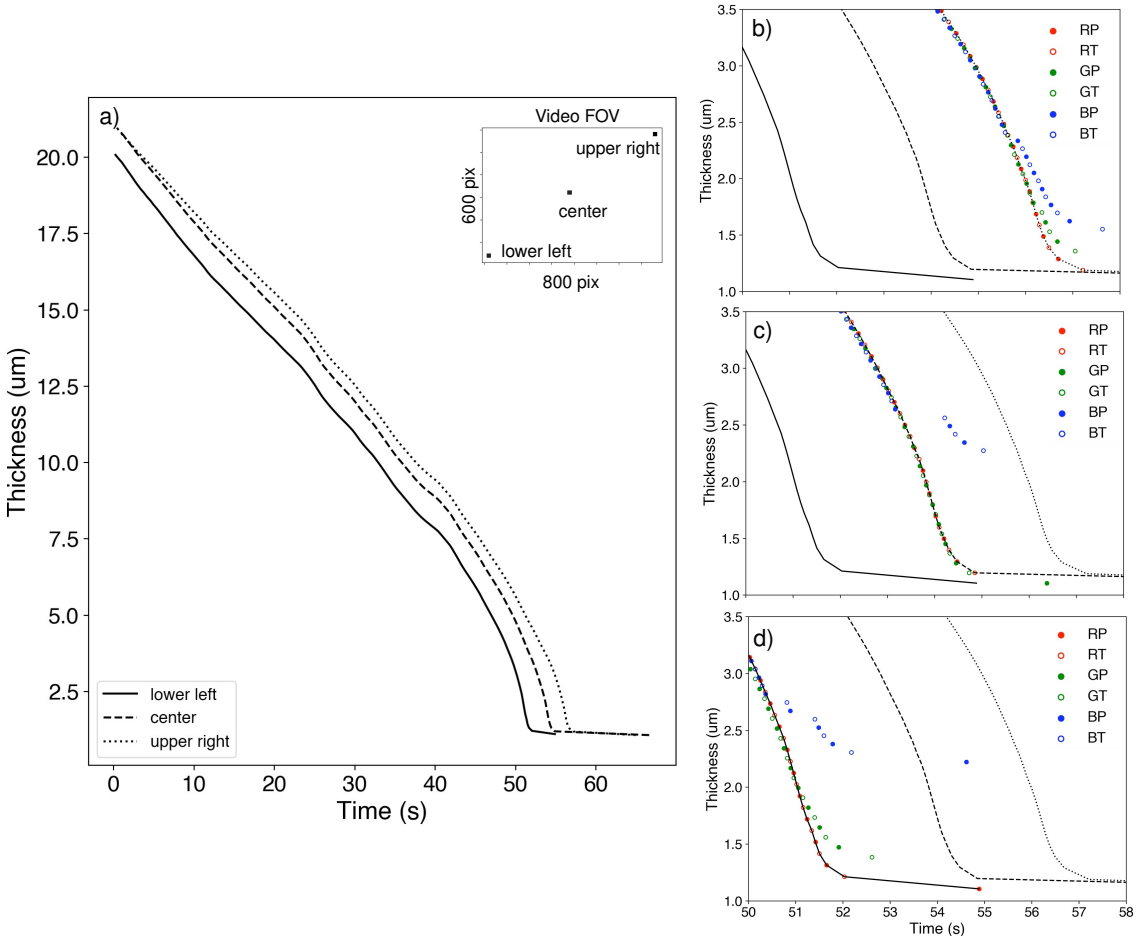

Figure 5.11: a) A selection of three different points thickness profiles reconstructed from the red colour signals using a linear refractive index change, the inset shows the positions of the reconstructions on the video field of view (b-d) enlargements of the drying point with the red, green and blue peaks and troughs added for each reconstructed point upper right, centre and lower left respectively.

After the thicknesses were reconstructed and averaged a median filter thresholding (kernel size 5, threshold value 195 nm) and 3D linear interpolation process reported previously [1] was implemented to remove probably incorrectly identified thicknesses, for example due to the debris present causing disturbances in the peak detection, and then to fill any missing values.

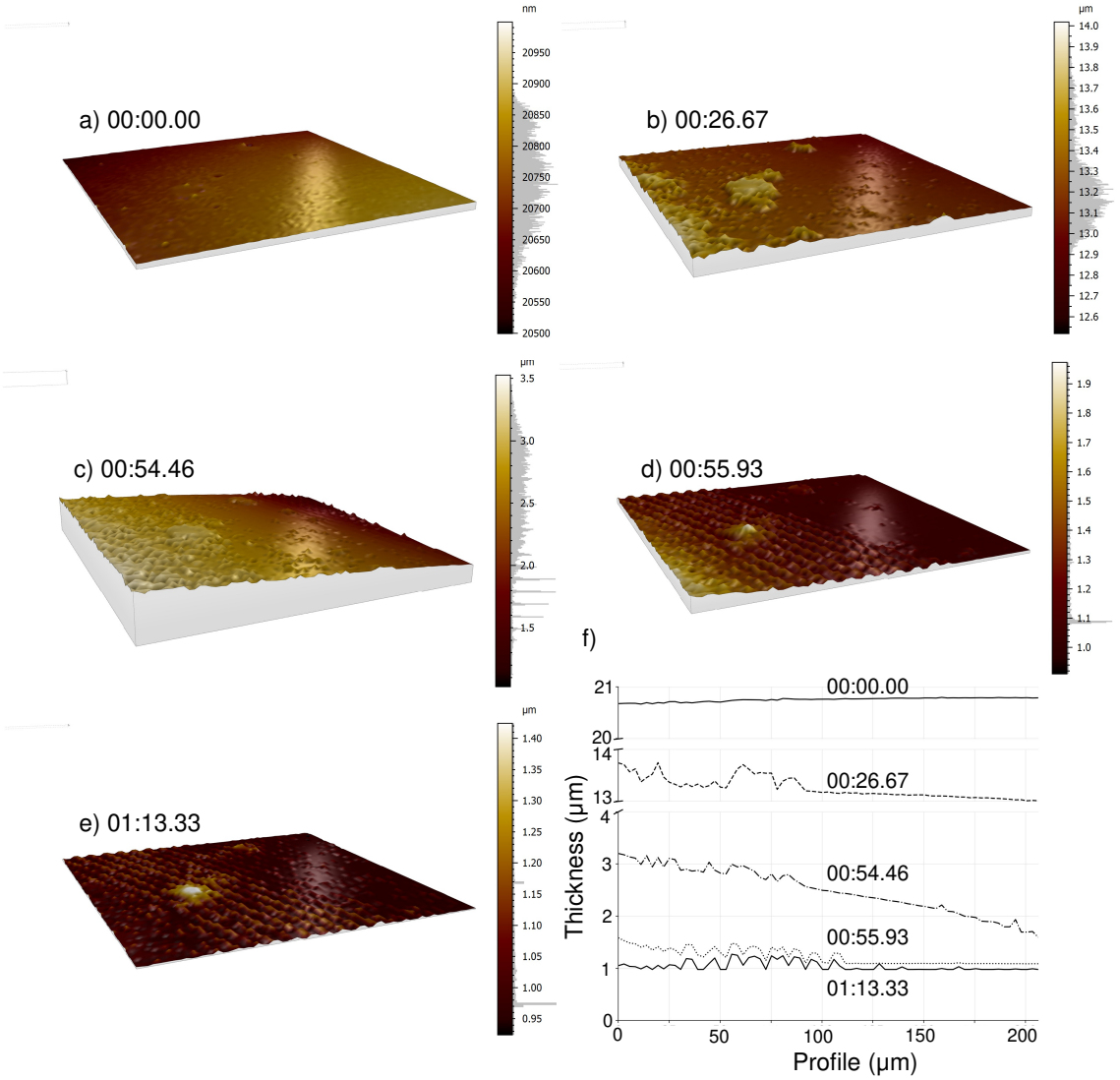

Figure 5.12: (a-e) Renders of the surfaces recovered from the images shown in Figure 5 at frames 1, 400, 817, 839 and 1100 respectively where the colour bar is annotated with the histograms of thicknesses in the frame and the timestamp of the frame is marked on each subfigure. The height of each surface has been scaled in accordance with the range of the thickness data f) a line profile taken in the x direction at the centre point of each of the frames (a-e), note the breaks in the y-axis.

Figure 5.12 gives 3D thickness renders of the images shown in Figure 5.8, which agree with the qualitative understanding of film drying gained from inspection of the video. Video

5.2 shows the thickness as a heatmap side-by-side with the crosstalk corrected images, played at native speed. The surface starts with a shallow thickness gradient from bottom right to top left (5.12a), and then during the first few seconds of thinning this gradient changes direction from top right to bottom left (5.12b). This relative surface then persists until the drying front comes into frame, which is associated with a much larger thickness gradient (5.12c). The thinner top right corner stops thinning first (5.12d) and the bottom left continues thinning until a relatively uniform film is left (5.12e). This frame, removing the area containing the defect, has a mean thickness of 997 nm and a standard deviation of 54 nm. Larger pieces of debris, and the disturbances to thickness reconstruction this creates can be seen. Figure 12 shows a profile of this surface at 1 s time intervals, areas of faster and slower thinning can be distinguished by the relative spacing of the lines.

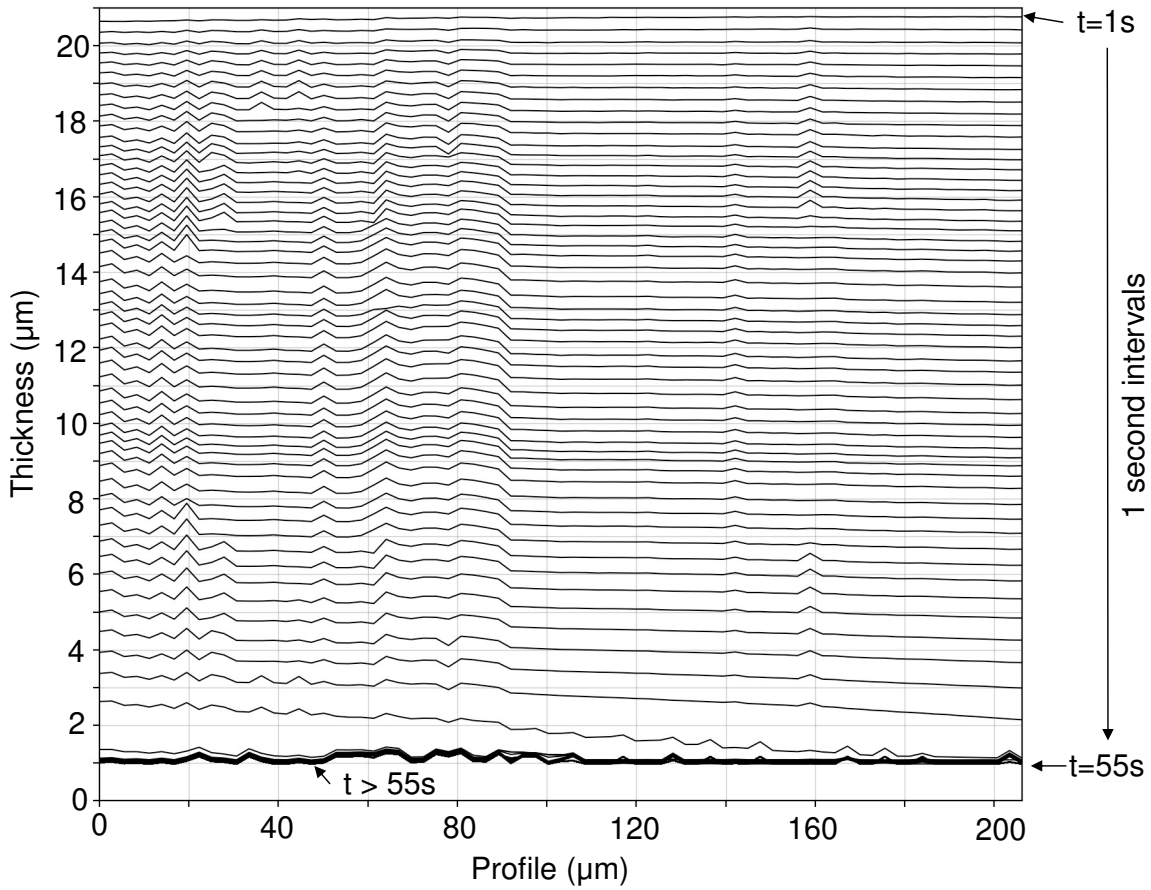

Figure 5.13: A line plot of the centre profile of the surfaces shown at 1 s time intervals

The thicknesses extracted from the last frame for the final thickness will be an overestimate, as thinning is likely to occur after the last recorded peak/trough (and before the next peak/trough). Once the last peak is found other methods that would usually suffer

from order ambiguities can be used easily as the thickness is constrained to a range that will be much smaller than the one-to-many mappings.

Thickness of PS on silicon determined with spectroscopic ellipsometry (SE) (J.A. Woollham, Alpha 2.0) at roughly (by eye) the same spot. The spot size used was reduced to 0.3 mm x 1 mm using the focusing probes and this gave a thickness measurement of 883 nm. In addition to the known overestimation of this technique, we attribute the discrepancy to movement between the video FOV and the probed area with the SE, and the different areas of spot size between the techniques.

5.5.3 Strategy and robustness

With any automated sequence matching approach, the performance of the search can be quantified. A match score is assigned to each case, for each element in the sequence +2 is given for match and -1 for a mismatch or gap (maximum score with the sequence of length 50 used here being 100 and the minimum being -50). Figure 5.14a shows each pixel score that has been scaled between 0 and 1, when searching through all time.). This metric can be interpreted as a confidence for each match and shows here that although this does not fall below 0.6, there is a large variation between different areas. It is worth noting that a lower match score does not necessarily mean that the matched point is incorrect, just that the signal sequence is further from the reference sequence. A reduction in match score is likely in areas where the signal sequence has less well resolved fringe features, such as when the rate of drying is higher.

From the match score, match point time and match point thickness are determined across the area and are shown in Figure 5.14c and 5.13d respectively. The match point time gives the time of the earliest element in the matched sequence, and matched thickness gives the thickness at this time. In the previous example shown in Figure 5.7, these values are 54.30 s and 2754 nm and extracted from RP_{14}. The matched thickness stays roughly constant over the field of view as a result of the algorithm running on blocks of peaks and troughs at the same stage of the drying process and the final film being relatively uniform in thickness. The matched time varies in a gradient from the top right to the bottom left of the FOV following the drying pattern observed qualitatively in the video and giving the time where a matched point thickness of roughly 2750 nm is shown.

In all three of the heatmaps, the particles of debris in view have and effected the

data can be picked out and these areas are consistent between metric, these areas can be compared with the image of the final film.

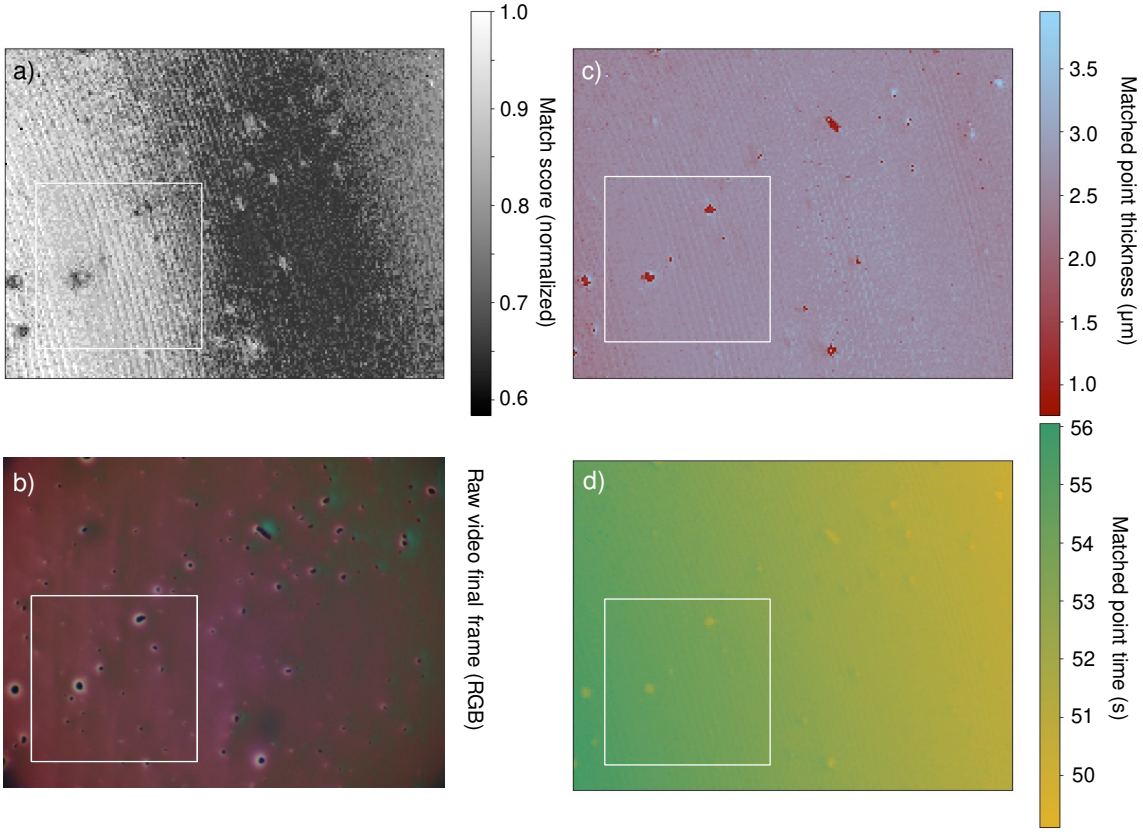

Figure 5.14: Heatmaps showing the a) match score b) the videos final frame and c) matched point thickness and d) the match point time, across the whole field of view, with the processed video ROI added as a white square.

The length of sequence matching was chosen as 50 sequence elements. Figure 5.15 shows the number of unique matches for a subsequence (query sequence) as a function of length and start position of the subsequence in the reference sequence. The area with a single unique matching position (and therefore an unambiguous match) is shown in green. Unique matches for sequences containing more than 50 elements is consistently seen.

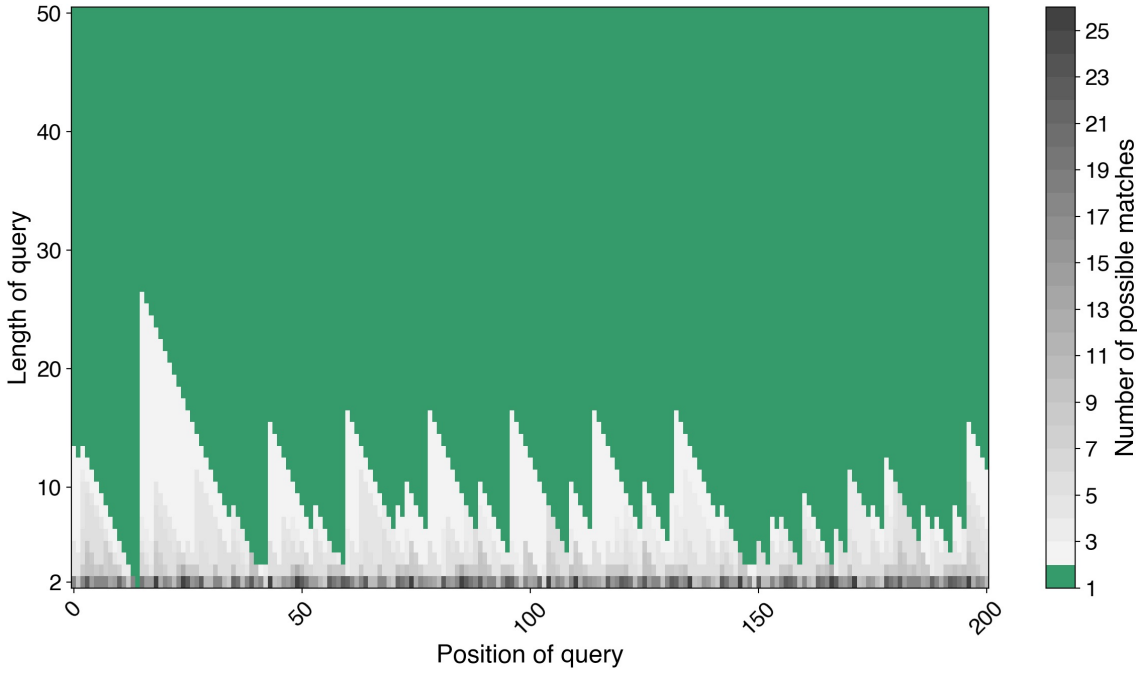

Figure 5.15: A heatmap showing the number of possible matches to the reference sequence as a function of the query sequence length and starting position, the area that gives unique matches is coloured in green.

5.5.4 Future implementation

The robustness of the technique described here will increase as both the sampling rate increases and integration time decreases, possibly utilising a stroboscopic approach for rapidly evolving films, irrespective of the specific implementation or film processing method. In this particular case, this can be achieved either by increasing the framerate of the camera, or by utilising a solvent with a lower vapour pressure to reduce the evaporation rate, however this may not be suitable as it effects film morphology. This will result in more accurate peak/trough positioning rendering the sequence identification and matching more accurate. The peak/trough positioning can also be improved by utilising hardware that removes the crosstalk, rather than the software post-processing approach used here. Examples of this may include the use of a prism camera, or a narrow multi bandpass filter with appropriate bandpass characteristics compared to the lasers used, or a multi sensor camera (or equivalent). In addition, optimisation of the laser wavelengths would result in sequences where the peak/troughs are separated on average by a larger OPD change, which would also help to avoid peak sequencing errors.

Finally, noise in the images should be kept to a minimum. This can be achieved in the standard way by utilising the full dynamic range of the camera and lowering the gain as

much as possible. This means that a higher incident intensity is preferable, however, we note that with the normal incidence setup used here the beamsplitter constrains the images to a maximum of 25% of the laser's intensity. This is likely to be especially problematic if the technique is to be used *in situ* with demanding requirements, such as short exposure time to freeze film movement that would be present in several fabrication techniques, most notably spin coating. Identified solutions are a) using a substrate that maintains good fringe visibility and increases reflectance, such as Ti (this can also be used on R2R applications by coating into PET) b) moving to a non-normal incidence specular setup to remove the beam splitter and focusing the film (that would then be out of alignment with the focal plane) using the Scheimpflug principle [165].

The technique is powerful because it can be used with any colour imaging optical system, in a trade-off between sensor size, field of view and lateral resolution. By using a less magnifying lens, and an array of cameras positioned along the web, colour inspection across whole web areas on R2R coatings would be possible. If the web speed is known, the technique can be run on peak sequences that appear in the direction of the web movement as evaporation occurs, giving film thickness measurements across the length of the web. In addition, a less magnifying lens will give a larger film thickness range where the film stays in focus, improving the quality of the data and thickness reconstructions. Resolving fringes perpendicular to the web direction is not recommended because the optical path difference is unlikely to vary monotonically in this direction.

5.6 Conclusion

This work presents the development of a novel "trichromatic" reflectance image sequencing technique capable of on-the-fly areal determination of thin film thicknesses and morphology over extended ranges. This method requires only a sufficient monotonic optical path difference in time or space to work effectively, making it applicable to a huge range of solution processed films that meet this criterion as they dry via evaporation. The underlying physical principles are outlined, demonstrating how the peak and trough sequences of RGB laser interference patterns can be leveraged to unambiguously resolve thicknesses and remove the necessity for costly and time-consuming ex-situ characterization techniques. The technique was successfully validated on a model blade-coated polystyrene film, showcasing

its ability to track thickness evolution during drying. Additionally, the robustness of the approach was evaluated, and potential improvements were suggested to enhance accuracy and extend its applicability to other fabrication processes. This method represents a significant step toward accessible, *in situ*, large-area thin film metrology for dynamic and scalable film fabrication.

5.7 Videos

Both videos play at native speed of 15 fps.

- Video 5.1: The raw video of 5 wt% polystyrene in butyl acetate being blade coat onto silicon under trichromatic illumination `https://drive.google.com/open?id=15GjVQSGBwD-lmT-lUstEe84B2WZuiJWv&usp=drive_fs`
- Video 5.2: The processed and annotated version of Video 5.1, side by side with the reconstructed thickness displayed as a heatmap `https://drive.google.com/open?id=15H9e-D6-G6ZOZiPHr1iokK_FbrOSmcHM&usp=drive_fs`

References

[1] Jack B.P. Atkinson and Jonathan R. Howse. "In-situ full-wafer metrology via coupled white light and monochromatic stroboscopic illumination". In: *Optics and Lasers in Engineering* 184.P2 (2025), p. 108692. DOI: 10.1016/j.optlaseng.2024.108692.

[13] Dietrich Meyerhofer. "Characteristics of resist films produced by spinning". In: *Journal of Applied Physics* 49.7 (1978), pp. 3993–3997. DOI: 10.1063/1.325357.

[15] Dunbar P. Birnie, Dylan E. Haas, and Carissa M. Hernandez. "Laser interferometric calibration for real-time video color interpretation of thin fluid layers during spin coating". In: *Optics and Lasers in Engineering* 48.5 (2010), pp. 533–537. DOI: 10.1016/j.optlaseng.2009.12.021.

[44] Dunbar P. Birnie and Manuel Manley. "Combined flow and evaporation of fluid on a spinning disk". In: *Physics of Fluids* 9.4 (1997), pp. 870–875. DOI: 10.1063/1.869519.

[50] Paul C. Jukes et al. "Time-resolved light scattering studies of phase separation in thin film semiconducting polymer blends during spin-coating". In: *Macromolecules* 38.6 (2005), pp. 2030–2032. DOI: 10.1021/ma0477145.

[51] Sasha Y. Heriot and Richard A.L. Jones. "An interfacial instability in a transient wetting layer leads to lateral phase separation in thin spin-cast polymer-blend films". In: *Nature Materials* 4.10 (2005), pp. 782–786. DOI: 10.1038/nmat1476.

[53] Dylan E. Haas and Dunbar P. Birnie. "Nondestructive measurement of striation defect spacing using laser diffraction". In: *Journal of Materials Research* 16.12 (2001), pp. 3355–3360. DOI: 10.1557/JMR.2001.0463.

[73] Steven J. Byrnes. *Multilayer optical calculations*. 2020. arXiv: 1603.02720 [physics.comp-ph].

[78] Jonas Bergqvist et al. "In situ reflectance imaging of organic thin film formation from solution deposition". In: *Solar Energy Materials and Solar Cells* 114 (2013), pp. 89–98. DOI: 10.1016/j.solmat.2013.02.030.

[86] L. M. Peurrung and D. B. Graves. "Film Thickness Profiles over Topography in Spin Coating". In: *Journal of The Electrochemical Society* 138.7 (1991), pp. 2115–2124. DOI: 10.1149/1.2085935.

[89] Stephen Ebbens et al. “In situ imaging and height reconstruction of phase separation processes in polymer blends during spin coating”. In: *ACS Nano* 5.6 (2011), pp. 5124–5131. DOI: 10.1021/nn201210e.

[91] Daniel T.W. Toolan et al. “In situ studies of phase separation and crystallization directed by Marangoni instabilities during spin-coating”. In: *Advanced Materials* 25.48 (2013), pp. 7033–7037. DOI: 10.1002/adma.201302657.

[94] Ehtsham Ul Haq et al. “Real time laser interference microscopy for bar-spread polystyrene/ poly(methyl methacrylate) blends”. In: *Journal of Polymer Science, Part B: Polymer Physics* 52.15 (2014), pp. 985–992. DOI: 10.1002/polb.23513.

[100] Garam Choi et al. “Simple method for volumetric thickness measurement using a color camera”. In: *Applied Optics* 57.26 (2018), p. 7550. DOI: 10.1364/ao.57.007550.

[128] Mihirsinh Chauhan et al. “Investigating two-step MAPbI3 thin film formation during spin coating by simultaneous: In situ absorption and photoluminescence spectroscopy”. In: *Journal of Materials Chemistry A* 8.10 (2020), pp. 5086–5094. DOI: 10.1039/c9ta12409h.

[129] Noura Alhazmi et al. “Perovskite Crystallization Dynamics during Spin-Casting: An in Situ Wide-Angle X-ray Scattering Study”. In: *ACS Applied Energy Materials* 3.7 (2020), pp. 6155–6164. DOI: 10.1021/acsaem.9b02470.

[139] Katsuichi Kitagawa. “Single-shot surface profiling by multiwavelength interferometry without carrier fringe introduction”. In: *Journal of Electronic Imaging* 21.2 (2012), p. 021107. DOI: 10.1117/1.jei.21.2.021107.

[152] D. E. Aspnes and A. A. Studna. “Dielectric functions and optical parameters of Si, Ge, GaP, GaAs, GaSb, InP, InAs, and InSb from 1.5 to 6.0 eV”. In: *Phys. Rev. B* 27 (2 Jan. 1983), pp. 985–1009. DOI: 10.1103/PhysRevB.27.985.

[155] Ambalanath Shan et al. “High-speed imaging/mapping spectroscopic ellipsometry for in-line analysis of roll-to-roll thin-film photovoltaics”. In: *IEEE Journal of Photovoltaics* 4.1 (2014), pp. 355–361. DOI: 10.1109/JPHOTOV.2013.2284380.

[156] Andrey Nazarov, Michael Ney, and Ibrahim Abdulhalim. “Parallel spectroscopic ellipsometry for ultra-fast thin film characterization”. In: *Optics Express* 28.7 (2020), p. 9288. DOI: 10.1364/oe.28.009288.

[157] Jacobus J. van Franeker et al. "Sub-Micrometer Structure Formation during Spin Coating Revealed by Time-Resolved In Situ Laser and X-Ray Scattering". In: *Advanced Functional Materials* 27.46 (2017). DOI: 10.1002/adfm.201702516.

[158] Pascal Picart et al. "Topography of nanometric thin films with three-wavelength digital interferometry". In: *Journal of Micro/Nanolithography, MEMS, and MOEMS* 14.4 (2015), p. 041309. DOI: 10.1117/1.jmm.14.4.041309.

[159] M. J. McPhail et al. "Correcting for color crosstalk and chromatic aberration in multicolor particle shadow velocimetry". In: *Measurement Science and Technology* 26.2 (2015). DOI: 10.1088/0957-0233/26/2/025302.

[160] Yaping Ye et al. "A crosstalk correction method to improve multi-wavelength LEDs imaging quality based on color camera and frame accumulation". In: *Signal Processing: Image Communication* 102.December 2021 (2022). DOI: 10.1016/j.image.2021.116624.

[161] Saif Al-Bashir. "Multi-Wavelength Polarising Interferometer for In-Process Metrology". PhD thesis. University of Huddersfield, 2019.

[162] T.F. Smith and M.S. Waterman. "Identification of common molecular subsequences". In: *Journal of Molecular Biology* 147.1 (Mar. 1981), pp. 195–197. DOI: 10.1016/0022-2836(81)90087-5.

[163] Mitsuo Takeda and Kazuhiro Mutoh. "Fourier transform profilometry for the automatic measurement of 3-D object shapes". In: *Applied Optics* 22.24 (1983), p. 3977. DOI: 10.1364/ao.22.003977.

[164] Moises Padilla, Manuel Servin, and Guillermo Garnica. "Fourier analysis of RGB fringe-projection profilometry and robust phase-demodulation methods against crosstalk distortion". In: *Optics Express* 24.14 (2016), p. 15417. DOI: 10.1364/oe.24.015417.

[165] Carsten Steger. "A Comprehensive and Versatile Camera Model for Cameras with Tilt Lenses". In: *International Journal of Computer Vision* 123.2 (2017), pp. 121–159. DOI: 10.1007/s11263-016-0964-8.

Chapter 6

Conclusion

This work has explored RGB imaging as a tool for *in situ* thin film metrology, using amorphous polymer film systems and a variety of solution-based processing methods. Although monochromatic imaging and point probe spectroscopic techniques are widespread for *in situ* film characterisation of this kind, colour imaging seems underutilised, especially when colour cameras are ubiquitous and widespread, offering high frame rates and resolutions. This is in contrast to the current state of snapshot HSI, the alternative. This failure to broadly adopt colour imaging as a facile single-shot technique suitable for dynamic film analysis is due to the relativity crude colour sensing by Bayer filters; by far the most common type of colour sensing in cameras.

The following research question was set out in the introduction of the thesis.

> *"Can Bayer filters in standard colour cameras be leveraged to develop new techniques, or improve existing ones, suitable for the* in situ *imaging metrology of solution-processed thin films?"*

The work has presented a number of ways in which this has been achieved. Firstly, it was shown that broadband LED illumination and standard colour imaging could be used to recover transient thickness profiles on spun-coat wafers. This approach mapped interference colours over full 3" wafers and overcame the commonly encountered many-to-one problem with a thickness selection algorithm informed with physical constraints. Here, the upper thickness limit was around 1.5 µm, and this was due to the combination of broadband illumination (LEDs) and wide detection of the Bayer filter.

Next, the imaging detection was modified with a multi-bandpass dichroic beam splitter, which enabled the development of a six-band multispectral camera. The additional spec-

tral information was exploited to reconstruct film thicknesses using a variety of methods, including spectral reconstruction techniques, an approach not previously applied in the context of thin film interference colours. This alternative strategy preserved the inherent advantages of LED illumination, ensuring high frame rates and cost-effectiveness while addressing some of the limitations seen with standard RGB imaging.

Lastly, trichromatic laser illumination was used, instead of LEDs, for reflectance imaging. This was developed into an entirely new type of peak sequencing optical metrology that effectively takes advantage of the Bayer filters three-channel detection to ensure that AFM or other ex-situ methods, that had been a major limitation of analogous monochromatic techniques, are not necessary for data interpretation. In addition, the upper thickness limit is vastly extended to films hundreds of microns thick.

Figures 6.1 to 6.3 use the illumination and detection combinations in Chapters 3 to 5, respectively, on the same (polymer film on silicon) sample to directly compare the optical difference. The film sample has thinner areas on the right hand side and thicker ridge-like areas on the left hand side.

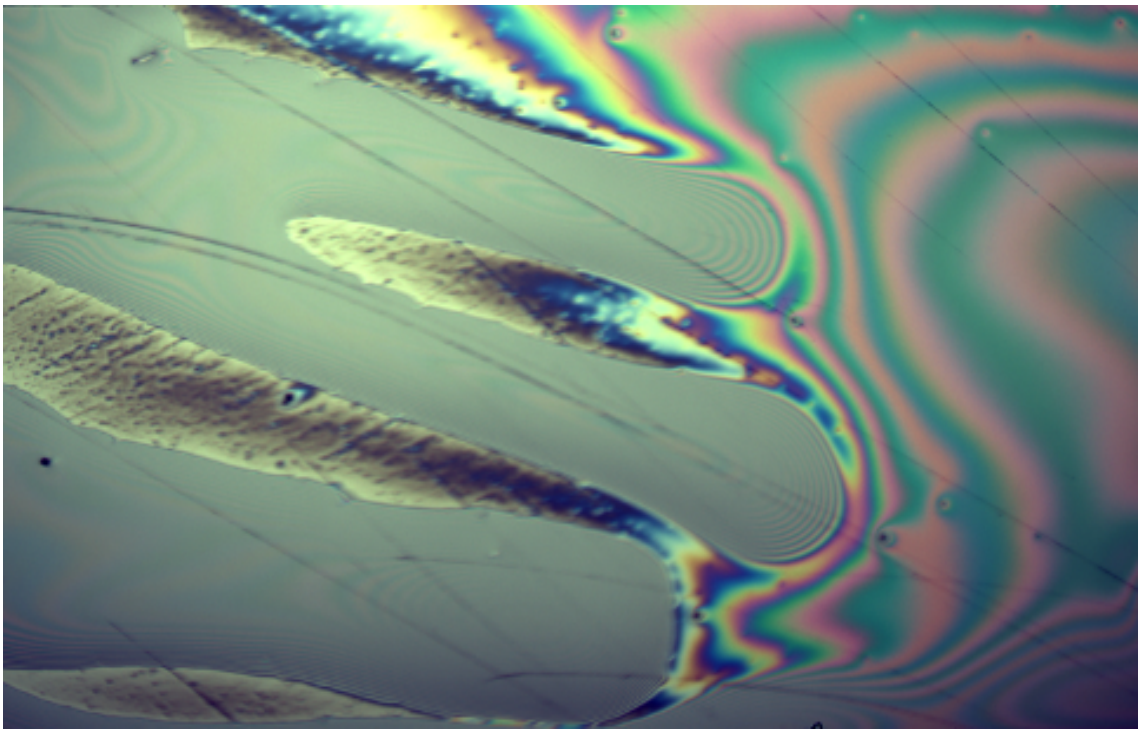

Figure 6.1: An uneven polymer film on silicon under Chapter 3 conditions, LED illumination and RGB Bayer detection

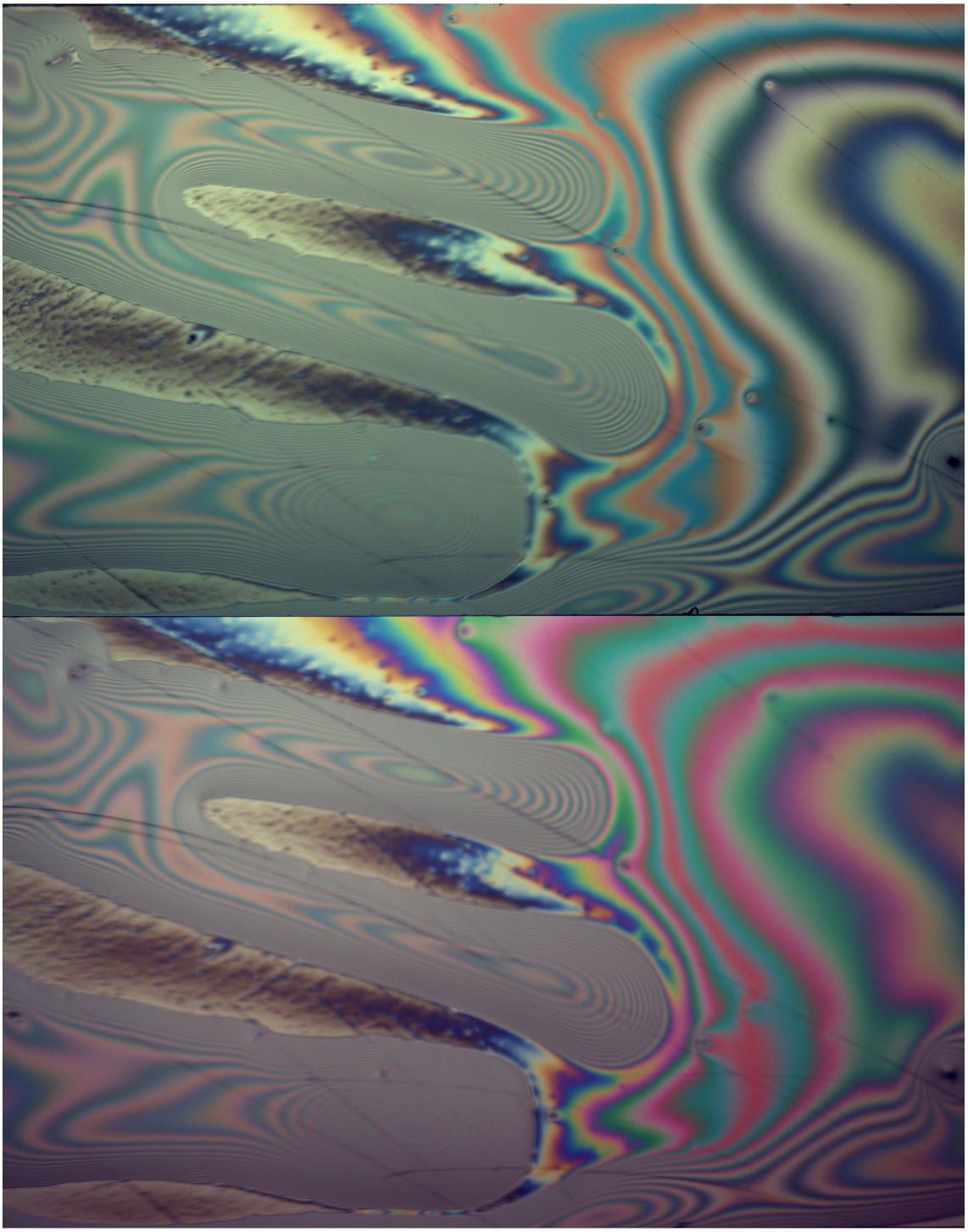

Figure 6.2: An uneven polymer film on silicon under Chapter 4 conditions, LED illumination and multispectral MBP dichroic beam splitter RGB(T) and RGB(R) detection (upper and lower respectively)

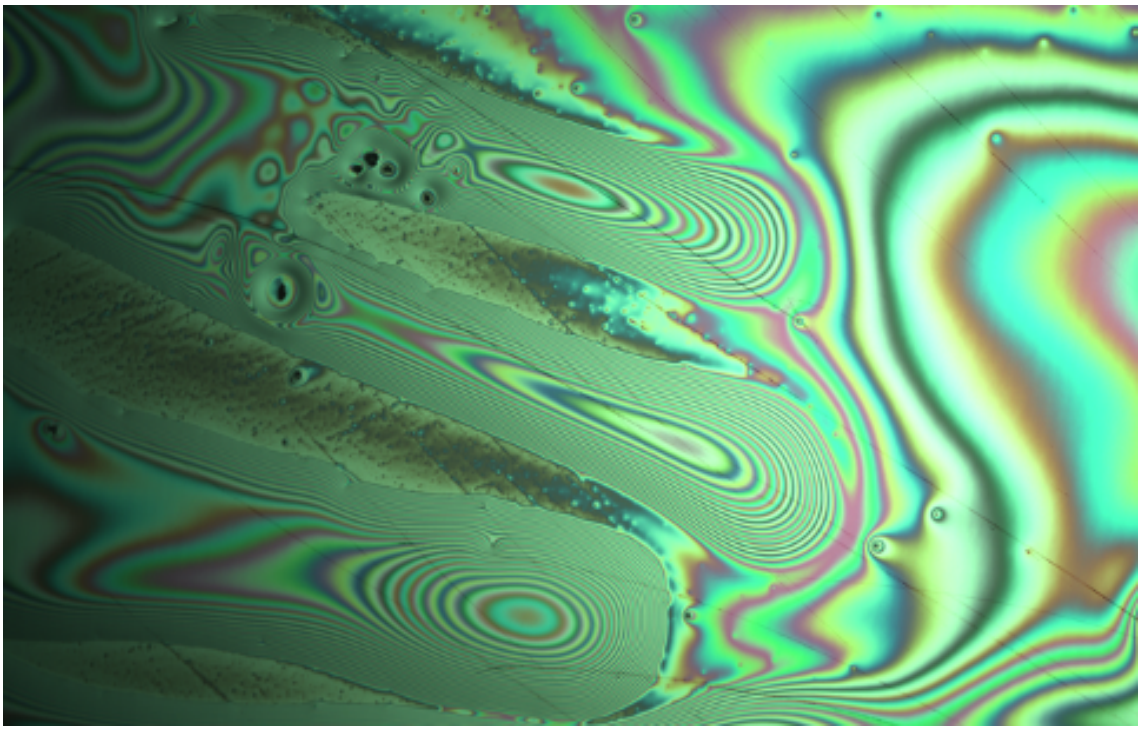

Figure 6.3: An uneven polymer film on silicon under Chapter 5 conditions, trichromatic illumination and RGB detection (the exact trichromatic illumination used in Chapter 5 is not used)

6.1 Major contributions

The significant contributions to the field can be made in reference back to the original aims of the thesis:

1. *Lay out a clear picture of the underlying physical principles, developments, trends and current state of techniques that meet the requirements for* in situ *thin film analysis*

Chapter 2 follows the historical development and trends of *in situ* thin film metrology, while laying out the underlying optical phenomena. Earlier monochromatic point reflectance and scattering studies are discussed, through to the widespread introduction of 2D measurements, for both large area reflectance imaging for drying kinetics and microscopy studies for direct imaging of morphology. The exploration of the literature emphasises the lack of use of RGB colour metrology for *in situ* processing, where most studies opt for a monochromatic approach. It also highlighted the power of spectral measurements for elucidating understanding of films, and how these largely have not followed the same trend as monochromatic measurements (being extended to imaging) because of the technological

difficulty of achieving snapshot HSI at satisfactory frame rates, at high resolution, and in a cost-effective manner.

2. *Develop a full and quantifiable understanding of the fundamental limits of broadband colour imaging for film characterisation*

Chapter 3 explores in depth the reasons for the limitations of broadband RGB film metrology. Due to integration over very wide band detection, the reflectance spectrum is not recoverable from RGB colour. In addition, this standard RGB colour detection results in an inherent upper-thickness recovery because the bulk colour of the film emerges very quickly, again due to the wide colour width. The necessary requirements in frame rate and and illumination time are also discussed for stroboscopic spin coating, however, these principles can also be applied to other processing methods.

3. *Overcome the many-to-one colour-to-thickness mappings experienced by broadband colour imaging of films*

Chapter 3 also proposes a technique for overcoming the colour-to-thickness ambiguity, by developing a novel *in situ* colour-to-thickness relationship. This is subsequently solved and a shortlist of many possible thicknesses is mapped to all points in the video. The most appropriate thickness is then selected using physical constraints of the process. This successfully demonstrated that the the many-to-one relationship could be overcome, and was the largest area reflectance imaging study of its kind, recovering the thickness profiles of spun-coated solvent films over 3" wafers.

4. *Explore the effectiveness of spectral reconstruction techniques to enhance the power of colour imaging for film metrology*

Chapter 4 extends normal RGB imaging by altering the detection method. A novel and inexpensive way to achieve multispectral (6 channel) imaging via a Bayer filtered colour camera and MBP dichroic beam splitter is presented, and the implications for film characterisation are explored. The reduced detection width extends the range and the additional spectral resolution makes thickness recovery more robust compared to that obtained with conventional RGB imaging. Besides this, spectral reconstruction techniques are applied for the first time to thin film thickness recovery using the 6 channel data, and

were shown to be successful in recovering some thicknesses, with a reduced amount of a priori information necessary compared to colour model based counterparts.

5. *Demonstrate the effectiveness of the Bayer filter as a tool in imaging metrology when paired with multiple wavelength monochromatic illumination*

Chapter 5 introduces trichromatic RGB illumination, used in conjunction with a Bayer filter camera, which allows interference patterns at three wavelengths to be recorded. The well-documented limitation of analogous monochromatic studies (peak order ambiguity) is then overcome by a completely novel extrema sequencing technique. The introduction of this method allows colour imaging metrology to be a powerful, independent, and inexpensive tool for spatially resolved *in situ* thin film metrology where other (ex situ) techniques were previously necessary.

6.2 Outlook and future work

A barrier to implementation of the work presented in Chapter 3 as an *in situ* method for thickness recovery is that processing times are currently excessive. The colour-to-thickness mapping process is fundamentally a good candidate for parallelisation because each pixel stack (through time) can be processed independently. Implementation of this should aim to reduce the processing time to matters of minutes, instead of hours, so that the tool has significant advantages over time-consuming ex situ methods.

The work in Chapter 4 presented a pseudoinverse spectral reconstruction technique from multispectral data; however, differing, more complex techniques are available and should be explored. The technique in Chapter 4 would certainly benefit from optimisation of the bandpass characteristics of the MBP dichroic beam splitter. Here an off-the-shelf component was used with sub-optimal characteristics. In addition, multispectral and hyperspectral datasets are conducive to the application of machine learning techniques in architectures such as CNN. Deep learning has already had successful applications on other HSI datasets, and its applicability to film characterisation could be further explored in future work.

The trichromatic sequencing technique developed in Chapter 5 has great potential for future advances. In the chapter, the proof of the concept was successfully demonstrated on the fringes of a thinning film through time. The technique should be explored on

nonuniform (either static or dynamic) films by sequencing across space instead of in time as demonstrated in Chapter 5. In addition, the processing time can be improved by sequencing at fewer points in the video and then using either 2D (framewise) of 3D (whole video) phase-unwrapping algorithms to easily generate the rest of the thicknesses from the sequence matched point. This may be able to increase the speed of the technique so that processing can be done at around the camera frame rate, meaning that the metrology could be achieved on the fly and in real time.

The use of a sufficiently narrow line width MBP filter (around 5 nm - 2 nm) in red, green, and blue camera bands would allow the technique to reliably work on thicker films. The advantage of this being that high power LED illumination could be used which mitigates some of the challenges of practically implementing the technique over large areas. Recently, commercially available laser projectors have also been used successfully as an effective illumination source for the technique (as yet unpublished work) because they contain laser diodes with two red wavelengths, two green wavelengths, and one blue wavelength. Using this 'pentachromatic' illumination comes with more complicated crosstalk and beat behaviour within the colour channels that needs extra consideration.

Finally, the technique could be applied to single-shot Michaelson interferometry for opaque discontinuous surfaces. For example, if a stepped surface was positioned appropriately so that trichromatic colour fringes could be observed and sequenced either side of the step, then the step height could be found. This is not possible in conventional monochromatic Michaelson interferometry, where the step height would remain ambiguous. It is possible to easily implement interferometry by using an interference objective rather than needing a reference beam/arm, this also makes the system more compact for integration onto film processing equipment.

Bibliography

[1] Jack B.P. Atkinson and Jonathan R. Howse. "In-situ full-wafer metrology via coupled white light and monochromatic stroboscopic illumination". In: *Optics and Lasers in Engineering* 184.P2 (2025), p. 108692. DOI: 10.1016/j.optlaseng.2024.108692.

[2] Aleksei Solomonov et al. "Flexible Soft-Printed Polymer Films with Tunable Plasmonic Properties". In: *ACS Materials Au* 3.6 (2023), pp. 699–710. DOI: 10.1021/acsmaterialsau.3c00023.

[3] Varun S. Prasath and Kenneth K.S. Lau. "Kinetically Limited Bulk Polymerization of Polymer Thin Films by Initiated Chemical Vapor Deposition". In: *Macromolecules* 56.24 (2023), pp. 10111–10118. DOI: 10.1021/acs.macromol.3c01868.

[4] Zhengran He, Kyeiwaa Asare, and Yeboah Sheng. "Polystyrene applications in organic electronics". In: *Discover Electronics* August (2024). DOI: 10.1007/s44291-024-00039-6.

[5] Longjian Xue, Jilin Zhang, and Yanchun Han. "Phase separation induced ordered patterns in thin polymer blend films". In: *Progress in Polymer Science (Oxford)* 37.4 (2012), pp. 564–594. DOI: 10.1016/j.progpolymsci.2011.09.001.

[6] Hannah J. Eggimann et al. "Efficient energy transfer mitigates parasitic light absorption in molecular charge-extraction layers for perovskite solar cells". In: *Nature Communications* 11.1 (2020). DOI: 10.1038/s41467-020-19268-w.

[7] Fei Qin et al. "Robust metal ion-chelated polymer interfacial layer for ultraflexible non-fullerene organic solar cells". In: *Nature Communications* 11.1 (2020), pp. 1–8. DOI: 10.1038/s41467-020-18373-0.

[8] Elena Missale, Marco Frasconi, and Maria F. Pantano. "Ultrathin organic membranes: Can they sustain the quest for mechanically robust device applications?" In: *iScience* 26.2 (2023), p. 105924. DOI: 10.1016/j.isci.2023.105924.

[9] Saif M.H. Qaid et al. "Tuning the optical properties of meh–ppv/pfo hybrid thin films via the incorporation of cspbbr3 quantum dots". In: *Coatings* 11.2 (2021), pp. 1–15. DOI: 10.3390/coatings11020154.

[10] Sam Coveney. "Fundamentals of Phase Separation in Polymer Blend Thin Films". In: *Springer Theses* September (2015), p. 179.

[11] Michael P. Howard, Arash Nikoubashman, and Athanassios Z. Panagiotopoulos. "Stratification in Drying Polymer-Polymer and Colloid-Polymer Mixtures". In: *Langmuir* 33.42 (2017), pp. 11390–11398. DOI: 10.1021/acs.langmuir.7b02074.

[12] Peter Petrik. "Optical thin film metrology for optoelectronics". In: *Journal of Physics: Conference Series* 398.1 (2012). DOI: 10.1088/1742-6596/398/1/012002.

[13] Dietrich Meyerhofer. "Characteristics of resist films produced by spinning". In: *Journal of Applied Physics* 49.7 (1978), pp. 3993–3997. DOI: 10.1063/1.325357.

[14] Joana Moreira, A. Catarina Vale, and Natália M. Alves. "Spin-coated freestanding films for biomedical applications". In: *Journal of Materials Chemistry B* 9.18 (2021), pp. 3778–3799. DOI: 10.1039/d1tb00233c.

[15] Dunbar P. Birnie, Dylan E. Haas, and Carissa M. Hernandez. "Laser interferometric calibration for real-time video color interpretation of thin fluid layers during spin coating". In: *Optics and Lasers in Engineering* 48.5 (2010), pp. 533–537. DOI: 10.1016/j.optlaseng.2009.12.021.

[16] Alfred G. Emslie, Francis T. Bonner, and Leslie G. Peck. "Flow of a viscous liquid on a rotating disk". In: *Journal of Applied Physics* 29.5 (1958), pp. 858–862. DOI: 10.1063/1.1723300.

[17] Kangkang Weng et al. "Optimized active layer morphology toward efficient and polymer batch insensitive organic solar cells". In: *Nature Communications* 11.1 (2020), pp. 1–9. DOI: 10.1038/s41467-020-16621-x.

[18] Bradley P. Kirk et al. "Printing and Coating Techniques for Scalable Organic Photovoltaic Fabrication". In: *Materials* 17.11 (2024). DOI: 10.3390/ma17112511.

[19] Yoshiro Yamashita. "Organic semiconductors for organic field-effect transistors". In: *Science and Technology of Advanced Materials* 10.2 (2009). DOI: 10.1088/1468-6996/10/2/024313.

[20] Yongbo Yuan et al. "Ultra-high mobility transparent organic thin film transistors grown by an off-centre spin-coating method". In: *Nature Communications* 5 (2014), pp. 1–9. DOI: 10.1038/ncomms4005.

[21] Nam Koo Kim et al. "High-Performance Organic Field-Effect Transistors with Directionally Aligned Conjugated Polymer Film Deposited from Pre-Aggregated Solution". In: *Chemistry of Materials* 27.24 (2015), pp. 8345–8353. DOI: 10.1021/acs.chemmater.5b03775.

[22] Liangkun Lu et al. "High-performance flexible organic field effect transistors with print-based nanowires". In: *Microsystems and Nanoengineering* 9.1 (2023). DOI: 10.1038/s41378-023-00551-x.

[23] Niranjan Sahu, B. Parija, and S. Panigrahi. "Fundamental understanding and modeling of spin coating process: A review". In: *Indian Journal of Physics* 83.4 (2009), pp. 493–502. DOI: 10.1007/s12648-009-0009-z.

[24] Severin Siegrist et al. "Understanding Coating Thickness and Uniformity of Blade-Coated SnO2 Electron Transport Layer for Scalable Perovskite Solar Cells". In: *Solar RRL* 7.14 (2023). DOI: 10.1002/solr.202300273.

[25] Maël Le Berre, Yong Chen, and Damien Baigl. "From convective assembly to landau - Levich deposition of multilayered phospholipid films of controlled thickness". In: *Langmuir* 25.5 (2009), pp. 2554–2557. DOI: 10.1021/la803646e.

[26] Ryungeun Song et al. "Physics-informed machine learning for optimizing the coating conditions of blade coating Physics-informed machine learning for optimizing the coating conditions of blade coating". In: *Phys. Fluids* 34 (2022). DOI: 10.1063/5.0098666.

[27] Xiaodan Gu et al. "The meniscus-guided deposition of semiconducting polymers". In: *Nature Communications* 9.1 (2018). DOI: 10.1038/s41467-018-02833-9.

[28] Sebastian A. Schneider et al. "Controlling Polymer Morphology in Blade-Coated All-Polymer Solar Cells". In: *Chemistry of Materials* 33.15 (2021), pp. 5951–5961. DOI: 10.1021/acs.chemmater.1c01050.

[29] Dawei Wu et al. "Blade Coating Aligned, High-Performance, Semiconducting-Polymer Transistors". In: *Chemistry of Materials* 30.6 (2018), pp. 1924–1936. DOI: 10.1021/acs.chemmater.7b04835.

[30] Farshad Jafarzadeh et al. "Stable and sustainable perovskite solar modules by optimizing blade coating nickel oxide deposition over 15 × 15 cm2 area". In: *Communications Materials* 5.1 (2024), pp. 1–9. DOI: 10.1038/s43246-024-00576-3.

[31] Hidenobu Miura and Masato Yamamura. "Direct thickness measurement of doctor-bladed liquid film on gravure roll surface". In: *Journal of Coatings Technology and Research* 12.5 (2015), pp. 827–833. DOI: 10.1007/s11998-015-9714-z.

[32] Jadel Tsiba Matondo et al. "Slot-Die Coating for Scalable Fabrication of Perovskite Solar Cells and Modules". In: *Advanced Materials Technologies* 9.10 (2024), pp. 1–24. DOI: 10.1002/admt.202302082.

[33] Kenneth J. Ruschak. "Limiting flow in a pre-metered coating device". In: *Chemical Engineering Science* 31.11 (1976), pp. 1057–1060. DOI: 10.1016/0009-2509(76)87026-1.

[34] B Levich L Landau. "Dragging of a liquid by a moving plate." In: *Acta Physicochium URSS* 17 (1942), pp. 42–54.

[35] B G Higgins and L E Scriven. "Capillary pressure and viscous pressure drop set bounds on coating bead operability". In: *Chemical Engineering Science* 35 (1979), pp. 673–782.

[36] Xiaoyu Ding, Jianhua Liu, and A. L. Tequila Harris. "A Review of the Operating Limits in Slot Die Coating Processes". In: *AIChE Journal* 62.7 (2016), pp. 2508–2524. DOI: 10.1002/aic. arXiv: 0201037v1 [arXiv:physics].

[37] Nam Gyu Park and Kai Zhu. "Scalable fabrication and coating methods for perovskite solar cells and solar modules". In: *Nature Reviews Materials* 5.5 (2020), pp. 333–350. DOI: 10.1038/s41578-019-0176-2.

[38] J. Kedzierski et al. "Determination of ordinary and extraordinary refractive indices of nematic liquid crystals by using wedge cells". In: *Opto-Electronics Review* 18.2 (2010), pp. 214–218. DOI: 10.2478/s11772-010-0009-8.

[39] A. H. Jarrett. "Atlas of optical phenomena: M. Cagnet, M. Francon and J.C. Thrierr: Springer-Verlag 1962. 45 pp. 74 DM". In: *Planetary and Space Science* 11 (1963), p. 584.

[40] W H Bragg and W L Bragg. "The reflection of X-rays by crystals". In: *Proc. R. Soc. Lond. A.* 88 (1913), pp. 428–438.

[41] Frank L. Pedrotti, Leno M. Pedrotti, and Leno S. Pedrotti. *Introduction to Optics*. Pearson Education, 2008.

[42] F. Horowitz et al. "Real-time optical monitoring of spin coating". In: *Journal de Physique III* 3.11 (1993), pp. 2059–2063. DOI: 10.1051/jp3:1993253.

[43] F. Horowitz, A. F. Michels, and E. M. Yeatman. "Optical Viscometry of Spinning Sol Coatings". In: *Journal of Sol-Gel Science and Technology* 13.1-3 (1998), pp. 707–712. DOI: 10.1023/a:1008697023104.

[44] Dunbar P. Birnie and Manuel Manley. "Combined flow and evaporation of fluid on a spinning disk". In: *Physics of Fluids* 9.4 (1997), pp. 870–875. DOI: 10.1063/1.869519.

[45] Dunbar P. Birnie and Manuel Manley. "Combined flow and evaporation of fluid on a spinning disk". In: *Physics of Fluids* 9.4 (1997), pp. 870–875. DOI: 10.1063/1.869519.

[46] Dylan E. Haas et al. "Effect of solvent evaporation rate on skin formation during spin coating of complex solutions". In: *Sol-Gel Optics V* 3943.May 2000 (2000), pp. 280–284. DOI: 10.1117/12.384348.

[47] B. Reisfeld, S. G. Bankoff, and S. H. Davis. "The dynamics and stability of thin liquid films during spin coating. I. Films with constant rates of evaporation or absorption". In: *Journal of Applied Physics* 70.10 (1991), pp. 5258–5266. DOI: 10.1063/1.350235.

[48] Y. Mouhamad et al. "Dynamics of polymer film formation during spin coating". In: *Journal of Applied Physics* 116.12 (2014). DOI: 10.1063/1.4896674.

[49] A. D.F. Dunbar et al. "A solution concentration dependent transition from self-stratification to lateral phase separation in spin-cast PS:d-PMMA thin films". In:

European Physical Journal E 31.4 (2010), pp. 369–375. DOI: 10.1140/epje/i2010-10592-4.

[50] Paul C. Jukes et al. "Time-resolved light scattering studies of phase separation in thin film semiconducting polymer blends during spin-coating". In: *Macromolecules* 38.6 (2005), pp. 2030–2032. DOI: 10.1021/ma0477145.

[51] Sasha Y. Heriot and Richard A.L. Jones. "An interfacial instability in a transient wetting layer leads to lateral phase separation in thin spin-cast polymer-blend films". In: *Nature Materials* 4.10 (2005), pp. 782–786. DOI: 10.1038/nmat1476.

[52] Dunbar P. Birnie. "Optical video interpretation of interference colors from thin transparent films on silicon". In: *Materials Letters* 58.22-23 (2004), pp. 2795–2800. DOI: 10.1016/j.matlet.2004.04.018.

[53] Dylan E. Haas and Dunbar P. Birnie. "Nondestructive measurement of striation defect spacing using laser diffraction". In: *Journal of Materials Research* 16.12 (2001), pp. 3355–3360. DOI: 10.1557/JMR.2001.0463.

[54] Stefan Walheim et al. "Structure formation via polymer demixing in spin-cast films". In: *Macromolecules* 30.17 (1997), pp. 4995–5003. DOI: 10.1021/ma9619288.

[55] Parvaneh Mokarian-Tabari. "Controlling the Morphology of Spin coated Polymer Blend Films". PhD thesis. University of Sheffield, 2009.

[56] Jacobus J. Van Franeker et al. "A real-time study of the benefits of co-solvents in polymer solar cell processing". In: *Nature Communications* 6 (2015), pp. 1–8. DOI: 10.1038/ncomms7229.

[57] Yanfeng Liu et al. "In Situ Optical Studies on Morphology Formation in Organic Photovoltaic Blends". In: *Small Methods* 5.10 (2021). DOI: 10.1002/smtd.202100585.

[58] B. Schmidt-Hansberg et al. "In situ monitoring the drying kinetics of knife coated polymer-fullerene films for organic solar cells". In: *Journal of Applied Physics* 106.12 (2009). DOI: 10.1063/1.3270402.

[59] Nusret S. Güldal et al. "Real-time evaluation of thin film drying kinetics using an advanced, multi-probe optical setup". In: *Journal of Materials Chemistry C* 4.11 (2016), pp. 2178–2186. DOI: 10.1039/c5tc03448e.

[60] Simon Ternes et al. “Drying Dynamics of Solution-Processed Perovskite Thin-Film Photovoltaics: In Situ Characterization, Modeling, and Process Control”. In: *Advanced Energy Materials* 9.39 (2019). DOI: 10.1002/aenm.201901581.

[61] R Swanepoel. “Determination of the thickness and optical constants of amorphous silicon”. In: *Journal of Physics E: Sci. Instrum.* 16 (1983), p. 1214. DOI: 10.1080/14786430902835644.

[62] Lyashenko S. P. “A simple method for the determination of the thickness and optical constants of semiconducting and dielectric layers”. In: *Opt. Spectrosc.* 16 (1964), pp. 80–81.

[63] J Wales, GJ Lovitt, and RA Hill. “Optical properties of germanium films in the 1–5 μ range”. In: *Thin Solid Films* 1.2 (1967), pp. 137–150.

[64] J Szczyrbowski and A Czapla. “Optical absorption in DC sputtered InAs films”. In: *Thin Solid Films* 46.2 (1977), pp. 127–137.

[65] Abdelaziz Tchenka, Abdelali Agdad, and Elmaati Ech-Chamikh. “Determination of the thickness and optical properties by reflectance method”. In: *Infrared Physics and Technology* 137.September 2023 (2024). DOI: 10.1016/j.infrared.2024.105117.

[66] I. Chambouleyron et al. “Retrieval of optical constants and thickness of thin films from transmission spectra”. In: *Appl. Opt.* 36.31 (1997), pp. 8238–8247.

[67] Jiři Luňáček, Petr Hlubina, and Milena Luňáčková. “Simple method for determination of the thickness of a nonabsorbing thin film using spectral reflectance measurement”. In: *Applied Optics* 48.5 (2009), pp. 985–989. DOI: 10.1364/AO.48.000985.

[68] Jingtao Dong and Rongsheng Lu. “Characterization of weakly absorbing thin films by multiple linear regression analysis of absolute unwrapped phase in angle-resolved spectral reflectometry”. In: *Opt. Express* 26.9 (2018), pp. 12291–12305. DOI: 10.1364/OE.26.012291.

[69] Kwangrak Kim, Soonyang Kwon, and Heui Jae Pahk. “Fast analysis of film thickness in spectroscopic reflectometry using direct phase extraction”. In: *Current Optics and Photonics* 1.1 (2017), pp. 29–33. DOI: 10.3807/COPP.2017.1.1.029.

[70] M. D. Heinemann et al. “Evolution of opto-electronic properties during film formation of complex semiconductors”. In: *Scientific Reports* 7.April (2017), pp. 1–9. DOI: 10.1038/srep45463.

[71] Min Gab Kim. “Improved Measurement of Thin Film Thickness in Spectroscopic Reflectometer Using Convolutional Neural Networks”. In: *International Journal of Precision Engineering and Manufacturing* 21.2 (2020), pp. 219–225. DOI: 10.1007/s12541-019-00260-4.

[72] Stephan Van Duren et al. “Investigation of reflectometry for in situ process monitoring and characterization of co-evaporated and stacked Cu-Zn-Sn-S based thin films”. In: *Journal of Alloys and Compounds* 779 (Jan. 2019). DOI: 10.1016/j.jallcom.2018.11.337.

[73] Steven J. Byrnes. *Multilayer optical calculations*. 2020. arXiv: 1603.02720 [physics.comp-ph].

[74] Timo Raab et al. “Resolving the Spin Coating Process via in Situ Transmission Measurements”. In: *Journal of Physical Chemistry C* 126.45 (2022), pp. 19542–19548. DOI: 10.1021/acs.jpcc.2c06337.

[75] Hyun Wook Ro et al. “Morphology changes upon scaling a high-efficiency, solution-processed solar cell”. In: *Energy and Environmental Science* 9.9 (2016), pp. 2835–2846. DOI: 10.1039/c6ee01623e.

[76] Maged Abdelsamie et al. “In situ UV-visible absorption during spin-coating of organic semiconductors: A new probe for organic electronics and photovoltaics”. In: *Journal of Materials Chemistry C* 2.17 (2014), pp. 3373–3381. DOI: 10.1039/c3tc32077d.

[77] Jörg Rappich et al. “Fast Optical Reflectance Measurements during Spin Coating and Annealing of Organic–Inorganic Perovskite Precursor Solutions”. In: *Physica Status Solidi (B) Basic Research* 258.5 (2021), pp. 1–8. DOI: 10.1002/pssb.202000479.

[78] Jonas Bergqvist et al. “In situ reflectance imaging of organic thin film formation from solution deposition”. In: *Solar Energy Materials and Solar Cells* 114 (2013), pp. 89–98. DOI: 10.1016/j.solmat.2013.02.030.

[79] Simon Ternes et al. “Correlative In Situ Multichannel Imaging for Large-Area Monitoring of Morphology Formation in Solution-Processed Perovskite Layers”. In: *Solar RRL* 6.3 (2022). DOI: 10.1002/solr.202100353.

[80] Nina Taherimakhsousi et al. “A machine vision tool for facilitating the optimization of large-area perovskite photovoltaics”. In: *npj Computational Materials* 7.1 (2021). DOI: 10.1038/s41524-021-00657-8.

[81] Chuan Liu et al. “Self-assembly of semiconductor/insulator interfaces in one-step spin-coating: A versatile approach for organic field-effect transistors”. In: *Physical Chemistry Chemical Physics* 15.21 (2013), pp. 7917–7933. DOI: 10.1039/c3cp44715d.

[82] Youna Choi, Byoung Hoon Lee, and Heejoo Kim. “Bicontinuous network of electron donor-acceptor composites achieved by additive-free sequential deposition for efficient polymer solar cells”. In: *Current Applied Physics* 20.6 (2020), pp. 760–764. DOI: 10.1016/j.cap.2020.03.011.

[83] Kang Wei Chou et al. “Spin-cast bulk heterojunction solar cells: A dynamical investigation”. In: *Advanced Materials* 25.13 (2013), pp. 1923–1929. DOI: 10.1002/adma.201203440.

[84] Kui Zhao et al. “Vertical Phase Separation in Small Molecule:Polymer Blend Organic Thin Film Transistors Can Be Dynamically Controlled”. In: *Advanced Functional Materials* 26.11 (2016), pp. 1737–1746. DOI: 10.1002/adfm.201503943.

[85] Loni M. Peurrung and David B. Graves. “Spin Coating Over Topography”. In: *IEEE Transactions on Semiconductor Manufacturing* 6.1 (1993), pp. 72–76. DOI: 10.1109/66.210660.

[86] L. M. Peurrung and D. B. Graves. “Film Thickness Profiles over Topography in Spin Coating”. In: *Journal of The Electrochemical Society* 138.7 (1991), pp. 2115–2124. DOI: 10.1149/1.2085935.

[87] Kang Wei Chou et al. “Late stage crystallization and healing during spin-coating enhance carrier transport in small-molecule organic semiconductors”. In: *Journal of Materials Chemistry C* 2.28 (2014), pp. 5681–5689. DOI: 10.1039/c4tc00981a.

[88] Jung Hun Lee et al. “Effect of Crystallization Modes in TIPS-pentacene/Insulating Polymer Blends on the Gas Sensing Properties of Organic Field-Effect Transistors”. In: *Scientific Reports* 9.1 (2019), pp. 1–9. DOI: 10.1038/s41598-018-36652-1.

[89] Stephen Ebbens et al. “In situ imaging and height reconstruction of phase separation processes in polymer blends during spin coating”. In: *ACS Nano* 5.6 (2011), pp. 5124–5131. DOI: 10.1021/nn201210e.

[90] Daniel T.W. Toolan et al. “Direct observation of morphological development during the spin-coating of polystyrene-poly(methyl methacrylate) polymer blends”. In: *Journal of Polymer Science, Part B: Polymer Physics* 51.11 (2013), pp. 875–881. DOI: 10.1002/polb.23288.

[91] Daniel T.W. Toolan et al. “In situ studies of phase separation and crystallization directed by Marangoni instabilities during spin-coating”. In: *Advanced Materials* 25.48 (2013), pp. 7033–7037. DOI: 10.1002/adma.201302657.

[92] Daniel T.W. Toolan et al. “Directed phase separation of PFO:PS blends during spin-coating using feedback controlled in situ stroboscopic fluorescence microscopy”. In: *Journal of Materials Chemistry A* 1.11 (2013), pp. 3587–3592. DOI: 10.1039/c3ta01530k.

[93] Daniel T.W. Toolan, Richard Hodgkinson, and Jonathan R. Howse. “Stroboscopic microscopy - Direct imaging of structure development and phase separation during spin-coating”. In: *Journal of Polymer Science, Part B: Polymer Physics* 52.1 (2014), pp. 17–25. DOI: 10.1002/polb.23410.

[94] Ehtsham Ul Haq et al. “Real time laser interference microscopy for bar-spread polystyrene/ poly(methyl methacrylate) blends”. In: *Journal of Polymer Science, Part B: Polymer Physics* 52.15 (2014), pp. 985–992. DOI: 10.1002/polb.23513.

[95] Tsengelidis Savvas. “Algebraic modelling of transformations from Bayer to RGB images”. PhD thesis. Technical University of Crete, 2006.

[96] Yoshie Kobayashi et al. “Reconstructing Shapes and Appearances of Thin Film Objects Using RGB Images”. In: *Proceedings of the IEEE Computer Society Conference on Computer Vision and Pattern Recognition* 2016-Decem (2016), pp. 3774–3782. DOI: 10.1109/CVPR.2016.410.

[97] Michal Urbánek et al. “Imaging reflectometry in situ”. In: *Applied Optics* 46.25 (2007), pp. 6309–6313. DOI: 10.1364/AO.46.006309.

[98] Jiao Bai et al. “A new method to measure spectral reflectance and film thickness using a modified chromatic confocal sensor”. In: *Optics and Lasers in Engineering* 154.September 2023 (2022). DOI: 10.1016/j.optlaseng.2022.107019.

[99] L. Gustafsson, E. Hglund, and O. Marklund. “Measuring Lubricant Film Thickness with Image Analysis”. In: *Proceedings of the Institution of Mechanical Engineers, Part J: Journal of Engineering Tribology* 208.3 (1994), pp. 199–205. DOI: 10.1243/PIME_PROC_1994_208_371_02.

[100] Garam Choi et al. “Simple method for volumetric thickness measurement using a color camera”. In: *Applied Optics* 57.26 (2018), p. 7550. DOI: 10.1364/ao.57.007550.

[101] Nils Bornemann and Edgar Dörsam. “A flatbed scanner for large-area thickness determination of ultra-thin layers in printed electronics”. In: *Optics Express* 21.19 (2013), p. 21897. DOI: 10.1364/oe.21.021897.

[102] Garima Jaiswal, Arun Sharma, and Sumit Kumar Yadav. “Critical insights into modern hyperspectral image applications through deep learning”. In: *Wiley Interdisciplinary Reviews: Data Mining and Knowledge Discovery* 11.6 (2021), pp. 1–22. DOI: 10.1002/widm.1426.

[103] V. Chandran Suja et al. “Hyperspectral imaging for dynamic thin film interferometry”. In: *Scientific Reports* 10.1 (2020), pp. 1–8. DOI: 10.1038/s41598-020-68433-0.

[104] Gary A Shaw and Hsiao-hua K Burke. “Spectral imaging for remote sensing”. In: *Lincon laboratory journal* 14.1 (2003), pp. 3–28.

[105] Olesya Daikos et al. “Near-infrared hyperspectral imaging for monitoring the thickness distribution of thin poly(3,4-ethylenedioxythiophene):poly(styrene sulfonate) (PEDOT:PSS) layers”. In: *Talanta* 223.1 (2021), p. 121696. DOI: 10.1016/j.talanta.2020.121696.

[106] Gilbert El-Hajje et al. “Quantification of spatial inhomogeneity in perovskite solar cells by hyperspectral luminescence imaging”. In: *Energy and Environmental Science* 9.7 (2016), pp. 2286–2294. DOI: 10.1039/c6ee00462h.

[107] Dhritiman Saha and Annamalai Manickavasagan. "Machine learning techniques for analysis of hyperspectral images to determine quality of food products: A review". In: *Current Research in Food Science* 4.December 2020 (2021), pp. 28–44. DOI: 10.1016/j.crfs.2021.01.002.

[108] Rong Wong et al. "HSI-IPNet: Hyperspectral Imagery Inpainting by Deep Learning with Adaptive Spectral Extraction". In: *IEEE Journal of Selected Topics in Applied Earth Observations and Remote Sensing* 13 (2020), pp. 4369–4380. DOI: 10.1109/JSTARS.2020.3012443.

[109] Chao Zuo et al. *Deep learning in optical metrology: a review*. Vol. 11. 1. Springer US, 2022. DOI: 10.1038/s41377-022-00714-x.

[110] Doo-Hyun Cho et al. "High-speed wafer film measurement with heterogeneous optical sensor system". In: *SPIE Vol. 11611 116110H-3*. 2021. DOI: 10.1117/12.2584200.

[111] Ville Heikkinen et al. "Evaluation and unification of some methods for estimating reflectance spectra from RGB images". In: *Journal of the Optical Society of America A* 25.10 (2008), p. 2444. DOI: 10.1364/josaa.25.002444.

[112] Noriyuki Shimano. "Recovery of spectral reflectances of objects being imaged without prior knowledge". In: *IEEE Transactions on Image Processing* 15.7 (2006), pp. 1848–1856. DOI: 10.1109/TIP.2006.877069.

[113] Filiz Yesilkoy et al. "Ultrasensitive hyperspectral imaging and biodetection enabled by dielectric metasurfaces". In: *Nature Photonics* 13.6 (2019), pp. 390–396. DOI: 10.1038/s41566-019-0394-6.

[114] Kerry Maize et al. "Real-Time Metrology for Roll-To-Roll and Advanced Inline Manufacturing: A Review". In: *Advanced Materials Technologies* 8.2 (2023). DOI: 10.1002/admt.202200173.

[115] Si Joon Kim, Seokhyun Yoon, and Hyun Jae Kim. "Review of solution-processed oxide thin-film transistors". In: *Journal of Applied Physics* 53 (2014). DOI: 10.7567/JJAP.53.02BA02.

[116] Hiroyuki Matsui, Yasunori Takeda, and Shizuo Tokito. "Flexible and printed organic transistors: From materials to integrated circuits". In: *Organic Electronics* 75.September (2019), p. 105432. DOI: 10.1016/j.orgel.2019.105432.

[117] Zhicheng Hu, Fei Huang, and Yong Cao. "Layer-by-Layer Assembly of Multilayer Thin Films for Organic Optoelectronic Devices". In: *Small Methods* 1.12 (2017), pp. 1–12. DOI: 10.1002/smtd.201700264.

[118] Chunyang Li et al. "Preparation and optical properties of nanostructure thin films". In: *Applied Nanoscience (Switzerland)* 11.7 (2021), pp. 1967–1976. DOI: 10.1007/s13204-021-01930-4.

[119] Xu Dong Wang et al. "Recent Advances in Halide Perovskite Single-Crystal Thin Films: Fabrication Methods and Optoelectronic Applications". In: *Solar RRL* 3.4 (2019), pp. 1–27. DOI: 10.1002/solr.201800294.

[120] Pan Zhao et al. "Research and Application Progress of Conductive Films in Energy Storage Devices". In: *Advanced Materials Technologies* 2300194 (2023), pp. 1–23. DOI: 10.1002/admt.202300194.

[121] Li Hui Chou et al. "Semiconducting small molecule/polymer blends for organic transistors". In: *Polymer* 191.January (2020), p. 122208. DOI: 10.1016/j.polymer.2020.122208.

[122] K. Dalnoki-Veress et al. "Phase separation morphology of spin-coated polymer blend thin films". In: *Physica A: Statistical Mechanics and its Applications* 239.1-3 (1997), pp. 87–94. DOI: 10.1016/S0378-4371(96)00471-2.

[123] Peng Jiang and Michael J. McFarland. "Large-scale fabrication of wafer-size colloidal crystals, macroporous polymers and nanocomposites by spin-coating". In: *Journal of the American Chemical Society* 126.42 (2004), pp. 13778–13786. DOI: 10.1021/ja0470923.

[124] Moorthi Pichumani et al. "Dynamics, crystallization and structures in colloid spin coating". In: *Soft Matter* 9.12 (2013), pp. 3220–3229. DOI: 10.1039/c3sm27455a.

[125] Daniel T.W. Toolan, Richard Hodgkinson, and Jonathan R. Howse. "Stroboscopic microscopy - Direct imaging of structure development and phase separation during spin-coating". In: *Journal of Polymer Science, Part B: Polymer Physics* 52.1 (2014), pp. 17–25. DOI: 10.1002/polb.23410.

[126] Junhu Zhang et al. "Colloidal self-assembly meets nanofabrication: From two-dimensional colloidal crystals to nanostructure arrays". In: *Advanced Materials* 22.38 (2010), pp. 4249–4269. DOI: 10.1002/adma.201000755.

[127] Tao Wang et al. “The development of nanoscale morphology in polymer:fullerene photovoltaic blends during solvent casting”. In: *Soft Matter* 6.17 (2010), pp. 4128–4134. DOI: 10.1039/c0sm00343c.

[128] Mihirsinh Chauhan et al. “Investigating two-step MAPbI3 thin film formation during spin coating by simultaneous: In situ absorption and photoluminescence spectroscopy”. In: *Journal of Materials Chemistry A* 8.10 (2020), pp. 5086–5094. DOI: 10.1039/c9ta12409h.

[129] Noura Alhazmi et al. “Perovskite Crystallization Dynamics during Spin-Casting: An in Situ Wide-Angle X-ray Scattering Study”. In: *ACS Applied Energy Materials* 3.7 (2020), pp. 6155–6164. DOI: 10.1021/acsaem.9b02470.

[130] Dounya Barrit et al. “Processing of Lead Halide Perovskite Thin Films Studied with In-Situ Real-Time X-ray Scattering”. In: *ACS Applied Materials and Interfaces* 14.23 (2022), pp. 26315–26326. DOI: 10.1021/acsami.2c03153.

[131] Daniel T.W. Toolan et al. “On the mechanisms of colloidal self-assembly during spin-coating”. In: *Soft Matter* 10.44 (2014), pp. 8804–8812. DOI: 10.1039/c4sm01711k.

[132] O S Heavens. “Optical Properties of Thin Films”. In: *Reports on Progress in Physics* 23.1 (1960). DOI: 10.1080/713818200.

[133] John M. Frostad et al. “Dynamic fluid-film interferometry as a predictor of bulk foam properties”. In: *Soft Matter* 12.46 (2016), pp. 9266–9279. DOI: 10.1039/C6SM01361A.

[134] S. Sett, S. Sinha-Ray, and A. L. Yarin. “Gravitational drainage of foam films”. In: *Langmuir* 29.16 (2013), pp. 4934–4947. DOI: 10.1021/la4003127.

[135] Eiki Goto et al. “Computer-Synthesis of an Interference Color Chart of Human Tear Lipid Layer, by a Colorimetric Approach”. In: *Investigative Ophthalmology and Visual Science* 44.11 (2003), pp. 4693–4697. DOI: 10.1167/iovs.03-0260.

[136] Yiran Zhang and Vivek Sharma. “Domain expansion dynamics in stratifying foam films: Experiments”. In: *Soft Matter* 11.22 (2015), pp. 4408–4417. DOI: 10.1039/c5sm00066a.

[137] C. Willert et al. “Pulsed operation of high-power light emitting diodes for imaging flow velocimetry”. In: *Measurement Science and Technology* 21.7 (2010). DOI: 10.1088/0957-0233/21/7/075402.

[138] Dunbar P. Birnie. "Combined flow and evaporation during spin coating of complex solutions". In: *Journal of Non-Crystalline Solids* 218 (1997), pp. 174–178. DOI: 10.1016/S0022-3093(97)00141-5.

[139] Katsuichi Kitagawa. "Single-shot surface profiling by multiwavelength interferometry without carrier fringe introduction". In: *Journal of Electronic Imaging* 21.2 (2012), p. 021107. DOI: 10.1117/1.jei.21.2.021107.

[140] P. Hlubina et al. "Spectral interferometry and reflectometry used to measure thin films". In: *Applied Physics B: Lasers and Optics* 92.2 (2008), pp. 203–207. DOI: 10.1007/s00340-008-3093-4.

[141] Jungjae Park et al. "A Review of Thickness Measurements of Thick Transparent Layers Using Optical Interferometry". In: *International Journal of Precision Engineering and Manufacturing* 20.3 (2019), pp. 463–477. DOI: 10.1007/s12541-019-00105-0.

[142] Xingchen Dong et al. "Line-Scan Hyperspectral Imaging Microscopy with Linear Unmixing for Automated Two-Dimensional Crystals Identification". In: *ACS Photonics* 7.5 (2020), pp. 1216–1225. DOI: 10.1021/acsphotonics.0c00050.

[143] Prabuddha Mukherjee et al. "Relating Post-yield Mechanical Behavior in Polyethylenes to Spatially Varying Molecular Deformation Using Infrared Spectroscopic Imaging: Homopolymers". In: *Macromolecules* 51.10 (2018), pp. 3836–3844. DOI: 10.1021/acs.macromol.8b00363.

[144] Meguya Ryu et al. "Hyperspectral molecular orientation mapping in metamaterials". In: *Applied Sciences (Switzerland)* 11.4 (2021), pp. 1–13. DOI: 10.3390/app11041544.

[145] Dominic Lepage et al. "Conic hyperspectral dispersion mapping applied to semiconductor plasmonics". In: *Light: Science and Applications* 1.SEPTEMBER (2012), pp. 1–8. DOI: 10.1038/lsa.2012.28.

[146] Changhyeong Yoon et al. "Toward realization of high-throughput hyperspectral imaging technique for semiconductor device metrology". In: *Journal of Micro/Nanopatterning, Materials and Metrology* 21.2 (2022), pp. 1–13. DOI: 10.1117/1.JMM.21.2.021209.

[147] Susanne Dogan-surmeier et al. “Towards in-line real-time characterization of roll-to-roll produced ZTO/Ag/ITO thin films by hyperspectral imaging”. In: *J. Phys. D: Appl. Phys* 56 (2023).

[148] Jonas Skovlund Madsen et al. “In-line characterization of nanostructures produced by roll-to-roll nanoimprinting”. In: *Optics Express* 29.3 (2021), p. 3882. DOI: 10.1364/oe.411669.

[149] Jingang Zhang et al. “A survey on computational spectral reconstruction methods from RGB to hyperspectral imaging”. In: *Scientific Reports* 12.1 (2022), pp. 1–17. DOI: 10.1038/s41598-022-16223-1. arXiv: 2106.15944.

[150] Noriyuki Shimano, Kenichiro Terai, and Mikiya Hironaga. “Recovery of spectral reflectances of objects being imaged by multispectral cameras”. In: *Journal of the Optical Society of America A* 24.10 (2007), p. 3211. DOI: 10.1364/josaa.24.003211.

[151] Noriyuki Shimano and Mikiya Hironaga. “Recovery of spectral reflectances of imaged objects by the use of features of spectral reflectances”. In: *Journal of the Optical Society of America A* 27.2 (2010), p. 251. DOI: 10.1364/josaa.27.000251.

[152] D. E. Aspnes and A. A. Studna. “Dielectric functions and optical parameters of Si, Ge, GaP, GaAs, GaSb, InP, InAs, and InSb from 1.5 to 6.0 eV”. In: *Phys. Rev. B* 27 (2 Jan. 1983), pp. 985–1009. DOI: 10.1103/PhysRevB.27.985.

[153] Xiaoning Zhang et al. “Complex refractive indices measurements of polymers in visible and near-infrared bands”. In: *Appl. Opt.* 59.8 (Mar. 2020), pp. 2337–2344. DOI: 10.1364/AO.383831.

[154] Krishnamurthi Ramesh, Vivek Ramakrishnan, and C. Ramya. “New initiatives in single-colour image-based fringe order estimation in digital photoelasticity”. In: *Journal of Strain Analysis for Engineering Design* 50.7 (2015), pp. 488–504. DOI: 10.1177/0309324715600044.

[155] Ambalanath Shan et al. “High-speed imaging/mapping spectroscopic ellipsometry for in-line analysis of roll-to-roll thin-film photovoltaics”. In: *IEEE Journal of Photovoltaics* 4.1 (2014), pp. 355–361. DOI: 10.1109/JPHOTOV.2013.2284380.

[156] Andrey Nazarov, Michael Ney, and Ibrahim Abdulhalim. "Parallel spectroscopic ellipsometry for ultra-fast thin film characterization". In: *Optics Express* 28.7 (2020), p. 9288. DOI: 10.1364/oe.28.009288.

[157] Jacobus J. van Franeker et al. "Sub-Micrometer Structure Formation during Spin Coating Revealed by Time-Resolved In Situ Laser and X-Ray Scattering". In: *Advanced Functional Materials* 27.46 (2017). DOI: 10.1002/adfm.201702516.

[158] Pascal Picart et al. "Topography of nanometric thin films with three-wavelength digital interferometry". In: *Journal of Micro/Nanolithography, MEMS, and MOEMS* 14.4 (2015), p. 041309. DOI: 10.1117/1.jmm.14.4.041309.

[159] M. J. McPhail et al. "Correcting for color crosstalk and chromatic aberration in multicolor particle shadow velocimetry". In: *Measurement Science and Technology* 26.2 (2015). DOI: 10.1088/0957-0233/26/2/025302.

[160] Yaping Ye et al. "A crosstalk correction method to improve multi-wavelength LEDs imaging quality based on color camera and frame accumulation". In: *Signal Processing: Image Communication* 102.December 2021 (2022). DOI: 10.1016/j.image.2021.116624.

[161] Saif Al-Bashir. "Multi-Wavelength Polarising Interferometer for In-Process Metrology". PhD thesis. University of Huddersfield, 2019.

[162] T.F. Smith and M.S. Waterman. "Identification of common molecular subsequences". In: *Journal of Molecular Biology* 147.1 (Mar. 1981), pp. 195–197. DOI: 10.1016/0022-2836(81)90087-5.

[163] Mitsuo Takeda and Kazuhiro Mutoh. "Fourier transform profilometry for the automatic measurement of 3-D object shapes". In: *Applied Optics* 22.24 (1983), p. 3977. DOI: 10.1364/ao.22.003977.

[164] Moises Padilla, Manuel Servin, and Guillermo Garnica. "Fourier analysis of RGB fringe-projection profilometry and robust phase-demodulation methods against crosstalk distortion". In: *Optics Express* 24.14 (2016), p. 15417. DOI: 10.1364/oe.24.015417.

[165] Carsten Steger. "A Comprehensive and Versatile Camera Model for Cameras with Tilt Lenses". In: *International Journal of Computer Vision* 123.2 (2017), pp. 121–159. DOI: 10.1007/s11263-016-0964-8.

Appendix A

Calibration and training (Chapter 4)

This appendix contains information on the 25 spun coat samples used as calibration (methods 1 and 2) and training (methods 3 and 4) data in Chapter 4. The preparation condition of the samples is contained in Figure 4.4a in the main body of the thesis. Figure A.1 contains information on the recorded spectrums of these samples as they were used for the training and calibration, coloured by thickness obtained from ellipsometry. Table A.1 contains the corresponding colour values recorded simultaneously to the spectrums.

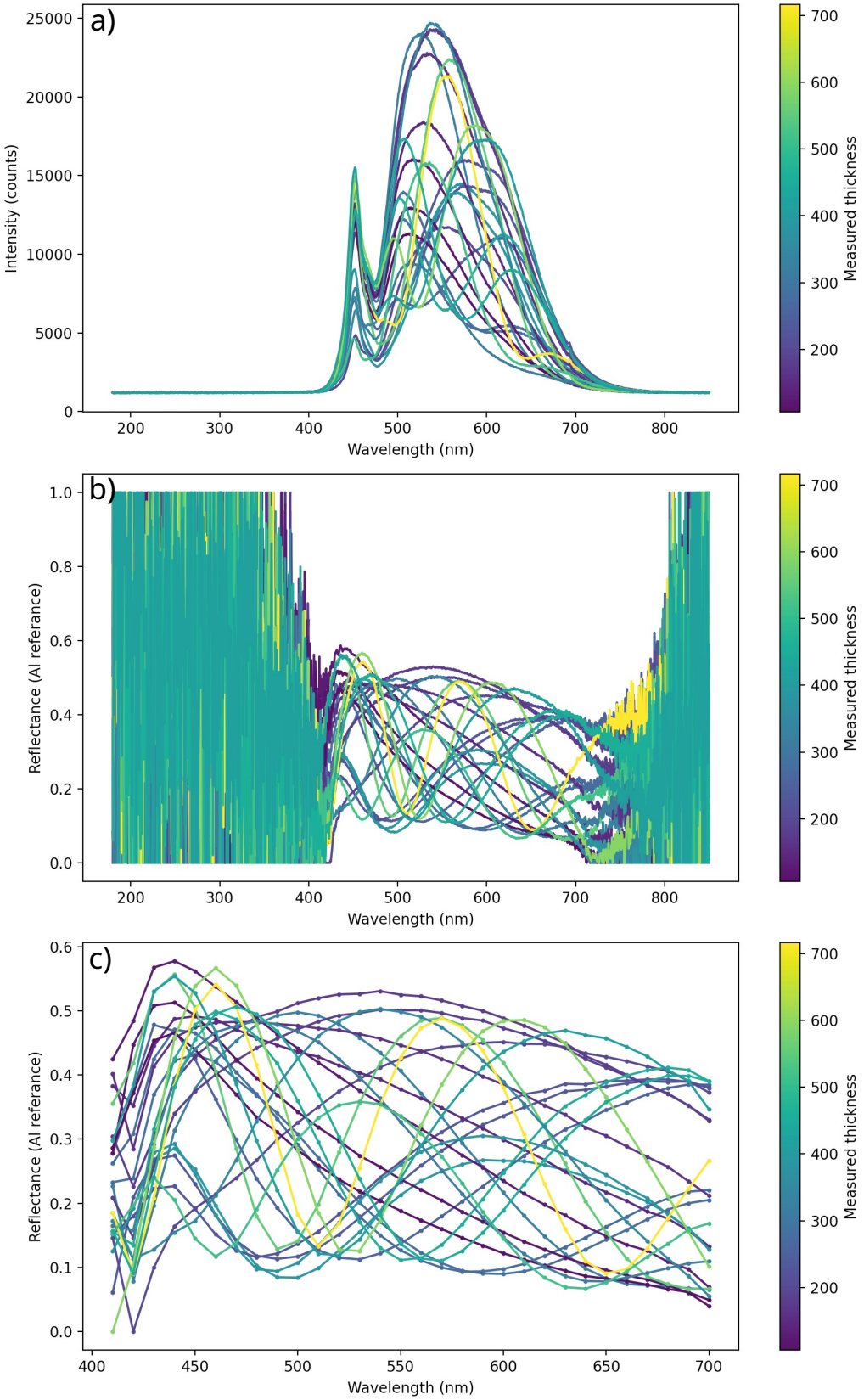

Figure A.1: For each of the 25 (6 channel) training samples is displayed a) raw spectrometer reading b) reflectance spectrum with bare aluminium used as a reference and c) the regularly spaced reflectance spectrum for the spectral reconstruction training dataset

Table A.1: The 3-channel (RGB) and 6-channel (R and T are reflection and transmission respectively) colours recorded from a 700 pixel × 700 pixel ROI at the centre of the images

Sample	R	G	B	R(T)	R(R)	G(T)	G(R)	B(T)	B(R)
1	140.28	167.33	38.69	74.25	90.62	80.51	110.98	14.53	29.86
2	63.60	175.84	56.87	42.32	33.34	101.95	111.32	24.62	44.04
3	40.67	97.68	55.11	20.35	27.15	58.13	55.67	20.06	43.69
4	81.01	85.70	35.21	40.09	60.97	45.11	58.28	11.60	30.46
5	114.48	126.59	27.60	60.84	81.11	66.53	86.36	11.66	20.92
6	44.87	91.88	53.44	21.94	31.40	53.56	52.20	18.65	42.22
7	119.69	136.19	27.58	60.53	70.21	68.07	78.02	11.89	18.03
8	136.60	193.42	39.39	78.83	92.71	110.95	130.50	19.31	28.88
9	125.91	206.52	55.33	75.10	85.21	120.97	140.77	24.95	44.02
10	126.25	222.91	67.34	75.46	75.28	129.19	135.09	28.81	48.46
11	135.23	217.11	55.95	80.81	88.11	128.30	143.02	25.95	43.12
12	105.97	203.87	68.78	62.65	65.63	115.30	129.88	27.85	53.17
13	66.53	146.38	58.16	42.81	42.80	87.54	98.01	23.43	47.50
14	48.78	114.84	51.10	28.46	27.25	63.16	69.04	18.78	39.62
15	38.21	88.12	41.54	21.98	21.16	48.75	52.13	15.16	32.46
16	114.82	182.57	47.10	70.75	58.52	93.78	120.10	18.52	34.07
17	88.64	112.27	55.82	39.17	65.48	70.09	65.50	19.75	46.63
18	138.12	173.09	37.45	77.97	89.00	88.37	114.71	15.82	27.95
19	107.59	210.28	46.12	68.12	62.26	119.41	133.63	23.04	30.94
20	54.93	170.06	63.38	32.80	25.83	92.45	97.55	25.13	48.40
21	88.64	165.08	50.45	62.34	43.70	76.58	122.35	13.72	45.91
22	140.07	152.79	53.40	74.78	83.98	74.98	99.36	14.10	44.43
23	63.13	186.12	43.35	44.16	27.86	104.26	109.33	24.02	24.48
24	71.83	115.93	55.19	29.18	55.09	69.45	67.52	19.73	45.32
25	136.16	139.21	47.03	71.54	92.43	69.59	93.82	14.14	40.08

Table A.2 shows the values used for calibration from simulation value to recorded value, taken from the graphs in Figure 4.4. Figure A.2 shows how the colour values of the 25 spun coat samples compare with the simulation values once they have been calibrated.

Table A.2: The calibration factor applied to each channel for converting from simulation colour values to camera colour values

	R	G	B	R(T)	R(R)	G(T)	G(R)	B(T)	B(R)
Constant	8.753	31.65	5.536	1.194	12.03	14.60	15.30	2.942	2.535
Gradient	9.581	7.578	7.439	11.84	12.03	9.26	9.665	7.652	9.572
CoD	0.953	0.860	0.963	0.956	0.900	0.848	0.884	0.888	0.922

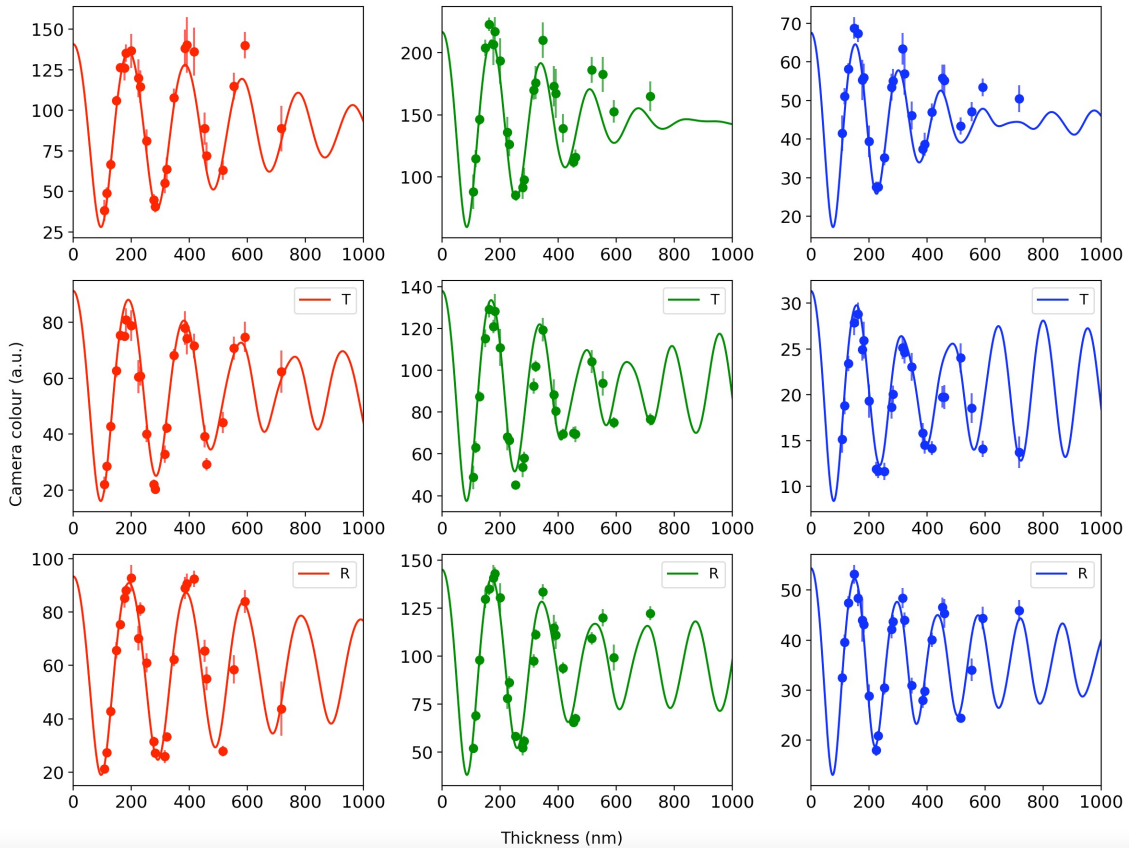

Figure A.2: Simulation values (lines) with the 25 calibrated samples (points) for standard RGB (row 1), RGB transmission (row 2) and RGB reflection (row 3).

Finally, Table A.3 presents the thickness recovery (global minima) of the four methods.

Table A.3: The measured thickness (via ellipsometer) and recovered thicknesses (methods 1, 2 and 3 global minima) of each spun-coat calibration/training sample used for the thickness recovery methods, sorted by ascending measured thickness

Sample ID	Measured Thickness (nm)	Recovered thicknesses (nm)			
		Method 1	Method 2	Method 3	Method 4
1	392	56	45	376	500
2	322	317	323	156	–
3	282	106	278	284	–
4	253	244	239	417	393
5	231	222	215	215	–
6	277	272	274	280	–
7	225	220	214	213	–
8	199	193	53	51	–
9	177	177	0	172	–
10	161	156	167	0	–
11	181	7	0	174	–
12	148	142	142	155	–
13	128	130	127	140	–
14	115	119	117	129	–
15	106	109	110	117	–
16	554	33	30	548	608
17	452	440	436	433	446
18	384	51	49	46	–
19	347	158	345	178	–
20	315	473	105	105	–
21	717	38	694	717	752
22	592	379	381	573	582
23	516	468	117	502	–
24	459	449	449	443	497
25	416	388	387	408	485

A dash (–) indicates where the recovered spectrum did not have enough extrema to compute Δm.